From MAX to MXenes : synthesis, characterization and electronic properties

Lu Shi

UNIVERSITÉ CATHOLIQUE DE LOUVAIN

Ecole Polytechnique de Louvain
Institut de la Matière Condensée et des Nanosciences

FROM MAX PHASES TO MXENES: SYNTHESIS, CHARACTERIZATION AND ELECTRONIC PROPERTIES

Dissertation présentée en vue de l'obtention du grade de docteur en sciences de l'ingénieur

par

Lu Shi

Membres du jury:

Prof. Dr. Benoît Hackens, promoteur (UCL)

Prof. Dr. Thierry Ouisse, co-promoteur (INPG, UGA)

Prof. Dr. Bernard Piraux, président (UCL)

Prof. Dr. Vincent Bayot (UCL)

Prof. Dr. Jean-Christophe Charlier (UCL)

Prof. Dr. Sylvain Dubois (Université de Poitiers)

Prof. Dr. Matthieu Verstraete (Université de Liège)

Louvain-la-Neuve, 2017

Communauté UNIVERSITÉ Grenoble Alpes

UCL Université catholique de Louvain

THÈSE

Pour obtenir le grade de

DOCTEUR DE LA COMMUNAUTE UNIVERSITE GRENOBLE ALPES

préparée dans le cadre d'une cotutelle *entre la Communauté Université Grenoble Alpes* et *l'Université catholique de Louvain*

Spécialité : **Ingéniere-matériaux mécanique énergétique environnement procédés production**

Arrêté ministériel : le 6 janvier 2005 - 7 août 2006

Présentée par

Lu SHI

Thèse dirigée par **Thierry OUISSE**
codirigée par **Benoît HACKENS**

préparée au sein des **Laboratoires des Matériaux et du Génie Physique**

dans **les Écoles Doctorales I-MEP2**

Des phases MAX au MXènes: synthèse, caractérisation et propriétés électroniques

Thèse soutenue publiquement le **12 Décembre 2017**
devant le jury composé de :

Prof. Dr. Sylvain, DUBOIS
Professeur, Université de Poitiers (Rapporteur)
Prof. Dr. Matthieu, VERSTRAETE
Professeur, Université de Liège (Rapporteur)
Prof. Dr. Jean-Christophe, CHARLIER
Professeur, Université catholique de Louvain (Examinateur)
Prof. Dr. Vincent, BAYOT
Professeur, Université catholique de Louvain (Examinateur)
Prof. Dr. Benoît, HACKENS
Professeur, Université catholique de Louvain (Co-directeur de thèse)
Prof. Dr. Thierry, OUISSE
Professeur, Université Grenoble Alpes (Directeur de thèse)

In loving memory of my beloved grandparents

Acknowledgements

After an intensive period of four years, today is the day: writing this note of thanks is the finishing touch on my dissertation. It has been a period of intense learning for me, not only in the scientific arena, but also on a personal level. At the end of this, I should take some time to express my gratitude to those without whom this thesis would never have been possible.

First and foremost I offer my sincerest gratitude to my two enthusiastic supervisors, Prof. Benoît Hackens and Prof. Thierry Ouisse. They have taught me, both consciously and unconsciously, how good experimental physics is done. I appreciate all their contributions of time, ideas, and funding to make my Ph.D experience productive and stimulating. The joy and enthusiasm they have for the research was contagious and inspiring for me, even during tough times in the Ph.D. pursuit. My PhD has been an amazing experience and I thank Benoît and Thierry wholeheartedly, not only for their tremendous academic support, the systematic guidance that put into training me in the scientific field, but also for their patience and kindness helped me overcome tough situations. Thank you to pick me four years ago and offered me this great opportunity to work in two great labs.

I would like then to take a moment to thank my thesis committee members. Thank you to Prof. Sylvain Dubois and Prof. Matthieu Verstraete for being my rapporteurs. Also thank you to Prof. Jean-Christophe Charlier and Prof. Vincent Bayot for being examiners of my thesis. I appreciate greatly of your time investing on my thesis and valuable insights for the thesis revisions. I feel honoured that you have accepted to be on my committee.

I am grateful to LMGP members with whom I have interacted during my first stage of thesis, Didier Chaussende, Jean-Marc Dedulle and Eirini Sarigiannidou for good advices on my research, Odette Chaix for the Raman analysis, Herve Roussel for the

XRD analysis, Joseph La Manna, Serge Quessada and Lucile Parent-Bert for technical support, and Benjamin Piot (LNCMI,CNRS) for helping me with LowT measurements in Grenoble. The members of the Cristallogenese group in LMGP have contributed immensely to my personal and professional time at Grenoble. Special thanks to our closed team members: Nikolaos Tsavdaris, Kanaparin Ariyawong, Yunji Shin, Sven Tengeler, Demitrios Zevgitis, Shiqi Zhang, Hoang-Long Le Tran. From our first Christmas party at Yunji's home to the laser game, rock climbing, weekend hiking, and our magic table always with snacks and beverage at lab, I spent so many joyful and lighthearted moments with all of you. Your great support and accompany all ease the adaptation to the new changes of my life in Europe. And to my friends in Grenoble, my dear roommate Xuexin Ma and Yunxia Yao. I will never forget those moments filled with laughters and tears lighting up this snowy mountain city.

Similar, profound gratitude goes to those with whom I have interacted during my research time in UCLouvain. To members of BSMA, Prof.Luc Piraux for LowT measurement, Delphine Magnin for SEM analysis, Cécile D'Haese for AFM analysis, Sergey Basov and Pedro Sá for helping me changing Helium and endless gas and water pressure checking. Special to Pascale Lipnik for TEM analysis and thanks to your effort, I finally get the TEM results on my samples. To members of MOST, Prof. Sophie Hermans for support of all chemical experiments, Jean-François Statsyns for technical support, Koen Robeyns for crystallography analysis. Special thanks to Nadzeya Kryvutsa, for all the advices and support from chemical side and to be honest, I could not image if the time spending at Building Lavoisier without you. To members of ICTEAM, Ferran Urena Begara for valuable suggestions on the Raman analysis. To members of NAPS, Aurélie Champagne, for all your ideas and discussions on this topic. To members of Winfab, Sébastien Faniel for helps on Ebeam lithography and metal deposition, Ester Tooten for the laser machining, Milout Zitout for the wafer processing. Thank you all for helping my works in Louvain-la-neuve.

I am hugely appreciative to our fun group 'Fridge': Damien Cabosart, Thanh Nhan Bui, Andra-Gabriela Iordanescu, Boris Brun-Barrière, Sébastien Toussaint, Nicolas Moreau, Hui Shang and our previous group member Frederico Matins and Cristiane Nascimento Santos. Starting from the beginning of my presentation for FRIA, they have been a source of friendships as well as good advice and collaboration. Nhan, thank you for you've helped me so much with day and night endless recycling of cooling down and warming up, pumping vacuum and refilling Helium, and for electronic measurement advices; Damien, hey three year's officemate, thank you for your help

on lithography training and advices on the 2D exfoliation and of course, fun jokes; Seb, from all the memories of March meeting to every daily conversations we've shared, you are like walking encyclopaedia to me; and Andra, you are so earnest with generous heart, thanks for all your warm-hearted encouragement and support and all the sweets to cheer me up. My dear group members, you have offered much advices and insights throughout my work by your knowledge and for nurturing my enthusiasm for solid state physics. You guys have never refused any of my requests and do me favours as possible as you could. I would never forget all the discussions and tremendous moments spending with you all.

I am deeply thankful to my maman belge, Claire Schollaert-Nguyen and my papa belge Pierre Nguyen and their family members, Claude, Marianne, Nathalie, Pascale and petite Ambre. Leaving home to go and study in another country is an exciting prospect, while also quite challenging. Almost three years staying with this family, they are so thoughtful and generous in sharing and giving, how can I ever thank them enough for all they've done for supporting my life here. And to whom I met in the house, Marta Rabbione, my best Italien friend for your heart-warming supports through all my difficult times.

Very special gratitude goes to my closed friend in Louvain-la-neuve, Meng Liao, Xiaomeng Zhang, Xiaoya Li, Shouwei Zhang, Zimin Li, Xiaoqin Gao for all the emotional support, friendship, and joyful memories. I cannot image the life in Louvain-la-neuve without you all, you always gave me a power and the words inspired me. As a member of the IDS-Funmat project, I also would like to thank my IDS-Funmaters, the friendship with them is irreplaceable. Not remembering how many times passing the night and waking up alone at A1 floor, I feel also grateful to someone who accompanied me for the experiments till late midnight during weekends and the most lovable coffee machine of BSMA cafeteria.

Finally, but by no means least, to my mum Lihua Qin, my dad Jianmin Shi and to all my family members in China for their long-lasting and unwavering support. During my thesis, I lost two most important and beloved persons in my world, my beloved grandma and grandpa. Life is never predictable, in which I will never know if it is right to quit the job and leave away from home, yet, the one and only certain thing is that you two would be so proud of me, right? my dearest grandma and grandpa. I still remember the day you sent me to the airport, and will always remember the things you have taught me and how much you love me. I dedicate this thesis to you, my beloved grandparents.

Abstract

During recent years, new types of materials have been discovered with unique properties. One family of such materials is two-dimensional (2D) materials with unusual electronic, mechanical and optical properties, which led to their extensive study for diverse applications. Transition metal carbides, carbonitrides and nitrides (MXenes) are among the latest additions to the 2D world, which are derived from their layered precursors, MAX phases, layered early transition metal ternary carbides and nitrides, composed of M, an early transition metal, A, a group A element and X is C and/or N. In this thesis, as its self-telling title indicates, we present our work on the synthesis, structural characterization and the electron transport in the MAX phases and 2D MXenes.

For MAX phase: using high temperature solution growth and slow cooling technique, several MAX phases single crystals have been successfully grown, including Cr_2AlC, V_2AlC, Ti_3SiC_2, etc. Structural characterization confirms the single crystalline character of the samples. Experimentally, a set of transport data was obtained from single crystals of V_2AlC and Cr_2AlC as a function of temperature and magnetic field. Theoretically, a general 2D nearly free electron model was proposed for describing the weak field magneto-transport properties of MAX phases.

For MXene: large scale V_2CT_x (T stands for the surface terminations, hydroxyl, oxygen or fluorine)) MXene flakes were successfully synthesized. Mechanical delamination of multilayered V_2CT_x flakes into few layer flakes and transfer on the substrate was also achieved. We then detailed the electrical device fabrication and proceeded with electrical measurements down to low temperature, with the aim to extract information on charge carrier behaviour. First-hand transport data were obtained on V_2CT_x MXenes, which brings new understandings to this novel type of 2D material.

Contents

Introduction

MAX phases are layered early transition metal ternary carbides and nitrides so called because they are composed of M, an early transition metal, A, a group A element and X is C and/or N. MAX phase structure is composed of near close-packed planes of M atoms with the X atoms occupying all the octahedral sites between them. They combine some of the best properties of ceramics and metals. Their physical properties (stiffness, damage and thermal shock resistance, high thermal and electrical conductivity) along with the fact they are readily machinable, make them extremely attractive in terms of the potential technological applications.

In 2011, it was discovered that by immersing Al-containing MAX phases in hydrofluoric(HF) acid, it was possible to selectively etch the Al, resulting in two-dimensional (2D) materials, that were labelled MXene to denote the removal of the A-group element and make the connection to another conducting 2D material, graphene. This new member of 2D materials family owns stronger, more chemically versatile, and have higher conductivity than other materials. As such they are highly interesting on new applications, e.g. specialized in vivo drug delivery systems, hydrogen storage, or as replacements of common materials in e.g. batteries, sewage treatment, and sensors. The list of potential applications is long for these new materials.

In this thesis, as its self-telling title indicated, we present our work on the synthesis, structural characterization and the electron transport in the MAX phases and their 2D derivatives, MXenes.The manuscript is organized as follows:

Chapter 1 An general introduction of MAX phases and its derivative MXene is given, including lattice and electronic structure, experimental and theoretical research work on synthesis, characterization and properties.

For MAX phase:

Chapter 2 Motivated by the theoretically expected anisotropic properties of these layered materials, producing bulk single crystals is a natural way to obtain samples where the anisotropy of the physical properties can be experimentally probed. Also, knowledge of low-temperature behaviour of single crystal is vital because it can provide insight into MAX intrinsic physical properties. Using high temperature solution growth and slow cooling technique, several MAX phases single crystals have been successfully grown. Structural characterization confirms the single crystalline character of the samples.

Chapter 3 Experimentally, a set of experimental data are obtained from single crystals of V_2AlC and Cr_2AlC as a function of temperature and magnetic field. In comparison with the resistivity of polycrystalline samples, that of Cr_2AlC and V_2AlC, are correspondingly much lower. In particular, we obtain a substantial anisotropy ratio between the in-plane and c-axis resistivity, in the range of a few hundreds to thousands. From Magneto-resistance and Hall effect measurement, in-plane transport behaviours of MAX phases have been studied.Theoretically, a general model is therefore proposed for describing the weak field magneto-transport properties of nearly free electrons in 2D hexagonal metals, which is then modified to be applicable for the transport properties of layered MAX phases.

For MXene:

Chapter 4 We report on a general approach to etch V_2AlC single crystal and mechanically exfoliate multilayer V_2CT_x (T= termination group, -OH, -F, =O) MXenes. We then investigate the structural characterization of the obtained MXene by means of XRD, SEM, TEM, Raman and AFM techniques. The second part of this chapter discusses the process with the aim of obtaining Ti_2CT_x MXene from Ti_2SnC single crystals.

Chapter 5 We then further pursuit the electrical device fabrication process and proceeded with electrical measurements, performing down to low temperature, with the aim to extract electronic transport parameters. We successfully attain some first hand data on V_2CT_x MXenes, including the average value for the resistivity of V_2CT_x MXenes, the filed effect measurement indicates field effect mobility μ_{FE} and the Hall mobility μ_H, which contributes to the understanding of this class of materials.

chapter 1

From MAX phases to MXene: Background, History and Synthesis

This introductory chapter aims to bring a brief overview of MAX phases and its derived two-dimensional (2D) material-MXene.

In the first part, the history of MAX phases is given, including the salient properties and the status of current understanding of the MAX phases. Their potential applications are also highlighted. The up-to-date theoretical and experimental understandings on the electronic transport properties of MAX phases are reviewed as well.

The second part is dedicated to the discovery of 2D MXene, encompassing both theoretical and experimental studies of relevance to their synthesis, properties and potential applications in the field of transparent conductors, environmental treatment and energy storage.

1.1 MAX phases

1.1.1 History of MAX phases

Back up to the 1960s, Nowotny's group discovered one kind of new carbides and nitrides, so-called "Hagg phases" or "H phases" with chemical formula of M_2AX, which are constituted by the M_2X units (where M is transition metal, X is C and/or N), separated by the A-element plane (mostly IIIA or IVA element of periodic table). These phases remained largely unexplored until the 1990s, when the breakthrough accomplished by M.W. Barsoum triggered its renaissance and the term $M_{n+1}AX_n$ phase was applied for the first time by him in 2000 [1]. Since then, MAX Phases have become known as an emerging class of ternary carbides and nitrides which bridge the gap between typical properties of metals and ceramics.

They follow the general formula $M_{n+1}AX_n$, where M represents an early transition metal, A represents an A group element (mainly IIIA, IVA), X represents C and/or N, and n=1, 2, 3. The M_2AX, M_3AX_2 and M_4AX_3 phases are usually referred to as 211, 312 and 413 phases respectively, depending on the values of n. Experimental or calculated evidences have also been advanced for the existence of higher order MAX phases such as 514, 615 and 716 [2]. Figure 1.1 shows elements in the periodic table that commonly form MAX phase compounds. More than 60 MAX phases have been synthesized to date, most of them in polycrystalline bulk form.

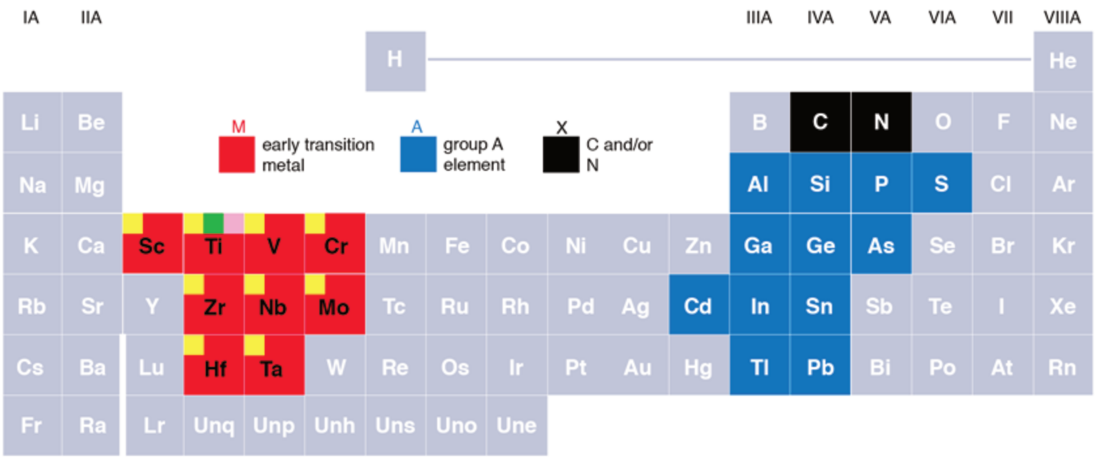

Figure 1.1: *Periodic table illustrating elements forming all MAX phases known to date [3].*

1.1.2 Structure of MAX phases

MAX phases acquire a hexagonal layered structure with space group $P6_3/mmc$ with two formula units per cell. They consist of alternate near close-packed layers of [M6X] octahedral interleaved with layers of pure group A-atoms. The [M6X] octahedral are connected to each other by shared edges. The main difference, in terms of the structures, among so called 211, 312 and 413 phase, is the numbers of M layers between every two A layers. As can be seen in Figure 1.2, two M layers are intercalated between two A layers in 211 phase, three M layers and four M layers between two A layers in 312 and 413 phase, respectively. It also shows the corresponding unit cell with nanolamelar structure where the presence of metallic M-A bonds and covalent M-X bonds results in a combination of metallic and ceramic properties.

MAX phases are typically good thermal and electrical conductors, as well as thermodynamically stable at high temperatures and oxidation resistant. MAX phases exhibit extreme thermal shock resistance, damage tolerance and are easily machinable. All these characteristics make MAX phases promising candidates for various industrial applications.

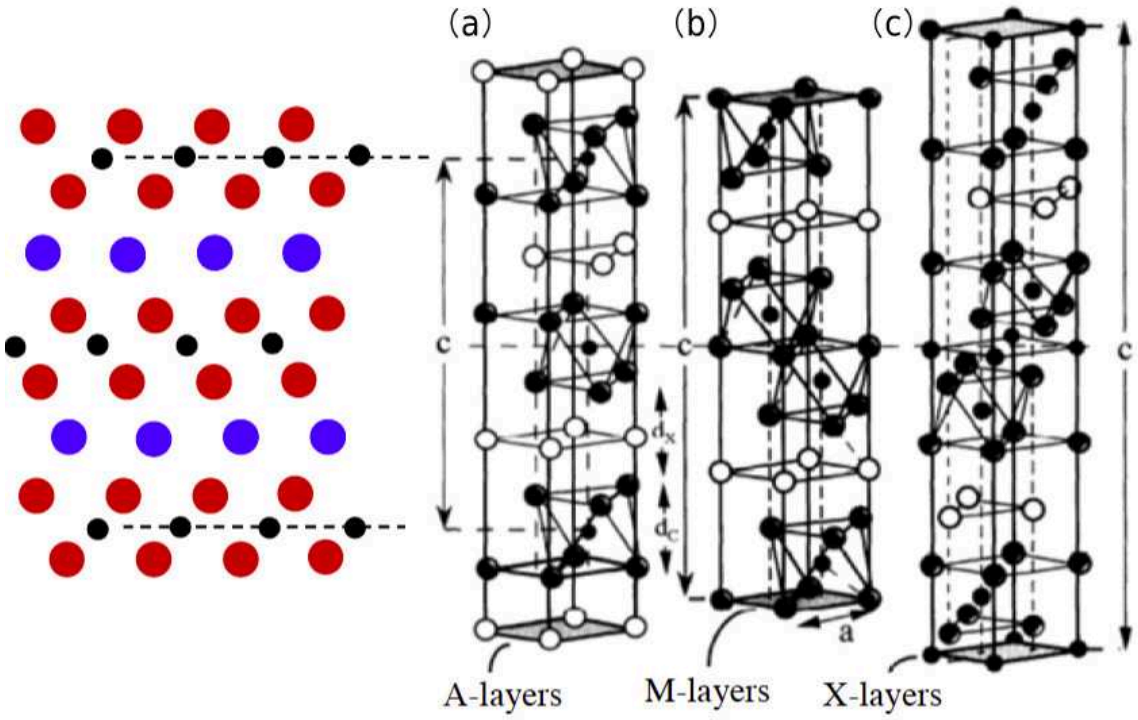

Figure 1.2: *Unit cell of representative MAX phase for (a) 211 (b) 312 (c) 413 [4].*

1.1.3 Synthesis of MAX phases

In last two decades, substantial efforts have been placed on the synthesis and characterization of MAX phases. Here we summarize the methods applied to synthesize MAX phase powders, bulk material and thin films. We can see from the Table 1.1 that, up to now, most of MAX phases are usually produced in a highly polycrystalline form, except in a limited number of reported cases dealing either with thin single-crystalline layers [5], or single-crystalline platelets [6]. Producing bulk single crystals is a natural way to obtain samples where the anisotropy of the physical properties can be experimentally probed, and which can also be used for developing technological processes leading in turn to the production of macroscopic two dimensional MXene samples with acceptable area. Until recently, the difficulty to produce single crystal MAX phases prohibited a thorough investigation of their physical properties. In 2011, our LMGP team found the way to produce such single crystals [7, 8], and this opened the door to new lines of research in a field which already triggers an intense international research activity. More details about the crystal growth of MAX phases will be discussed in Chapter II.

1.1.4 Electronic properties of MAX phases

From various aspects, MAX phases exhibit interesting and unusual properties. The present thesis will mainly focus on their electrical properties. Herein, we will summarize some of magneto-electronical transport properties of MAX phases in polycrystalline form. In order to highlight the electrical conduction mechanism in the MAX phases, Hall effect, Seebeck Effect and magnetoresistance measurement are presented.

1.1.4.1 Resistivity

In general, most of the MAX phases are excellent metal-like electrical conductors, particularly, the conductivity of MAX phases is higher than that of the corresponding binary transition metal carbides or nitrides. Some of them, such as Ti_3SiC_2, Ti_3AlC_2 , are better conductors than Ti itself. Up to now, the resistivity of most studied MAX phases was found to be metallic-like: in the phonon-limited regime, the resistivity, ρ, increases linearly with increasing temperature. This behaviour can be described by a linear fit according to the relation

$$\rho(T) = \rho_0[1 + \beta(T - T_{RT})] \tag{1.1}$$

	Method	Example	Reference
Powder	Mechanical Alloying (MA)	Ti_3SiC_2	[9]
	Self-propagating high-	Ti_3AlC_2	[10]
	temperature synthesis(SHS)	Ti_2AlC	[11]
	(in-situ)Solid state reaction pressure-less sintering	Ti_3SiC_2	[12][13]
Bulk materials (Polycrystalline MAX and its composites	Hot isostatic pressing (HIP) sintering	Ti_3SnC_2,Ti_2SnC	[14]
		Hf_2PbC, Zr_2PbC	[15]
		V_2AlC	[1]
	Hot pressing (HP) sintering	Cr_2AlC	[16]
		Nb_2AlC	[17]
	Spark plasma sintering (SPS)	Ti_3SiC_2	[18]
		Ti_2AlC	[19]
Thin film	Slip casting (SC)	Ti_3AlC_2	[20]
	Physical vapor deposition(PVD)	Ti_3GeC_2,Ti_2GeC	[21]
	Chemical vapor deposition (CVD)	Ti_3SiC_2	[22]
	Solid-state reactions	Ti_2AlN	[23]
	Thermal spraying	Ti_2AlC	[24]

Table 1.1: *Synthesis of various forms of MAX phases.*

where ρ_0 is the resistivity at room temperature, β is the temperature coefficient of resistivity expressed in K^{-1} [3, 25]. The temperature coefficient of the resistivity is an essential factor which provides information about the electron-phonon coupling. It is well known that at low temperature, lattice defects and impurity atoms affect the resistivity and limited to a constant value, which is called the residual resistivity. Therefore, residual resistivity ratio ($RRR = \rho(RT)/\rho(LT)$) is used to indicate the degree of defects. The high RRR value reflects a low degree of defects or impurities in crystals. The temperature dependences of resistivity of different MAX phases are shown in Figure 1.3. The physical properties of ceramics are very sensitive to synthesis processes and crystal quality, and most importantly, grain boundaries are types of the defects playing a crucial role in the transport properties. So it is expected that the RRR value of single crystal MAX phases will be higher than their polycrystalline counterparts.

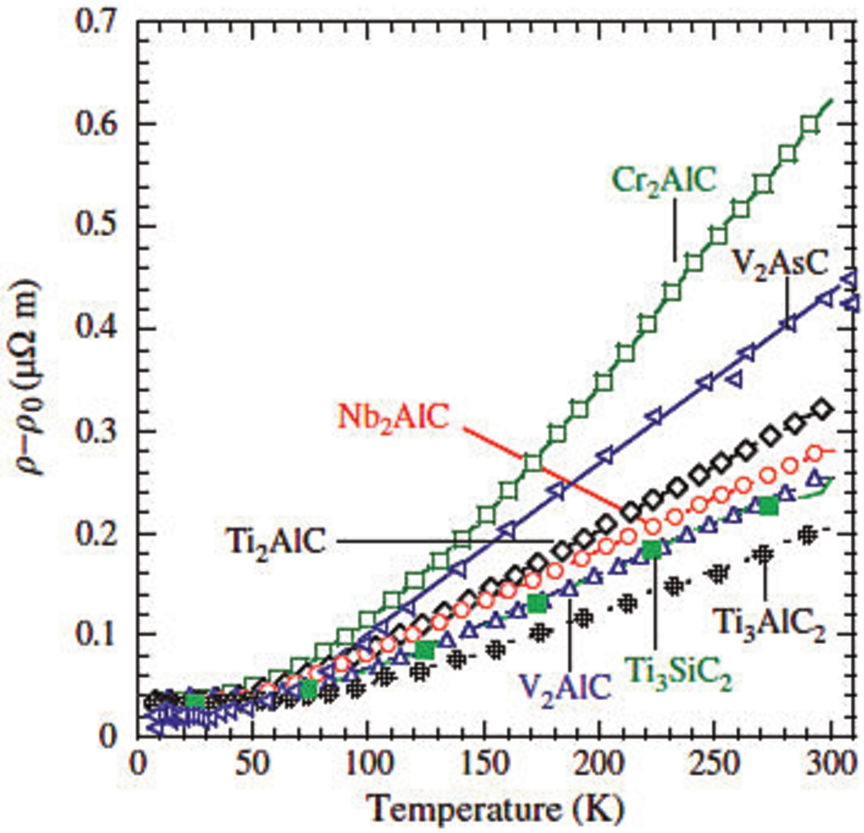

Figure 1.3: *Temperature dependence of resistivity of selected MAX phases [26].*

1.1.4.2 Hall Coefficient and magneto-resistance

In order to fully investigate electronic transport, charge carrier density and mobility should be identified. Typically, Hall coefficient (R_H) measurement are used to obtain

the charge carrier concentration and type of majority charge carriers. Table 1.2 is a summary of the available Hall constants for MAX phases at room temperature. We can see from Table 1.2 that R_H of MAX phases, like most other metallic conductors, has quite small value. The measured Hall coefficients tend to fluctuate around zero and give either slightly positive or negative values.

Furthermore, most MAX phases exhibit a quadratic, positive, non-saturating magnetoresistance where the MR is defined as $\triangle\rho/\rho = \frac{\rho(B)-\rho(B=0)}{\rho(B=0)}$.

The combination of small R_H , the linearity of the Hall voltage with magnetic field and finally the parabolic non saturating magnetoresistance strongly suggested that most of the MAX phases are compensated conductors [27, 28, 29]. An assumption on the fact that both electron-like and hole-like states contribute approximately equal to the electrical conductivity allows to interpret the transport data by using traditional two band model. The electrical conduction is assured by electrons and holes and it is described by the relation

$$\sigma = \frac{1}{\rho} = e(n\mu_n + p\mu_p) \tag{1.2}$$

where e is the electronic charge, n and p are the electron and hole densities, μ_n and μ_p are electron and hole mobilities.

The R_H in low field limit is defined by

$$R_H = \frac{(p\mu_p^2 - n\mu_n^2)}{e(p\mu_p + n\mu_n)^2} \tag{1.3}$$

The magnetoresistance behaviour is described by the following expression

$$MR = \frac{\triangle\rho}{\rho(\mathrm{B=0})} = \alpha B^2 \tag{1.4}$$

where B is the magnetic field and α is the magnetoresistance coefficient. For two types of carriers, the two band model is required and α is given by

$$\alpha = \frac{np\mu_n\mu_p(\mu_n + \mu_p)^2}{(n\mu_n + p\mu_p)^2} \tag{1.5}$$

In these equations, n, p , μ_n and μ_p are unknown. Assuming that MAX phases are compensated conductors lead to n=p which allows simplifying the Eqs 1.2 1.3 and

1.5 where the conduction is governed by either electrons or holes, these relations are simplified to:

$$\sigma = \frac{1}{\rho} = en(\mu_n + u_p)$$

$$R_H = \frac{(\mu_p - \mu_n)}{en(\mu_p + \mu_n)} \tag{1.6}$$

$$\alpha = \mu_n \mu_p \tag{1.7}$$

If we assume that, $\mu_n = \mu_p$, then this implies that R_H=0. The mobility values are close to each other as deduced from 1.6 and relatively low value of measured R_H. The electron-like and hole-like mobilities were determined by Barsoum and co-workers[27, 28, 29, 30], the results are summarized in the Table 1.2.

From the results listed, it is suggested that MAX phases can be considered as compensated conductors and a traditional two band model seems to give the range of magnitude for the mobility and charge carrier density: charge carrier densities are typically in the range of 1.1- 6.3 $\times 10^{27}$ m^{-3} and both n and p are temperature independent due to their metal-like character. Mobilities are in the range of (0.55-9) $\times 10^{-3}$ $m^2/V{\cdot}s$.

1.1.5 Electronic band structure of MAX phases

The electronic structure of a large number of MAX phases has been calculated through Density Functional Theory(DFT). In general, simulation results show that there is no gap between the valence band and the conduction band of MAX phases, which is consistent with metal-like conductivity as demonstrated experimentally. At the Fermi level, the total densities of states (TDOS) is mainly dominated by M 3d states, suggesting that the 3d states of the M element dominate the MAX phase's electronic conductivity. In this section, we will focus on the electronic band structure and DOS of 211 phase (Cr_2AlC and V_2AlC) and one 312 phase (Ti_3SiC_2), which are the main phases involved in the present experimental work.

1.1.5.1 Cr_2AlC

The crystallographic, electronic, dielectric function and elastic properties of Cr_2AlC were studied by means of pseudo-potential plane-waves method using the density functional theory. The energy band structure of Cr_2AlC is shown in Figure 1.4(a)[31].

MAX	ρ_0	R_H	n	p	μ_n	μ_p	α	Ref.
	($\mu\Omega$·m)	(10^{-11} m^3/C)	(10^{27} m^{-3})	(10^{27} m^{-3})	($10^{-3}m^2$/V·s)	(10^{-3} m^2/V·s)	(T^{-2})$10^{-5}m^4/V^2{\cdot}s^2$	
	300K, 4K	300K, 4K	300K mobility		300K density		300K	
Ti_2AlC	0.36 , 0.07	-27 , -8	1.39	1.2	5.1	5.1	2.6	[30]
Ti_2AlN	0.25 , 0.03	-3.9 , 6.1	1.02	1.05	12	12	17	[30]
Ti_2AlCN	0.43, 0.17	45.6 , 60	1.1	1.8	5.9	5.9	3.5	[30]
V_2AlC	0.26 , 0.04	-10 , -6.5	2.7	2.7	4.6	3.9	2	[26]
Cr_2AlC	0.74 , 0.15	15 , 0	1.2	1.2	3.4	3.6	0.73	[26]
Nb_2AlC	0.39 , 0.14	-25 , -37	2.7	2.7	3.8	3.1	0.9	[26]
Ti_3SiC_2	0.22 , 0.03	38 , 30	2.65	2.65	6	5	2.65	[28][29]
Ti_3GeC_2	0.28 , 0.05	18 , 2.5	1.5	1.5	9	8	15	[28]
Ti_3AlC_2	0.35 , 0.18	-1.2, 1.0	6.3	6.3	1.4	1.41	3.7	[30]
Ti_3AlCN	0.40 , 0.27	17.4 , 33	2.5	2.5	3.5	2.5	0.03	[30]
Ti_4AlN_3	2.61	90, 90	3.5	3.5	0.55	0.55	0.03	[27]

Table 1.2: *Summary of electrical transport parameters of some MAX phases that have been measured.*

The Fermi level is set to 0 eV. One can notice that there are many bands crossing the Fermi level, no gap between the valence band and conduction band, suggesting that Cr_2AlC would demonstrate metallic conductivity.

Moreover, these bands around Fermi energy are mainly from Cr 3d states, indicating Cr 3d states dominate the conductivity of Cr_2AlC. One can also notice that, no band is crossing the Fermi level along the short H-K, Γ-A and M-L directions (*c*-axis direction) whereas many bands are crossing the Fermi level along the Γ-K and Γ-M directions (directions located in the basal plane). Such result suggests a very strong anisotropy of the electronic properties (might give zero conductivity along the *c*-axis direction).

The DOS and LDOS of Cr_2AlC is shown in Figure 1.4(b). The lowest states around 10 eV below the Fermi level, originate from C 2s states, which are separated from the upper part of the valence band. The upper part of the valence band mainly consists of Cr 3d, C 2p, Al 3s and Al 3p states. The Cr_2AlC valence band shows the hybridizations of Cr 3d - C 2p(from −7 to −3.7 eV) and Cr 3d - Al 3p (from −3.1 to −1.6 eV), implying strong ionic-covalent Cr-C bonds and weaker Cr-Al ones. At the Fermi level, pure Cr d states are predominant, indicating that, in a first approximation, the electronic properties of Cr_2AlC are dominated by the Cr d states.

The charge density contour is shown in Figure 1.4(c) for the Cr-C bonds in Cr_2AlC and the metastable rock salt structure CrC with space group $Fm\bar{3}m$. Comparing the charge density of the Cr-C bonds in both phases the similarity is prominent. The ionic and covalent contribution to the overall bond character in the cubic CrC phase are essentially conserved in Cr_2AlC, as can be seen from the charge density around Cr and between the Cr and C atoms in both structures. It can be concluded that the bonding is characterized by covalent and ionic contributions and that this character is essentially conserved in the M_2AC ternaries. The chemical bonding in both materials therefore appears to be rather similar.

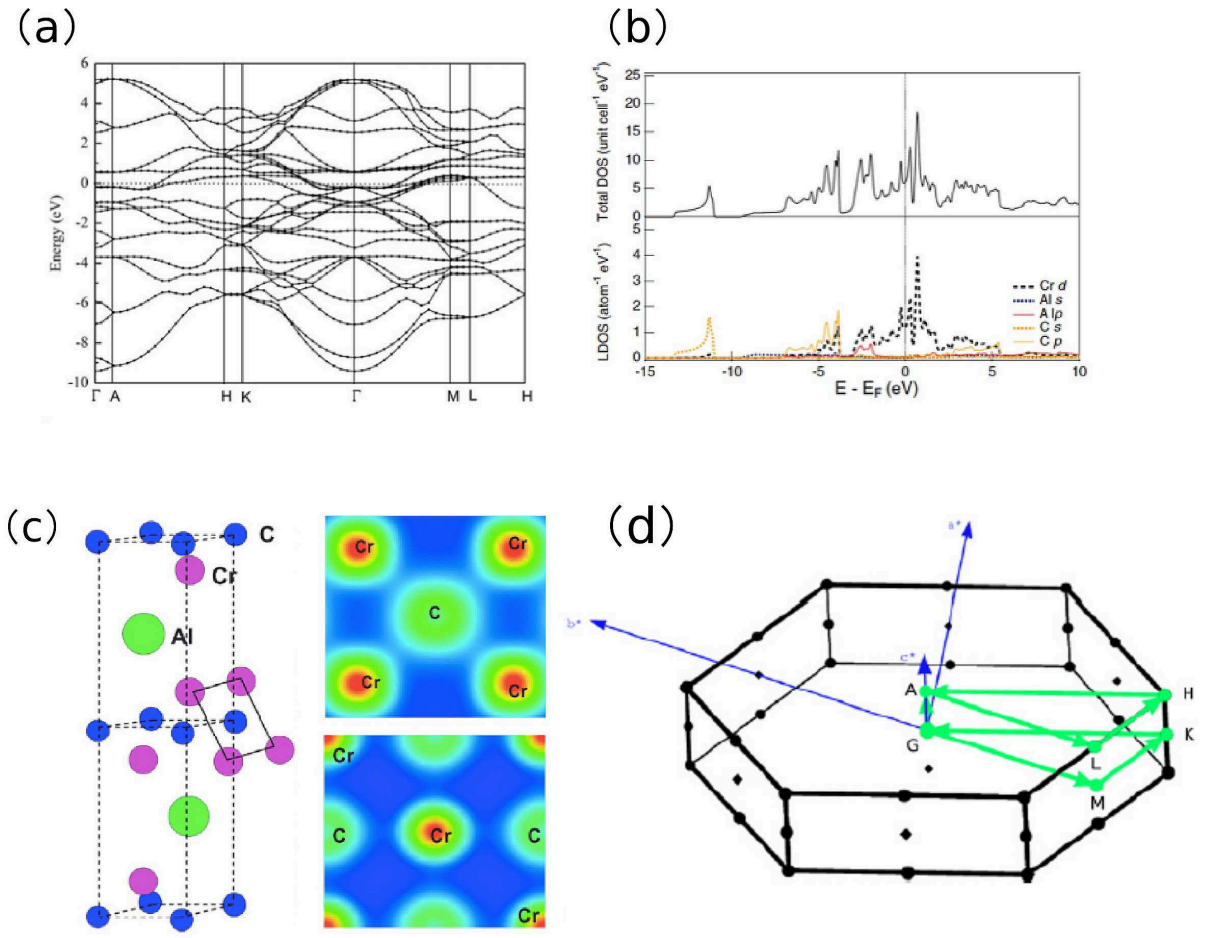

Figure 1.4: *(a) Energy band structure of Cr_2AlC [31] (b)Total and local DOS of Cr_2AlC [32] (c) Charge density contour for the Cr-C bond. upper image:in Cr_2AlC for a cut in the plane marked in left structure. down image: in rock salt structure CrC for a cut in the (100) plane [33] (d) Primitive Brillouin zone of the hexagonal unit cell.*

1.1.5.2 V_2AlC

For the case of V_2AlC, as is shown in Figure 1.5, the metallic nature can be observed with the bands crossing the Fermi level. Also, around Fermi level, weak energy dispersions along M-L and Γ-A directions appeared, which leads to anisotropic character of the conductivity in this compound (i.e., a weaker conductivity along the *c*-axis).

Previous discussions on Cr_2AlC have demonstrated that the hybridized M 3d - C 2p states dominate the bonding of this type of MAX phase. The calculated V_2AlC confirmed such conclusions again, and demonstrates that Al p states also contribute to the orbital bonding. Further analysis of PDOS shows that the hybridization peaks V 3d - C 2p are located at a lower range with respect to that of V 3d - Al 3p, suggesting a stronger V- C bond but a weaker V - Al bond. Actually, the valence DOS can roughly be divided into three major regions: (i) from −12 eV to −10 eV with mainly C 2s states,

which is mainly because of the localized or tightly bound electrons; (ii) from −6.5 to −1.0 eV with strongly hybridized V 3d and C 2p or Al 3p states; and finally (iii) from −1.0 eV to 0 eV with mainly V 3d states. The Fermi level is situated halfway between the peak and the valley, which leads to the stability and conductivity of these materials.

In comparison between DOS of Cr_2AlC and V_2AlC, difference in bonding between two structures can be inferred from the weakly hybridized M 3d - A 3p states which are closer to the Fermi level for V_2AlC (−2 eV) than for Cr_2AlC (−2.5 eV), which indicates that the V-Al bond is slightly weaker than the Cr-Al bond. Meanwhile, similarities can also be concluded as M 3d - C 2p bonds are stronger than M 3d - A 3p bonds, which therefore is mainly responsible for the high modulus and strength of both M_2AlC MAX phase. The metal-like behaviour of electronic properties is attribute to the M 3d states near Fermi energy level.

From the electron band structure of both cases, it is clearly indicated that, for both Cr_2AlC and V_2AlC, the bands are much less dispersive (or even no crossing) along the *c*-axis than along the basal plane, suggesting that the electronic properties of both MAX phase are anisotropic. The Fermi velocity ($\frac{\partial E}{\partial k}$) along the basal plane is higher than that along the *c*-axis.

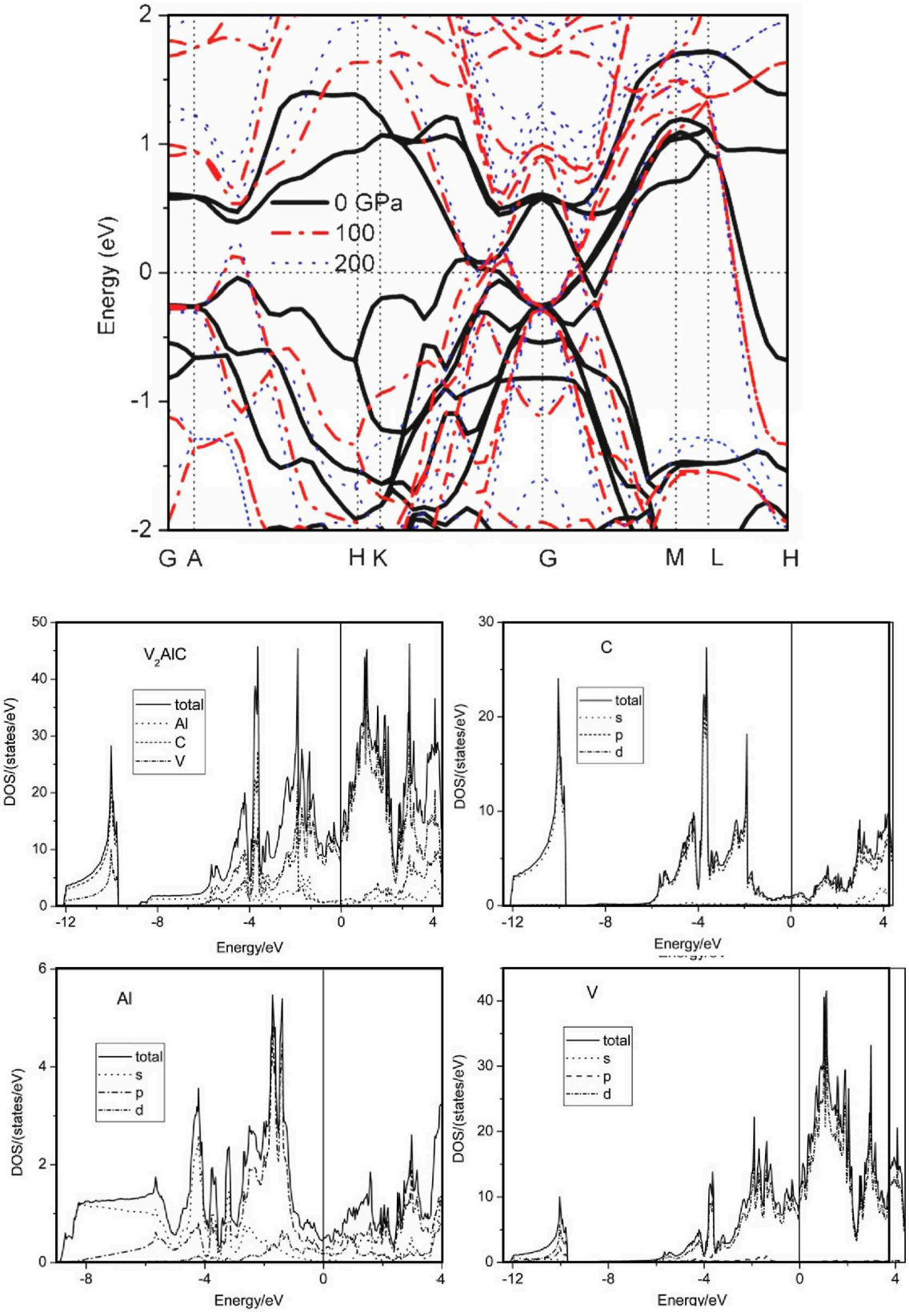

Figure 1.5: *Band structure of V_2AlC via first principles under different pressures [34] (upper image) and TDOS and PDOS (down image)of V_2AlC [35].*

1.1.5.3 Ti_3SiC_2

Herein, we would like to discuss Ti_3SiC_2 as representative of 312 MAX phases, whose thermopower S is almost zero over a wide range of temperature [36]. First of all, it is essential to distinguish two independent type of M element: Ti(1) and Ti(2) as in the Figure 1.6(a) illustrating the crystal structure and the electronic orbitals across and in the laminate plane for Ti_3SiC_2. In general, Ti(2) 3d states less contributes to the Ti 3d- Si 3p chemical bonding because Ti(2) atoms are located in between two octahedral layers. Electronic band structure of Ti_3SiC_2 presented in the Figure 1.6(b) exhibits similar anisotropic features as 211MAX phases, in which near Fermi level there is almost no band crossing the Γ-A, M-L and few along H-K direction while there are large numbers of bands crossing along Γ-K, Γ-M.

Moreover, it is demonstrated by theoretical calculation that Ti_3SiC_2 presents hole-like properties along the basal plane and electron-like properties along the *c*-axis, as experimentally proved by the different sign of Seebeck coefficient along two directions. Two particular bands are also shown on their Fermi surface in Figure 1.7(a) [37]. The Fermi surface of the upper band is very flat and is located around the c/2 plane. Since the velocities are normal to the Fermi surface they are mainly along the c-axis direction. It explains the predominant role of this band along the c component and its relatively minor role in the basal plane. On the other hand, the normals to Fermi surface of downside band have large components in the ab plane and therefore contribute to the component in the basal plane. Evidence for the anisotropic thermopower of Ti_3SiC_2 has also been given by Magnuson [38] that in the polycrystalline bulk sample, the Seebeck coefficient is about zero whereas a positive value in the range of 4-6 μV/K is measured on (000l)-oriented thin film, as shown in 1.7(b).

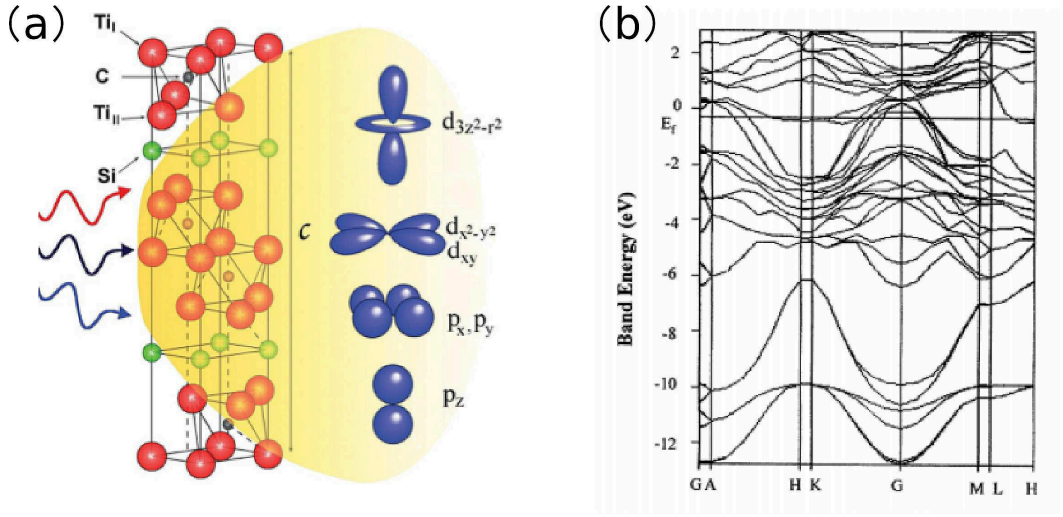

Figure 1.6: *Crystal structure [38] and electronic band structure of Ti_3SiC_2 [39].*

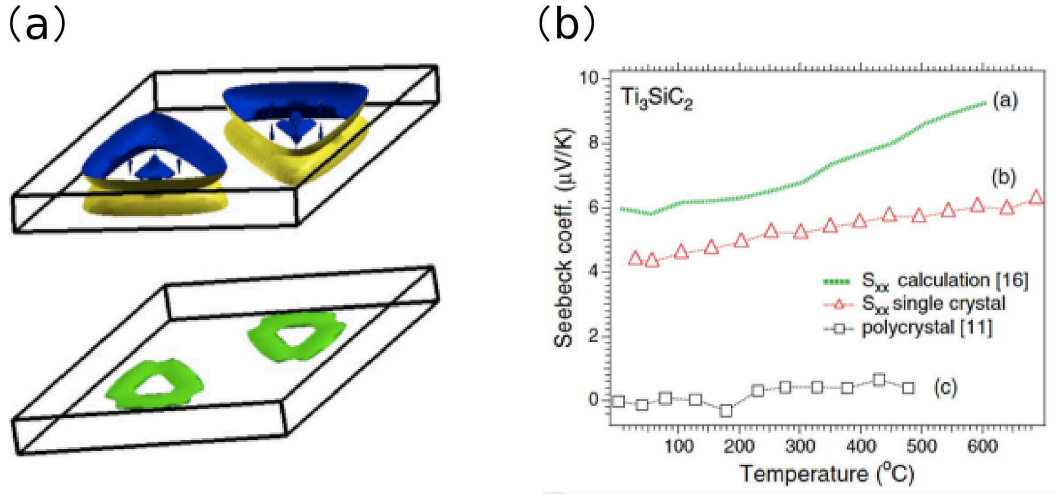

Figure 1.7: *(a) Fermi surfaces for two adjacent bands crossing Fermi level indicating hole-like (upper) and electron-like features (down) [37] and (b) calculated and measured Seebeck coefficients of Ti_3SiC_2(a (000l)-oriented thin film of Ti_3SiC_2(triangle) and polycrystalline sample (square) [38].*

1.1.6 PhD work on MAX phase

The primary objective of the present PhD thesis is to deal with the synthesis of single crystal MAX phases (Cr_2AlC and V_2AlC) and the characterization of their intrinsic properties. Thermodynamics and kinetics of crystal nucleation and growth were deduced from the synthesis of different single crystal MAX phases (See Chapter II).

The main physical properties, mainly magneto-electronic transport properties of the MAX phases were also studied and the consistency of results obtained in experiments and from simulations was checked. More specifically, probing the anisotropic properties was also achieved thanks to the crystalline samples (See Chapter III).

1.2 MXene

1.2.1 2D materials

1.2.1.1 2D family

Since the pioneering work on graphene, world-wide enthusiasm for 2D materials including inorganic graphene analogues (IGAs) has rapidly grown. These IGAs include hexagonal boron nitride (h-BN),transition metal oxides and hydroxides, transition metal dichalcogenides (TMD), etc. Due to the fact that the thickness is significantly smaller than the other two dimensions, which always results in dramatic changes in electronic structure and lattice dynamics, these 2D materials exhibit unique properties compared with their three-dimensional counterparts. Figure 1.8 represents current 2D materials families.

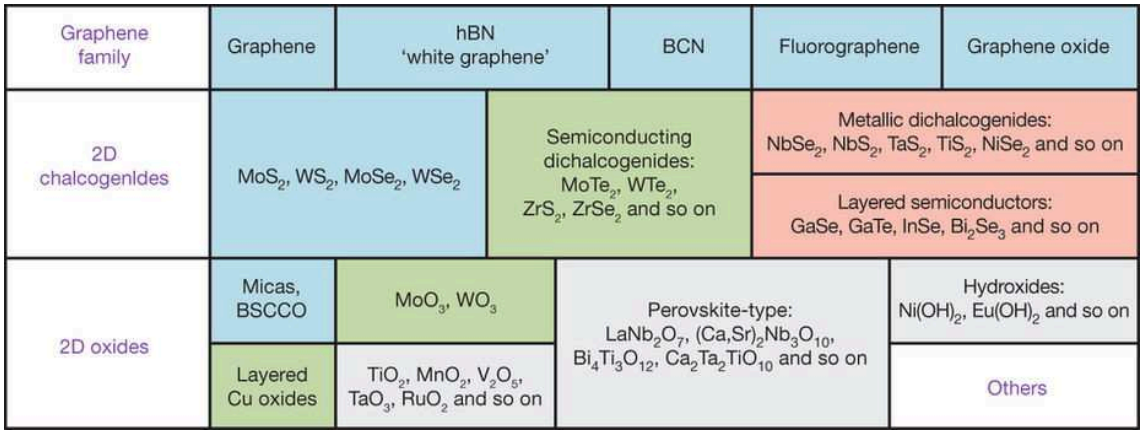

Figure 1.8: *Current 2D material library [40].*

1.2.1.2 Synthesis of 2D materials

Generally, synthesis techniques for 2D materials can be classified into two approaches:

Top-down Approaches

Mechanical Cleavage Micromechanical cleavage, as originally used in peeling off graphene from graphite, can be extended to other layered materials with weak van der Waals (vdW) forces or hydrogen bond between layers. It proves that 2D layers can be readily exfoliated from 3D crystals mechanically by cleaving the crystals against another surface. The micromechanical cleavage was applied to the isolation of h-BN, MoS_2, $NbSe_2$, from their layered phases. The resulting 2D sheets are stable under ambient conditions, exhibit high crystal quality, with the obtained thickness ranging from 1 to 10 atomic layers.

Micromechanical cleavage has proven an easy and fast way of obtaining highly crystalline atomically thin nanosheets. However, this method produces a large quantity of thicker sheets, while the thinner or monolayer ones only reside in a very minor proportion; thus this method is not scalable to mass production for potential engineering applications. Also, the size of the 2D sheets produced by this technique is limited by the size of the parent 3D crystal and only work for weakly bonded layered materials.

Chemical Exfoliation As an alternative method, chemically derived exfoliations, such as liquid-phase exfoliation, and ion-intercalation induced exfoliation, have been demonstrated to effectively isolate single layer and few layers from those thicker structures in large quantities. Chemical exfoliation of 3D layered material is used for the production of a wide range of 2D materials chemistries, as varied as graphene and its oxide [41], h-BN [42], TMDs [43] metal oxide and hydroxide [44, 45].

The principle of chemical exfoliation is to break the bonds between the layers by chemical, chemical-thermal treatment, or chemical reaction assisted by sonication procedures. Most of the chemical exfoliation processes are conducted in the aqueous environment, relying upon strong polar solvents, reactive reagents, or ion intercalation, which is versatile and up-scalable. The fabricated 2D materials can be re-dispersed in common organic solvents, or in various environments and substrates, which is not feasible for mechanical cleavage methods. These methods step up a wide range of potential large-scale preparations and applications of 2D materials for nano devices, composites, or liquid phase chemistry.

Bottom-up Approaches

Chemical Vapour Deposition (CVD) The main technique that uses a bottom-up approach to synthesize 2D materials is CVD. 2D layers of graphene [46], h-BN [47], and MoS_2 [48] have been successfully obtained by using this technique. Compared to the mechanical and chemical exfoliation, the main asset of CVD method is the feasibility of scaling-up. More than 30 inch screen size graphene film used as transparent electrodes can be successfully fabricated by roll-to-roll production [49]. CVD also allows for the fabrication of electronic devices such as transistors [50]. Yet, compared with the simple and easily-handled chemical exfoliation methods, the CVD strategy is costly.

Surface-assisted Epitaxial Growth Surface-assisted epitaxial growth can be regarded as a modification of CVD method, in which the substrate surface serves as a seed crystal other than a template or a catalyst. This method is alternatively considered as molecular beam epitaxy (MBE) growth. The epitaxial growth has been successfully applied to fabricate one-atom-thick Si sheets (silicene), and the un-reactive metal Ag with sixfold surface symmetry provides a promising substrate to facilitate growth of hexagonal silicene or Si nanoribbons [51].

1.2.1.3 Application of 2D materials

According to the definition that all 2D materials have high aspect ratios of lateral dimension compared to the thickness of few atoms, they typically result in very high specific surface areas. This unique property of 2D materials suggest that they can be applied in energy storage systems, which is a keystone in today's world technologies. Considerable research efforts have been dedicated to exploring and developing new anode materials for lithium ion battery (LIBs), with the aim of developing new materials with higher capacities and lifetimes than current graphite or lithium titanate anodes. As a host materials for metal ion batteries, 2D materials have unique morphology that enables fast ion diffusion and ion insertion channels [52].

Another general merit is that most 2D materials show properties that differ from those of their 3D counterparts, which bring themselves wide applications: reinforcement for polymer composites to produce light weight, high strength and conductive composites [53]; transparent flexible electronic devices due to their good electronic properties and flexibility [54].

1.2.2 MXenes

1.2.2.1 Structure of MXenes

Herein, a new member of 2D materials family is now introduced. MXene, a derivative of MAX phase, is a group of two-dimensional materials consisting of atomic layers of transition metal carbides, carbonitrides and nitrides, consisting of a few atomic layers of two elements (Mono-M), or more than two elements (solid-solution M or double-M element). MXenes, were denoted to emphasize the loss of the A element from the MAX parent phase and to highlight their 2D nature, which is similar to graphene. The ideal MXene composition can be described by $M_{n+1}X_n$, in general, at least three different formulas have been discovered: M_2X, M_3X_2, M_4X_3. The structure is shown in the Figure 1.9. They can be made in different forms: mono-M elements, a solidsolution of at least two different M elements or ordered double-M elements. Chemical-exfoliated MXene exhibits surface groups and is denoted $M_{n+1}X_nT_x$, where T_x describe the surface groups, –OH, =O, –F. MXene sheets are almost stacked, where ions and/or molecules may be positioned in between sheets without strong chemical bonding (intercalants). These intercalated MXenes are described by $M_{n+1}X_nT_x$-IC, where IC denote the intercalants.

Since the first MXene $Ti_3C_2T_x$ was reported in 2011 [55], up to date, over 19 MXenes have been synthesized while another 25 more have been predicted according to the Density Functional Theory (DFT) calculations. The element composition of these MXenes is also shown in the Figure 1.9, of which $Ti_3C_2T_x$ and $Ti_2CT_x$are still the most studied MXenes to date.

MXenes originate from MAX phases. That is to say, the MAX phase can be described as 2D layers of early transition metal carbides and/or nitrides stuck together with the A-element layer. Due to the fact that the M-A bond is metallic, it is difficult to separate the MX layers by simply mechanical shearing of MAX phases as graphene derivated from graphite. Nevertheless, as the M-X bond has mixed covalent/metallic/ionic bond character, which is stronger than M-A bonds, selective etching becomes possible to remove the A-element layers without destroying the M-X bonds, which is the primitive principle to access MXenes. In plane view, the structure of MXene sheets is hexagonal with space group $P6_3/mmc$ (See Figure 1.10). Take MXene Ti_3C_2 as an example, the unit cell has lattice parameter a and b = 3.05 Å, while the lattice parameter c is 19.86 Åfor ideal Ti_3C_2[56], while the surface groups and intercalants expand the separation between sheets and increase the lattice parameter c [57].

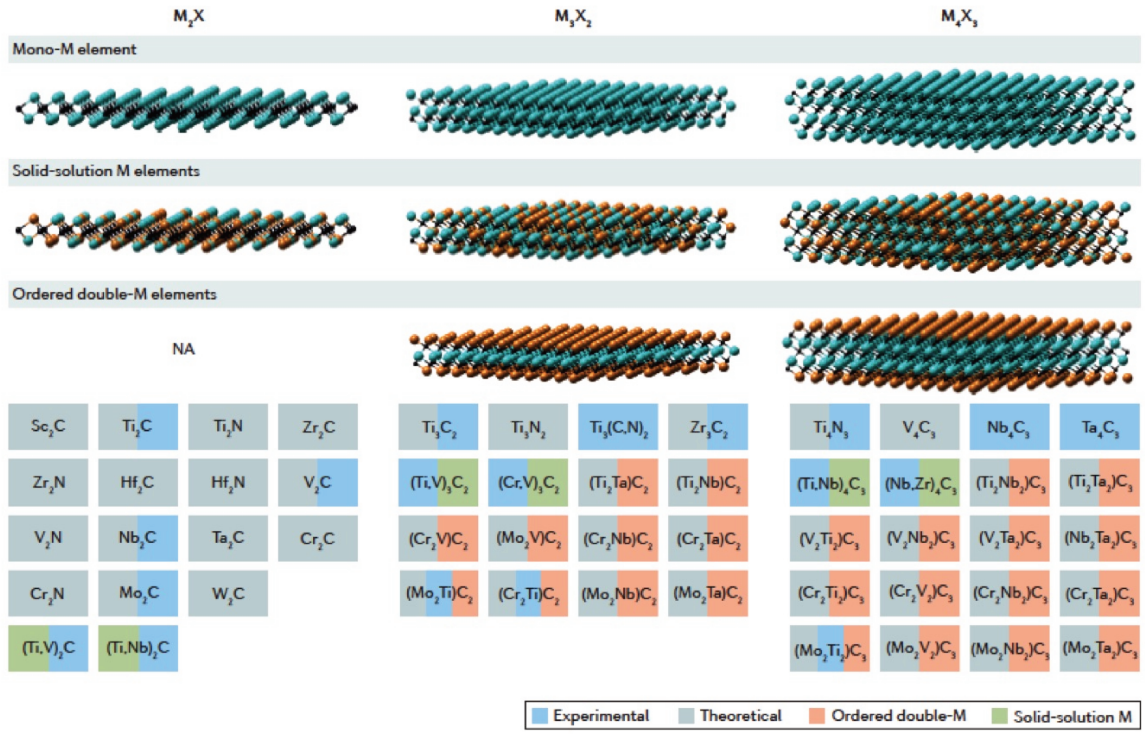

Figure 1.9: *Variety of MXenes reported so far [58].*

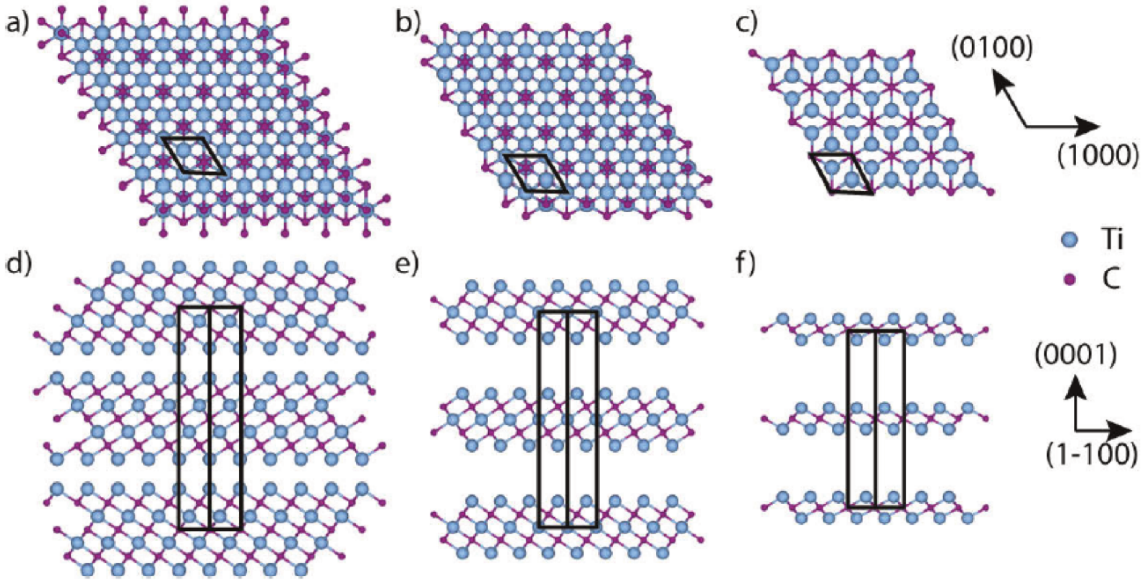

Figure 1.10: *Structure model of ideal Ti_4C_3 (a, d), Ti_3C_2 (b, e) and Ti_2C (c, f) [59].*

1.2.2.2 Synthesis of MXenes

Etching with hydrofluoric acid Attempts on etching A layers from MAX phase have been made by heating MAX phase under vacuum or in molten salts at high temperatures, which results in the selective loss of the A element, whereas the formation of 3D $M_{n+1}X_n$ rock salt structure were also formed due to the detwinning of $M_{n+1}X_n$ layers at elevated temperature [60]. Moreover, the operation of strong etchants, such as Cl_2 gas, at temperatures over 200 °C results in the etching of both the A and M atoms, to yield carbide derived carbons (CDC).

In 2011, the pioneering work has been done by selective etching of Al from Ti_3AlC_2 using aqueous HF at room temperature (RT), which can be seen in Figure 1.11(a)[55]. In this process, the Al atoms are replaced by O, OH and/or F atoms. The removal of the Al layers dramatically weakens the interactions between the $M_{n+1}X_n$layers, which allows them to be separated. This simple selective etching of Al from the parent MAX phases was then successfully extended and yielded multi-layered Ti_2CT_x, $Ta_4C_3T_x$, $(V_{0.5}Cr_{0.5})_3C_2T_x$, $Ti_3CN_xT_x$, Nb_2CT_x, V_2CT_x, $Nb_4C_3T_x$, $Mo_2TiC_2T_x$, $Mo_2Ti_2C_3T_x$, etc. [61, 62, 63]. Typical MXenes accordion-like morphology are shown in Figure 1.11(b, c).

This preferential etching of the M-A bond in MAX phases with Al may be summarized as:

$$M_{n+1}AlX_n + 3HF \rightarrow M_{n+1}X_n + AlF_3 + 1.5H_2 \tag{1.8}$$

$$M_{n+1}X_n + 2H_2O \rightarrow M_{n+1}X_n(OH)_2 + H_2 \tag{1.9}$$

$$M_{n+1}X_n + 2HF \rightarrow M_{n+1}X_nF_2 + H_2 \tag{1.10}$$

Eqs 1.9 and 1.10 indicate the surface terminations by a combination of –OH and –F as wet chemical etching of Al does not result in bare M layers. Due to the fact that etching is a kinetically controlled process, it is worth mentioning that etching conditions such as HF concentration, duration of immersion and temperature are essential to completely convert various parent MAX phases into MXenes. Also, etching conditions depend on the properties of various MAX phases including structure, atomic bonding and particle size of the raw materials. In general, MXenes with larger n in $M_{n+1}X_n$ require stronger etchants and longer etching time. While smaller particle sizes of the parent MAX phase

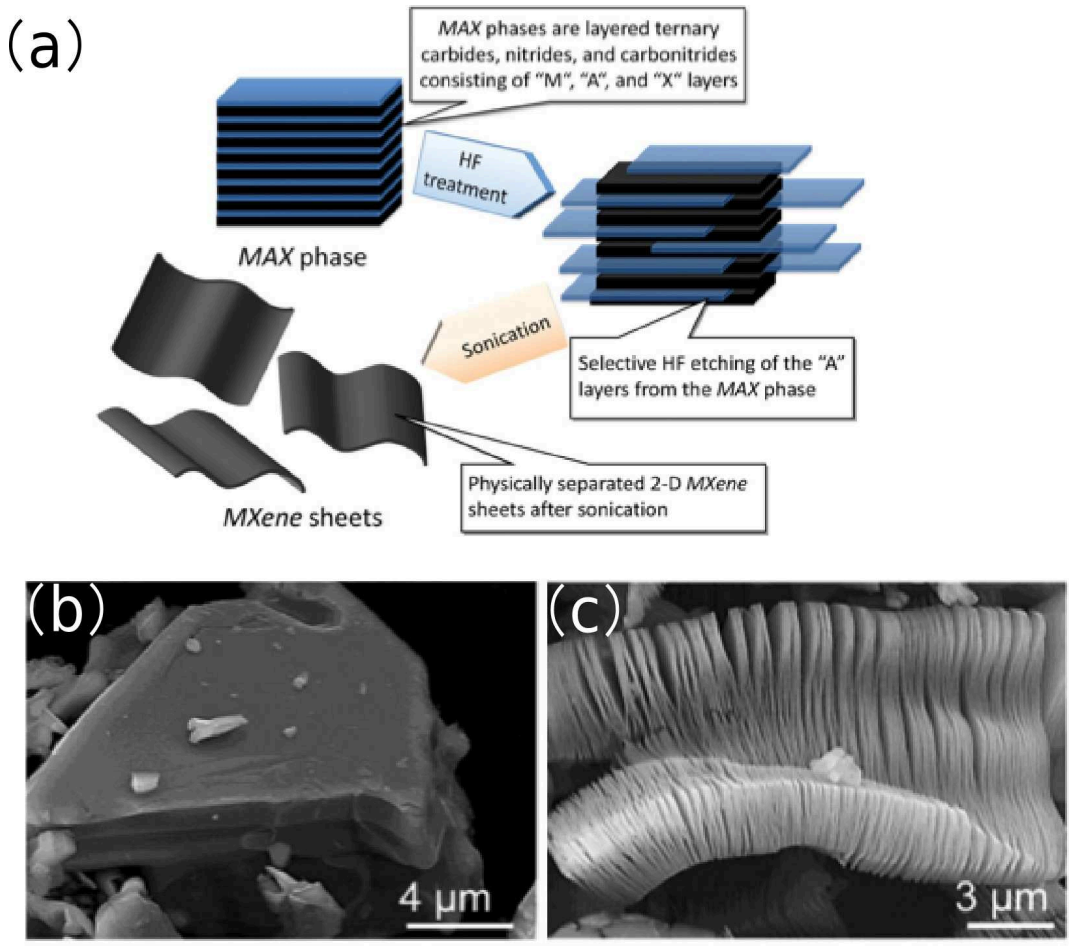

Figure 1.11: *(a) Schematic describing the synthesis process of MXenes from microcrystalline MAX phase by HF selectively etching. SEM images of Ti_3AlC_2 before (b) and after (c) HF etching [55].*

can effectively reduce the required etching duration and/or HF concentration, the as-synthesized MAX phase powders are usually subjected to attrition or ball milling and/or sieved prior to chemical exfoliation.

Etching with fluoride solution Instead of HF, different etchants were introduced for the etching of MAX phase. Even with various synthesis conditions and chemical reagents, fluoride compounds work as a decisive factor to produce 2D MXenes. Fluoride salts, such as lithium fluoride (LiF), sodium fluoride (NaF), potassium fluoride (KF), caesium fluoride (CsF), could be added into hydrochloric acid (HCl) or sulphuric acid (H_2SO_4) to produce the etchant solution [64]. It is convincing that a precise balance of etching conditions for different combinations with acid and salt, can potentially bring out multi-layered early transition metal carbides modified by surface chemistries and diverse pre-intercalated ions. This one-step method has been successfully applied to produce multi-layered Nb_2CT_x, Ti_2CT_x, $Cr_2TiC_2T_x$, $Mo_2TiC_2T_x$, $Mo_2Ti_2C_3T_x$, Mo_2CT_x,

etc [62, 63, 64]. Moreover, bifluoride solution (e.g., $NaHF_2$, KHF_2 or NH_4HF_2) were proved to be milder etchant as well [65].

Delamination and intercalation In principle, as the strong M-A bonds are replaced by weaker bonds, intercalation and delamination of multi-layered stacked MXenes into single or few layers is possible, which is essential for exploring its 2D nature. Multilayered MXenes have relatively stronger interlayer interactions than those in graphite or TMDs, simple mechanical exfoliation provides a low yield of single layers. There are only two reports of Scotch tape exfoliation of multilayer MXene into single flakes [66, 67].

The rest of the reports are mainly focused on the chemical intercalants which have been used successfully in other 2D materials. Figure 1.12 shows the schematic diagram of intercalation mechanism [68]. To date, intercalation of $Ti_3C_2T_x$ with a variety of organic molecules, such as hydrazine, urea and dimethyl sulphoxide (DMSO) was reported. Hydrazine can also intercalate Ti_3CN and $(Ti,Nb)_2C$. Intercalation of $Ti_3C_2T_x$ and $Mo_2TiC_2T_x$ with DMSO followed by sonication in water led to a colloidal solution of single- and few-layer MXenes [68, 69, 70]. By the use of isopropylamine or large organic base molecules such as tetrabutylammonium hydroxide (TBAOH), choline hydroxide, or n-butylamine, V_2CT_x, Nb_2CT_x and Ti_3CNT_x were delaminated [71]. However, TBAOH does not delaminate $Ti_3C_2T_x$, possibly due to its large size. Either DMSO or an alkali metal halide salt have been used for delaminating $Ti_3C_2T_x$.

MXene can also be intercalated with different metal cations by introducing aqueous solutions of ionic compounds. As etching with fluoride salt with acid, metal cations is intercalated spontaneously into layers. The possibility of intercalating MXenes with various organic molecules and metal cations goes beyond delaminating MXenes on a large scale. This phenomenon is of great significance for a range of MXene applications, from polymer reinforcements to energy storage systems.

1.2.2.3 Properties of MXenes

The main reason why the electronic properties of MXenes are of special interest is because they can be tuned by changing the MXene elemental composition and/or their surface terminations. The band structure and electron density of states (DOSs) of MXenes have been extensively studied by DFT, indicating that MXenes properties range from metallic to semiconducting. Bare MXene mono layers are predicted to be metallic, with a high charge carrier density near the Fermi level [72, 73, 74]. Interestingly, the

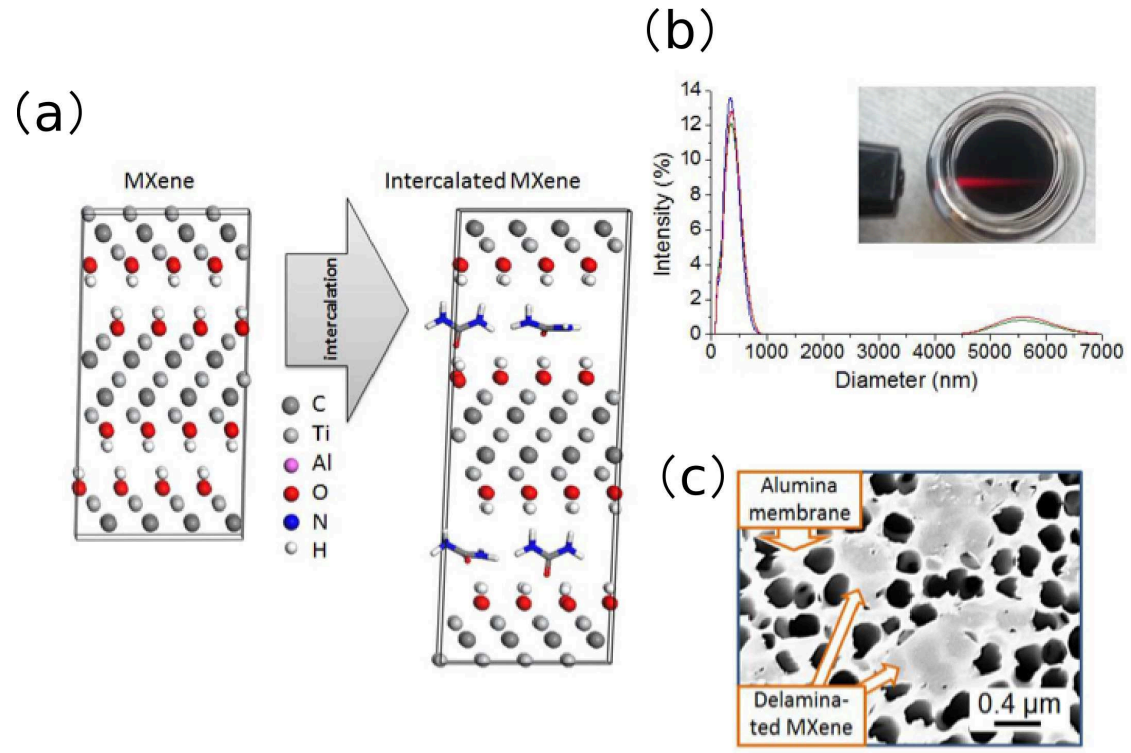

Figure 1.12: *(a) Schematic representation of the intercalation mechanism (b) Particle size distribution in aqueous colloidal solution; inset shows Tyndall scattering effect in the solution (c) Scanning electron microscope image of d-Ti_3C_2 single flake on alumina membrane [68].*

electron DOS near the Fermi level ($N(E_f)$) for bare individual MXene layers is higher than in their parent MAX phases. Some MXenes with heavy transition metals (Cr, Mo,W) are predicted to be topological insulators[72, 75]. Up to now, only electronic properties of Ti_2C, Ti_3C_2, Mo_2C, Mo_2TiC_2, and $Mo_2Ti_2C_3$ with terminations have been experimentally measured [66, 67, 76, 77, 78].

Surface terminations can influence other MXenes' electronic properties, such as their bandgaps. In the first MXene paper, it was theoretically shown that although Ti_3C_2 is a metallic conductor, small bandgaps of 0.05 eV and 0.1 eV open up for $Ti_3C_2(OH)_2$ and $Ti_3C_2F_2$, respectively. Recent reports evidence that transition metal can affect the electronic properties dramatically: $Ti_3C_2T_x$ is metallic, but the Mo-substituted $Mo_2Ti_2C_3T_x$ MXenes might exhibit semiconductor characteristics [79], which means that it would be possible to tune the electronic structure of MXenes by varying termination group and transition metal.

Ferromagnetic and anti-ferromagnetic properties have been predicted for some pristine MXenes, whereas magnetism disappears with surface terminations for some cases [80]. Only two MXenes Cr_2CT_x and Cr_2NT_x have been predicted to be magnetic even with surface terminations, yet their magnetic nature is not clear, also no experimental

Cr-MXene have been successfully synthesized except for Cr-Ti-containing MXenes.

High Seebeck coefficients were predicted for MXenes by DFT calculations [72]. Thermoelectric calculations based on the Boltzmann theory imply that semiconducting MXenes attain very large Seebeck coefficients at low temperatures, which opens a novel potential applications for these surface terminated MXenes.

The mechanical properties of MXenes are also of great interest as the M–C and/or M–N bonds are some of the strongest known. M_2X MXenes are predicted to be stiffer and stronger than their M_3X_2 and M_4X_3 counterparts. Though experimental mechanical testing has been conducted only for MXene films and not for single-layer, a cylinder with walls made of 5 μm thick $Ti_3C_2T_x$ film can support over 4000 times of its own weight [81]. MXenes/polymer composites have also been developed with improved mechanical and electrical properties. Thin films of MXenes are transparent and its optoelectronic properties can be tuned by the chemical and electro-chemical intercalation of cations, which implies that MXenes films can be applied in transparent conductive coatings and optoelectronics [82].

1.2.2.4 Application of MXenes

Energy storage application

Battery: Similar to graphene, MXene are promising candidate electrode materials for Lithium-ion battery (LIBs) and super-capacitors by the intercalation of Li ions into the MXene layers. Owing to their wide chemical variety, it has more tunable performance compared to the elementary graphene. MXenes are promising LIB anode materials, since they have excellent electronic conductivity, low operating voltage range, low diffusion barriers which are favourable for high rate performance and exceptional mechanical properties that are invariant to Li adsorption. Unlike typical diffusion limited battery electrode materials, intercalation of ions in MXenes can paradoxically occur at a high rate, without significantly depreciating their energy storage capacities. Based on the theoretical calculations, it is proved that MXenes with low formula weights (M_2X MXenes) are the most promising in terms of theoretical gravimetric capacity. Encouraged by the first application of HF-etched multilayered Ti_2CT_x as anode material in LIBs, other MXene materials, such as $Ti_3C_2T_x$, $Mo_2TiC_2T_x$, Nb_2CT_x, V_2CT_x, $Nb_4C_3T_x$, and Mo_2CT_x, have also been examined as potential anode for LIBs.[63, 69, 76, 83]

Supercapacitor: Supercapacitors provide alternative energy storage with rapid power density but low energy density compared to batteries. Research efforts have been made

on improving their volumetric capacity, i.e. energy density per volume. Depending on their charge-discharge mechanisms, supercapacitors are classified as either electrical double-layer capacitors (EDLCs) or pseudo-capacitors. In general, pseudo-capacitors possess higher volumetric capacitances and lowered cycling stability. MXenes, with their 2D characteristics, large surface areas, present themselves as promising electrode materials for super-capacitors. $Ti_3C_2T_x$ is the most studied MXenes for super-capacitors, the volumetric capacitances of free standing $Ti_3C_2T_x$ MXene electrodes in neutral and basic electrolytes have been demonstrated to be 300-400 $F{\cdot}cm^{-3}$, which is higher than the best carbon-based EDLCs [84]. Also, no change in capacitance was reported after 10000 cycles for $Ti_3C_2T_x$ electrode , indicating their excellent cyclability [64].

MXene-based composites have opened a new pathway in various energy storage systems, due to the possible synergistic effect in agglomeration prevention, facilitating electronic conductivity, improving electrochemical stability, enhancing pseudo-capacitance and minimizing the shortcomings of individual components.

Other application Energy storage systems is the primary and most studied application for MXenes, yet, due to their rich chemistries and diverse structures, there are potentially many other applications of MXene, such as hydrogen storage medium [85], photocatalysis [86, 87], biosensor [88, 89] and sewage purification [90, 91].

1.2.3 Summary

For most MXenes, theoretical predictions about their electrical, thermoelectrical, magnetic and other properties should be verified experimentally, especially on the single or fewer layers MXenes. Understanding and controlling surface chemistry is of great importance to allow tailoring the material structure and properties. Regardless of the advancement of these 2D layered MXenes and their composites in Li-ion batteries (LIBs), super-capacitors, transparent conductors, environmental protection, electrocatalysts, etc, more works remain to be conducted, in particular aiming at understanding the exact mechanisms behind certain properties.

1.2.4 PhD work on MXenes

The second part of the PhD thesis is focused on the V_2C MXenes derived from large V_2AlC MAX phase crystals by using a combination of chemical modification and

ultrasonic technique. "Large"(>10 μm) and homogeneous V_2C MXenes were obtained by following mechanical exfoliation method. Synthesis and characterization of V_2C MXenes are detailed in Chapter IV. MXene-based devices were fabricated and their electronic properties were examined down to low temperature and in high magnetic field as discussed in Chapter V.

chapter 2

MAX Phase Single Crystal Growth and Characterization

In the present work, several MAX single crystals were grown from liquid phase by high temperature solution growth and slow cooling technique. The high temperature growth reactor is firstly presented in this chapter. Then the development of growth process for various MAX single crystals is introduced. Single crystalline characterization as well as the mechanical cleavage of the as-grown MAX phases single crystal are also discussed.

2.1 Single Crystal Growth

2.1.1 Growth setup

A modified Czochralski (Cz) puller, named "memere", has been adapted to MAX phase crystal growth. Figure 2.1 shows photo of the puller. It consists of three main parts:

(1) The Heat unit. It is composed of an induction coil, a capacitor box and a power generator.

(2) The reactor includes the growth chamber, gas lines (only Ar 99.9% was used in this work), and recycling cooling water line. Rotation units are located at the top of the chamber, as well as an optical non contact infrared temperature sensor to focus on the crucible through a quartz window to measure the temperature.

(3) The computer based monitor which contains a control panel (not listed in the figure) to tailor the growth conditions by programming heating and cooling sequences. It is also equipped with safety elements who are able to alarm when in the absence of cooling water in the generator and chamber. Besides, a pressure meter is also applied to monitor the pressure in the chamber in order to avoid the overheating.

It is worth mentioning that two quartz windows are implanted at the side of the chamber, among which, one is used for the temperature measurement of crucible and the other is for the observation when rotating the graphite into the solution.

Three main steps can be explained as follows: firstly, meltdown of alloy (e.g. Cr and Al , V and Al) ;secondly, dissolution of carbon in the fused solution and thirdly, crystallization of MAX phase single crystal in the crucible.

2.1.2 The crucible kit

The crucible kit is composed of crucibles and insulators. The solution growth process is launched at high temperature, therefore the crucible material must be thermally stable for long time operation at high temperature. There are some requisite characteristics for the crucible materials: high-temperature and thermal shock resistant, high electrical and thermal conductivity, easily machinable. Therefore, the most suitable material is graphite as it fulfils all the criteria listed above. So in the previous growth experiment for Ti_3SiC_2 [7], graphite crucible can be used when the temperature reach up to above

2000 °C. The carbon content was obtained by partial dissolution of the graphite walls (See Figure 2.2(a)).

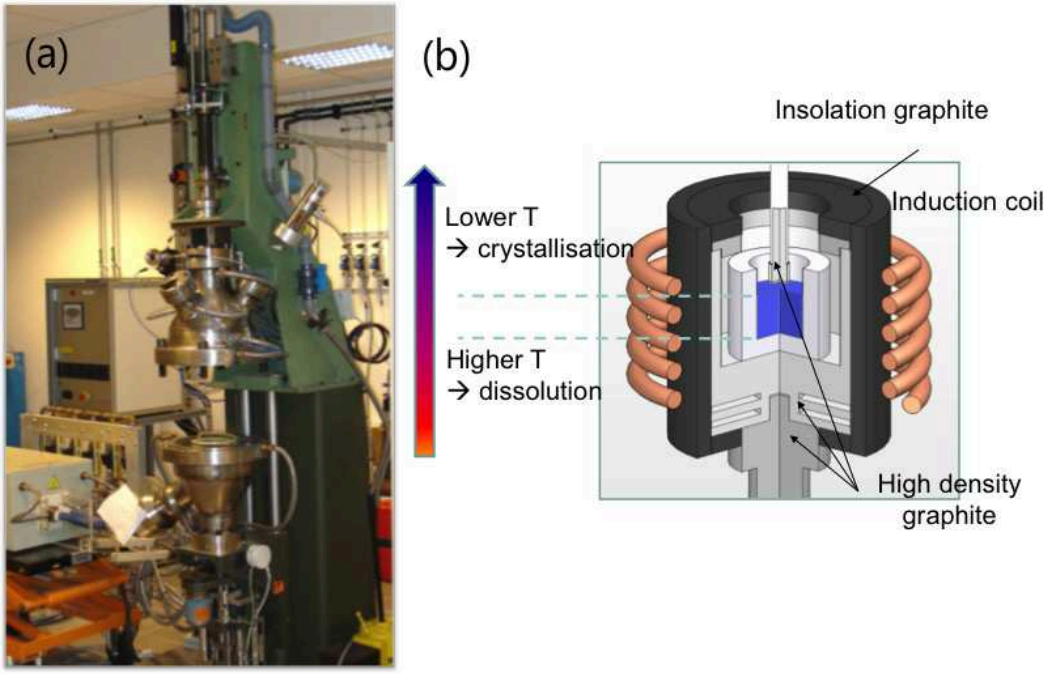

Figure 2.1: *(a) Photo of the puller with heat unit and reactor (computer control panel not included) (b) schematic diagram of the experimental set-up used for high temperature solution growth.*

This has two drawbacks: on one hand, this does not allow precise control of graphite incorporation, and when it comes to Al-containing MAX phase, this can lead to the unwanted formation of Al_4C_3 during the initial heating process. On the other hand, if the temperature becomes higher than 1400 °C before the transition metal melts, then liquid Al reacts extremely fast and violently with graphite, so that in a very short time and at the hot point, most of the crucible is consumed until it breaks.

For Cr_2AlC, this is not a problem because Cr melts before reaching 1400 °C. While in the case of V_2AlC, it becomes crucial when using more refractory metals (such as Vanadium), as the transition metal melt before introducing the carbon. This imposes the choice of another materials for the crucible. So for this thesis, concerning the Al-containing MAX phase growth, the alumina crucible is used instead of graphite crucible, though the highest temperature achieved is 1700-1800 °C (See Figure 2.2(b)).

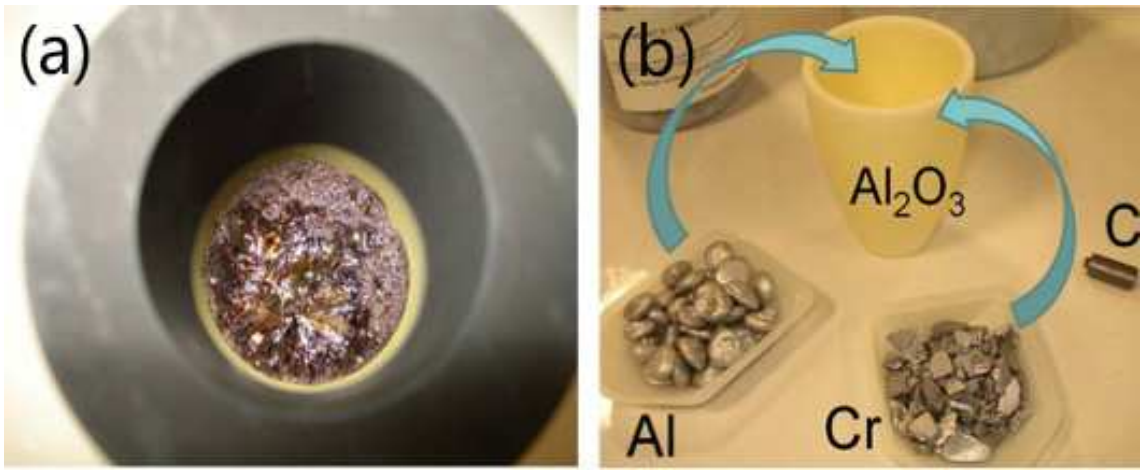

Figure 2.2: *(a) Graphite crucible (for Ti_3SiC_2, Ti_2SnC) (b) Alumina crucible (for Cr_2AlC,V_2AlC) and the raw materials used for growth of Cr_2AlC.*

2.1.3 Reactor geometry

Figure 2.3 shows the details of the reactor geometry. The crucible can be separated in two parts: the inner alumina crucible where growth takes place and the outer graphite crucible, which is directly heated by the electromagnetic field applied by induction coil. The resistance of the graphite material will lead to its Joule heating. On the top of the outer graphite crucible, several pieces of titanium-zirconium alloy as oxygen absorber material are placed between graphite lip and top insulation, because they can prevent the heterogeneous nuclei from solvent due to the floating oxide particles generated from the the native oxide layers on the metal. It is proved that Zr is a very effective de-oxidizing metal, while Ti exhibit a wide range of solubility against both oxygen and nitrogen. Temperature limitation of Ti-Zr alloy is around 1520 °C, hence even it is placed far from the heating zone, it would start to melt when the growth temperature reaches up to 1800 °C.

2.1.4 Growth procedure

Growth is achieved by maintaining the solution for several hours at high temperature, with a partial Ar pressure p_{Ar}=1.5 bar. Different stages of growth are summarized in Figure 2.4 for the high temperature solution growth and slow cooling methods. In general, the crucible is manually heated up to a temperature T_1 (higher than 1000 °C) which is possible to be detected by the pyrometer. From T_1 to T_2, it is the period of meltdown alloys, T_2 is dependent on the binary phase diagram (Cr-Al, V-Al, etc.). Here, we set T_2 equals to 1600 °C for V-C system while 1650 °C for Cr-C system. The time period lasting from t_1 to t_2 varied from 40 min to 1h according to the raw materials

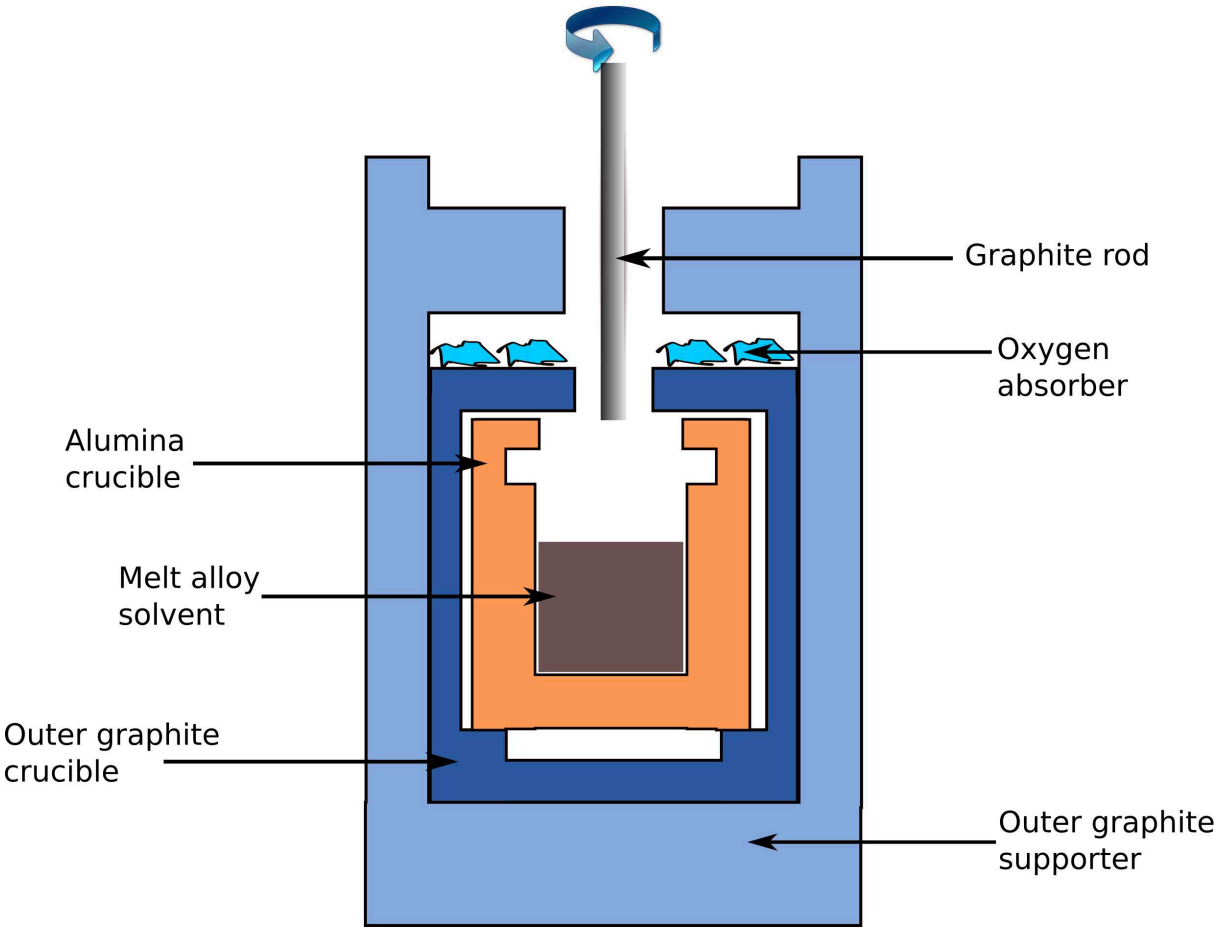

Figure 2.3: *Reactor configuration indicating the melt solvent and crucible structure.*

quantities. Once crucible is heated to T_2, a graphite rod is put into the melt with continuous rotation to dissolve carbon into the melt. The amount of carbon dissolved should be precisely calculated based on the ternary phase diagram. As long as the carbon is all dissolved in the melt, the graphite rod should be pulled out from the melt. Done with high temperature meltdown of all raw materials, next critical procedure came out, which is slow cooling. The less nuclei, the better. Here, a pre-cooling procedure (t_3-t_4) was introduced to reduce the number of nuclei .

Besides, since no seed crystal is available to be introduced, spontaneous nucleation in the flux is the key factor. A way to decrease the nucleation and increase the crystal size is to start at a temperature at which the flux can be completely converted into a liquid phase, and then to decrease the temperature slowly, so that the first nucleated crystals reduce subsequent nucleation by Ostwald ripening. This is essentially the strategy which we would follow for growth. So, a fairly slow cooling starts, which could last several hours or days (under proper monitoring conditions). In the end, when the system is cooled down to acceptable temperature, the solidified sample can

be taken out from the chamber. It is worth mentioning the chamber pressure should be monitored strictly during the carbon dissolution procedure, which is at highest temperature, because the low-melting-point metal vapour will form precipitates on the monitor window, making the pyrometer unable to work in proper conditions. If the temperature indicated is much lower than the real one, the feedback power will keep increasing, leading to a destructive result.

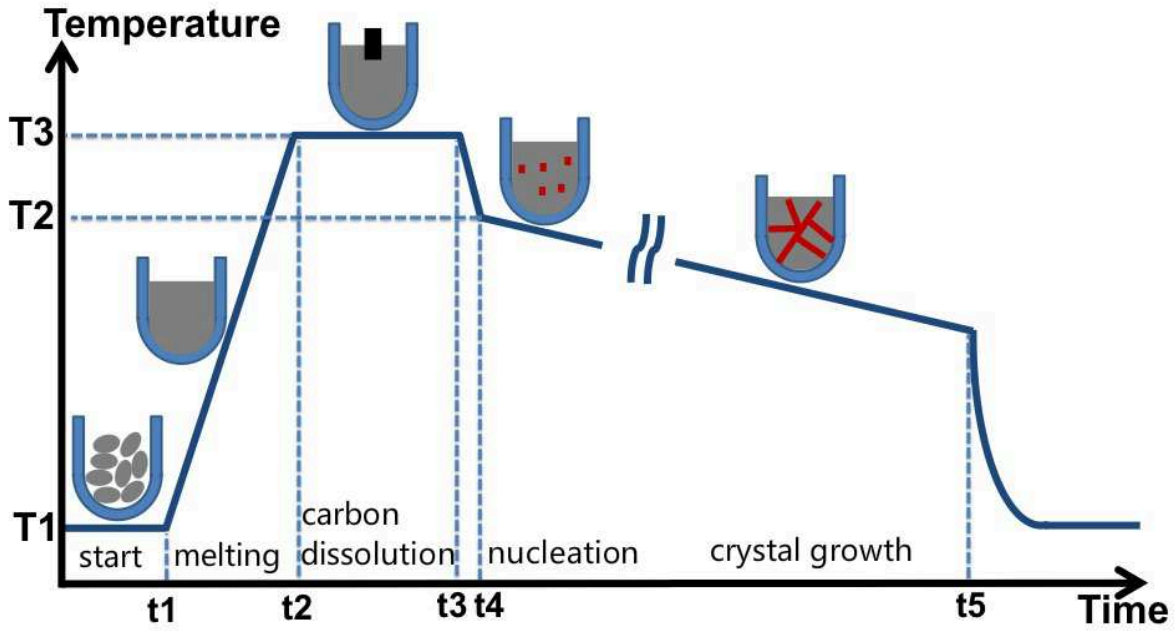

Figure 2.4: *Experimental process profile of all the crystal growth in the current work.*

To collect the crystal from the flux "cupcake" (See Figure 2.5(a)), diluted HCl acid is applied. Alternatively, after a few weeks under air, the solidified flux hydrolysed and turns into powders as can be seen in Figure 2.5(b,c).

2.1.5 Cr_2AlC crystal growth

Figure 2.6(a) is the Cr -Al-C ternary phase diagram, in which a liquid surface expands along the Al-Cr line of the isothermal sections at a temperature higher than the melting point of Al. At temperature in the 1400 °C range, and starting from a binary Cr-Al melt with a Cr atomic fraction roughly below χ_{Cr}=0.4, dissolving a small amount of carbon in the melt allows one to obtain a composition for which the liquid is in equilibrium either

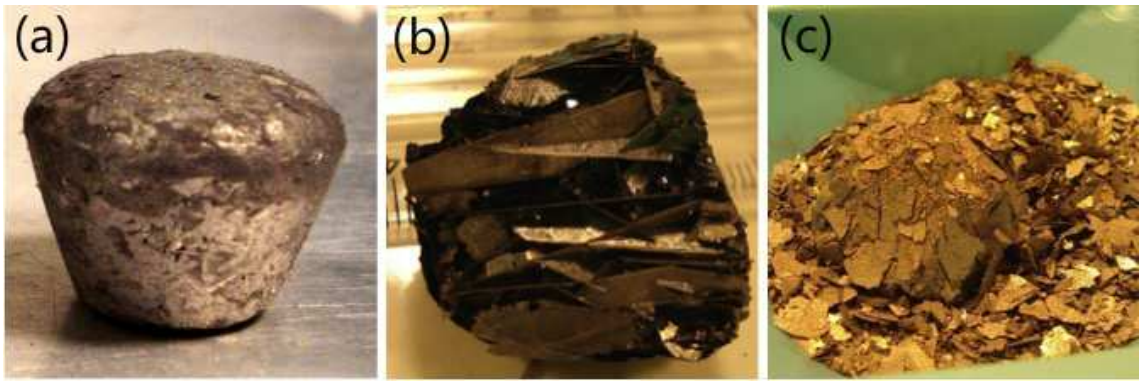

Figure 2.5: *(a) Flux "cupcake" taken immediately from crucible after cooling process (b) Flux "cupcake" after immersed in the dilute HCl for few hours (c) Flux "cupcake" standing in the air after for few weeks.*

with Al_4C_3 alone, Al_4C_3 and Cr_2AlC , Cr_2AlC alone, or Cr_2AlC and Cr_7C_3 . Therefore, it is possible to grow Cr_2AlC from a liquid phase.

The solution growth in our experiment differs from Czochralski method because the liquid composition is different from that of the solid, exhibiting non-congruent melting characteristics. According to the Cr-C binary phase diagram (See Figure 2.6(b)), dissolution of carbon in the Cr starts at 1527 °C and solubility of carbon in liquid Cr is high. In our experiment, a molar ratio of Cr:Al =3:7 is chosen. We typically use a few tens of grams of Al and Cr for one run. More than 10 runs of growth have been conducted to find the optimized dissolved carbon amount required to obtain large crystal.

Figure 2.7 shows the cross section of the flux cake with different molar ratio of Al:Cr:C. It is obvious that by changing the carbon dissolution amount in the solvent, the numbers of nuclei and size of the crystals vary. Figure 2.7(a) shows that if the dissolution amount is too low, there is no sufficient carbon resource to grow continuously, which leads to a small amount of crystals. On the contrary, excessive carbon will result in plenty of nuclei and form the undesirable by-products Al_4C_3 which appeared as gold color phase in Figure 2.7(b). Figure 2.7(c, d) give the optimized example with 7.2at% of carbon, before and after washing with HCl acid, from which we can determine the nucleation is generated from the bottom and wall of the crucible.

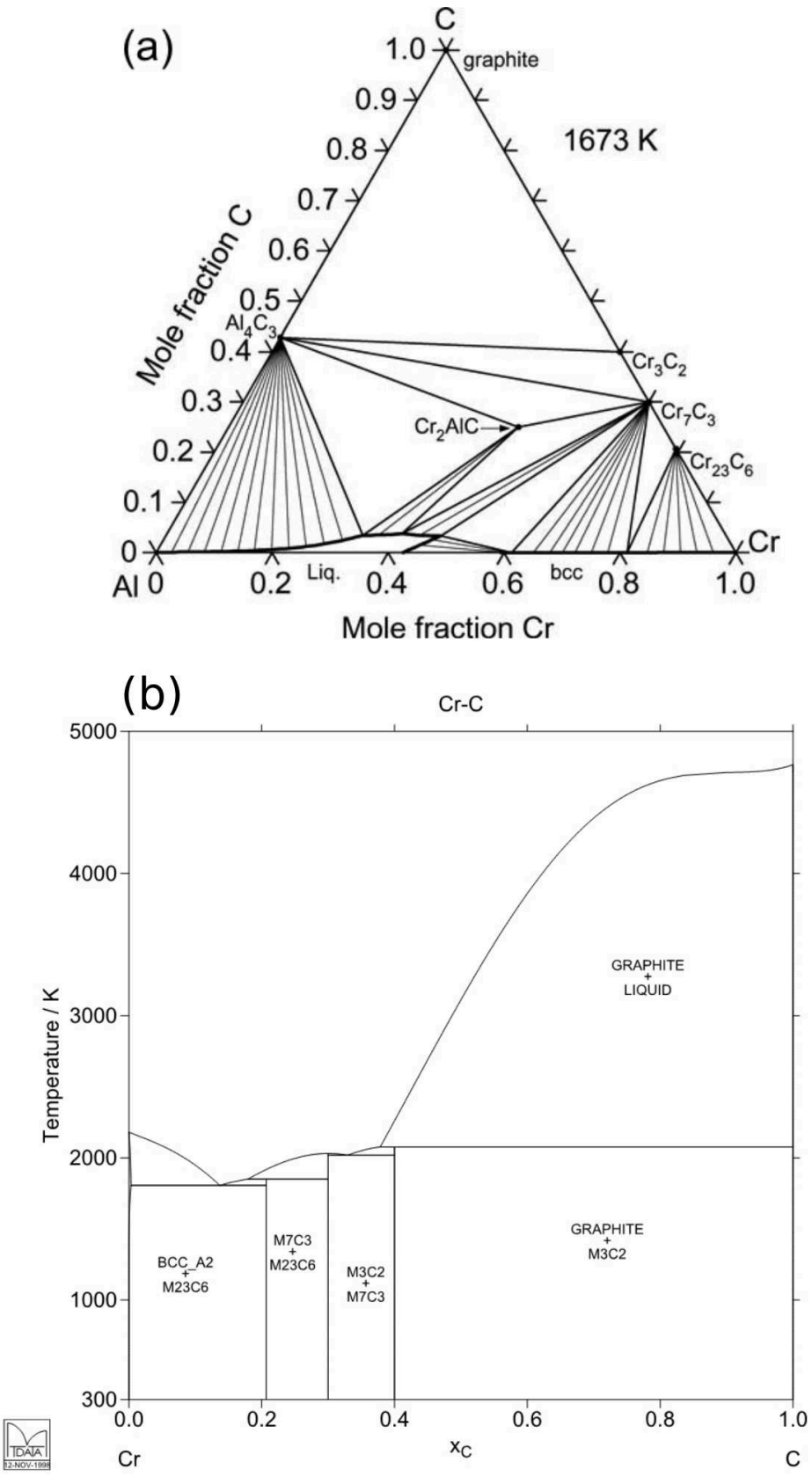

Figure 2.6: *Phase diagrams of (a) Cr-Al-C[92] (b) Cr-C.*

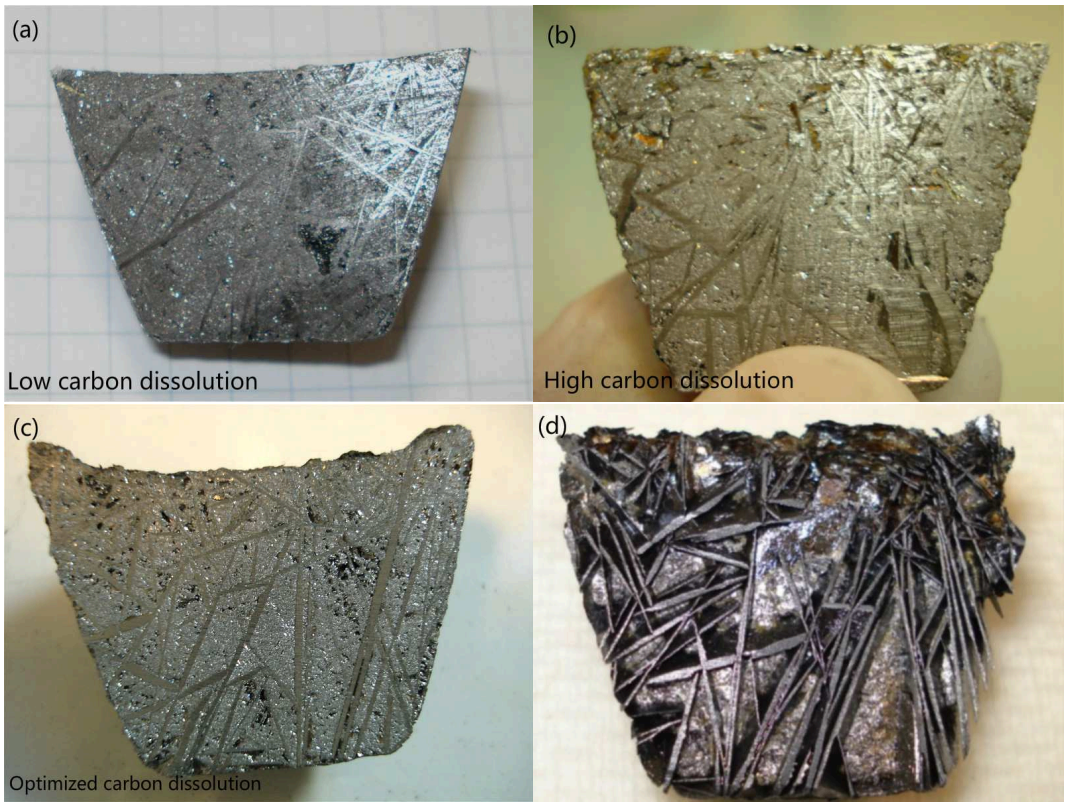

Figure 2.7: *Cross section images of various flux cupcakes with different molar ratio of raw materials (a) n(Cr) : n(Al) : n(C) = 37.5% : 56.9% : 5.6% (b) n(Al) : n(Cr) : n(C) = 53.9% : 33.5% : 12.6% (c) n(Cr) : n(Al) : n(C) = 35.6% : 57.2% : 7.2% (d) etching of (c).*

Figure 2.8: *Photo of as-grown crystals.*

Figure 2.8 shows the photos of the as-grown Cr_2AlC crystals, with an average size in the centimeter range. We can see from the photos that the crystals are platelet-like, indicating a highly anisotropic high-oriented growth.

2.1.6 V_2AlC crystal growth

As for the Ti-Si-C and Cr-Al-C systems, the V-Al-C system has also been evaluated in detail, so that the isothermal sections as well as the liquids surface have been calculated and/or measured with a reasonable accuracy. In any case, one has to find a temperature and flux composition for which the desired MAX phases is in equilibrium with a liquid phase. Figure 2.9(a) is the V-Al-C ternary phase diagram. For the V-Al-C system, this can be achieved, for example, at V mole fractions below 0.2 and temperatures above 1500 °C. As applied in the Cr-Al-C system, combined with the V-Al binary phase diagram (See Figure 2.9(b)), we tried several growth processes with different vanadium atomic ratio from 10% to 20%, the optimized value is around 15%, so we maintained this for all the following experiments.

In the case of V_2AlC, we typically maintain the melt at 1650 °C for 1h, and then introduced and dissolved the carbon. On contrary to the case of Cr_2AlC , the carbon solubility is not high enough. We increased temperature up to 1700-1750 °C , which did not successes due to the thermoresistant limit of the crucible. We also tried to preheat the crucible before growth in order to maintain the flux at high temperature for long time (e.g. 90 min) in order to increase the carbon solubility. Depending on the size of crucible, if we use 8 g V and 24 g Al, the melted carbon amount is around 0.44 g.

After a slow cooling stage for 7 h from 1650 °C to 1100 °C, a solidified flux was obtained. Unlike Cr_2AlC, the solidified flux did not turn into powder after few weeks, so that in order to extract the crystals from the flux, we had to dip the flux in HCl for a few hours. Since alumina crucible is not as easy machinable as graphite one, the whole crucible was put into the concentrated HCl. From the Figure 2.10(a) showing the crucible and the crystals inside, we can see that the numbers of V_2AlC crystals is not as high as for Cr_2AlC, while the size and thickness are also smaller than that of Cr_2AlC. As shown in Figure 2.10(b), this process results in the complete dissolution of the flux, leaving the crystals free and almost unaffected by the acid treatment. After the reduction of the solidified flux, the remaining platelets were cleaned and sonicated in ethanol or propanol.

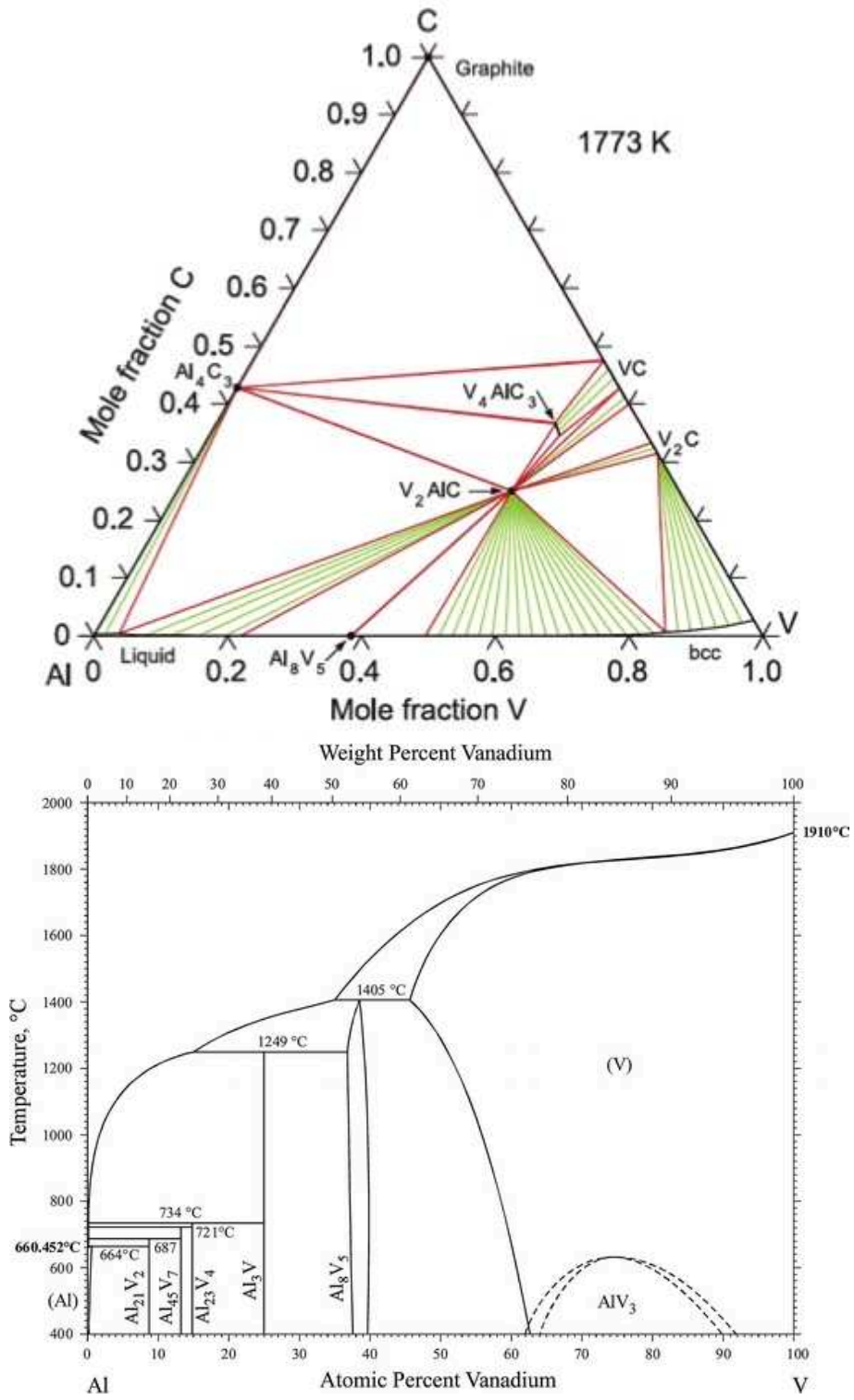

Figure 2.9: *Phase diagrams of (a) V-Al-C [93](b) V-Al [94].*

2.1.7 Other MAX phases crystal growth

The solution growth is clearly limited by the carbon solubility in the flux. This makes it, for instance, very difficult to grow phase such as Ti_2SnC by this technique, because

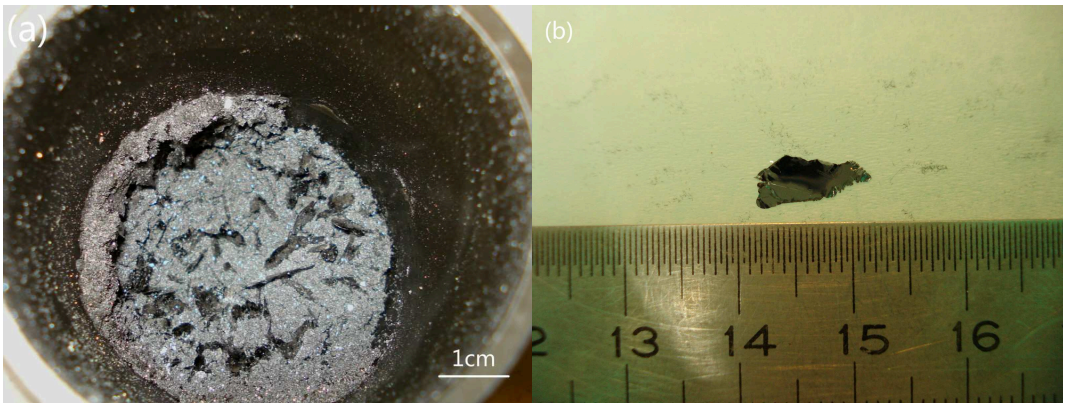

Figure 2.10: *Optical photos of V_2AlC single crystal growth (a) solidified flux after immersed in diluted HCl acid for several hours and (b) single crystal after washed with ethanol or propanol and rinsed with water.*

the carbon solubility is so limited, which is not even measurable in a reliable way. The most favourable case is that of Cr-Al-C, because carbon solubility can be achieve very high and better still, at very acceptable temperature. For a given crucible size, the final platelet area mainly depends on carbon solubility: in our experimental set-up, some 10^{-4} cm^2 for Ti_2SnC, some 0.25 cm^2 for Ti_3SiC_2, 1cm^2 for V_2AlC and several cm^2 for Cr_2AlC , as can be seen in Figure 2.11.

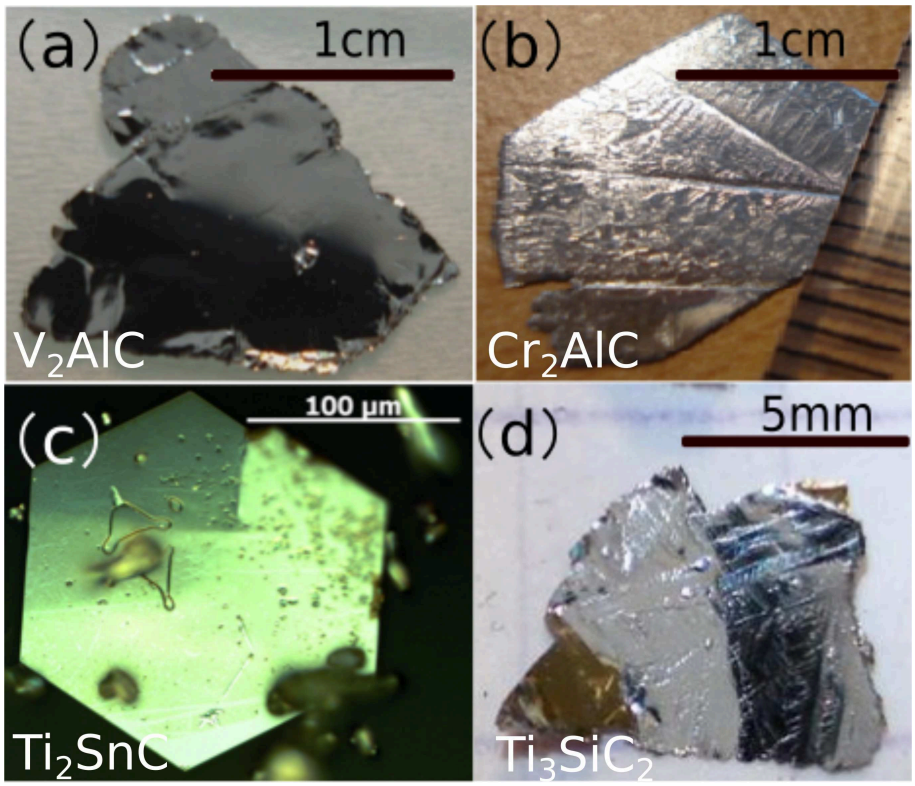

Figure 2.11: *Photos of different MAX crystals showing the typical sizes.*

2.2 Structural characterization

Characterization details

Crystal identification was firstly achieved by X-ray diffraction, using a Siemens-Bruker D5000 diffractometer (Cu, $K_{\alpha 1}$ radiation). The X-ray source was copper anode and diffraction of $K_{\alpha 1}$ and $K_{\alpha 2}$ lines were measured. The data was collected in the 2θ range 10°-115°, with a step size of 0.05°, duration of 2s/step. The pole figures were recorded using a setup comprising a four-circle goniometer (Schultz geometry), and an incident beam of diameter 1 mm, a nickel filter for attenuating the CuK_{β} radiation and a point scintillation detector. The illuminated sample surface consisted of a 4 mm $\times$3 mm ellipse. The penetration depth corresponding to 99% of the diffraction beam was about 8-10 μm. For each pole figure, complete ϕ-scans (-180° up to 180°) were performed at different χ values (0° up to 90°). Our goals, by using XRD analysis, are the identification of the phases present in the as-grown sample and the determination of the crystal quality.

Micro-Raman measurement were performed at room temperature on different crystals using a He-Ne laser as the exciting line (λ=632.8 nm) of a Jobin Yvon/Horiba LabRam spectrometer equipped with a liquid nitrogen cooled CCD detector. Experiments were carried out using a laser power inferior to 1 mW with a focus spot of about $1\mu m^2$ under the microscope to avoid sample heating.

The chemical composition of the crystals were analysed by Energy Dispersive X-ray Spectroscopy (EDS) using a BRUKER Silicon Drift Detector (SDD) mounted on a Quanta 250 FEI field Emission Gun (FEG) Scanning Electron Microscope (SEM) operated at 15 keV. Observation of the surface is achieved with an optical microscope.

2.2.1 Cr_2AlC crystal characterization

2.2.1.1 Crystal structure and identification

Three different kinds of pole figures were obtained, among which, each one corresponding to one or two different plane orientations with same interplane distance:(a) (0006) (1 peak) and $10\bar{1}3$ (6 peak), (b) $10\bar{1}9$ (6 peak), (c) $(20\bar{2}3)$ (6 peaks) and $(11\bar{2}6)$ (6 peaks) (See Figure 2.12). Particularly, the $10\bar{1}3$ pole figure displays exhibits the expected peaks, all located at the apex of a hexagon. It is noticeable that the interplane

distance of the (0006) planes is very close to that of the $(10\bar{1}3)$ planes, (0.214073 nm and 0.214592 nm, respectively), so that for the crystal orientation along *c*-axis, an additional diffraction peak appears at the origin. For the other crystal orientations, we obtained a set of diffraction peaks which are scattered over the circle including the hexagonal distribution expected from a single crystal.

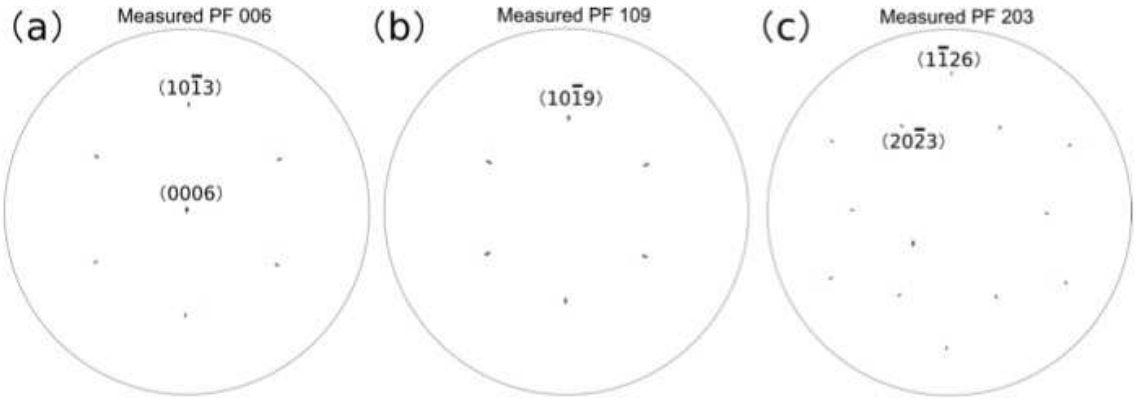

Figure 2.12: *X-ray pole figure of Cr_2AlC platelet with an area of several mm^2.*

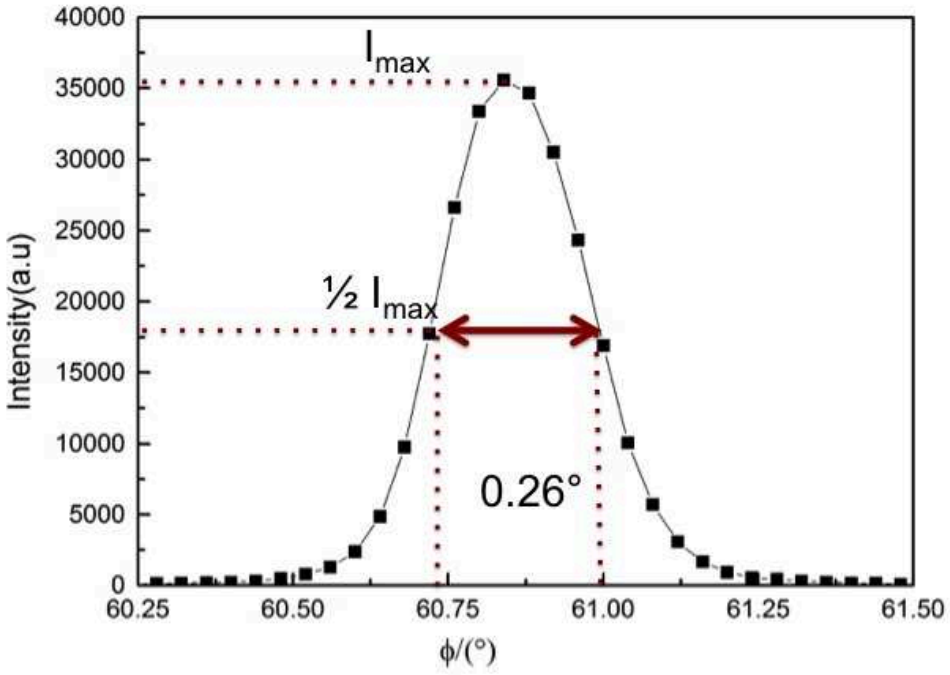

Figure 2.13: *FWHM of ϕ-scan pattern of* $(202\bar{3})$ *plane.*

Figure 2.13 shows that the FWHM (width at half-peak maximum) of ϕ-scans of the $(20\bar{2}3)$ plane is around 0.26°, which is in the order of magnitude 0.1°. In comparison with standard industrial semiconductors materials with the FWHM 0.05°- 0.1°, our single crystals are clearly not that of high quality. We attribute this to the fact that none of the platelets is perfectly flat and to the presence of defects, so that this value can be partly explained in terms of the relaxation of long range residual strain in samples with a very high aspect ratio. Our data indicate that the platelets are single crystals at least over an area of several mm^2 and a depth of order of 10 μm.

2.2.1.2 Raman spectrum

Fast identification can be achieved by Raman spectrum which is determined by the crystal structure. All samples exhibit similar spectra, and a typical Raman spectrum is reported in Figure 2.14(a). Among the four Raman active vibration modes calculated by the factor group analysis of Cr_2AlC ($2E_{2g} + E_{1g} + A_{1g}$, See Figure 2.14(b) [95]), two well-defined Raman peaks appear at 248 and 336 cm-1, which is in agreement with values reported in the literature. Another weaker mode which exhibit as shoulder in the as-shown spectrum at 238 cm^{-1} can be identified to the mode at 237, 263,and 250 cm^{-1} according to various reports [96, 97, 98]. The crystal orientation of our platelet (basal plane perpendicular to the c axis) constrains the observation of E_{1g} modes. So these two intense peaks are determinate to be E_{2g} and A_{1g}. The large band close to 564 cm^{-1} can be attributed to a combination band of two modes of the first order spectrum.

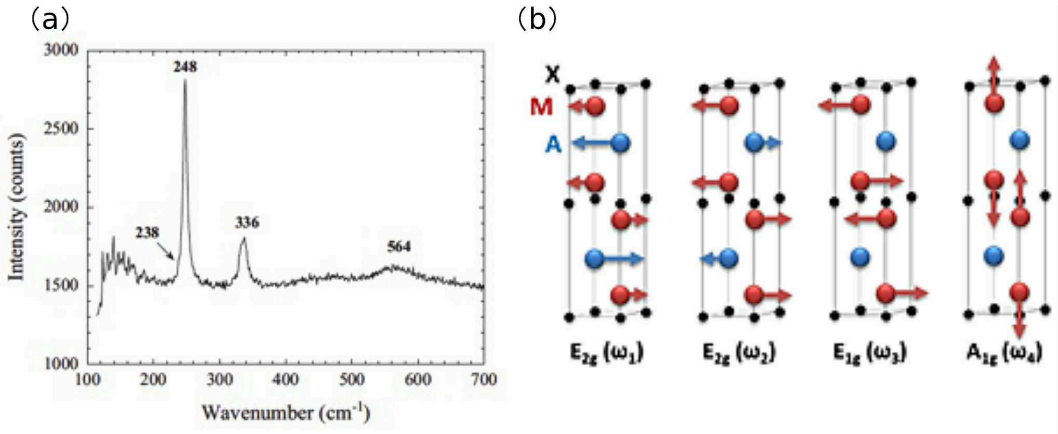

Figure 2.14: *(a) Raman spectrum of Cr_2AlC platelet with an excitation laser parallel to the c-axis (b) Assignment of atomic displacements to the different Raman active vibrational modes in 211MAX phases[95].*

2.2.1.3 Surface morphology of as grown crystals

Crystal growth in the melt can be considered as a two step-process: nucleation and growth. Nucleation can be homogeneous, in the absence of foreign particles or crystals in the solution, or heterogeneous, in the presence of foreign particles in the solution. Both types are known as primary nucleation. Secondary nucleation takes place when nucleation is induced by the presence of crystals of the same substance. No seed crystal is introduced into our growth process, so it is assumed that the primary nucleation occurred spontaneously in the melt during the cooling down. The actual nucleation and growth mechanism of Cr_2AlC crystal is still unclear, as crystallization occurs in the whole volume of the liquid despite the applied temperature gradient. We assumed some heterogeneous nucleation induced by foreign particles or drops [99].

Besides, growth and solidification of other compounds also happen during the cooling stage. Depending on the various growth parameters (temperature, time and cooling down rate), the Cr_2AlC crystals can be forced to grow very close to one another, or in competition with other phases. As a consequence, the final growth stage involves usual solidification phenomena, including but not limited to dendrite growth occurring at the surface of the crystals during final solidification. The accumulation of solute and heat ahead of the interface can lead to circumstances in which the liquid in front of the solidification front is supercooled. The interface thus becomes unstable and in appropriate circumstances solidification gives rise to dendrite. A dendrite tends to branch because the interface instability applies at all points along its growth front. The branching gives it a tree-like character which is the origin of the term dendrite. The aspect of the crystal surface may therefore result in a high variety of morphologies at microscopic scale.

Figure 2.15 shows the optical microscope images of various samples observed in the Normarski mode. Figure 2.15(a) shows the bumpy and tangled surface of the as-grown crystals after cleaning. The dendrite islands can be clearly observed in Figure 2.15(b), which is roughly self-organized.

Crystal surface structure can also be the evidence to explain growth mechanism. One of the most commonly used models was that provided by Kossel [100]. This model envisions the crystal surface as made of cubic units (See Figure 2.16) which form layers of atomic height limited by steps. These steps contain a number of kinks along their length. The area between steps is referred to as a terrace, and it may contain single adsorbed growth units, clusters, or vacancies. According to this model, growth units attached to the surface will form one bond, whereas those attached to the steps and

kinks will form two and three bonds, respectively. Growth will then proceed by the attachment of growth units to kink sites in steps. Then, a new step will be formed by the nucleation of an island of monolayer height on the crystal surface.

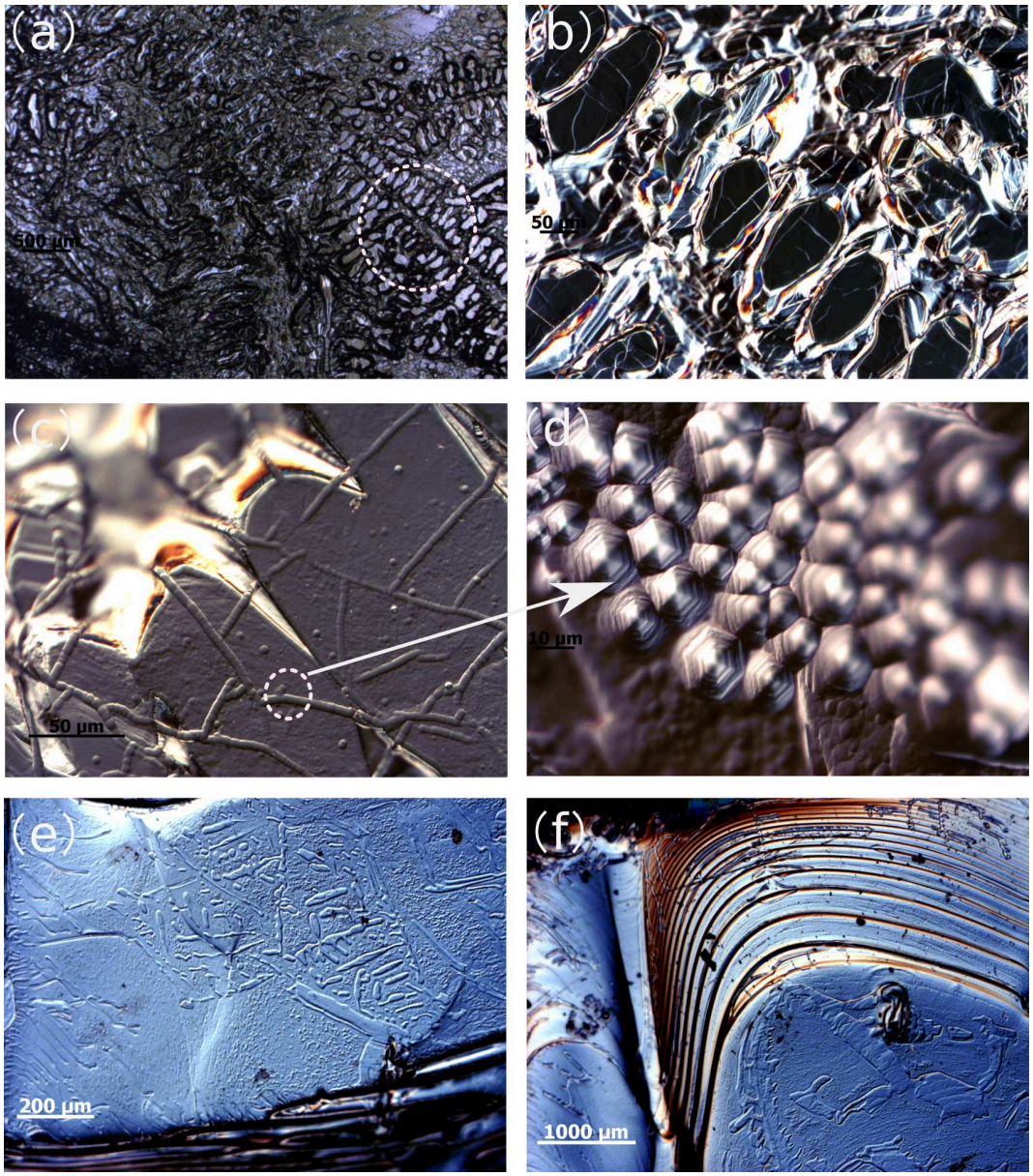

Figure 2.15: *Optical microscope views of the surface of the Cr_2AlC crystals obtained in the Nomarski mode (Differential interference contrast (DIC) microscopy) (a) Bumpy and tangled surface of the as-grown crystals after cleaning (b) Dendrite islands (c-e) Dendrite morphology and (f) Growth terrace.*

However, when the nucleation rate is faster than the time required for the step to cover the whole crystal surface, 2D nuclei will form all over the surface and on top of other nuclei. These nuclei will spread and coalesce forming layers. Growth terrace can

be obviously observed on the surface of our as-grown crystal from the Figure 2.15(f) , we can see the transport and diffusion of solute on the crystal surface. Concurrently, no clear spirals growth phenomenon were obtained.

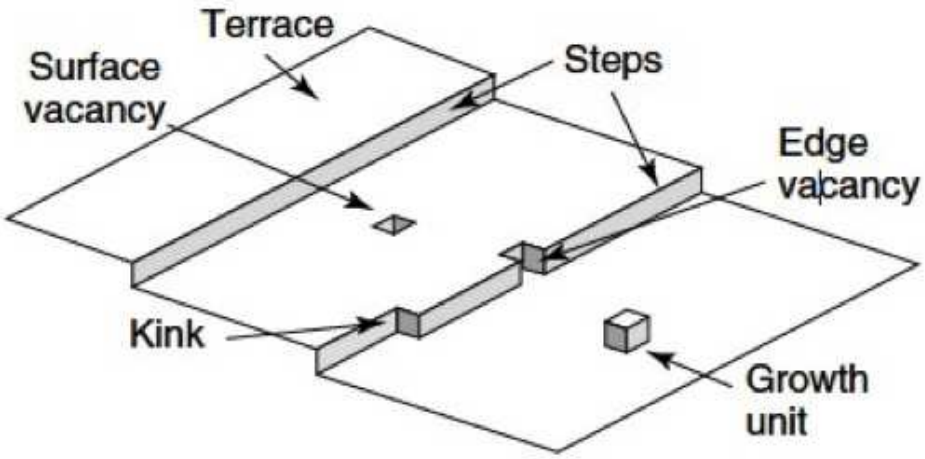

Figure 2.16: *Kossel model of a crystal surface[101].*

SEM analysis has been conducted in order to investigate the nature of the growth. Figure 2.17 shows the typical terrace morphology of the as-grown surface, particularly the peninsulas grown on the terrace as features of 2D instability growth (highlighted with red line in Figure 2.17(b)). As already observed for other materials, it can therefore be inferred that the Ehrlich-Schwoebel (ES) effect, give rise to these Bales-Zangwill instabilities. The mechanism and models of these 2D-growth instabilities have been discussed in detail in the previous experiment of our group for the growth of Ti_3SiC_2 [99]. In such experiments, the presence of foreign particles induces formation of elongated peninsulas or islands on terrace, followed by highly anisotropic growth parallel to the step edges. The instabilities often occur for a larger terrace width, in comparison to the stable and narrow terrace.

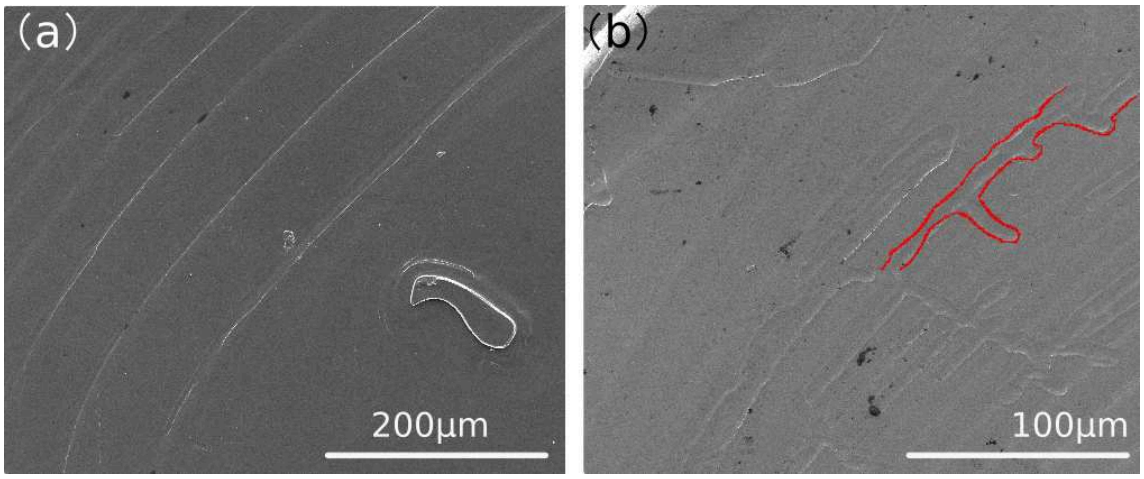

Figure 2.17: *SEM images of as-grown Cr_2AlC crystal surface.*

2.2.2 V_2AlC crystal characterization

2.2.2.1 Crystal structure and identification

Figure 2.18 is a typical XRD patterns of the as-grown V_2AlC platelet. Only (000l) peaks are observed, indicating that the crystal is highly oriented. According to Bragg's law, the extracted lattice parameter are a=2.9149 Åand c=13.1174 Å, which is consistent with the values reported [6].

We essentially observed three different kinds of pole figures, each one corresponding to one or two different plane orientations with the same interplane distance: (a) $20\bar{2}3$ (6 peaks) and ($11\bar{2}6$ (6 peaks), (b) $21\bar{3}3$ (12 peaks) and (c) (0006) (1 peak) and $10\bar{1}3$ (6 peak). Typical pole figures can be seen in Figure 2.19, which experimentally proves the single crystalline nature of the platelets. Usual full widths at half maximum of the diffraction peaks (FWHM) of the ϕ-scans of the V_2AlC crystals range from 0.1 to 0.4°, obviously very far from what is obtained for usual industrial semiconductors. Besides, the peak broadening is usually much larger when plotted as a function of the polar angle χ than versus the azimuth angle ϕ (this is particularly visible for the $21\bar{3}3$ pole figure in Figure 2.19).

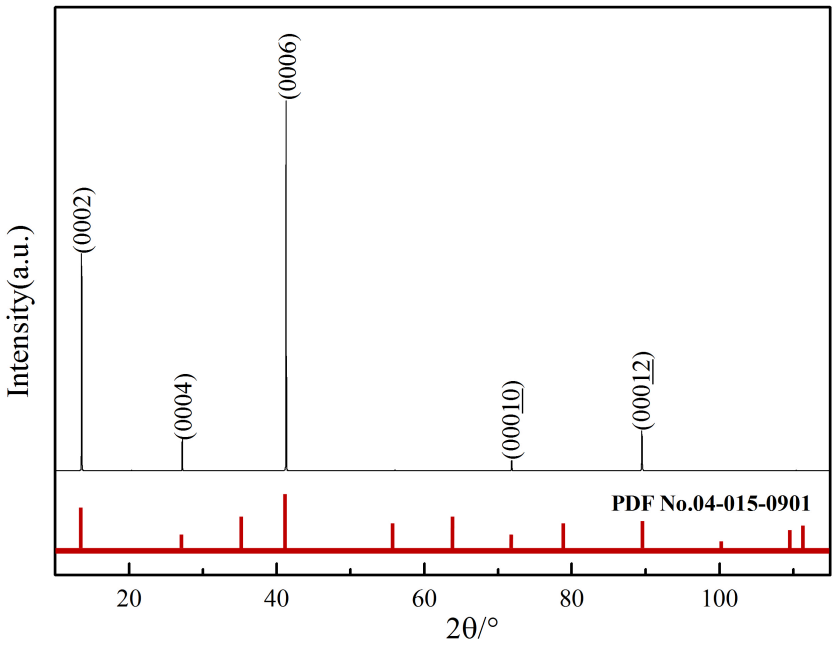

Figure 2.18: *XRD pattern of as-grown V_2AlC platelet.*

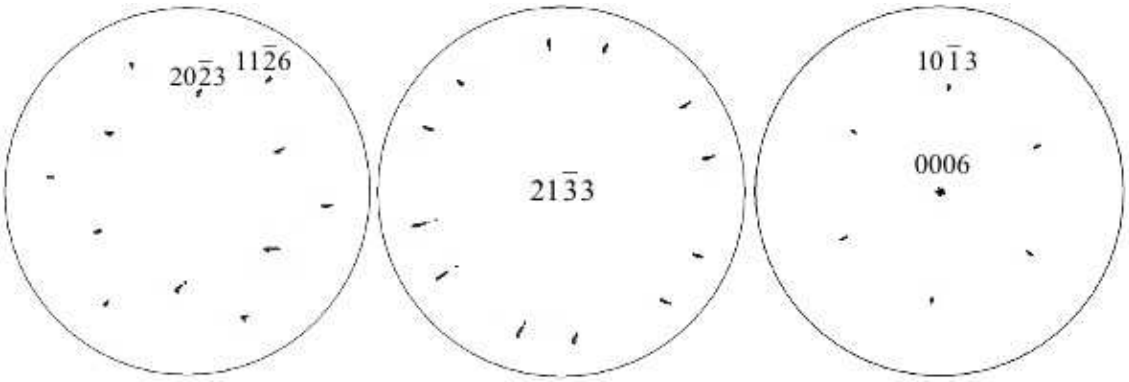

Figure 2.19: *X-ray pole figures measured from a V_2AlC platelet and obtained from different interplane distances. Diffraction peak indexations are shown in the figures.*

We explain this as follows: initially, the crystals are supposed to grow totally flat inside the solution, for they are not subject to any constraint as long as they do not meet each other or the opposite crucible wall. However, upon cooling and during the final solidification stage of the flux, they are submitted to a high stress and a subsequent deformation, enhanced by their small thickness and the ease with which they can be

plastically bent. We expect such an induced curvature to affect mainly the peak width along χ, whereas a coalescence of crystal planes with the same orientation of the c-axis, but rotated with respect to one another around this axis, or any rotation disorder or mosaicity in the basal plane would rather lead to a broadening of the ϕ-scan peaks. This explanation is also made plausible by the fact that in the case of much thicker Cr_2AlC crystals (around 400 μm-thick), such a wide broadening along χ is not observed.

2.2.2.2 Raman spectrum

Raman measurements performed on different flat and large crystals led to the typical spectrum shown in Figure 4.19 (top spectrum). All the four Raman active optical modes predicted by the factor group analysis of V_2AlC are observed at 158, 239, 259 and 362 cm^{-1} in the backscattering configuration used with the laser beam propagation along the c axis, which is in good agreement with the spectra reported by Spanier et al. [97] and Presser et al. [102]. The similarity between Raman spectra of Cr_2AlC and V_2AlC, both compounds belonging to the same 211 MAX phase family with the same crystal structure, and the V_2AlC mode assignment reported in [97] allow us to assign the different modes to E_{2g}, E_{1g}, E_{2g} and A_{1g}, respectively.

In our spectra, only the mode E_{1g} at 239 cm^{-1} slightly differs in intensity and position from one crystal to another one. Theoretically, this mode should not be observed in this backscattering configuration according to the Raman selection rules. Its observation probably results from some polarization leakage due to a slight misorientation between the laser beam and the crystal c axis, its amplitude varying with the misorientation angle. Together with the E_{2g} modes, this mode is also observed in polarized spectra collected using crossed polarization configuration (Figure 2.20, bottom), which is not predicted by the selection rules. This confirms that the crystal is not strictly horizontal. As expected for A_{1g} symmetry modes, the mode pointed at 362 cm^{-1} is not observed in this configuration.

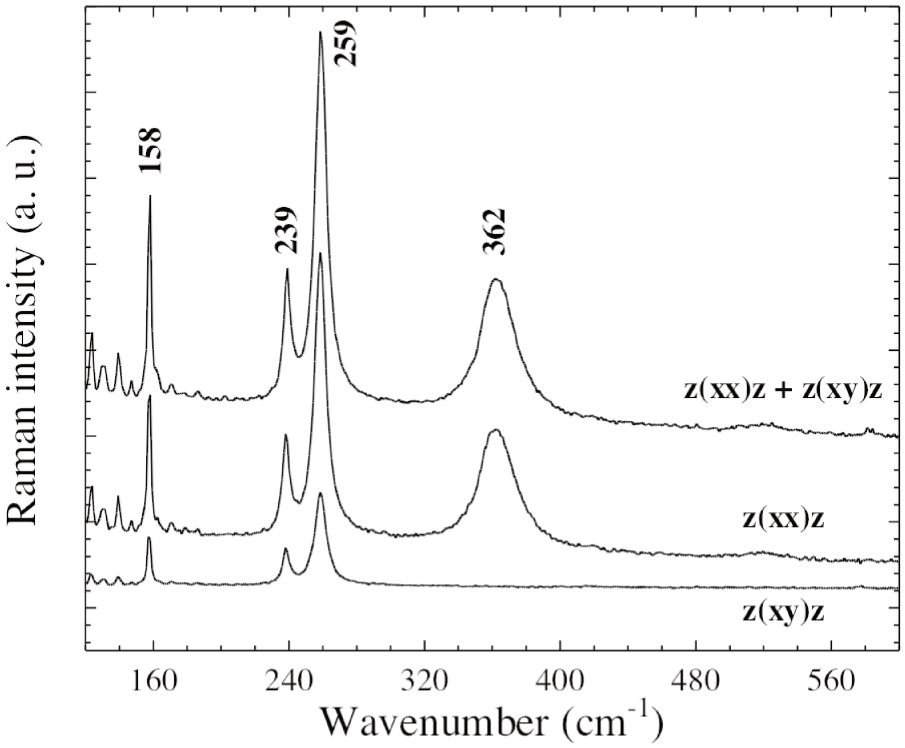

Figure 2.20: *Raman spectra collected from V_2AlC single-crystalline platelet in the configuration with an excitation laser beam parallel to the c axis: unpolarized spectrum.*

2.2.2.3 Surface morphology of as grown crystals

With reference to Cr_2AlC, Figure 2.21 show the optical views of V_2AlC crystals in the Nomarski mode. Generally, V_2AlC exhibits flat, even and smooth surface compared to that of Cr_2AlC, though some dendrite structure can also be detected. (See Figure 2.21(c)). As we discussed, carbon solubility in V-Al melts is not as high as Cr-Al melt, the numbers of nuclei consequently is lower, which allow the crystals can grow independently and less effected by other solidified compounds. As explained in the previous section, 2D nuclei formed on the surface or on top of other nuclei depend on the nucleation rate and growth rate (See Figure 2.21(b)). After etching with concentrated HCl, hexagonal holes, known as etch pits, appeared on the surface, especially in the defective region.

Normally, the energetics of layer growth predict that growth takes place at relatively high supersaturation (needed to overcome the energy barrier associated with 2D nucleation). However, it has been observed that crystals can still grow at lower supersaturation than predicted. This dilemma was solved by Frank who proposed that crystal surfaces are intercepted by screw dislocations. These dislocations will create steps in the surface, obviating the necessity for 2D nucleation.The theory of crystal growth by spiral

dislocation was further refined by Burton, Cabrera, and Frank, giving rise to what is known as the BCF theory[103]. In our experiment, the unpredictable growth process can be attribute to the absence of seed crystal and designed temperature gradient. Hence, we find there may be several nucleation and growth synergy mechanism.

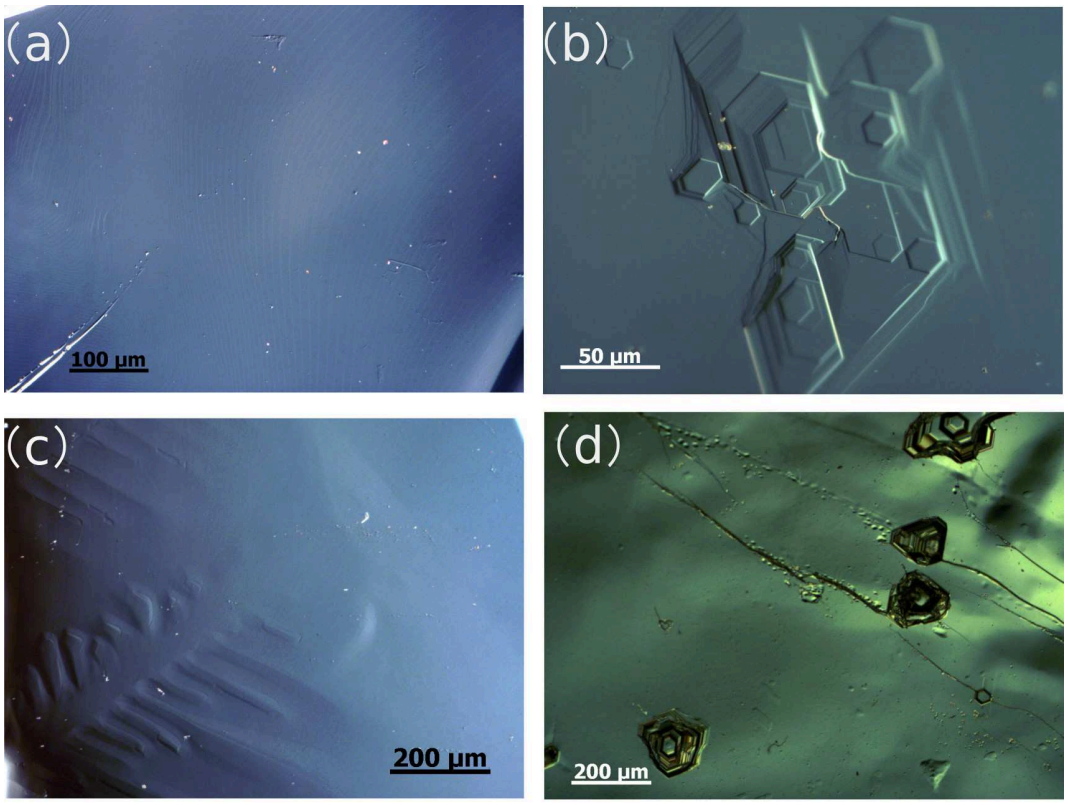

Figure 2.21: *Optical microscope views of the surface of V_2AlC crystals obtained in the Nomarski mode(a) Flat surface (b) Heterogeneous nuclei (c) Dendrite structure (d) Etch pits.*

The V_2AlC crystals are usually very flat at microscopic scale, in contrast to their Cr_2AlC counterparts, which often exhibit surface dendrites. This may be connected to a lower growth density of the V_2AlC crystals, which generally remain isolated from one another inside the solution, whereas in the case of Cr_2AlC they are located quite close to one another and their growth in the basal plane is often stopped after meeting another crystal.

Investigation of the surface by means of atomic force microscope shows that the underlying surface morphology is characteristic of a step flow growth process, with well defined steps and terraces (Figure 2.22(a)). On the flat parts, the step height is most often equal to *c*, the lattice base vector along the *c*-axis (*c*=1.31nm), and those regions are

separated by highly bunched steps. Locally, the terrace width is generally regular. The physical origin of the step flow process is still unknown, and we never found particular surface structures indicating mechanisms such as, e.g., spiral growth, nor a particular morphological pattern which might be responsible for the birth of the step and terrace structure.

It is worth noting that even if the HCl etching step used for dissolving the solidified flux does not appreciably modify the crystals, it nevertheless induces a partial etching of the step edges which is clearly visible in Figure 2.22(a) and which is substantially aggravated in regions exhibiting a higher defect density (Figure 2.22(b)). In some unusual cases, the surface can even exhibit microscopic etch pits which might indicate the presence of threading dislocations, as observed for other materials with appropriate etchants[104]. Immersing crystals in concentrated HF (40%) for 5 days does not appreciably change their macroscopic appearance, but modify their surface. However, we did not obtain any delamination of the MX planes by removal of the A plane. This is most probably due to the fact that in a highly polycrystalline structure, HF penetration is greatly favoured, in contrast to the case of our single crystals.

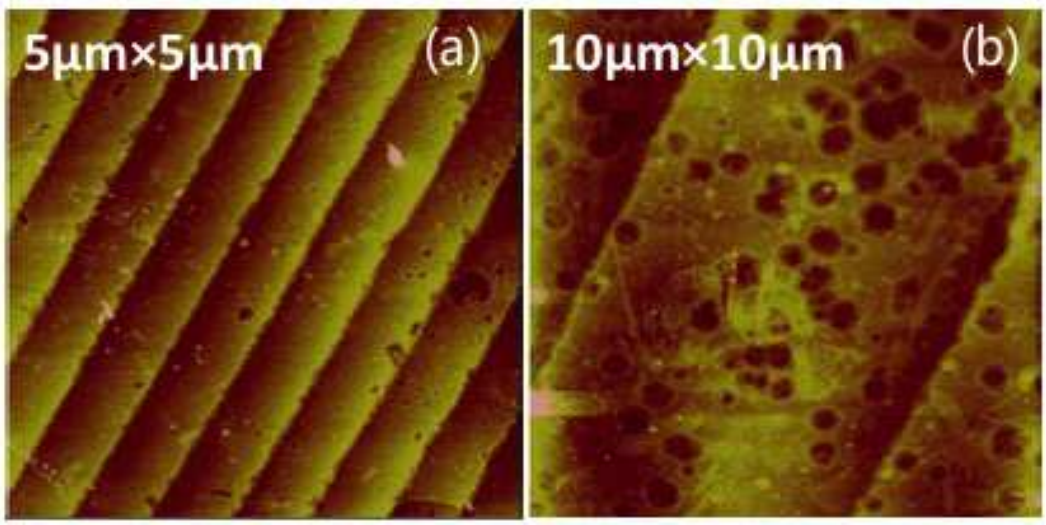

Figure 2.22: *AFM topographic images of the surface of V_2AlC platelets after dissolution of the solidified flux in concentrated HCl during several hours. A terrace and step structure characteristic of a step flow growth process is visible. In both images all the step heights are equal to c.*

2.2.2.4 Surface morphology of platelets cleaved along the basal plane

An outstanding illustration of the MAX phase nano-lamellar structure and of the weakness of the A atomic bonds is given by the ease with which the platelets can be cleaved along the basal plane, using a process almost similar to producing graphene from graphite. Sticking a platelet onto a strong adhesive tape (gorillaTM), folding the tape onto the crystal and separating the folded parts again is enough for cleaving the platelets in the basal plane, a fact which would be clearly impossible to realize with materials characterized by a strong covalent bonding. As for graphite, the separation can occur not only because basal atomic planes are not tightly bound, but because the detached layer can be deformed without systematically breaking, so that all the "weak" detachment force is applied at the separation line, and not over the full surface (in the latter case, even bonding through van der Waals forces would be too strong to allow plane separation).

We already observed such a cleavage with Cr_2AlC and Ti_3SiC_2, but it is in general not possible to obtain a separation over the full sample area for those two materials. This can be ascribed to the fact that the Cr_2AlC samples are rougher and thicker, so that the adhesion of the tape depends on the position and is not homogeneous. As a consequence, only some top regions of the Cr_2AlC sample or regions devoid of surface dendrites sufficiently adhere to the tape to lead to a partial mechanical cleavage. V_2AlC platelets are thinner and flatter, so that the adhesion is more homogeneous and so more efficient. In some cases, this allows us to obtain cleavage over the full crystal area, as exemplified by the photograph of Figure 2.23. The remaining part of this section is devoted to the AFM observation of the produced cleaved surfaces.

The surface usually exhibits terraces often ending with a triangular shape (Figure 2.23). Most terraces are separated by unit or half-unit steps, and sometimes by higher steps, but then still equal to an integer number of half-units. This strongly supports the assumption that local cleavage is always obtained at the A atomic planes, since those planes appear twice in a unit cell. In some regions, only a very few steps appear on areas as large as 50 μm $\times$50 μm, and in other regions the cleavage results in more disturbed patterns (Figure 2.23)).

In some regions, half-unit sharp triangular tears, either terraces or grooves, all start from a single line, and basically exhibit two different kinds of shape, as shown in Figure 2.24 for which we chose an image including both kinds of patterns. The tears are either roughly symmetrical in the direction of the pulling or asymmetrical. The crack orientation is determined by the competition of several factors, since the tearing

angle corresponds to the minimum energy variation and depends on a number of other parameters, such as the initial curvature, the film thickness and the width of the flap to be delaminated [105]. We attribute the origin of asymmetrical shapes to the fact that, once a crack is initiated along a direction with a weaker number of bonds, then it goes on in that direction.

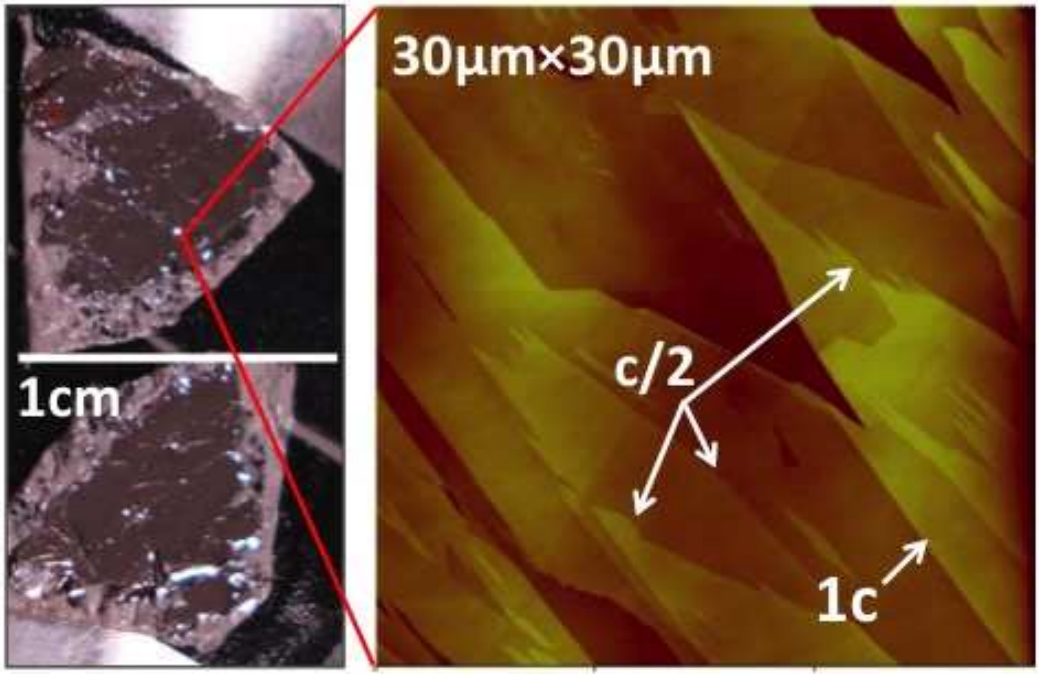

Figure 2.23: *The left photograph shows the two parts of a V_2AlC crystal after cleavage with a strong adhesive tape (the tape has been cut around the cleaved crystal and corresponds to the white color). The right image is an AFM topography of the cleaved surface in a region with a high density of tears.*

Focusing on the symmetrical patterns, such tears are usually observed during the pulling of a simple adhesive tape [105] or of a graphene sheet [106], and we also observed it with Cr_2AlC samples. More specifically, it has been shown that if the ratio between the flap width W (i.e. the basis of our triangles) and the flap thickness t is much larger than the ratio between the adhesive energy per unit surface τ and the energy of the edge to be cracked γ, then the tear angle θ behaves as $\sin\theta \propto (2B\tau)1/2/2\gamma t$, where B is the bending modulus, so that it is independent of W [107].

Even if the atomic bonding between the A atoms and the M sublayer atoms is weaker than M-M or X-X bonding coming into the play for cracking the flap edge, the corresponding ratio is certainly much smaller than $2\,W/c$, since we observed W values larger than 0.1 μm. This implies that locally, the angle of symmetrical tears should

remain constant, so that the dependence of the height h of these triangles on the triangle basis b should be linear. We produced statistics from an AFM image including many such triangles, and the experimental plot of h versus b is reasonably linear (Figure 2.24), confirming the physical process at play during the cleavage. We do not know if the line from which starts a series of triangles is due to the existence of a particular defect, such as a partial dislocation in the basal plane.

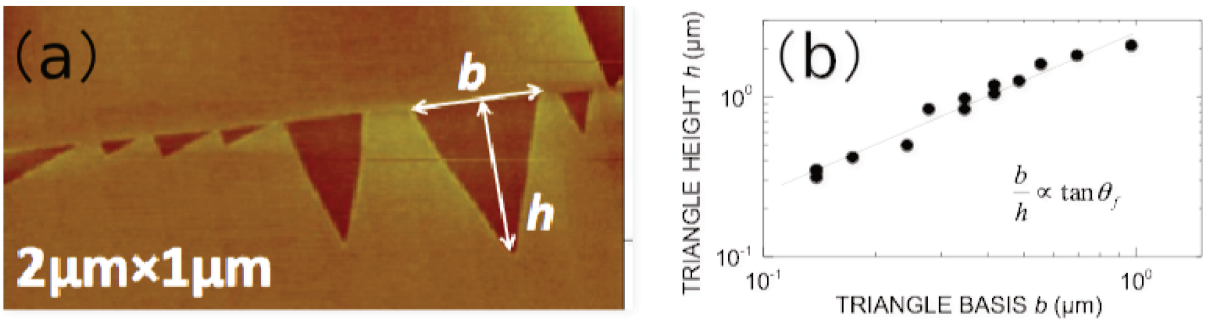

Figure 2.24: *(a) AFM micrograph showing symmetrical and asymmetrical triangular tears starting from a common line (b)Plot of the height versus the basis of symmetrical triangles contained in a region of area 40 µm ×40 µm.*

A terrace of a cleaved surface is not atomically flat, but presents a residual roughness (Figure 2.25). We found two different kinds of surfaces, but since the samples were measured under air, and sometimes after several days, we do not know if these variations in roughness are intrinsic to the materials or due to a surface modification as oxidation or water adsorption. In the first case, the surface is almost flat, with a root mean square value of the roughness below 0.06 nm. In the second case, the roughness is higher, in the range of 0.18 nm, but still below that of a full atomic layer.

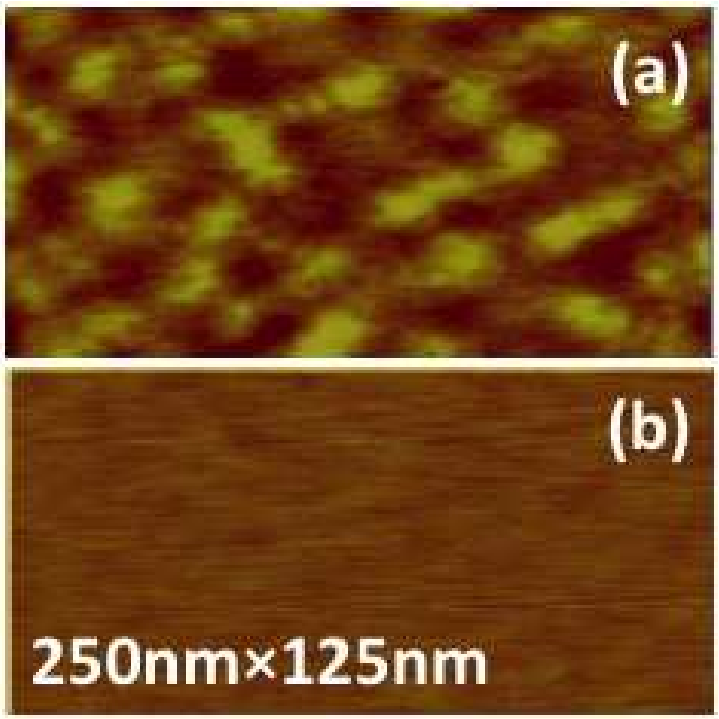

Figure 2.25: *AFM images of the top surface of a terrace (the color range corresponds to a much smaller height than in the previous figures). The extracted RMS value of the roughness is 0.18 nm for image (a) and 0.06 nm for image (b).*

2.2.3 Ti_2SnC crystal charaterization

Structural characterization were conducted on the as-grown Ti_2SnC single crystals as well. In order to compare with the as-etched crystals according to the attempts on Ti_2C MXene from Ti_2SnC in Chapter IV, some results are briefly demonstrated in Figure 2.26. The hexagonal morphology of the crystal as resulted from the SEM micrographs, combined with the EDX results, undoubtedly prove the harvest of Ti_2SnC crystals. Due to the lack of reported data on the Raman spectrum of Ti_2SnC, we can only refer to our results on other M_2AX MAX phase, the peak at 246.8 cm^{-1} can be assigned to E_{2g} mode, which is generated by the M-A atoms in-plane vibrations.

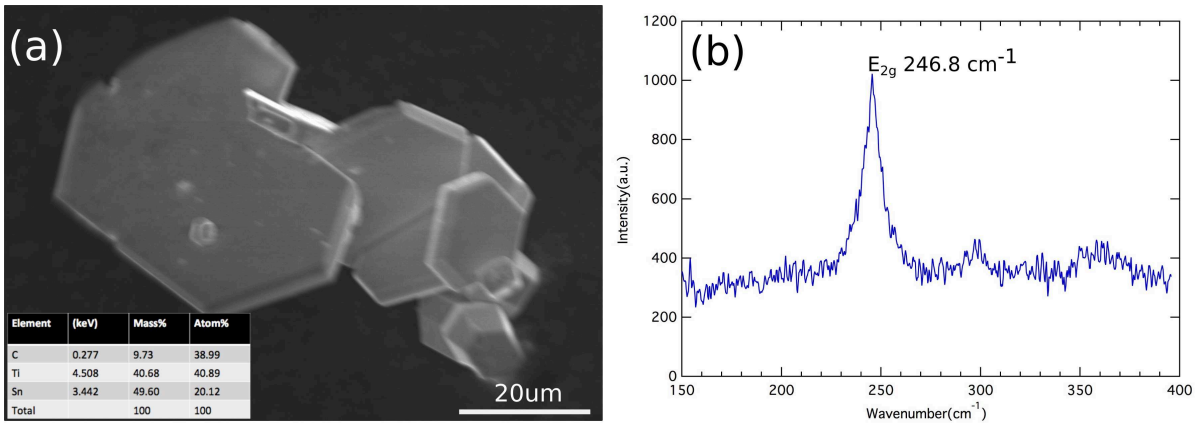

Figure 2.26: *(a) SEM image indicating the hexagonal morphology of the crystal (inserted EDX results showing the atomic ratio of Ti:Sn:C) and (b) Raman spectrum of Ti_2SnC.*

2.3 Conclusion

Using high temperature solution growth and slow cooling technique, several MAX phase single crystals were successfully grown:

The solution growth is clearly limited by the carbon solubility in the flux. The most favourable case is that of Cr-Al-C, because carbon solubility can be achieved very high and better still, at very acceptable temperature. For a given crucible size, the final platelet area mainly depends on carbon solubility: some 10^{-4} cm^2 for Ti_2SnC, some 0.25 cm^2 for Ti_3SiC_2, 1 cm^2 for V_2AlC and several cm^2 for Cr_2AlC were obtained in in our experiment set-up.

Structural characterization confirms the single crystalline character of the samples by X-ray measurements and Raman spectroscopy. The surface morphology of V_2AlC crystals is flat without dendrites observed on the surface of Cr_2AlC. Well defined steps and terraces indicates a step flow growth process. Emphasis is put on the mechanical cleavage of the sample which can be achieved in the basal plane thanks to the existence of the weakly bonded Al atomic planes.

The nano-lamellar structure of the crystals permits to cleave the platelets parallel to the basal plane just by sticking and folding a strong adhesive tape on each face. The initial flatness of the crystal surface allowed us to obtain cleaved areas almost equal to that of the entire platelet. Since the transformation of HF-treated, polycrystalline V_2AlC into MXene nano- or micro-crystals has already been proved, our crystals might be used as a starting basis for forming MXenes with macroscopic area. This will be the main objective of next step work, along with the assessment of the transport properties.

chapter 3

Transport properties of MAX phases

In this chapter, in-plane and out-of-plane magneto-electronic transport properties of MAX phase have been investigated experimentally and theoretically. For in-plane transport, we firstly investigated the in-plane resistivity as the function of temperature and magnetic field, followed by the Hall effect measurement. Thermal transport measurement was also conducted on MAX single crystal samples. For out-of-plane transport, out of plane resistivity was measured and a substantial anisotropy ratio was observed. Results on the out-of-plane magnetoelectronic transport are also discussed. Theoretically, a general model is proposed for describing the weak field magneto-transport properties of nearly free electrons in two-dimensional hexagonal metals. It was then modified to be applicable for the transport properties of layered MAX phases.

3.1 Experiment details

3.1.1 Measurement configuration

3.1.1.1 In-plane transport

Four probes method Four probes method was adopted to eliminate contact resistance for these low resistivity materials [108]. Figure 3.1(a) is schematic of the four probes method.

$$\rho = R\frac{s}{l} = R\frac{wt}{l} = \frac{1}{\sigma} \tag{3.1}$$

where: ρ is resistivity, R is resistance obtained from the measurement (V/I), S is cross section area perpendicular to the current direction, l is distance between two side contacts, w is sample width, t: sample thickness.

Van der Pauw geometry A schematic of a square Van der Pauw configuration is shown in Figure 3.1(b) [109]. In our exeriment, the Van der Pauw geometry was used for the temperature dependency of resitivity, not for Hall measurement.

Four voltage measurements yield the following four values of resistance

$R_{21,34} = V_{34}/I_{21}$, $R_{32,14} = V_{41}/I_{32}$, $R_{43,21} = V_{12}/I_{43}$, $R_{14,23} = V_{14}/I_{23}$,

Then the two characteristic resistance can be written as

$R_A = (R_{21,34} + R_{43,21})/2$, $R_B = (R_{32,41} + R_{14,23})/2$,

Van de Pauw demonstrated that R_A and R_B determinate the sheet resistance R_S through the Van der Pauw equation:

$$\exp\left(-\pi\frac{R_A}{R_S}\right) + \exp\left(-\pi\frac{R_B}{R_S}\right) = 1 \tag{3.2}$$

Thus, the resistivity can be calculated using $\rho = R_S \times t$, where t is the sample thickness.

Hall bar bridge Figure 3.1(c) is a typical Hall bar geometry, the Hall coefficient is defined as $R_H = \frac{V_H t}{IB}$, where t is sample thickness.

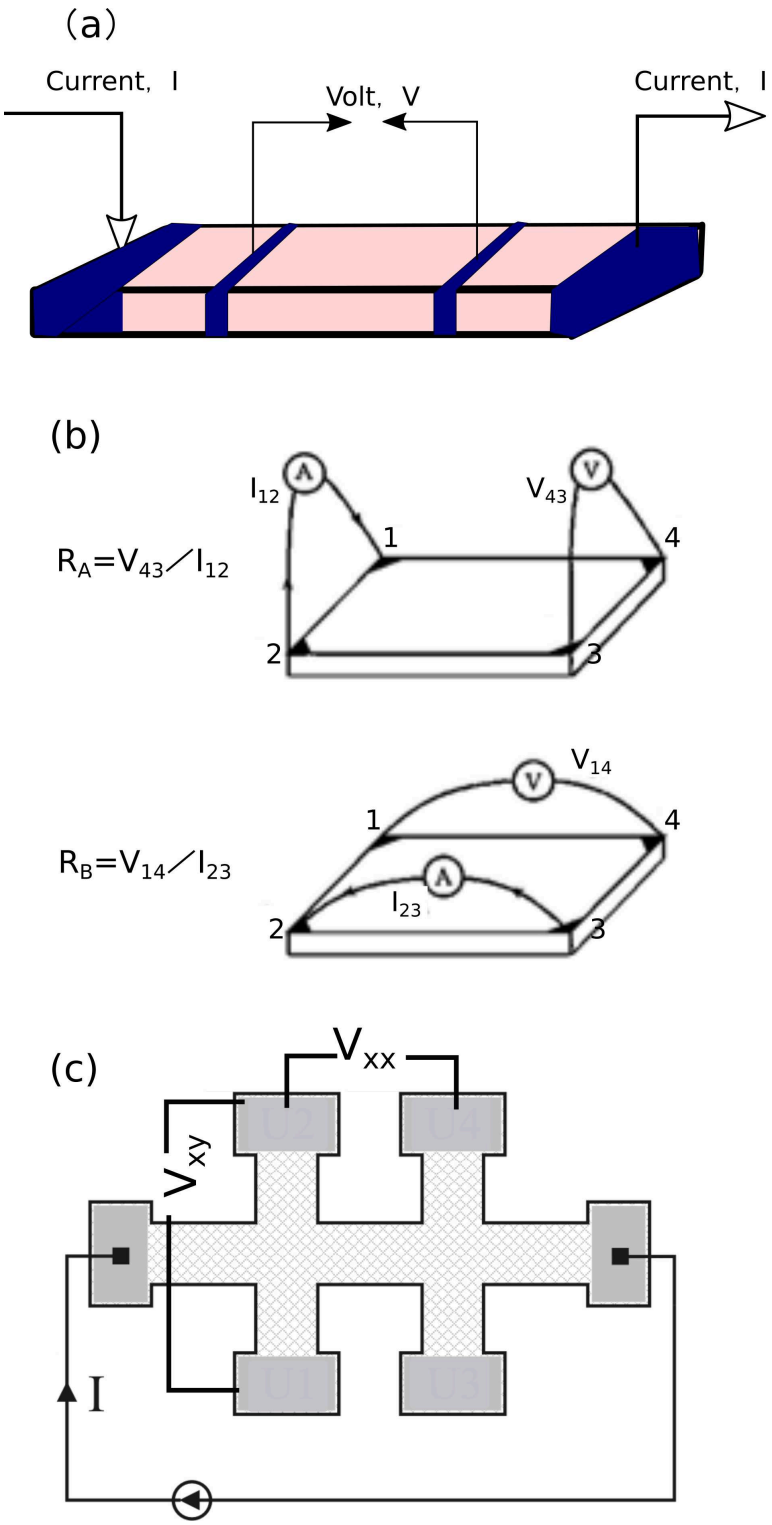

Figure 3.1: *Geometry of in-plane measurements: (a) Four probe (b) Van der Pauw [109] (c) Hall bar bridge.*

3.1.1.2 Out-of-plane transport

All samples exhibit a high aspect ratio, which makes difficult a correct extraction of the resistivity along the c-axis, ρ_c. For such geometries, the Montgomery method [110] is

not well suited, especially if the anisotropy ratio is large and varies with T, for one may then suffers from a crossing between different regimes of current distribution. The most appropriate strategy is to use conditions as close as possible to a direct measurement of ρ_c and ρ_{ab}. Here we use a specific geometry, as proposed by M. Charalambous a few decades ago for analysing the anisotropies of the normal state resistivity of $YBa_2Cu_3O_{7-x}$ [111, 112] . The device structure and measurement principle are illustrated by Figure 3.2(a). The current is injected through large rectangle contacts, which consist in a stack of Ti or Cr and Cu layers. The voltage is measured through smaller contact stripes patterned at the side of the squares.

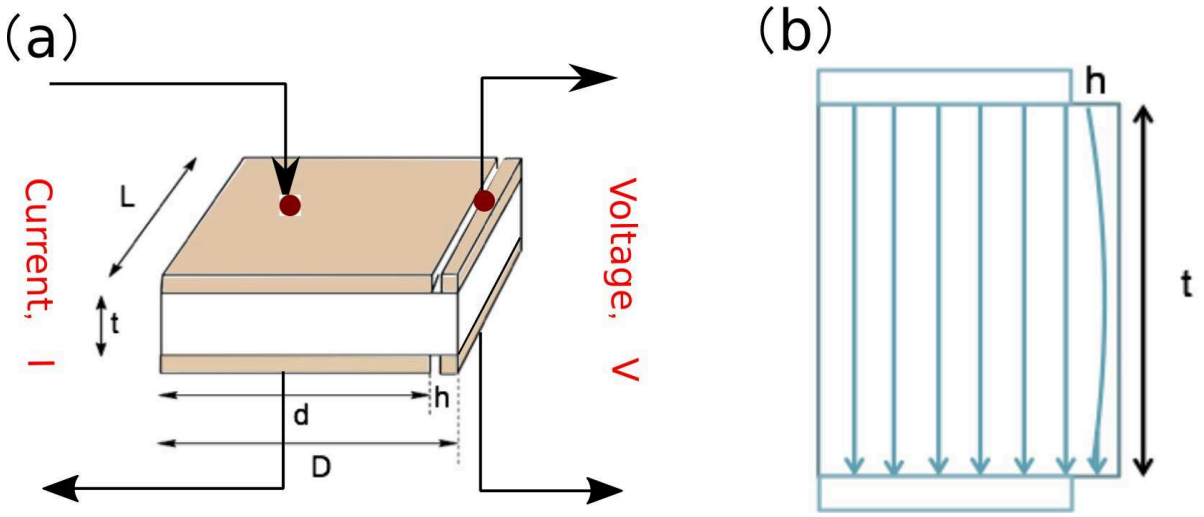

Figure 3.2: *Geometry of out-of-plane measurement: (a) Contact configuration and (b) Derivation of current lines along the edge.*

Large contacts for current ensure the homogeneous current line, yet, due to the derivation of current line at the edge (see Figure 3.2(b)), correction factor f has been taken into account to correct the measured raw resistance data. Here, f is a function of sample geometry and is computed by conformal mapping of the sample [111], as a function of the relevant geometrical factor h/e, where h is the extent of the lateral contacts and spacing, and e is defined by

$$e = t\sqrt{\frac{\rho_c(measured)}{\rho_{ab}}}.$$

Here we note that for practical purposes we found that the numerical integral giving f can be replaced by an analytical approximation, which is plotted in Figure 3.3:

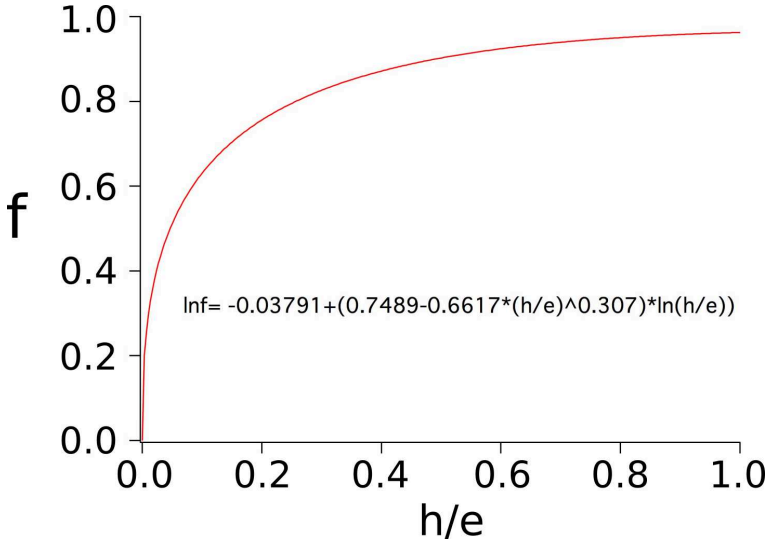

Figure 3.3: *Correction function curve.*

Then, the resistivity is calculated as

$$\rho_c(corrected) = R \times \frac{Ld}{t}(1-f)^{-1} \tag{3.3}$$

where R is the measured resistance, and L, d and t are dimensions defined in Figure 3.2(a). Once ρ_c is measured, the resistivity anisotropy ratio ρ_c/ρ_{ab} is obtained by using the in-plane tranport resistivity measured from a Van der Pauw sample or a Hall bar processed from crystal issued from the same process run in order to minimize the sample quality variations.

3.1.2 Sample fabrication

3.1.2.1 In-plane transport

Single crystals of Cr_2AlC, V_2AlC, Ti_3SiC_2 and Ti_2SnC were successfully grown. Among them, the size of the Ti_3SiC_2 and Ti_2SnC crystals remains quite small, so the data reported here are therefore restricted to Cr_2AlC and V_2AlC crystals of macroscopic size. The crystal plane is always perpendicular to the c-axis. The typical areas of the crystals are in the range of a few cm^2 for Cr_2AlC, and around 1 cm^2 for V_2AlC, with thicknesses t of order 200-300 µm for Cr_2AlC and 30-50 µm for V_2AlC. For all the geometries discussed above, sample has to be prepared based on following criterion: 1) sample should have flat surface with uniform and homogeneous thickness, 2) all contacts should be located at the edge of othe sample.

As demonstrated in the previous chapter, the as-grown surface of V_2AlC is flat and its initial thickness does not vary more than a few percent over the crystal area while

that of Cr_2AlC crystals needed to be firstly polished so as to obtain a good thickness homogeneity. The samples are processed in two different ways: some are cut with a diamond wire saw so as to form parallelepiped-shaped samples with well-defined dimensions. Some others are defined by laser cut, which allows one to produce more complicated shapes, such as Hall bars with well-defined and aligned lateral arms. Figure 3.4(a,b) shows the samples fabricated by these two different ways. In order to investigate the effect of high power laser on the samples, optical microscopic photos were shown as well , indicating that the sample did not burn heavily or not too many defects were generated in spite of few oxidation layers along the cutting edge.

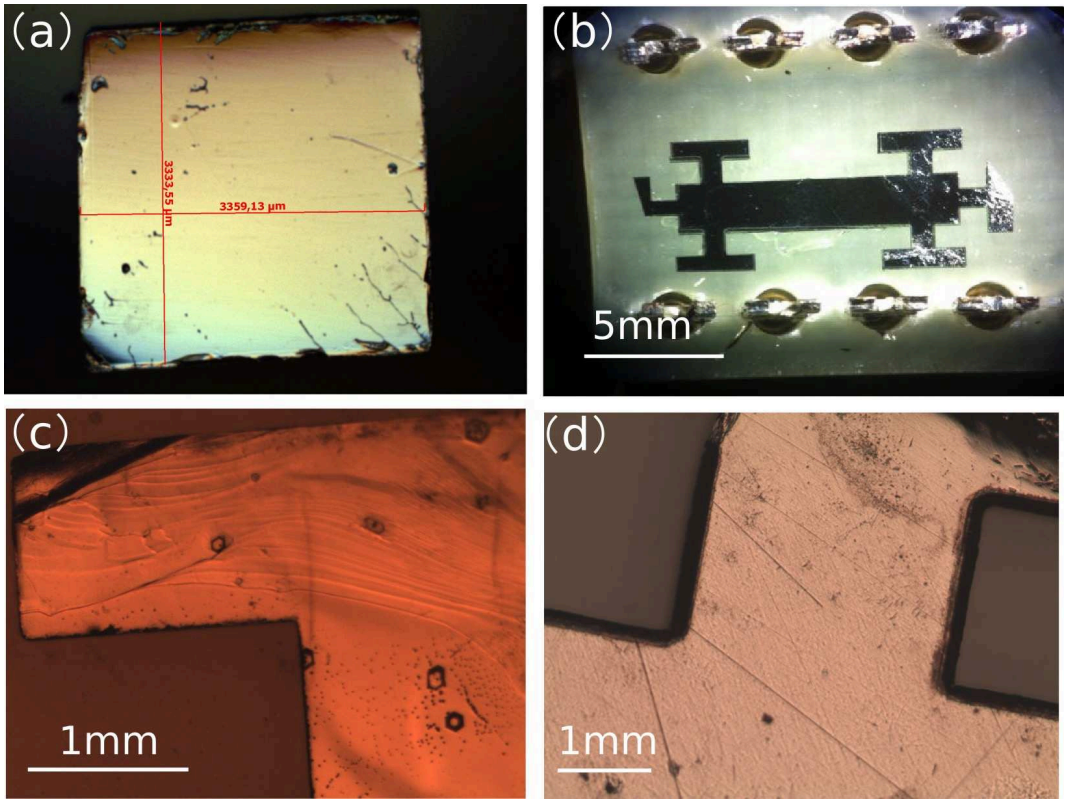

Figure 3.4: *(a) Diamond saw cutting of V_2AlC (b) Laser cutting of Cr_2AlC; Optical microscopic photos of the heat affect area of laser cutting of (c) V_2AlC and (d) Cr_2AlC.*

3.1.2.2 Out-of-plane

For the out-of-plane transport, a metallic mask was machined by laser patterning. (See Figure 3.5 (a)). Sample was placed in the high vacuum chamber of an E-gun Vacotec evaporation system available in the WINFAB cleanroom, Louvain-la-neuve. Then we proceeded a first metal deposition of a 5 nm-thick Ti/Cr layer followed by a second metallization of a 500 nm Cu layer. Here, the Ti/Cr layer is used as an adhesion layer,

Cr seemed perform better for Cr_2AlC sample than Ti. The deposition rate for Ti/Cr is 1 Å/s, for Cu is 3 Å/s. Meanwhile, a standard silicon sample was also prepared as reference (See Figure 3.5(b)). Figure 3.5(c) shows the optical microscopic view of contacts on the Cr_2AlC sample.

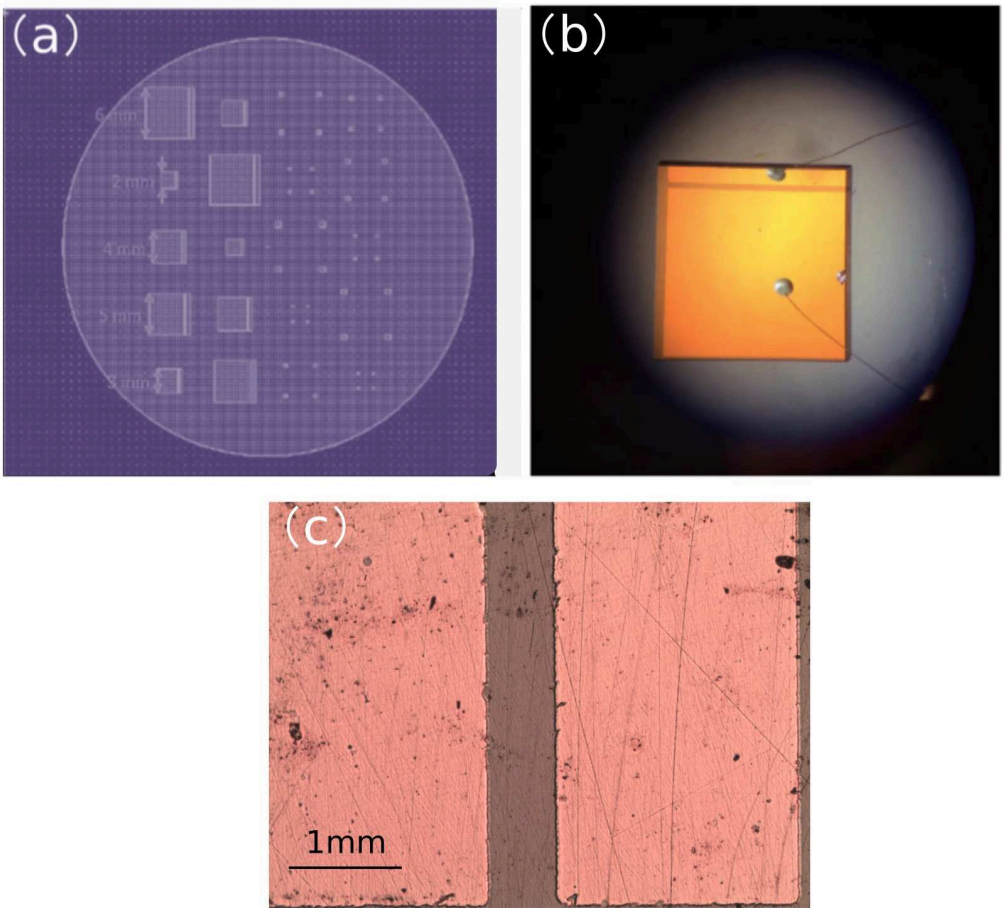

Figure 3.5: *(a) Metalization mask for contact deposition and designed for different size of MAX phase samples (b) Standard silicon sample (c) Microscopic photo of as-prepared Cr_2AlC sample.*

3.1.2.3 Lock-in setup

During our measurements, several types of Lock-in amplifiers have been used, which include SR124-200kHZ analog Lock-in Amplifier (Stanford Research System), 7265 Dual Phase DSP Lock-in Amplifier (SIGNAL RECOVERY) and MFLI 500kHz (Zurich Instruments). Figure 3.6 shows the connection of device under test (DUT) with Lock-in amplifiers. Low frequency (20-200 Hz) sinusoidal DC signal was sent into the DUT as the input, adjusting circuit current value in the range of 1 mA-10 mA. The typical

resistance measured in the present test is in the range of hundreds of $\mu\Omega$ to several mΩ. The most difficult part of these measurements practically lie upon the extreme small signals of only a few nanovolts in the presence of noise sources of much greater amplitude, especially for out-of-plane sample at low T. Figure 3.7 gives an example of c-axis resistivity measurement to indicate that at low T, even the out-of-phase signal value can be comparable to the in-phase value, yet it remains constant during all the temperature range.

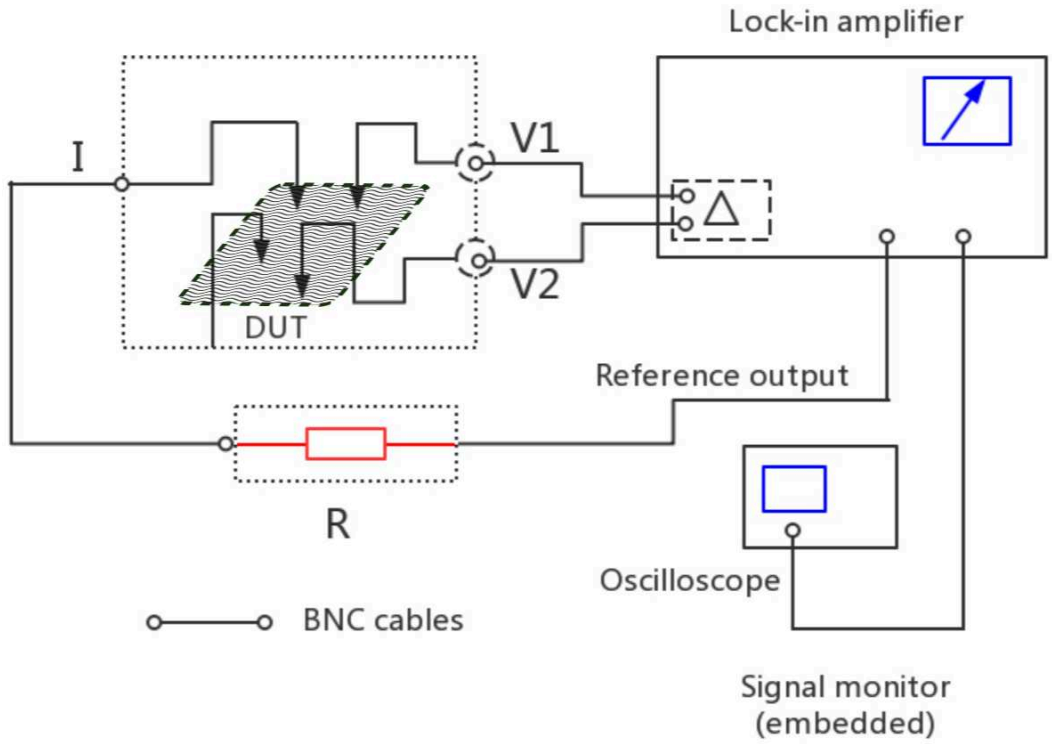

Figure 3.6: *Four probes measurement with Lock-in amplifiers in the present experiments.*

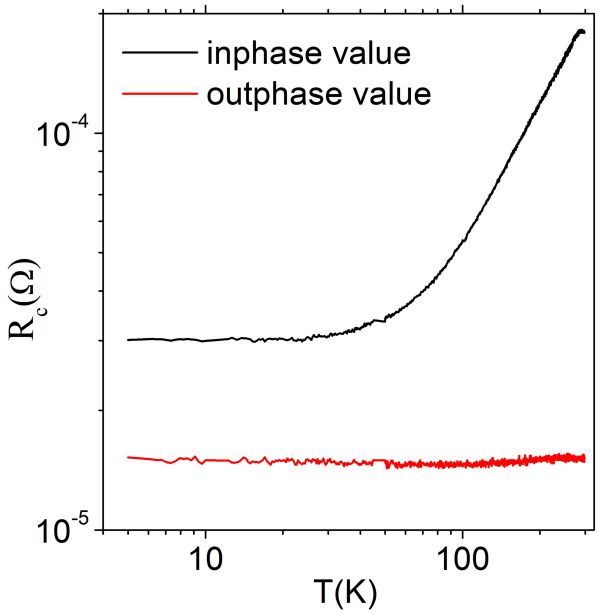

Figure 3.7: *Ratio of in-phase and out of phase signal (example: raw curve of V_2AlC out-of-plane resistivity measurement).*

3.2 MAX phase transport properties

3.2.1 In-plane resistivity

Figure 3.8 summarizes the temperature dependency of in-plane resistivity obtained in both cases of Cr_2AlC and V_2AlC. First of all, in the 100 K-300 K temperature range, there is a linear dependence of ρ as a function of T as generally observed of almost all MAX phases compounds [3]. The evolution is qualitatively similar to that already reported for polycrystalline phases, but the resistivity values are much smaller in the case of the single crystals. This typical metal-like behaviour is assumed to be simply due to the large density of states at Fermi level as explained in the Chapter I. Note that variations between the absolute in plane resistivity values measured among different samples are not negligible. Possible cause for these variations include different levels of defects (e.g. related to slightly different synthesis conditions), as well as imperfect electrical contacting of all the planes constituting the structure.

In comparison with the resistivity value of polycrystalline samples for both cases (1.5×10^{-7} Ω·m (4 K) and 7.4×10^{-7} Ω·m (300 K) for Cr_2AlC, 4×10^{-8} Ω·m (4 K) and 2.5×10^{-7} Ω ·m (300 K) for V_2AlC [3]), we can find that, for single crystal samples, though the value varies among samples, the resistivity of Cr_2AlC is three times lower, being 2.5×10^{-7}Ω·m (300K) and 5×10^{-8} Ω· m (4K). As for case of V_2AlC, the RT and 4K resistivity, being 1×10^{-7} Ω·m (300K) and 1 $\times10^{-9}$ Ω·m (4K) are four times lower

than its polycrystalline counterparts. Accordingly, this implies that single crystalline sample exhibits lower resistivity resulting from the absence of grain boundaries which consequently limits the mean free path at low temperature. Due to the imperfections of our as-grown crystals, it is highly probable that these values do not represent a lower intrinsic limit, and further improvement of the materials quality should result in an additional drop of the resistivity.

More specifically, the sample preparation method can also affect the resistivity substantially, the rectangle and VdP sample obtained by diamond saw cutting are considered to create less defects than that made by laser, that's why the lowest resistivity can be achieved on VdP sample in both cases. Here we also plot one "back and forth" curve for the procedure of cooling down and warming up in Figure 3.8 (left), which indicates that the contacts are robust during cooling process and the curves are reproducible.

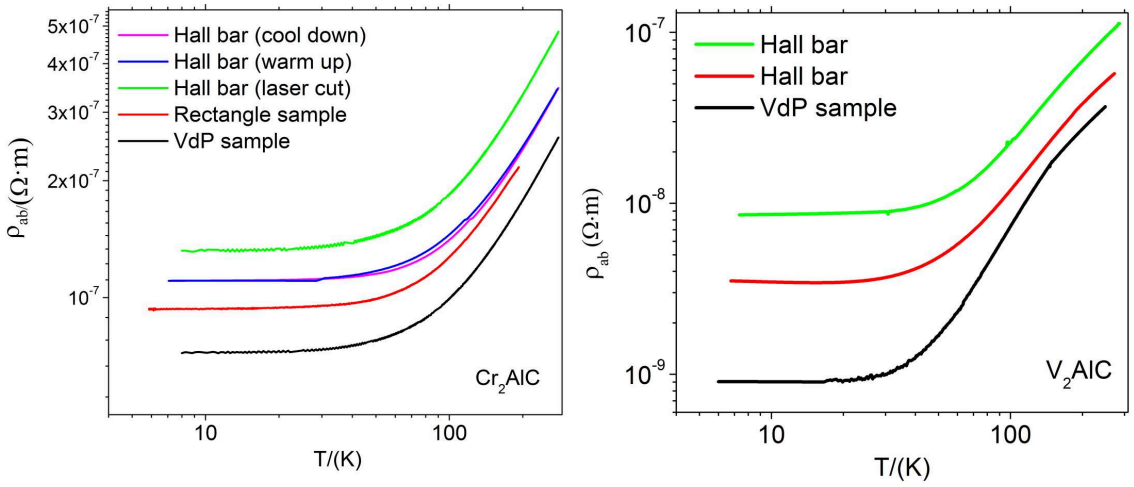

Figure 3.8: *Temperature dependence of in-plane resistivity of (a) Cr_2AlC and (b) V_2AlC.*

By using the Mathiessens's rule, we can extract the ideal resistivity (ρ_i), which is defined as $\rho_i(T) = \rho(T) - \rho_{residual}$.

Herein, if we do not considering the form factor, which is to say all contact are well connected at the edge of the sample and current pass through all the planes of the layered structure, ρ_i is an intrinsic characteristic which is supposed to be only dependent on the electron-phonon-scattering mechanism. Figure 3.9 shows the ideal resistivity of both cases, indicating noticeable uniformity for Cr_2AlC sample. As usually observed in MAX phases, ρ_i varies linearly with the temperature in the range from 150 - 300 K and

the slope of the linear variation can be calculated. It is clear that the slopes obtained from V_2AlC sample are smaller than those of Cr_2AlC sample, such behaviour can be attributed to the differences between two MAX phases in terms of 1) electron-phonon coupling, 2) electron band structure and 3) charge carrier densities.

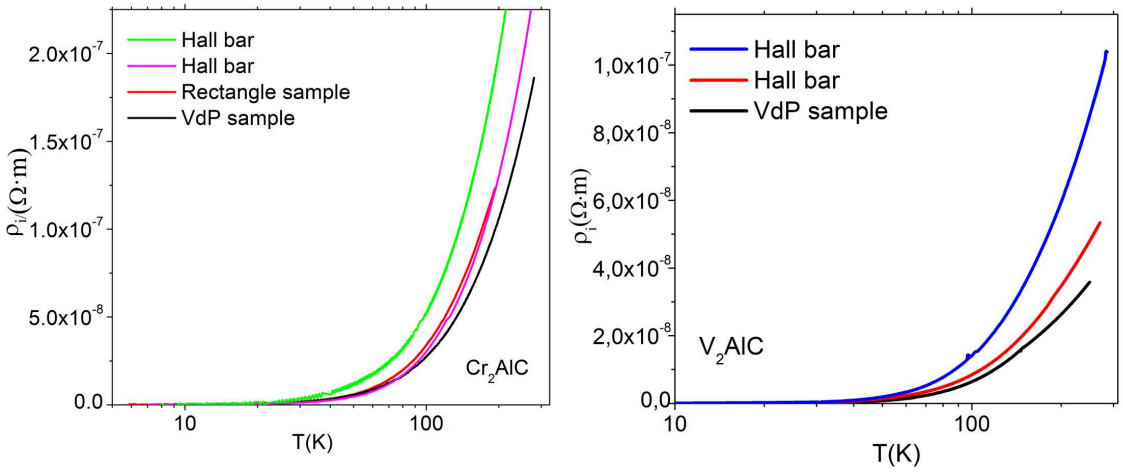

Figure 3.9: *Corresponding ideal resistivity of Cr_2AlC and V_2AlC.*

3.2.2 Out-of-plane resistivity

Figure 3.10 summarizes the temperature variation of corrected value ρ_c versus T. For Cr_2AlC (upper figures), though the correction does not merge all curves, the maximum difference between the five samples at low T does not exceed a factor of 1.5. Most likely, this variation is attributed to the fact that the crystals are all but perfect, so that some variability between samples issued from different runs is to be expected. The ratio is plotted as a function of the temperature in order to get more insights into resistivity anisotropy. It is very substantial, in the range of a few hundreds. The anisotropy ratio increases as T decreases as long as phonon scattering prevails, which did not exhibit the sample trend of temperature coefficient, as reported in the case of oriented grown thin film and bulk Ti_2AlC phase. This anisotropy is a combination of the Fermi surface anisotropy and that of scattering mechanisms, but a full understanding of temperature dependence of the coefficient of anisotropy is still unclear.

Plotting the same data for a V_2AlC sample shows that the anisotropy ratio is still higher, a few thousands (Figure 3.10, bottom). The hugh anisotropy ratio still needs to be verified by more samples, here, we found for the sample with larger thickness

has lower anisotropy ratio, which may be due to the higher level of defects caused by growth stress in the case of thinner sample.

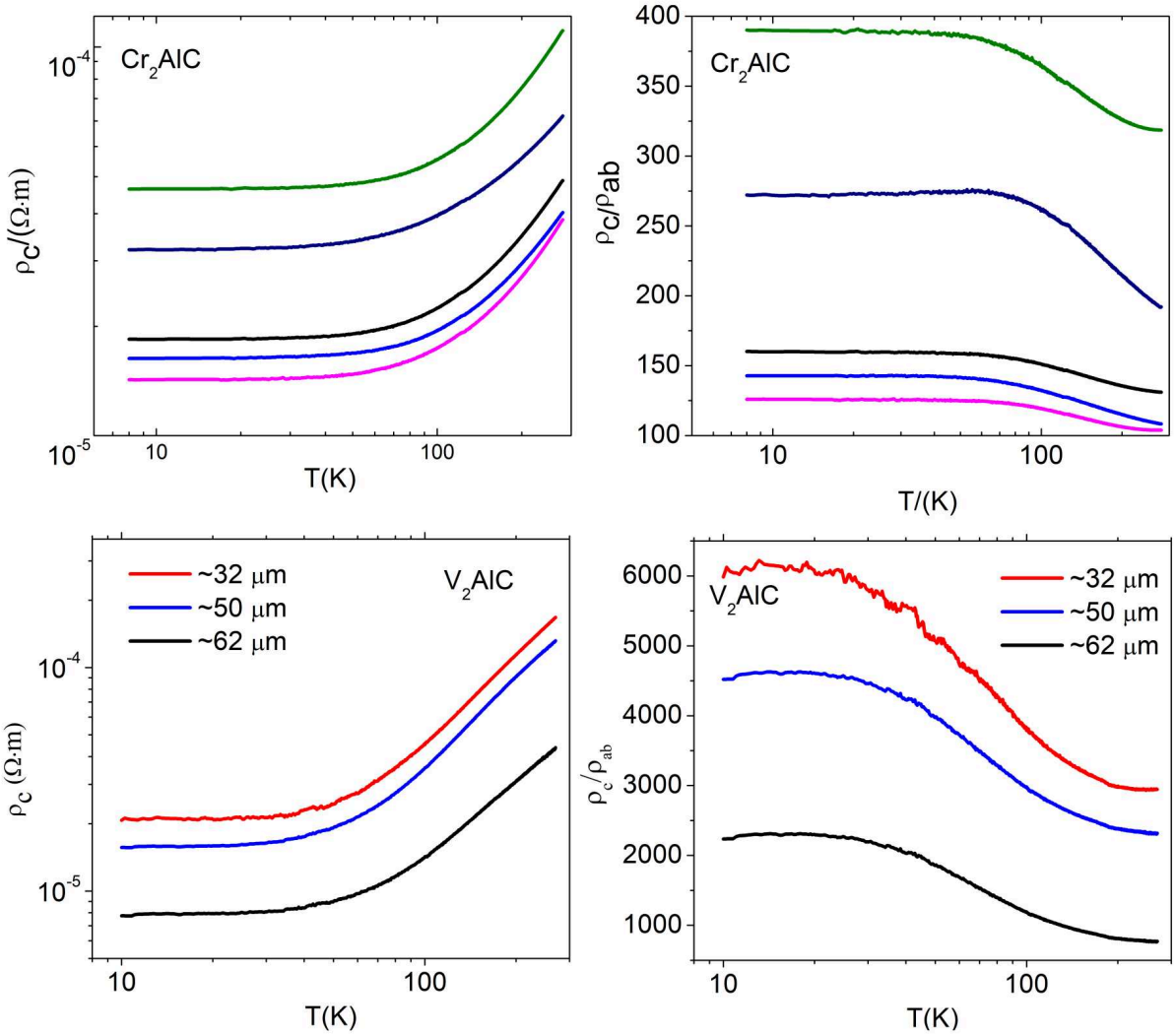

Figure 3.10: *Out-of-plane resistivity (all the values are corrected using correction functions) and anisotropy ratio ρ_c/ρ_{ab} of Cr_2AlC and V_2AlC.*

The anisotropies obtained for Cr_2AlC and V_2AlC are a spectacular illustration of the impact of the nano-lamellar structure of the MAX phases on electrical transport, and strongly support the assumption of a strong spatial confinement in the transition metal planes. The larger resistivity anisotropy found in V_2AlC, compared with Cr_2AlC, may come from a different topology and anisotropy of the Fermi surface itself, which could be described as more "tube-like" in one case than in the other case.

3.2.3 In-plane transport

In this part, three MAX phases will be discussed, including Cr_2AlC, Ti_2AlC, Ti_3SiC_2.

3.2.3.1 Magnetoresistance

Figure 3.11 shows the magnetoresistance (MR) variation with temperature at a magnetic field from 0 to 11 T. As in the case of the polycrystalline phases, we observe a magneto-resistance of a few per cent in both cases, higher for V_2AlC and Ti_3SiC_2 than for Cr_2AlC. In general, MR rapidly decreases with increasing temperature. In standard metals, the Lorentz force caused by an applied magnetic field changes the electron trajectory and gives rise to a positive MR which increases quadratically with the strength of the field.

Power function $y = Ax^B$ is used to fit the MR curve and the fitting curves at low T are plotted in Figure 3.12. In the cases of V_2AlC and Ti_3SiC_2, unlike Cr_2AlC, the exponents of power-law fits are around 1.4 for both cases.

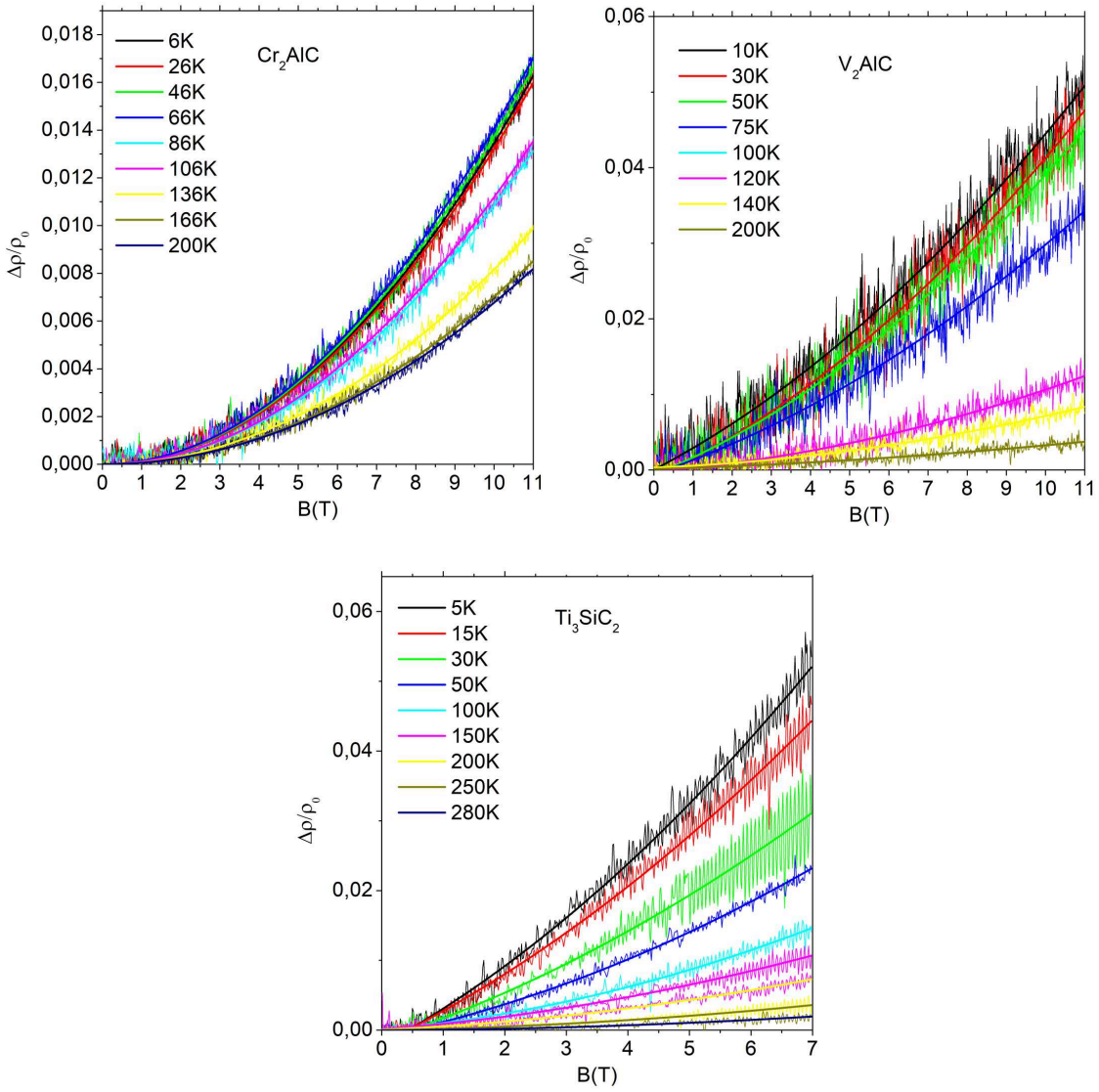

Figure 3.11: *Temperature dependency of magnetoresistance MR of Cr_2AlC, V_2AlC and Ti_3SiC_2.*

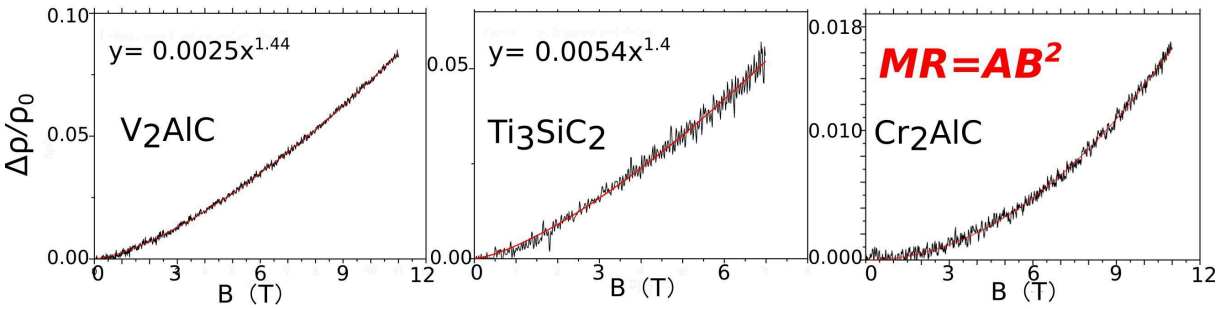

Figure 3.12: *Power fitting of MR of V_2AlC and Ti_3SiC_2 in comparison with to parabolic MR of Cr_2AlC.*

In the Figure 3.13, we also plotted the temperature dependence of fitting exponent of V_2AlC and Ti_3SiC_2. One can notice that the values vary considerably depending on the samples, between 1.3 to 1.8. In comparison with the MR curves of polycrystalline samples [3], non-parabolic MR curves were detected in our experiments, which is not possible to explain by the traditional two-band model.

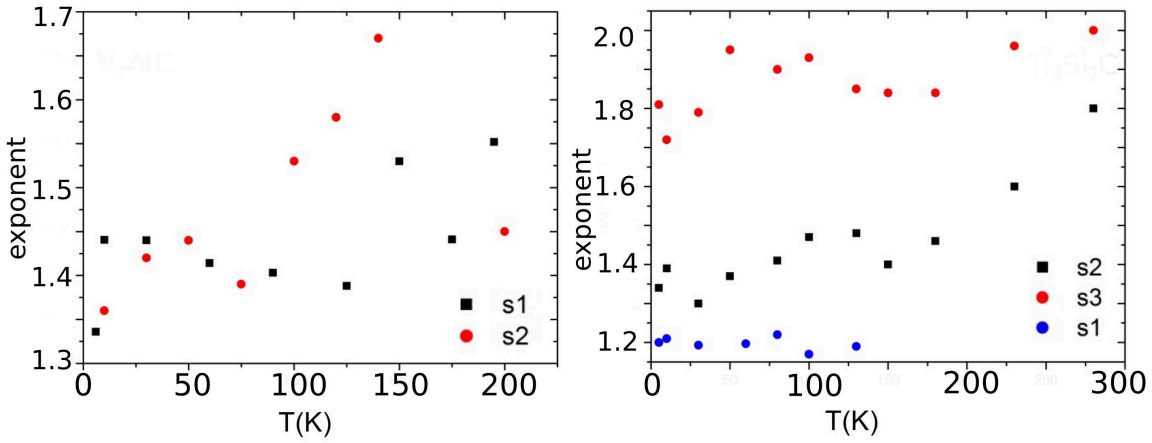

Figure 3.13: *Temperature dependence of exponent of power fitting for MR of V_2AlC and Ti_3SiC_2.*

For a conventional metal, the change in isothermal resistivity in an applied magnetic field (B) normally obeys a functional relation known as Kohler's law[113]. Semiclassical transport theory based on the Boltzmann equation predicts Kohler's law to hold if there is a single type of charge carrier and the scattering time τ is the same at all points on the Fermi surface. According to Kohler's law, MR at different temperatures can be scaled by the expression:

$$(\frac{\Delta\rho}{\rho_0}) = f(H\tau) = F(\frac{B}{\rho_0}) \tag{3.4}$$

where ρ_0 is the zero-field resistivity at given temperature. This relation follows from the fact that scattering time $1/\tau(T) \propto \rho(T)$. In the low field limit, most metals exhibits a quadratic dependence of the MR , so $\frac{\Delta\rho}{\rho_0} \propto \tau^2 B^2$. Hence, a plot of $\frac{\Delta\rho}{\rho_0}$ versus $(\frac{B}{\rho_0})$ is expected to collapse onto a single temperature-independent curve if charge carrier density is constant , regardless of the topology and geometry of the Fermi surface.

In general, this rule is applicable to single-band metals with temperature-independent charge carrier density. Thus, this condition can be satisfied most easily if there is only a

single temperature-dependent scattering time. Interestingly, this rule, although derived from the semiclassical Boltzmann theory, was found to be well obeyed in a large number of metals, including the metals with two types of carriers, the pseudo gap phase of the underdoped cuprates superconductors [114] as well as some other Q1D metals [115]. The violation is generally believed to result from the change of charger carrier density with temperature or from the fact that the anisotropic carrier scattering rates do not have the same T scaling on different sections of the Fermi surface.

Here, the Kohler plots of three MAX phases samples are shown in the Figure 3.14. For Ti_3SiC_2 Kohler's scaling is reasonably well obeyed below 50 K with small deviations from full scaling thereafter, which is consistent with reported (000l)-oriented thin film of Ti_3SiC_2[116]. So as for V_2AlC. In contrast, for Cr_2AlC, Kohler's rule is violated at all T. This difference in Kohler's scaling between Ti_3SiC_2 and Cr_2AlC, is striking if we consider the very similar $\rho(T)$ behaviour of t both crystals.

Such violation of Kohler's rule suggests several possibilities:(i) Charge carriers density is not temperature-independent while the electronic structure varies with temperature due to the formation of density waves; (ii) There is more than one type of carriers and their mobilities have different temperature dependences, in which a simple Boltzmann-type approach with its associated scattering time approximation is not valid; (iii)The scattering times associated with the magnetoresistance are distinct and have different temperature dependences.

3.2.3.2 Hall coefficients

Hall measurement was also conducted on three MAX phase single crystals. Figure 3.15 gives an example of the Hall resistivity of V_2AlC, measured versus magnetic field, at different temperatures. One can notice that Hall resistivity varies linearly with magnetic field, and this phenomenon is temperature independent, indicating the systems are in the weak-field limit. It is worth mentioning that within a sweep of magnetic field, four values were measured to obtain the average value for all the discussion afterwards (See Figure 3.15(b)) . Following by linear fitting, Hall coefficient (R_H) can be deduced from the slope of the fitting curves.

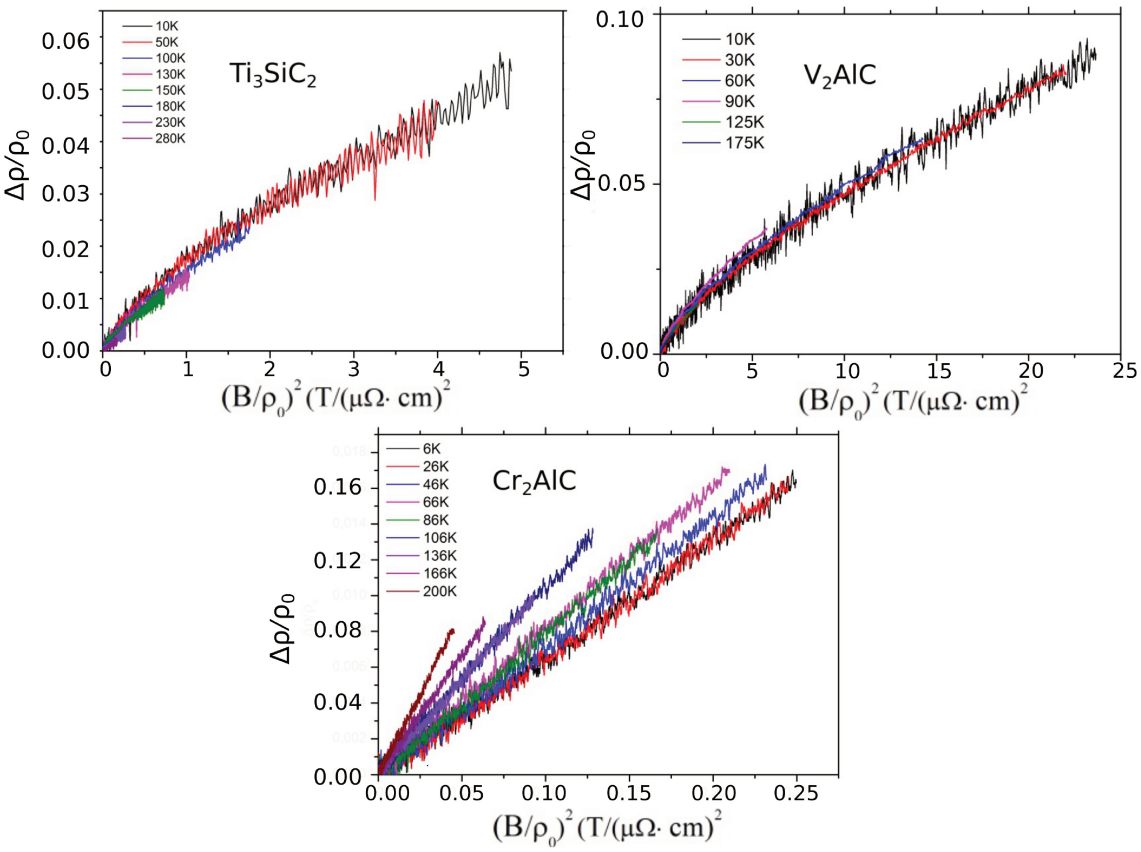

Figure 3.14: *Kohler's scaling for sample Ti_3SiC_2, V_2AlC and Cr_2AlC at different temperatures.*

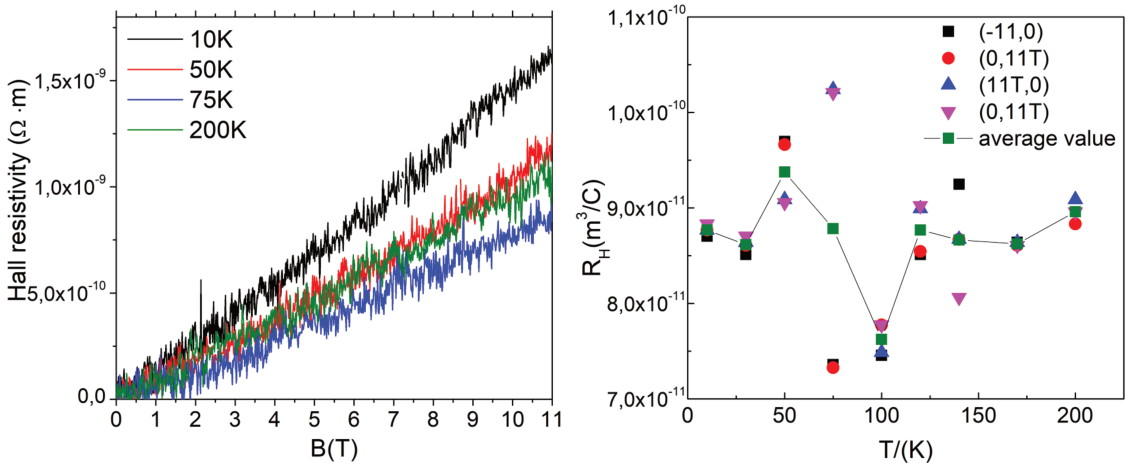

Figure 3.15: *(a) Hall resistivity vs magnetic field at different temperature and (b) the variation of Hall coefficient with temperature (noting: considering the sweep direction, values computed from within one sweep of magnetic field (-11T-11T) are also demonstrated.*

Figure 3.16 shows the R_H variation with temperature. Apparently, R_H is small, as previously noticed for polycrystalline samples, with some variability from sample to

sample. The sign of R_H is always positive. For Cr_2AlC and Ti_3SiC_2, these results are in qualitative agreement with the result found for the polycrystalline phases, but for V_2AlC, negative R_H values were always reported for polycrystals [3].

It is also worth noticing that though different samples can lead to different R_H values, there seems to be no substantial variation of R_H with T (See Figure 3.16). We ascribe the variability among samples to a change in their quality, which according to our simplified 2D model can lead to substantial variations of R_H for most cases. The small value of R_H makes it difficult to be measured, and we notice that a very slight temperature variation during a magnetic field sweep (less than 1K) may seriously affect the final value R_H . We suspect that some fluctuations, as well as those reported in the literature, might be due to this artifact.

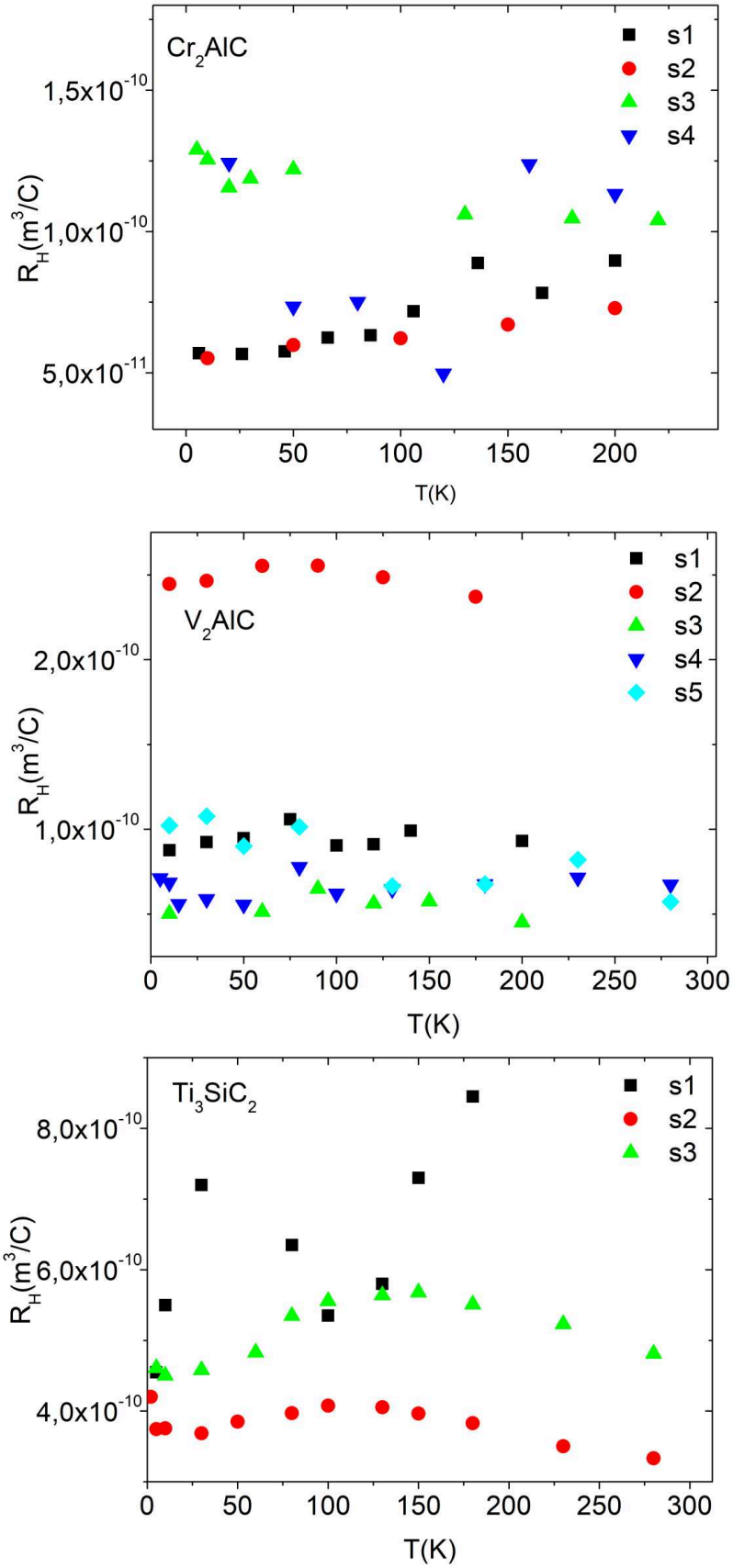

Figure 3.16: *Temperature dependency curves of Hall coefficient of R_H of Cr_2AlC, V_2AlC and Ti_3SiC_2.*

3.2.3.3 Charge carrier density and mobility

Using Cr_2AlC temperature data, we have extracted the carrier densities, mobilities and α using the conventional two band model (as plotted in Figure 3.17). We obtain a decrease in carrier density with T. This is a quite anomalous behavior for isotropic bands, which can be explained in terms of a variation in the ratio between τ_n and τ_p in the frame of a proposed 2D model which will be discussed in next section. Also, as predicted by this 2D model (and as reported in the case of polycrystalline phases), we find apparent densities in the range of $10^{27} m^{-3}$. Apparent mobilities also correspond to what would be predicted from typical values of the relaxation time in metals, and in the range from 120 to 50 cm^2/Vs when T is varied from 4 K to 200 K.

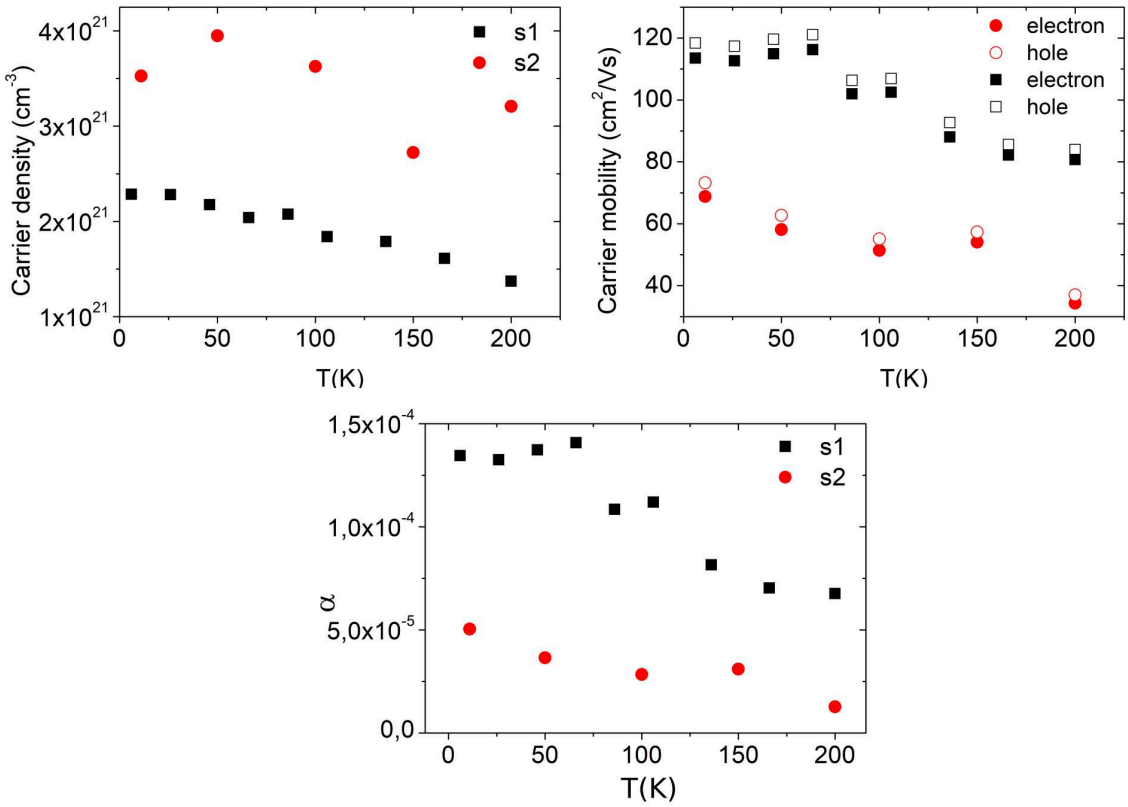

Figure 3.17: *Two band model density (a), mobilities(b) and fitting parameter α(c) as a function of temperature for Cr_2AlC Hall bar.*

3.2.3.4 Thermal transport measurement of Cr_2AlC

Thermal transport measurement was conducted on the as-grown Cr_2AlC crystal by my previous group in Shanghai Institute of Ceramic, China. Seebeck coefficient from

RT to high T were measured using an Ulvac ZEM-3, while Low T seebeck coefficient and thermoconductivity were conducted on Physical Property Measurement System (PPMS) (Quantum Design, Inc.)

Unlike higher electronic conductivity of single crystalline sample compared to their polycrystalline counterparts, no significant improvement on the thermal conductivity was observed compared to the reported results on the polycrystalline samples below room temperature[3] Among measurements taken on several samples, the average thermal conductivity at RT is around 20 W/Km (See Figure 3.18).

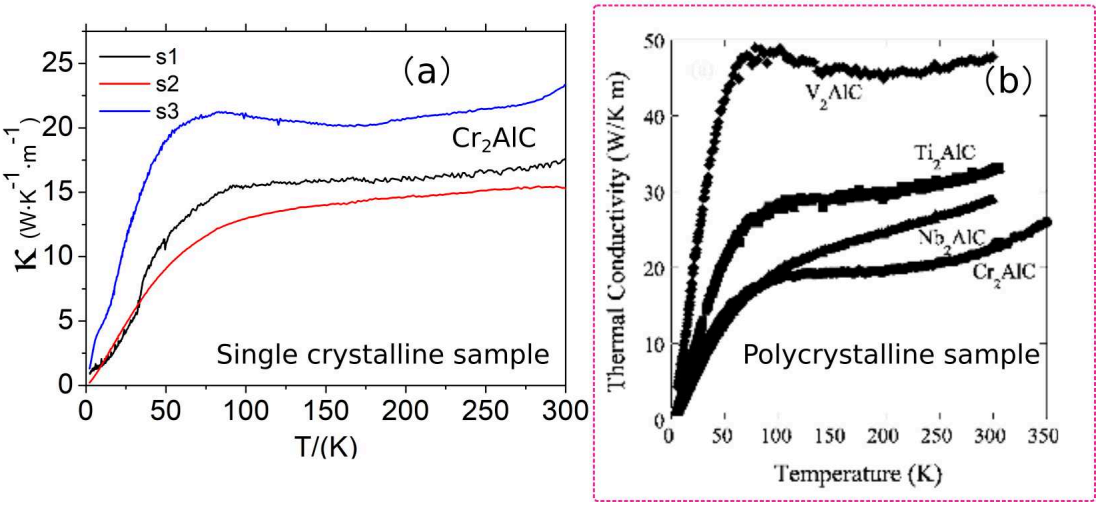

Figure 3.18: *(a) Thermal conductivity of Cr_2AlC single crystal and (b) In comparison with polycrystalline sample[3]).*

Moreover, the electron contribution to the thermal conductivity can be inferred according to the Wiedemann–Franz relation $\kappa = \sigma LT$, where L is $2.45\times10^{-8}\mathrm{W}\cdot\Omega\cdot\mathrm{K}^{-2}$, which is theoretical value for the contribution to thermal conduction from charge carriers only. The electronic contribution of thermal conductivity is plotted in Figure 3.19(a). Note that, experiments have shown that the value of L, while roughly constant, is not exactly the same for all materials. It is established that the Wiedemann–Franz relation is generally valid for high temperatures and for low (i.e., a few Kelvins) temperatures, but may not hold at intermediate temperatures[117].

To investigate the phonon contribution to the thermal conductivity, according to the calculated and measured value, we should consider the Debye temperature T_D of Cr_2AlC, which is 735 K [31].Our measurement is only conducted below RT, therefore, the following discussion concerns the at low temperature limit $(T_D/\ T \ll 1)$. Under this circumstance, thermal conductivity of a perfect infinite crystal is finite at low

temperatures only because of Umklapp processes(U-process). For U-process at least one of the initial phonons must have energy comparable to $\hbar\omega_D$. At $T_D/\ T \ll 1$, the number of such phonons is

$$n = \frac{1}{e^{\beta\hbar\omega} - 1} \cong \frac{1}{e^{T_D/T} - 1} \sim e^{-T_D/T}$$

As T decreases, the number of phonons that can take part in U-process falls exponentially. Thermal conductivity is inversely proportional to the number of U-processes, so the effective relaxation time for thermal scattering goes as:

$$\tau \sim e^{T_D/T}$$

Thus as T decreases, shows an increase till the mean free path, l , becomes limited by the scattering from the imperfections/boundaries of the crystal. Below this temperature, l becomes T-independent and is determined solely by the temperature dependence of specific heat C_v. So, at very low temperatures, thermal conductivity will be determined by C_v and should go as T^3.

However, in the Cr_2AlC, as indicated in the Figure 3.19(b, c): at low T, the deviation from Debye T^3 laws was observed. The thermal conductivity increased linearly with the temperature increased. Also, with the temperature keeping increasing, the thermal conductivity, after treaching a maximum, did not begin to fall exponentially with temperature as $e^{T_D/T}$. At higher temperatures, we observed the violation of 1/T power law fall of κ with increasing T.

When it goes to the Seebeck coefficient as shown in Figure 3.20, the curve does not display monotonous sign within all temperature range, which is not in agreement with Hall coefficient measurement results on Cr_2AlC. This is therefore another hint for a departure from the conventional isotropic two-band model. Compared to the polycrystalline sample, almost identical trends were obtained: at around 50 K, there is a knee point on both curves . The dominant transport carrier characteristic of single crystalline sample changed from electron-like to hole-like in the temperature range between 200 K-250 K, while for polycrystalline is 250 K-300 K. The values for both cases are strikingly comparable. It is worth noticing that due to the high thermal conductivity and low Seebeck coefficient , at low T , it is practically difficult to build large thermal gradient to obtain measurable thermopower, leading to noisy signal at low T.

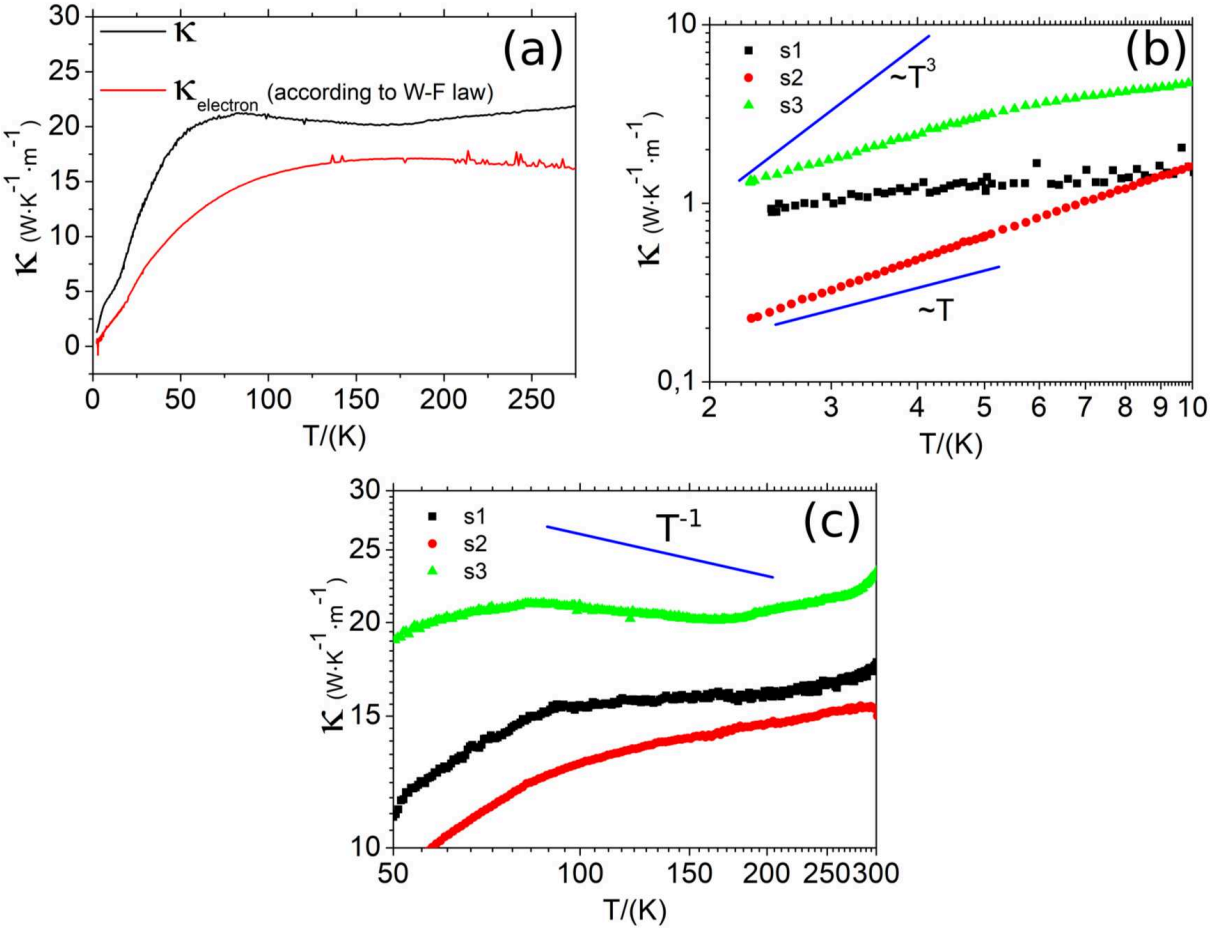

Figure 3.19: *(a)Electronic contribution and (b,c) Plotting curves indicating phonon behaviour to thermal conductivity of Cr_2AlC.*

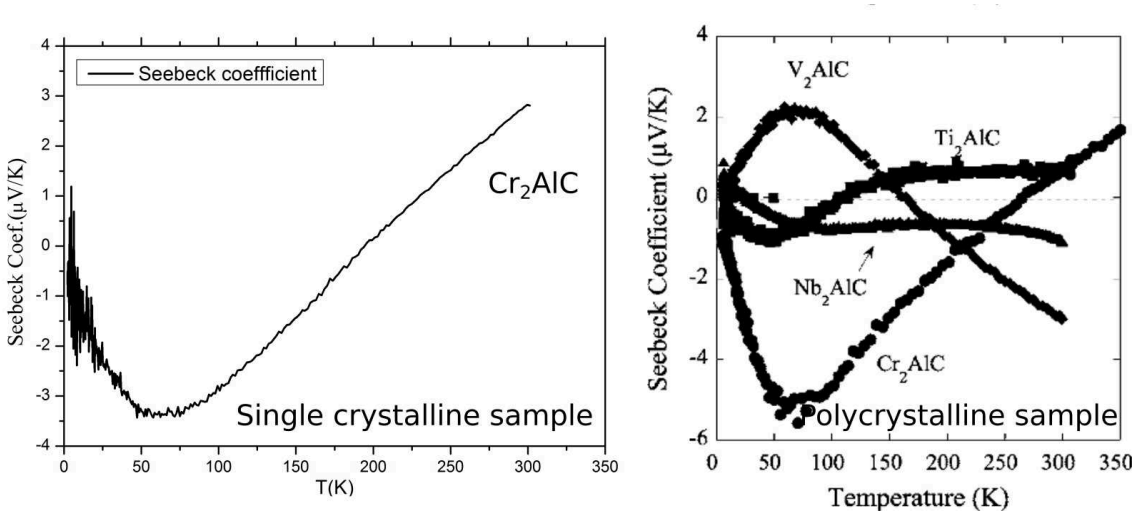

Figure 3.20: *Seebeck coefficient of Cr_2AlC single crystal (In comparison with polycrystalline sample [3]).*

3.2.4 Out-of-plane transport

Figure 3.21 shows the measurement configuration of out-of-plane magneto-electronic transport of MAX phases (modified Montgomery contact configuration [118]), where **B**//c, **I**//c. According to the function of Lorentz force: $\mathbf{F} = q\mathbf{E} + q\mathbf{v} \times \mathbf{B}$, when **B**//**v**, no magnetic force is applied on charge carriers. Hence, ideally, no magnetoresistance will be observed.Yet, it is not the case of our experimental results. For magnetic field applied perpendicular to the basal (a-b) plane, the out-of-plane (*c*-axis) resistivity displays a magnetic enhancement.

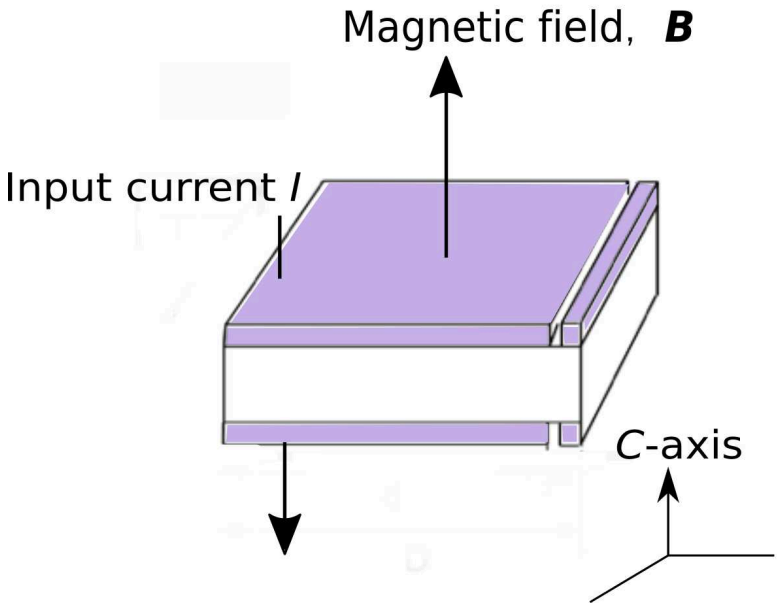

Figure 3.21: *Measurement configuration of c-axis magneto-electronic transport.*

3.2.4.1 Cr_2AlC

Figure 3.22 shows the out-of-plane magnetoresistivity ρ_c of the Cr_2AlC. The anisotropic ratio ρ_c/ρ_{ab} of this sample equals to 285. A clear change of resistivity is observed when changing B, and an negative MR was observed at low T (2K - 15K).

Nevertheless, we consider the case in which the contribution from in-plane resistivity component is non-negligible and can be extracted from the overall magnetoresistvity, as shown in Figure 3.23 .The derived MR is between 5%-8%, a reasonable value comparable to that obtained from our in-plane measurement. Hence, we use parabolic fitting to indicate the in-plane contribution:

$MR_o = MR - (\alpha B^2 - A)$

The fitting parameter α and intercept A as function of temperature were plotted in Figure 3.24, in which one can notice that as temperature increases, both α and A

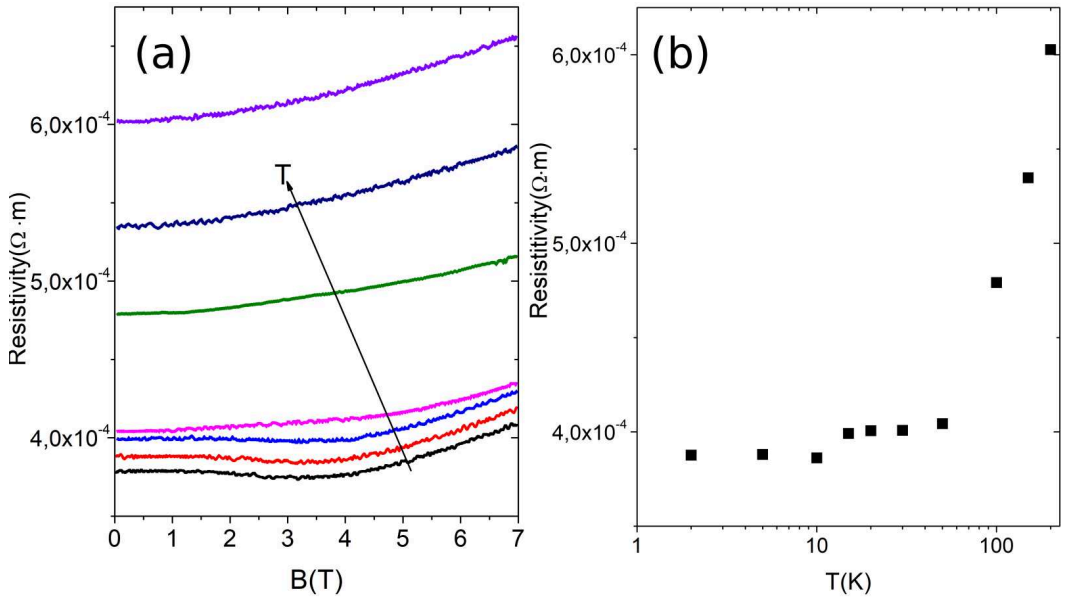

Figure 3.22: *Out-of-plane resistivity of Cr_2AlC (B//c. I//c) (a) magnetoresistivity (b) Zero field $\rho_c(T)$.*

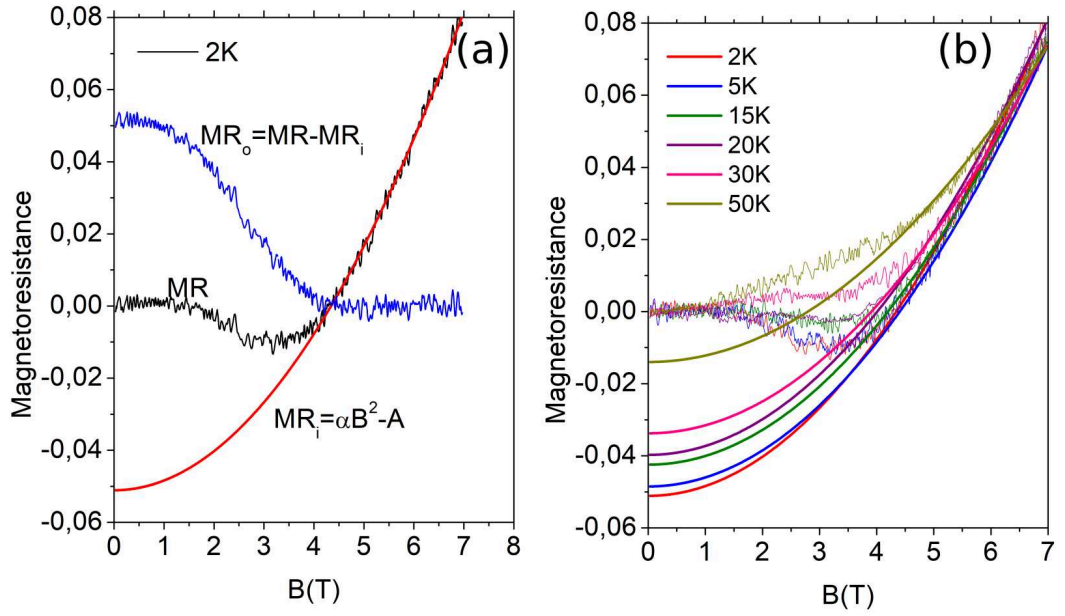

Figure 3.23: *Extraction the in-plane contribution from out-of-plane magnetoresistance.*

are accordingly reduced. It is not difficult to qualitatively understand the trend of α, determined by the charge mobility in the two-band model, decreasing with the temperature as the mobility is strongly effected by various scattering mechanisms. However, the physical meaning of intercept value, as the amplitude of the offset to the Zero point, remains unknown.

We use different fitting equations for the residual magnetoresistance (MR) demon-

strated in Figure 3.25. Among them, it seems that a Boltzmann-type equation fits better than others. Here we fixed the onset magnetic field at 2.5T, the residual magnetoresistance

$MR_o = \frac{A_1}{1+\exp\left(\frac{x-2.5}{dx}\right)}$

where the parameter$A1$ is equals to the intercept A in the parabolic fitting for the in-plane contribution.

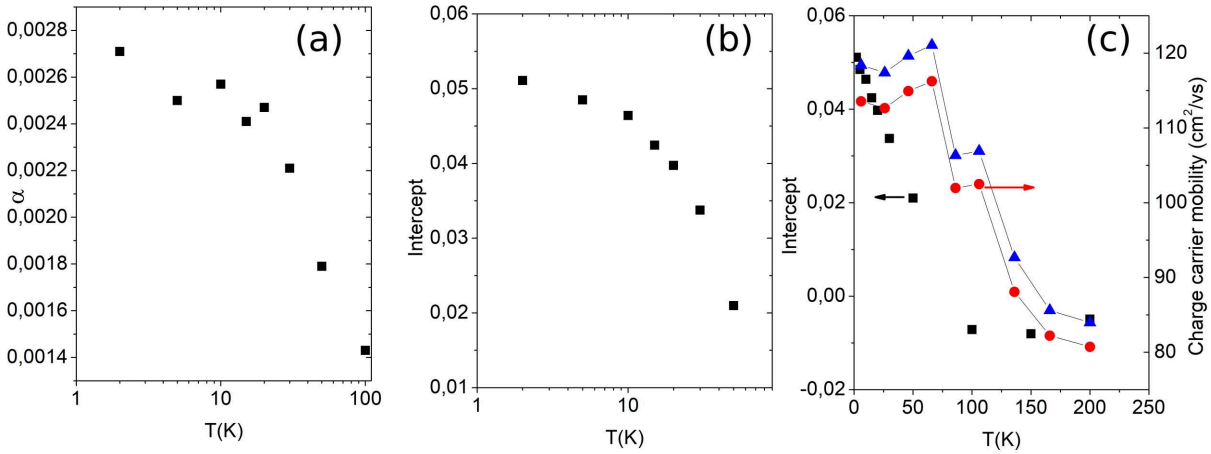

Figure 3.24: *Fitting parameters of in-plane contribution for out-of-plane magnetoresistivity vs T (a) α (b) A and its relation with corresponding charge moblity.*

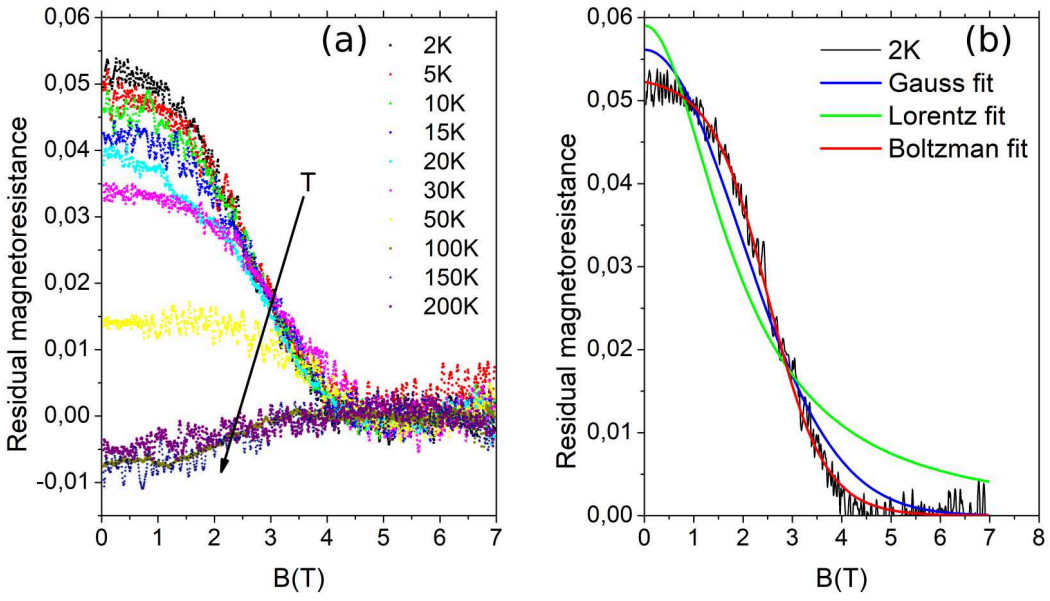

Figure 3.25: *(a) Residual magnetoresistance vs T and (b) various fitting curves.*

We now try to understand our results by referring to the literatures in which an analogous phenomenon was reported in lamellar structures. Considering the stacking of two dimensional layers in MAX phase, we firstly referred to out-of-plane magneto transport of two-dimensional electron gas in heterostructures [119] and graphene [120]

in the temperature range from 20 mK to 4.2 K. In magnetic fields less than about 1 T and before the onset of Shubnikov-de Haas (SdH) oscillations a large negative magnetoresistance was observed, which followed a quadratic dependence on the magnetic field. The observed negative magnetoresistance can be explained in terms of electron-electron interactions (weak localization) in two-dimension. Yet, in our case, we did not observe that the out-of-plane resistivity has a logarithmic dependence with temperature, which excludeds weak localization.

The data discussed here are somewhat anomalous to anisotropic magnetoresistance in the high-T superconductors[121, 122, 123], who also exhibit a striking feature of large anisotropic electronic properties, as our MAX phase samples. It was widely studied that the interlayer tunnelling or weak coupling were proposed for c-axis conduction and the presence of Josephson coupling between layers had been experimentally proved in Bi-based superconductor single crystals.

In our experiment, $\boldsymbol{B}$ is parallel to $\boldsymbol{I}$, in principle, so that a macroscopic Lorentz force is zero and the Lorentz-force-driven charge motion is not expected. However, if the carrier trajectories are not straight along c-axis, and there exists some sort of misalignment between $\boldsymbol{B}$ and $\boldsymbol{I}$, out-of-plane magnetoresistance may be produced even in the absence of Lorentz force.

It is worth mentioning another point related to defect scattering, as demonstrated in [118], the electrical conductivity anisotropy of Bi-based superconductor material is of order 10^4 and is strongly temperature dependent, which is also the case for V_2AlC sample. A defect scattering played an important role in out-of-plane transport mechanism. At this stage these hypothesis still need to be further investigated with more experimental results.

3.2.4.2 V_2AlC

Similar phenomena was detected in the V_2AlC sample as well. Here we simply list the measurement results (Figure 3.26 3.27 3.28) as reference. The anisotropy ratio of V_2AlC sample is around 10^3. Unlike Cr_2AlC, the onset magnetic field of negative MR for V_2AlC is lower , at 1.8 T. Besides, up to 50 K, the negative MR could still be observed. After extraction, we can clearly find out the MR value for V_2AlC is much larger than Cr_2AlC sample, which might imply that higher mobilities leading to lower resistivity.

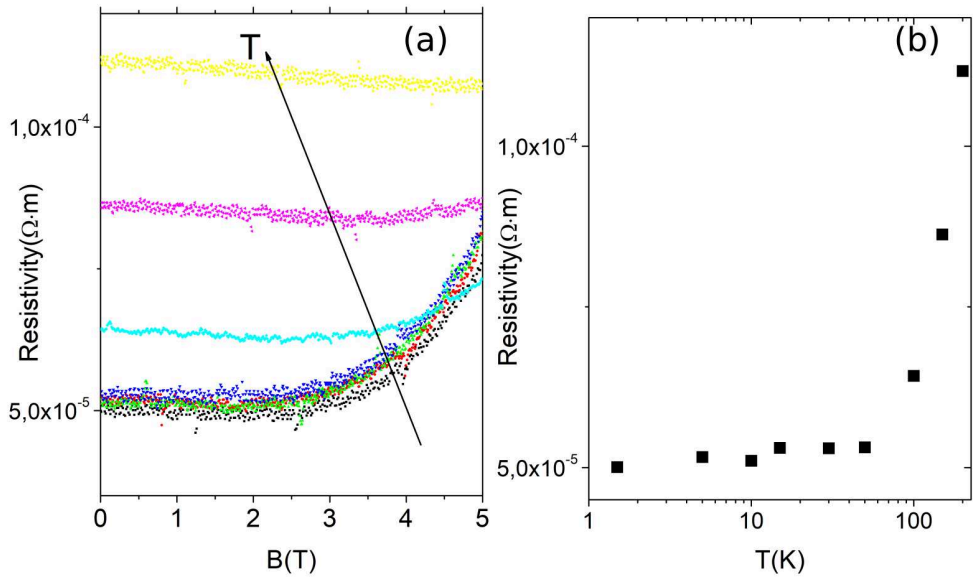

Figure 3.26: *Out-of-plane resistivity of V_2AlC (B//c. I//c) (a) $\rho_c(B)$ (b) magnetoresistance at 1.5K and (c) Zero field $\rho_c(T)$.*

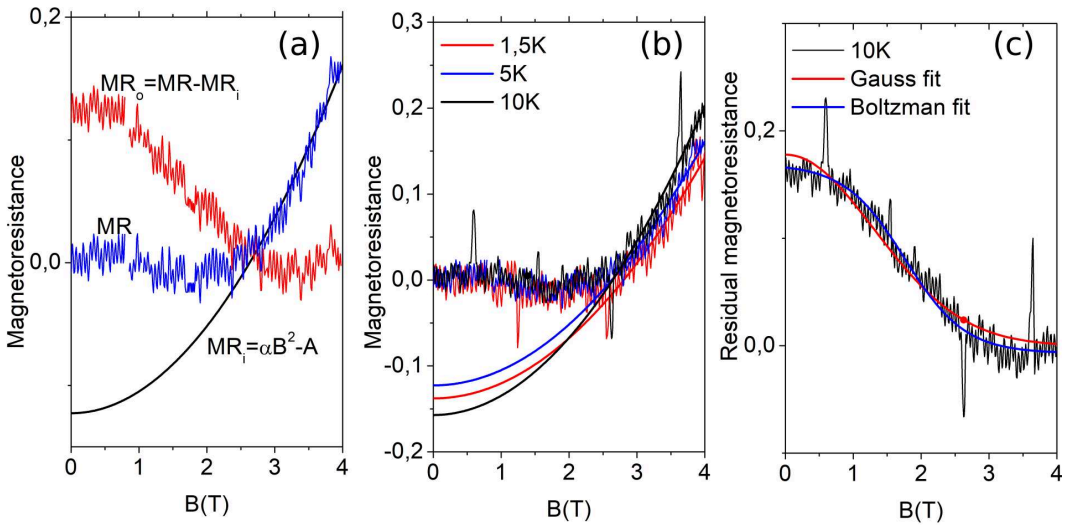

Figure 3.27: *Extraction the in-plane contribution from out-of-plane magnetoresistance and the fitting of residual magnetoresistance.*

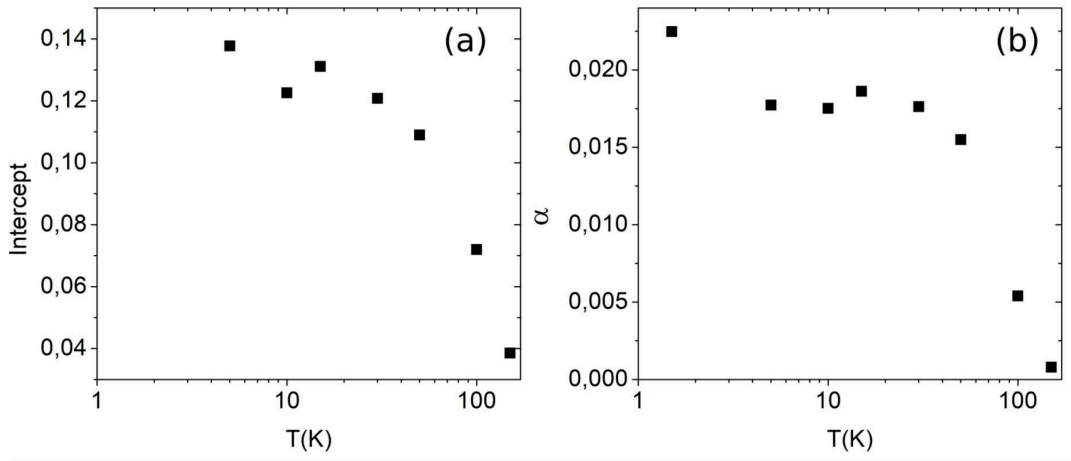

Figure 3.28: *Fitting parameters of in-plane contribution for out-of-plane magnetoresistivity vs T (a) α (b) A.*

3.3 Theoretical calculation of MAX phase transport properties

3.3.1 Introduction of a 2D hexagonal metal with nearly free electrons

As emphasized by N.W. Ashcroft and N. D. Mermin many years ago, the nearly free-electron-like Fermi surfaces are essential in understanding the real Fermi surfaces of many metals [124]. Here we intend to argue that MAX phases probably make no exception. Determining the Fermi line of nearly free electrons in a pure 2D hexagonal metal is elementary. The origin of the hole and electron bands can be seen by plotting several Brillouin Zones (BZ) along with the Fermi circles corresponding to the filling of the free electrons states up to the Fermi energy in each zone . We focus on cases where the free electron circle extension is larger than that of the corresponding BZ. Then, restricting oneself to the first hexagonal BZ, one obtains free electron pockets at the corners of the hexagon and a hole band centred at the origin (See Figure 3.29). To get the dispersion curves is a trivial matter, obtained by solving the following secular equation (justification of this procedure can be found, e.g., in Eqs 3.5):

$$\begin{vmatrix} E_0 - E & U & U & U & U & U & U \\ U & E_1 - E & U & 0 & 0 & 0 & U \\ U & U & E_2 - E & U & 0 & 0 & 0 \\ U & 0 & U & E_3 - E & U & 0 & 0 \\ U & 0 & 0 & U & E_4 - E & U & 0 \\ U & 0 & 0 & 0 & U & E_5 - E & U \\ U & U & 0 & 0 & 0 & 0 & E_6 - E \end{vmatrix} = 0 \qquad (3.5)$$

where E is the unknown energy and the E_i is the free electron parabolic relations of $E_i = \hbar^2(\mathbf{k} - \mathbf{k}_i)^2/2m_0$ centred in the first BZ (index zero, $\mathbf{k_0}$=0) and all BZ's adjacent to it (See Figure 3.29(a)). In the latter expressions $\mathbf{k}$ is the wave vector and the $\mathbf{k}_i$'s coordinates are that of the centres of the BZ's. U represents the Fourier component of the periodic potential for a wave vector joining the centres of two adjacent hexagonal BZ's. If the cell dimensions are specified, U is the only adjustable parameter. It splits

the free electron curves into a hole band and electron pockets (Figure 3.29(b)). Close to the corners of the hexagon, the secular equation might be reduced to the determinant of a 3×3 matrix, leading to analytical relationships between E and $\mathbf{k}$. The E vs $\mathbf{k}$ relation can be plotted for any value of $\mathbf{k}$, and the Fermi surface is computed by finding the line segments which satisfy E=E_F, where the Fermi energy E_F is determined by finding the level for which the sum of electrons in all bands is equal to the number of electrons per unit cell.

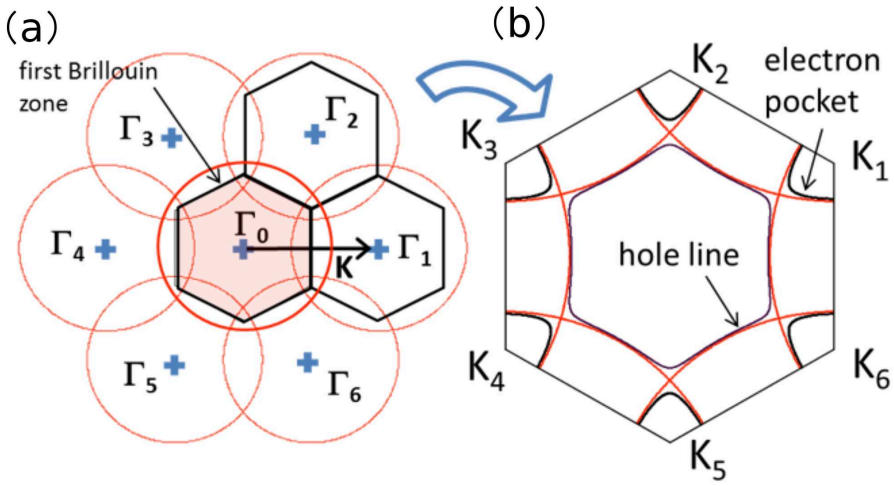

Figure 3.29: *Reproduction of adjacent Brillouin zones of a two-dimensional hexagonal lattice with the corresponding free electron disks (left) and Fermi line of the same lattice in the first Brillouin zone for nearly free electrons.*

An example of dispersion curves is given in Figure 3.30. For a large number of electrons per unit cell, the first band is filled with electrons. As in the case of graphene tight-binding treatment, it is easy to demonstrate that for nearly free electrons the first band touches the second at the so-called Dirac points K's. The second band is the hole band. It is separated from the third band – the upper electron band - by an energy gap close to $3U$ at points K's. Here we restrict our analysis to the case where the first band is totally filled (with two electrons per unit cell), and we define N as the number of electrons per unit cell populating all higher partially filled bands. In order to compare the model to the case of the M_2AX phases, or to compute 3D carrier densities from the 2D model, we assume that we have four 2D planes per unit cell (as a consequence, to get the number of electrons per plane in partially filled bands one must divide N by a factor of four).

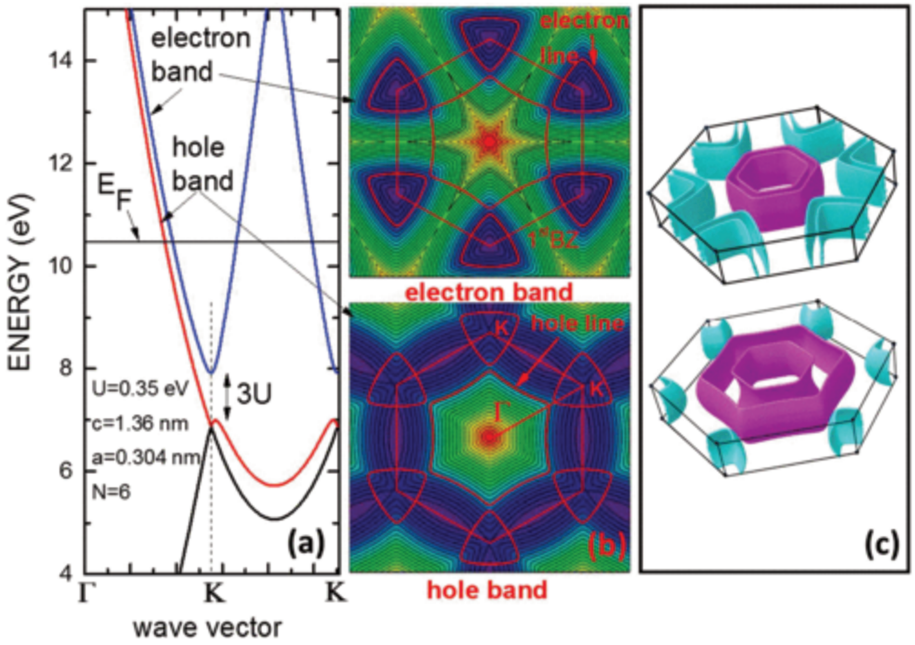

Figure 3.30: *Dispersion curves of nearly free electrons in a 2D hexagonal lattice (parameters are inserted in the graph and defined in the text).*

3.3.2 Adaptation to the MAX phases

If we compare the Fermi line of the pure 2D model described above to the 3D Fermi surface shape of several MAX phases as obtained by DFT calculations, a striking similarity can be noticed. While a major difference lies in the splitting of the hole bands.

We can adapt our simple model by assuming that the electrons in the partially filled bands are strongly confined in real space, and more specifically lie in the transition metal planes. This assumption is well supported by numerical calculations in k-space, which predict open tubes for the Fermi surfaces along the c-axis. Direct inspection of the atomic lattice (See Figure 3.31) shows that for a M_2AX phase, the M planes form close pairs separated by an X plane. These pairs are in turn separated from one another by the more distant A planes. In real space the electrons at the Fermi level are spatially confined in the M-planes. As a consequence, if one first neglects the different zigzag orientations between two adjacent A planes, one can form a reduced lattice with two inequivalent M planes per reduced unit cell, which are responsible for the large band splitting. Then, treating independently the electrons as nearly free in the M planes and as strongly confined along c in between two planes, one can apply a simple tight-binding approach to the wave vector component along c. The two planes per reduced unit cell lead to a treatment identical to that used, as for a 1D conjugated polymer, so

that each band is split in two, the dispersion of the split bands along c being of the form $E = E_0 \pm (\beta^2 + \gamma^2 + 2\beta\gamma cos(kc))^{1/2}$.

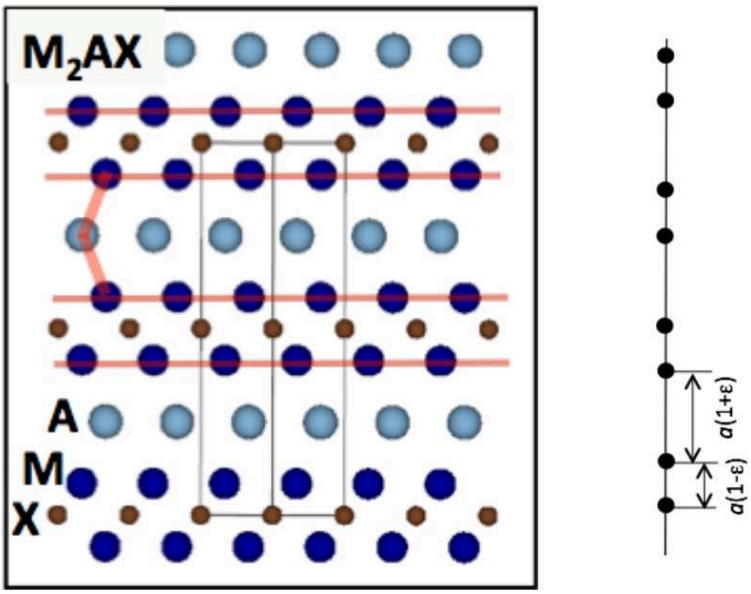

Figure 3.31: *1D-tight-binding with 2 atomic planes per unit cell showing large splitting.*

Combining the in-plane and out-of-plane energy contributions give rise to Fermi surfaces such as that of Figure 3.32 (where we assumed that the splitting is different for the hole and electron pockets). Although not perfect, the similarity with DFT calculations is prominent, even if so simple a model can obviously not reproduce the smallest details of the Fermi surface. This approach also neglects an additional but quite small splitting, which dissociates each of the hole and electron Fermi surfaces into almost indistinguishable surfaces, and which can be attributed to the fact that two consecutive A planes are inequivalent.

In order to further simplify the calculation of all transport parameters, we move one last step further, and replace the 3D structure by a fully 2D model, neglecting any energy variation along c (so that our model can only predict the values of in-plane transport coefficients). This gives Fermi lines such as the one presented in Figure 3.33 (red line). Comparing it to the projection of a full numerical computation in the basal plane demonstrates that in the case of Ti_2AlC(See Figure 3.33 right), only the small features are not reproduced. In the case of Ti_2AlC, the roughest approximation is to consider that the electron pockets form open tubes, which is actually not predicted by

DFT calculations . This means that the simplified model will probably slightly overestimate the contribution of electrons to in-plane transport. Such case can be empirically improved by finding a set of energy parameters which slightly underestimates the extent of those electron pockets.

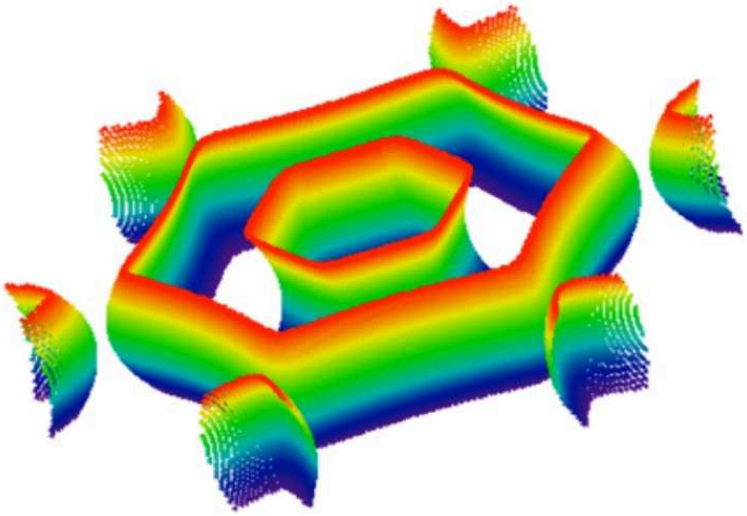

Figure 3.32: *Fermi surface obtained by combining an in-plane, 2D nearly-free electron dispersion and a tight-binding coupling between the transition metal planes.*

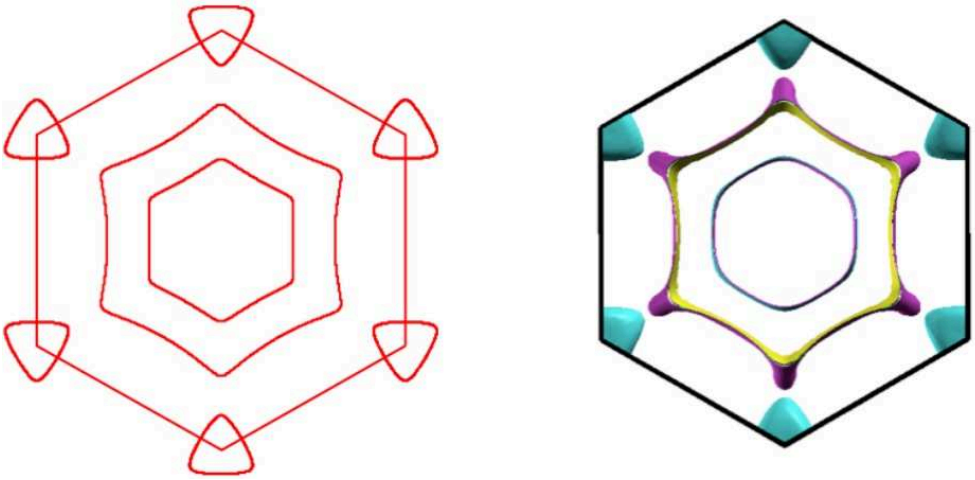

Figure 3.33: *Projection in the basal plane of the Ti_2AlC Fermi surface [125] along with the fitting Fermi line given by the 2D model using U=0.35eV and an appropriate splitting between the hole bands and electron pockets (red line).*

An interesting point is that compiling the published expectations for other Ti-based MAX phases shows that the overall structure of the Fermi surface is always formed by hexagonally-shaped hole bands in the center of the zone, and trigonal electron pockets extending over three hexagonal BZ's and centred at the corners of the BZ hexagon [126, 37, 125](Figure 3.34) .Very often, the electron pockets form open tubes too. The number of bulges appearing in the open tubes over one unit cell is a direct function of the integer n appearing in the $M_{n+1}AX_n$ formula. In one extreme case (Ti_3AlC_2), the tight-binding splitting is such that the electron bands are repelled at energies high enough for being totally unoccupied [126].

Although only a restricted number of Fermi surface calculations are presently available in the literature, many support the nearly-free electron explanation of the Fermi surface shape. Our purpose is therefore to use the 2D model as a reasonable approximation of the Fermi surface shape, because it allows one to simplify the calculation of the transport parameters to a considerable extent, and thus to discuss the physical aspects which govern the transport properties in a very convenient way. Apparently, this approximation restricts the analysis to in-plane transport.

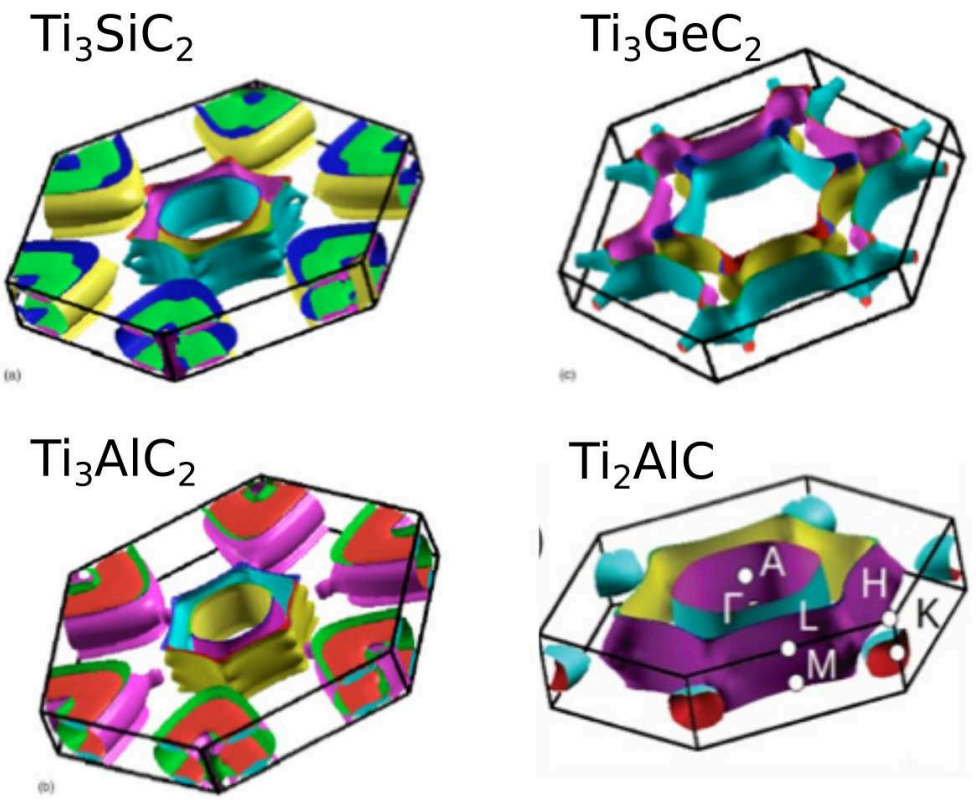

Figure 3.34: *Fermi surface of Ti_3AlC_2, Ti_3SiC_2 ,Ti_3GeC_2 [126]and Ti_2AlC[125].*

3.3.3 Transport formalism

Here, we briefly summarize the principle used for calculating the transport coefficients. As usual, we start from Boltzmann's equation, where **F** is the force, including the electrical and Lorentz contributions, f_0 is the equilibrium distribution and τ is the relaxation time:

$$\frac{\mathbf{F}}{\hbar}\nabla_k(f_0+\Delta f)+\frac{\Delta f}{\tau}=0 \tag{3.6}$$

From this equation, the out-of-equilibrium part Δf of the distribution function is expressed as

$$\Delta f=-(1-\frac{e\tau}{\hbar}(\mathrm{v}\times\mathbf{B})\frac{\partial}{\partial\mathbf{k}})^{-1}e\tau\mathbf{v}\mathbf{E}\frac{\partial f}{\partial E} \tag{3.7}$$

where **v** is the velocity, **B** the magnetic field and **E** the electric field. Expanding the denominator gives (Jones-Zener approximation)[127]

$$\Delta f=-(1-\frac{e\tau}{\hbar}(Bv_y\frac{\partial}{\partial k_x}-Bv_x\frac{\partial}{\partial k_y})+order2)e\tau\mathbf{v}\mathbf{E}\frac{\partial f}{\partial E} \tag{3.8}$$

The first term inside the parenthesis gives rise to the direct conductivity σ_{xx} (without the magneto-resistance contribution), the second term (first order in B) gives rise to the transverse conductivity σ_{xy}, and the third term (second-order term in B) is at the origin of the magneto-resistance. Δf is used to compute any current component by estimating

$$\mathbf{j}=e\int D(\mathbf{k})\mathbf{v}(\mathbf{k})\Delta f d^3\mathbf{k} \tag{3.9}$$

With $D(\mathbf{k})$ the density of states. Applying the electric field **E** along x, computing j_x gives σ_{xx} and the magneto-resistance, and j_y leads to R_H. Besides, a considerable simplification is obtained for a 2D system, since any transport integral can then be put in the form of a circulation along the Fermi line. Grouping all terms and $\partial f/\partial E$ under the form of a function $g(\mathbf{k})$, any transport integral can be put in the polar form

$$\int g(k_x,k_y)\frac{\partial f}{\partial E}dk_xdk_y\cong\int g(\mathbf{k}_F)\frac{d\mathbf{k}_F}{\hbar v_F}=\int g(\mathbf{k}_F)\frac{1}{\hbar v_F}\sqrt{\mathbf{k}_F^2+(\frac{\partial\mathbf{k}_F}{\partial\theta})^2}d\theta \tag{3.10}$$

Roughly speaking, this means that for interpreting magneto-transport we just have to examine what the holes and electrons do along the Fermi line as a function of time.

From the calculations of the direct conductivities and transverse conductivities for each band of index i, one can obtain the overall resistivity and Hall coefficient values from summations of

$$\rho_{ab} = \frac{\sum_i \sigma^i_{xx}}{(\sum_i \sigma^i_{xx})^2 + (\sum_i \sigma^i_{xy})^2} \tag{3.11}$$

$$R_H = \frac{\sum_i \sigma^i_{xy}}{(\sum_i \sigma^i_{xx})^2 + (\sum_i \sigma^i_{xy})^2} \frac{1}{B} \tag{3.12}$$

3.3.4 Predicted results for a simple 2D hexagonal metal

Herein, a simple model is introduced, not directly mimicking the MAX phase Fermi surface, so as to emphasize and isolate physical phenomena. The lattice parameters are that of Ti_2AlC, and then, these phenomena is shown to rule in the same way the transport properties associated to more complex Fermi lines (such as that of Figure 3.33).

As a first example, if we fill our 2D system with just a few electrons per unit cell to get a free carrier system (Figure 3.35(1)). Still, the transport calculations give a substantial magneto-resistance while R_H is quite small, equals to $1.178 \times 10^{-11} m^3 C^{-1}$as in Figure 3.35(1d). An isotropic 1-band model would lead to an apparent hole density $n = \frac{1}{eR_H} = 5.30 \times 10^{29} m^{-3}$, extremely far from the assumed value $2.30 \times 10^{28} m^{-3}$. In order to interpret the results for the Hall coefficient and magneto-resistance, we first remind that in a semi-classical approximation, the wave vector changes with time according to $\hbar \partial k / \partial t = e\mathbf{v} \times \mathbf{B}$ when submitted to the Lorentz force, and holes with an energy E_F cycle clockwise along the Fermi line, until they are scattered to another part by a collision. If one focuses on a concave part and in contrast to this clockwise rotation, the hole velocity, which is perpendicular to the Fermi line, clearly rotates counter-clockwise with time, which means that in real space the holes are thus turning counter-clockwise, so that during a fraction of time in between two collisions they truly exhibit an electron-like behaviour (See Figure 3.35(1a)).It is only at the corners with a convex shape that their velocity rotates clockwise with time, so that they rotate clockwise with time, as free holes would do in real space. This phenomenon is discussed in [128, 129] , and it is quite understandable that this feature can dramatically affect the value of the Hall coefficient.

An elegant way to describe this is provided by Ong's theorem for 2D metals [129]. It states that the transverse conductivity , σ_{xy} is given by

$$\sigma_{xy}^{2D} = \frac{2e^3}{h^2} A_l B \tag{3.13}$$

where A_l is the algebraic area spanned by the mean free path as the wavevector cycles with time over one full orbit. If the mean free path $\lambda = v_k \tau_k$is a constant (for pure impurity scattering), one obtains a circle with the sign corresponding to the type of carriers[129]. However, λ may vary with $\mathbf{k}_F$ (for instance if the relaxation time τ_k is isotropic and the velocity is not constant along the Fermi line (See Figure 3.35 (1b)(2b)). For holes, the oriented area now exhibits outer flaps affected by a negative sign (See Figure 3.35 (1c)), corresponding to the electron-like parts of the Fermi line. They must be subtracted from the hole-like contribution (the central part of the Figure 3.35 (1c)). If the flaps get bigger than the central part, the Hall coefficient can even reverse its sign, so that pure holes can be seen as electrons [129]. That is to say if holes partially behaving as electrons and leading to seemingly compensated transport, pure holes can obviously give rise to a magneto-resistance. This is the case of our hexagonal 2D model. (See Figure 3.35(1d)).

It is worth noticing that using the extraction procedure assuming the existence of two types of carriers and n=p(as described in traditional two band model in Chapter I), the parameters of Figure 3.35(1) would lead to almost equal mobilities (96.2 and 93.5 $cm^2/V{\cdot}s$, respectively) and a concentration n= p= $7.36{\times}10^{27}$ m^{-3}. Therefore an intermediate conclusion can be drawn as already indicated in [128]: the evidence of a small R_H value and a substantial magneto-resistance is by no means enough to prove the presence of two kinds of carriers. As in the Figure 3.35(1), a system involving just one type of carriers can even mimic compensated transport with almost perfectly balanced electron and hole properties.

Furthermore, with a higher N, we now have both hole and electron bands, and the considerations developed above now apply to both kinds of carriers (See Figure 3.35(2)). Increasing the value of U makes the hole Fermi line smoother, and tends to reduce the flap size. However, as long as the Fermi line appreciably deviates from a circle, the mean free path curve, even if it is devoid of flaps (as that of electrons in 3.35(2c)),also departs from a circle and lead to a substantial modification of R_H, as well as to magneto-resistance.

Following all above discussions, questions are generated : for such a simple system, can we rely on the extracted electron and hole densities in the frame of a conventional

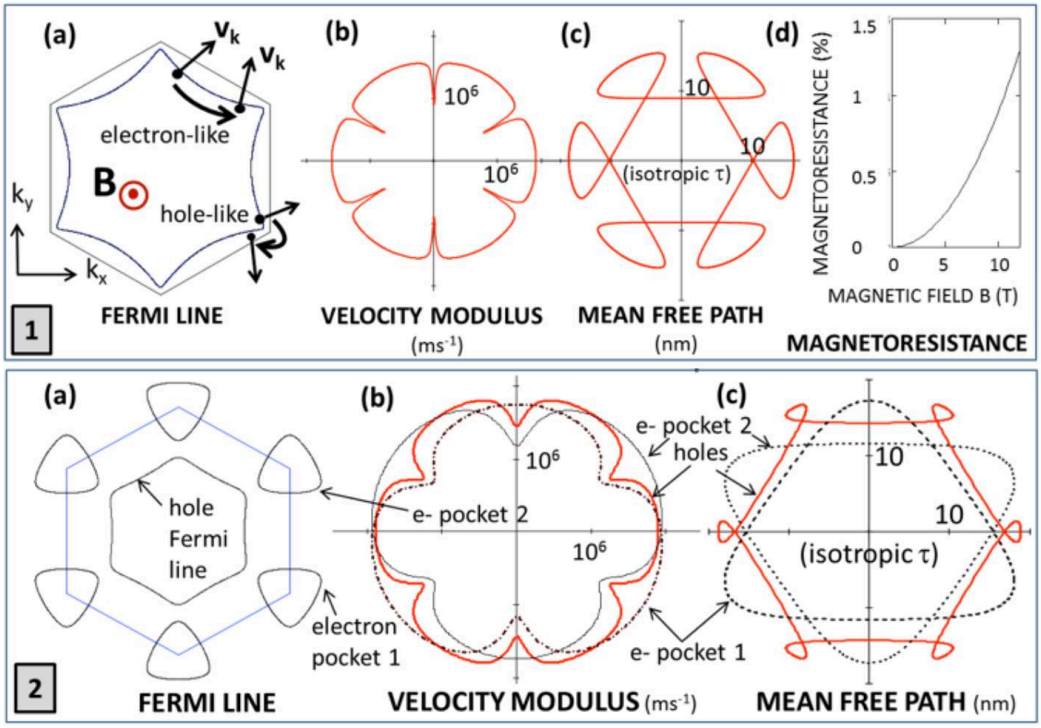

Figure 3.35: *(1) Top: from left to right: (a) Fermi line, (b) polar plot of the velocity along the Fermi line, (c) polar plot of the mean free path and (d) magneto-resistance of a 2D hexagonal system of nearly free electrons with a low number of electrons per unit cell (N=2, τ_p=10^{-14}s, U=0.25eV, four 2D planes per unit cell with c=1.36 nm and a=0.304 nm).(2) Bottom: from left to right: (a) Fermi line, (b) radial plot of the velocity and (c) mean free path for a higher value of N (N=6, τ_p=τ_n=10^{-14}s, U=0.75 eV, four 2D planes per unit cell with c=1.36 nm and a=0.304 nm).*

two-band model, and do they bear any similarity with the real values? In order to answer it, it is instructive to plot the electron and hole densities as a function of N (Figure 3.36), as well as the n_{app}=p_{app} values which would be extracted by using two-band model. Figure 3.36 demonstrates that the extracted values are quite different from the ones using hexagonal 2D nearly free electron model. The Hall coefficient is quite small, and depending on N, it can be either positive or negative. This example also shows that in spite of considerable variations of the real densities at the Fermi level, n_{app} can remain remarkably stable, whereas the sign of R_H may vary as well as its magnitude.

Another message can be taken from Figure 3.36 and from the nearly-free electron model which can explain a relative insensitivity of n_{app} to the electron band filling. A small value of R_H can indeed attribute to multiple reasons. It may be induced by a compensation between holes and electrons, or to a larger number of only one type of carriers. Yet, it is only in the isotropic case that the common observation of a small value of R_H indicate the presence of two types of carriers.

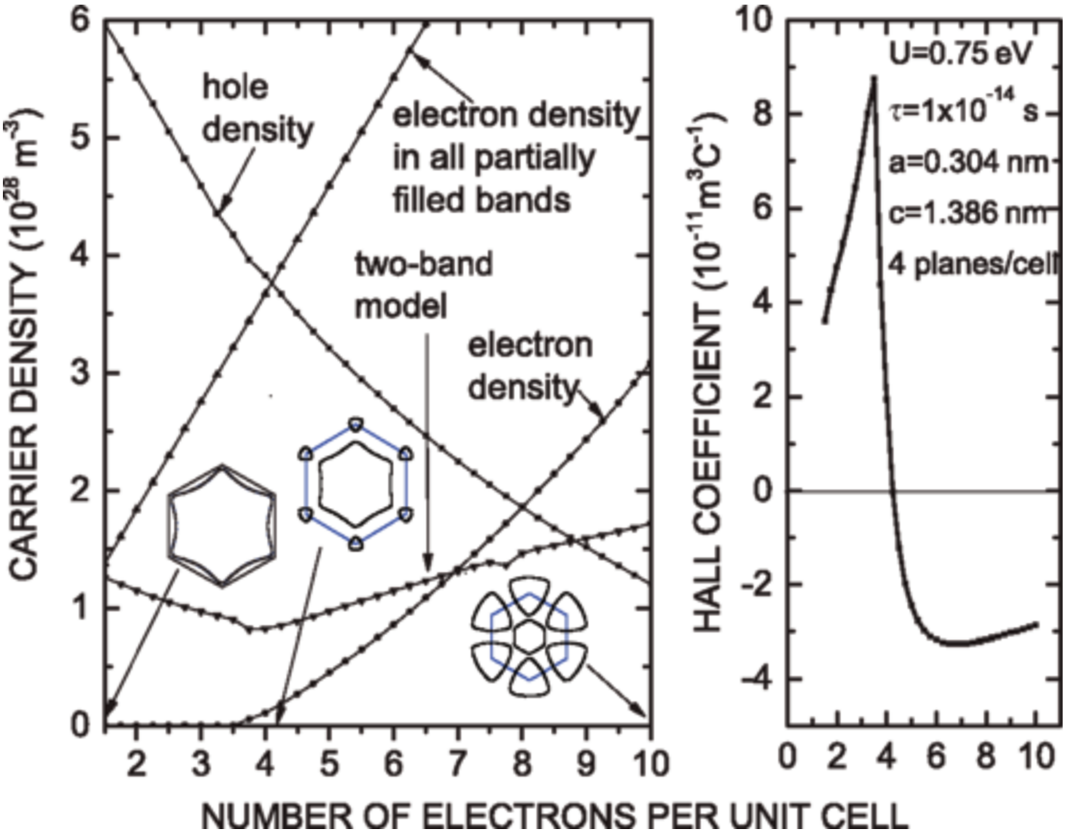

Figure 3.36: *Variation of carrier densities in the various bands as a function of the number of electrons per unit cell N (left) and Hall coefficient versus N (right).*

Besides, it is a common misconception to believe that Fermi lines of different perimeters (and thus of different densities) necessarily give rise to widely different σ_{xy} values. What really matters is the variation of the mean free path along the Fermi line, as indicated by Eqs 3.13. If the velocities and the scattering times exhibit similar values for both a hole and electron band, then the mean free paths plots will also be similar and the number of carriers in each band at the Fermi level is not necessarily the relevant factors as both bands give the same absolute contribution to σ_{xy} , yet with opposite signs,leading to compensation and a very small R_H.

In the present model, similar velocities are precisely expected because both bands are derived from the almost identical free electron curve (See Figure 3.35 (2b) for an example). In Figure 3.36, a small N value gives only holes. While increasing N, the electron pockets start to get filled after some threshold (and the hole concentration decreases). This produces a very steep variation of R_H on a narrow interval after the onset of electron filling. In this part (N$\leq$4), the electron pockets are tiny and cannot be assimilated to the free electron lines over much of their perimeter. As these pockets expand, one can very rapidly reach a kind of plateau with a negative value (See Figure 3.36). This plateau is a direct consequence of the statement expressed above. The mean

free path curves of the hole band and one of the two electron pockets almost contract one another, and what remains is the net contribution to σ_{xy} of the second electron pocket (See Figure 3.35(2c)). Since the velocity does not considerably vary with the filling, R_H exhibits a plateau, whose value is fixed by the electron pocket per unit cell which remains uncompensated. Yet the hole density substantially decreases, whereas the electron density does the opposite.

3.3.5 Predicted results for MAX phases

We simply use the lattice parameters of the MAX phases and select a set of energy parameters aimed at recovering the Fermi surface of a given MAX phase. Here we take the case of Ti_2AlC as an example and draw general conclusions which can be applied to other MAX phases. The contributions of each band are calculated (split hole bands and split or single electron pockets) and summed. Figure 3.37 gives the results obtained for a Fermi line mimicking the full Fermi surface of Ti_2AlC, obtained for equal electron and hole relaxation times τ_n=τ_p=10^{-14} s, representing a common order of magnitude for metals[124]. The valley degeneracy of electron g_n=1, of each hole band g_p=2. The fact indicates that in spite of a minor contribution of the electrons to ρ_{ab} (as postulated in [130]), there is a substantial contribution of all carriers to R_H and holes alone would lead to a considerably higher value . Any band, considered alone, exhibits a substantial magneto-resistance, with quite similar relative variations. But the measured magneto-resistance is due to holes, since they give the major contribution to the overall resistivity.

A two-band isotropic model would give n_{app}=p_{app}=3.94×10^{27}m^{-3} (staying the case of g_n=1 and g_p=2), and mobilities μ_p=148 cm^2/V·s and μ_n=125 cm^2/V·s, respectively (polycrystalline samples give values around 10^{27}m^{-3} [3]). A one-band model would give only holes with p_{app}=4.60×10^{28} m^{-3}. The values given by this 2D nearly free electrons model, are p=2.02×10^{28} m^{-3} and n=3.15×10^{27} m^{-3}.

So we can see from this case that it is quite obvious that neither a conventional 2-band model, nor a 1-band model can give reasonable estimations of the true densities. The small value of R_H and the apparent compensation must not be attributed to the fact that the hole and electron densities compensate one another, since they are indeed quite different. Firstly, the velocities remain the same order of magnitude in most parts (close to the free electron velocities). Secondly, with phonon scattering we can reasonably expect an almost isotropic scattering time. If the τ_n and τ_p are similar , the

mean free path curves of any hole and electron bands are thus more or less similar. In case of impurity scattering, we also expect similar mean free path values. Therefore, as explained in the previous section, we can reasonably expect that all bands give roughly similar σ_{xy}values . Moreover, if the hole and electron bands were in equal numbers (g_n= g_p=2), we would expect an even strong compensation which is not due to the similar electron and hole concentrations.

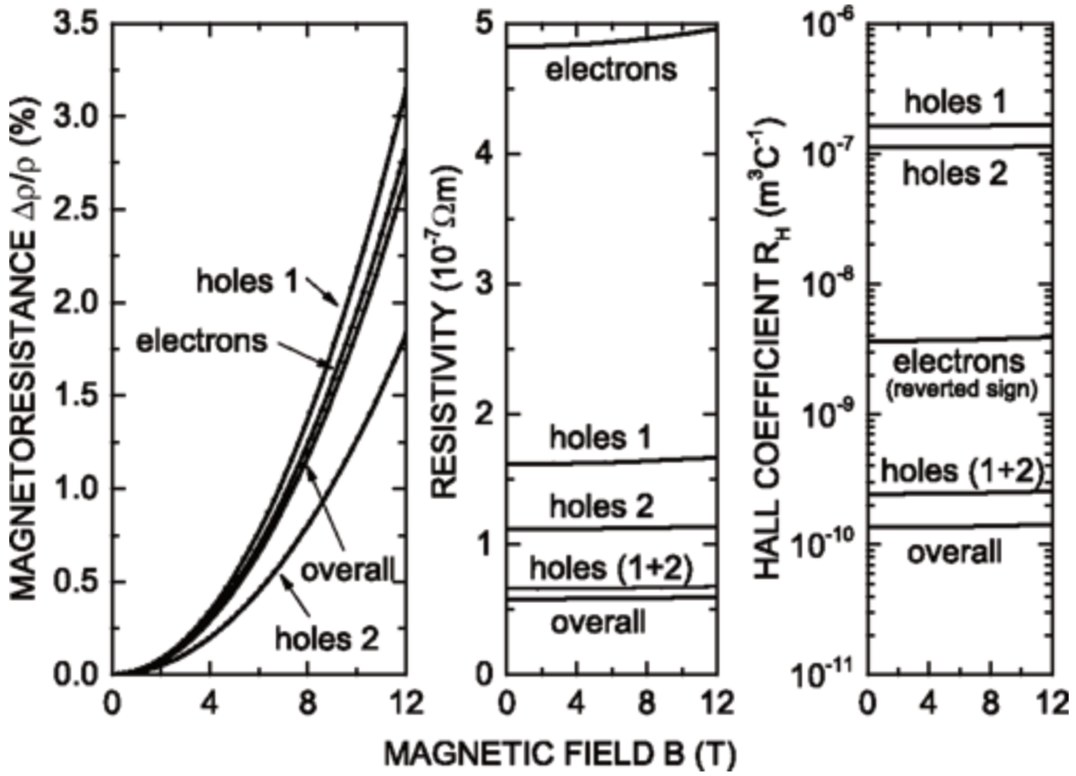

Figure 3.37: *Transport parameters corresponding to the 2D Fermi line mimicking the projection of the Fermi surface of Ti_2AlC as a function of magnetic field. Noting:the valley degeneracy of electron g_n=1, of each hole band g_p=2.*

Some modification are presented if τ_n and τ_p become different. Figure 3.38 shows the variation of the apparent 2-band model density as a function of the ratio between τ_p and τ_n(two cases are shown g_n= g_p=2 or g_n= 1 and g_p=2). Practically , this ratio can vary because phonon scattering depends on the number of final states, and the different length of Fermi lines of holes and electron. Impurity scattering may also differ for electrons and holes. Figure 3.38 shows that a moderate change in τ_n / τ_p can produce an appreciable change in the extracted density and even reverse the sign of R_H.

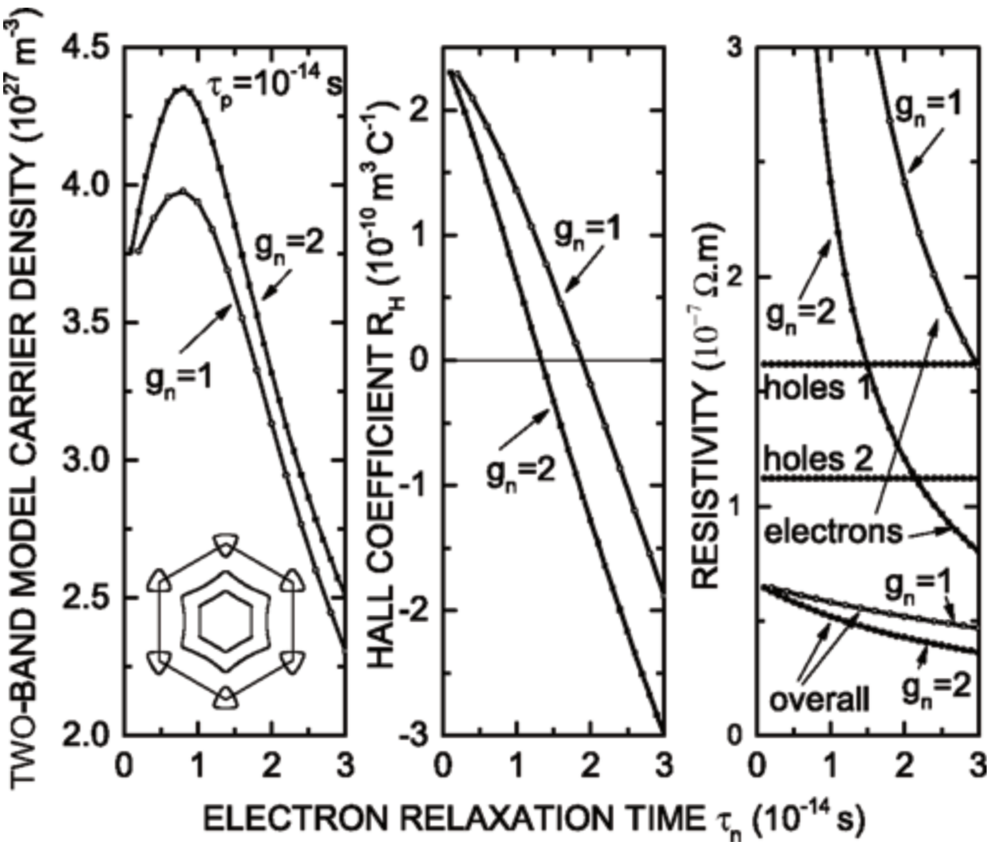

Figure 3.38: *For the same Fermi line as in Figure3.37, plot of the 2-band model carrier density, Hall coefficient and resistivity as a function of the electron relaxation time τ_n ($\tau_p$being fixed.)*

This sensitivity to moderate changes of some physical conditions is expected to affect the experimental data significantly. For instance, if the ratio τ_n / τ_p is modified by the temperature, this may induce a temperature variation of the Hall coefficient, a phenomenon which should not be observed with a conventional one or two-carrier model. To confirm this, we have incorporated a temperature dependence to the model, by combining the impurity and phonon scattering times $\tau_{imp}$and τ_{ph} according to Matthiesen' rule to obtain the overall relaxation time τ as $1/\tau$=$1/\tau_{imp}$+$1/\tau_{ph}$. If we take $1/\tau_{ph}$ proportional to T and maintain constant the mean free path for impurity scattering λ_{imp}, giving τ_{imp}=$\lambda_{imp}/\mathbf{v}_k$. Figure 3.39 shows the predicted temperature dependence of n_{app}=p_{app} (conventional two-band model). It is remarkable that a modification of the τ_n / τ_p ratio can lead to an apparent variation of the carrier density. Reasonable ratios can even lead to an apparent and substantial decrease of the carrier densities with T, a phenomenon which cannot be explained within the frame of a conventional 2-band model.

We can now list some properties predicted by our interpretation and the associated 2D model, so as to compare them with the experiment results. They are not only based on the data presented in the previous sections, but on additional calculations carried

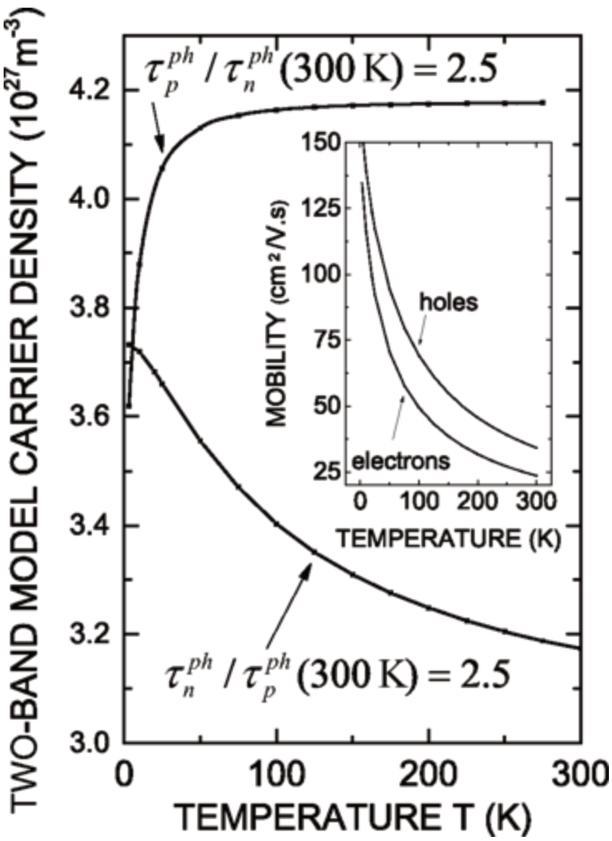

Figure 3.39: *For the same Fermi line as in Figure3.37, plot of the 2-band model carrier density with temperature, for different room temperature ratios between the electron and hole scattering times. The insert shows the mobility variation.*

out using, including but not limited to other energy values for U or for the separation between the split hole and electron bands, or other unit cell parameters. First, a large anisotropy should be observed to ensure applicability of this pseudo-2D model on the in-plane transport ($\rho_c >> \rho_{ab}$). Secondly, for transport in the basal plane and assuming reasonable relaxation times for metals (from 10^{-15} to 10^{-14}s), a conventional 2-band interpretation should give extracted densities of some 10^{27} m^{-3}, and mobilities in the range of 10-500 cm^2/Vs. R_H is between zero and some 10^{-10} m^3/C, and either negative or positive. The magneto-resistance is a few percent at B up to 10 T.

3.4 Conclusion

Experimentally, a set of experimental data were obtained from single crystals of V_2AlC and Cr_2AlC as a function of temperature and magnetic field. In comparison with the resistivity value of polycrystalline samples, the resistivity of Cr_2AlC single crystal is three times lower, while for that of V_2AlC, four times lower. In particular, we obtain a very high ratio between the in-plane and parallel to the c-axis resistivity, which is very

substantial, in the range of a few hundreds to thousands.

From MR and Hall effect measurement, in-plane transport behaviours of MAX phases have been studied. As in the case of the polycrystalline phases, we observe a magneto-resistance of a few per cent, among them, only MR curve of Cr_2AlC exhibits parabolic-like curves, as reported for polycrystalline MAX phases. One can notice that Hall resistivity varies linearly with magnetic field, and this phenomena is temperature independent, indicating the systems are in the weak-field limit. R_H is small, as previously noticed for polycrystalline samples. The extracted mobility is in the range from 50 to 120 cm^2/Vs, which is the same order of magnitude of polycrystalline sample.

Thermal transport measurements were also conducted on Cr_2AlC samples. Similar as higher electronic conductivity compared to its polycrystalline counterpart, higher thermal conductivity is verified. Non-monotone sign of charge carrier type was displayed in the curve of Seebeck coefficient, while similar phenomena was observed to Hall coefficient measurement. Yet this discrepancy can still be partly explained by a compensation between holes and electrons. Attempts on the out-of-plane magnetoelectronic transport were also performed. Though it is interesting to observe the anomalous magnetoresistance in the absence of Lorentz-force, the mechanism of a field-induced transport along c-axis is still unclear.

Theoretically, a general model was proposed for describing the weak field magneto-transport properties of nearly free electrons in two-dimensional hexagonal metals. It was then modified to be applicable for the transport properties of layered MAX phases. We argue that the values of the in-plane Hall coefficient and the in-plane parabolic magneto-resistance are due to the specific shape of the Fermi surface of almost two-dimensional hole and electron bands. If the contribution of the electron pockets to in-plane resistivity is often predicted to be a minor one, in contrast, both holes and electrons should substantially contribute to the overall value of the in-plane Hall coefficient.

The Fermi surface of MAX phases has never been experimentally probed. Yet, it is only the experimental verification of its shape for various MAX phases which can ultimately prove or invalidate some of our assumptions. The striking similarity between some polycrystalline and single-crystalline extracted data is yet to be explained.

chapter 4

MXenes synthesis and characterization

In this chapter, we report a general approach to etch V_2AlC single crystal and mechanically exfoliate multilayer V_2CT_x MXenes. We then detail the structural characterization of the obtained MXenes. Up to our knowledge, all MXenes reported up to now have been derived from the Al-containing MAX phases, the second part of this chapter discusses the process with the aim of obtaining Ti_2CT_x MXene from Ti_2SnC single crystals.

MXenes are derived from MAX phases, a class of layered ternary carbides and/or nitrides that have been introduced in the previous chapters. The motivations for extracting MXenes are multiple, as explained in the introduction, inspired by the highest metal uptake when testing V_2CT_x MXenes as electrodes for lithium battery compared to the other multilayer MXenes[131]. Herein, we selected V_2CT_x as a representative M_2XT_x MXenes.

4.1 V_2CT_x MXene Synthesis

4.1.1 Etching

Wet hydrofluoric acid (HF) treatment of MAX phases was the first efficient method to synthesize MXenes, which allows selective dissolution of the Al layers from the MAX phases [55]. Figure 4.1 shows the principle of the removal of Al from the V_2AlC 3D structure.

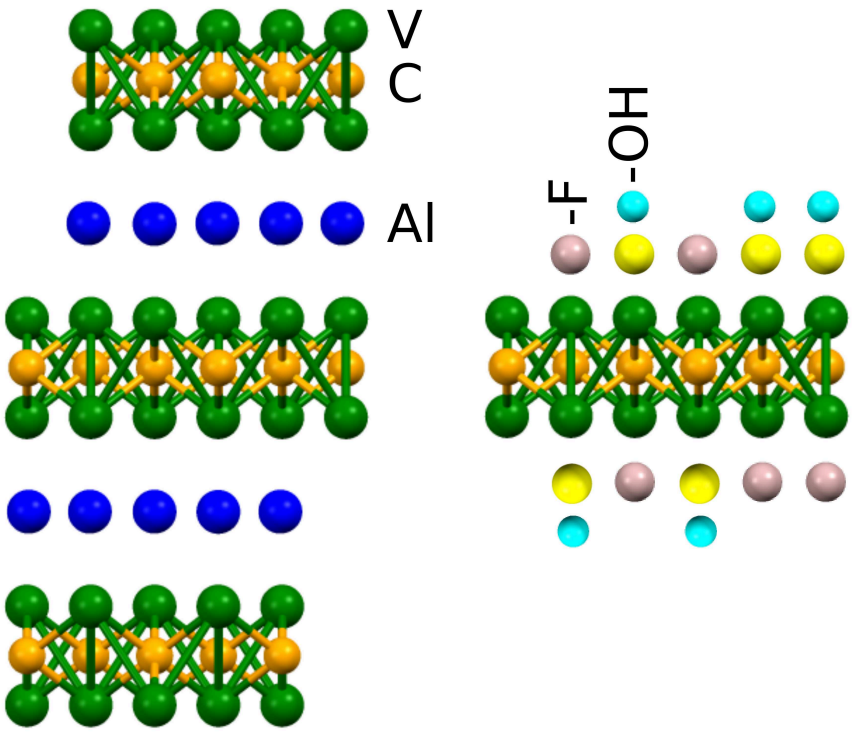

Figure 4.1: *Schematic diagram of Al removal from V_2AlC.*

Our process to synthesize V_2CT_x flakes is illustrated in Figure 4.2. First, we found that, in the case of mm-size V_2AlC single crystals, chemical dissolution of the Al layers was extremely slow. In order to hasten the etching procedure, as-grown V_2AlC single crystal were scratched heavily with a sharp blade to create defective surface, and then sonicated in 45% HF solutions at 80 °C for 12 h. Subsequently, dark green supernatant with V_2CT_x precipitates was collected, confirming the etching of V_2AlC (See Figure 4.3(a)). Those not fully etched large crystals at the bottom of the beaker were immersed in fresh HF solutions with same concentration at room temperature for 120 h. The collected suspension was separated by centrifugation at 6000 rpm for 10 min and washed by deionized water several times until the pH value of solution reached above 5. Thereafter, the wet sediment were vacuum dried at 40 °C for 24 h, marked as VC-p indicating the powder-like morphology (See Figure 4.3(b). The same rinsing procedure was applied for the larger crystals as well, marked as VC-f indicating the flake-like morphology (See Figure 4.3(c)), both can be referred to V_2CT_x, where T_x stands for terminated-surface groups.

In our present experiment, it is worth noting that some attempts have been made to improve the chemical etching process. First, the as-grown crystals were directly immersed into the HF without breaking into pieces, aiming at large-scale MXenes. The effect of sizes of crystals on the etching process will be discussed in the next section.

Moreover, dimethyl sulfoxide (DMSO), an effective intercalant for $Ti_3C_2T_x$-MXenes as evident by the observed shift in major XRD peaks towards lower angles in the $Ti_3C_2T_x$ samples [68], was also introduced in our experiment since other organic intercalants such as thiophene, ethanol, acetone, tetrahydrofuran, formaldehyde, chloroform, toluene and hexane, were found to be unsuitable. The as-etched V_2CT_x MXenes was added to the DMSO and stirring was employed. After 24 h of intercalation, the MXenes was centrifuged and the supernatant poured out to remove most DMSO and was washed with DI water followed by 4h sonication with ethanol. The effect of DMSO on our V_2CT_x will also be discussed in the next section. However, the prospect of intercalating DMSO is severely limited by its exclusive effectiveness towards delaminating $Ti_3C_2T_x$, and its difficulty of thorough removal due to high boiling point solvents. Furthermore, lamellar thickness can be undesirably increased by remnant DMSO molecules, which joined the delaminated sheets together. To date, the exact mechanism to explain how and why DMSO only interact with multi-layer $Ti_3C_2T_x$ remains unclear [70].

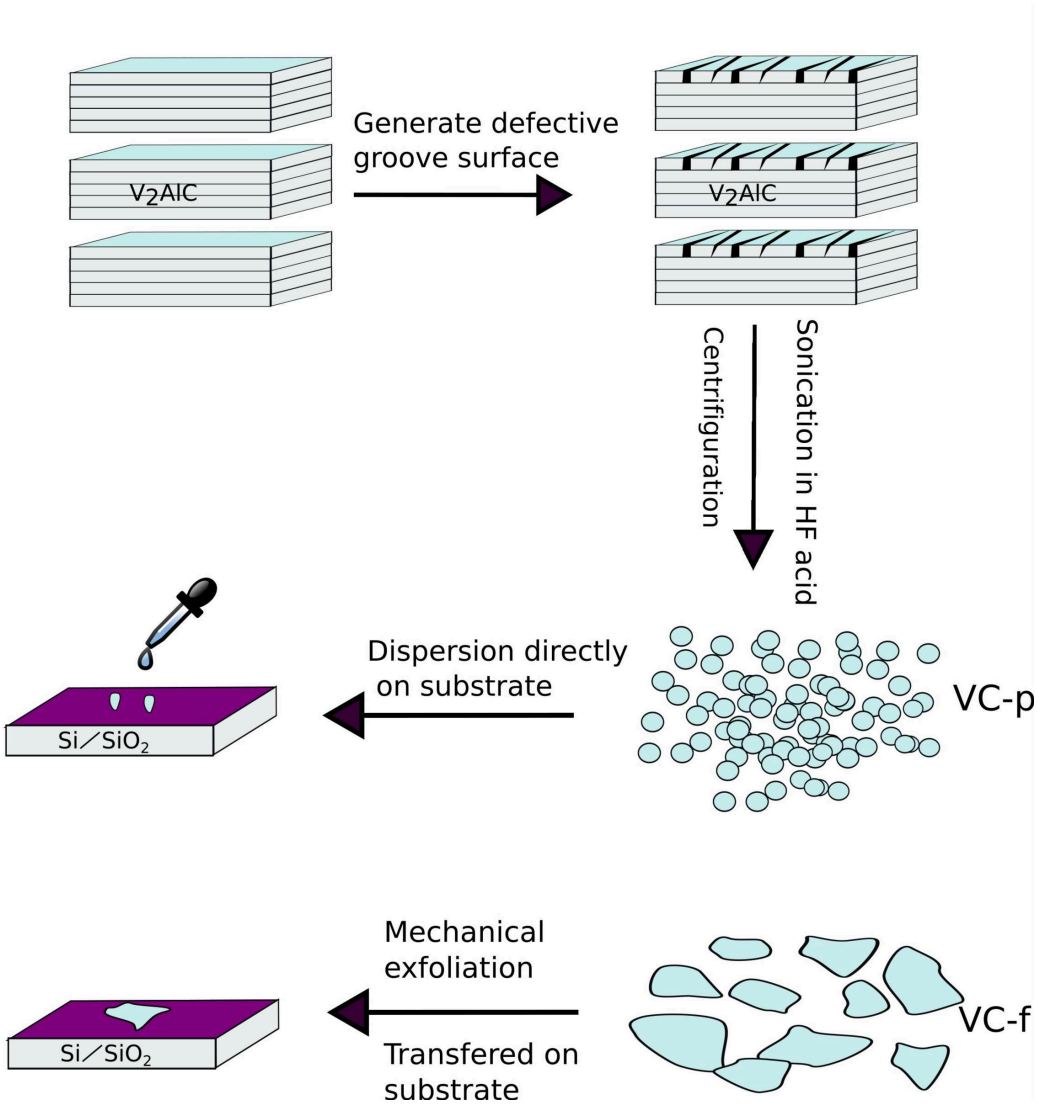

Figure 4.2: *Schematic diagram of synthesis process.*

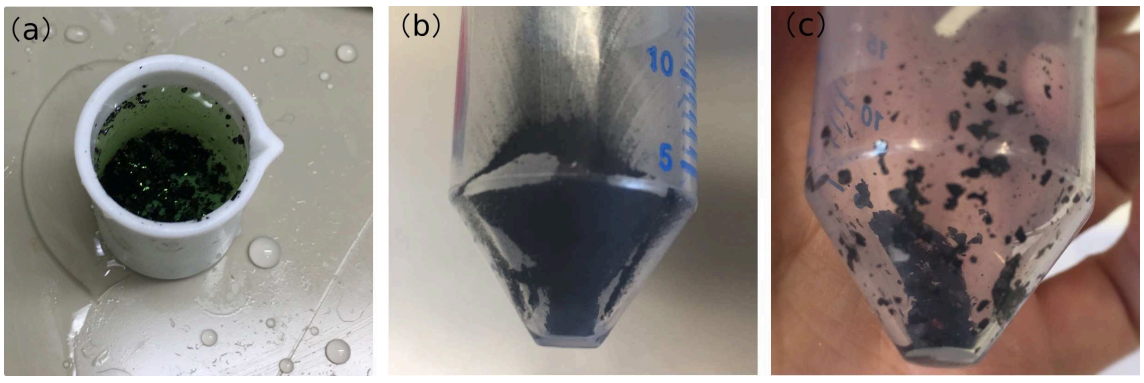

Figure 4.3: *(a)Dark green supernatant and collection of (b)VC-p (powder-like) and (c)VC-f (flake-like).*

4.1.2 Substrate preparation

In order to investigate the electronic properties of V_2CT_xMXene, the multilayer sheets should be isolated onto a substrate. Si/SiO_2 substrate is often used in the case of 2D crystals, as it offers the possibility to tune charge carrier densities according to the voltage applied on the backgate formed by the doped Si.

In this thesis, Si/SiO_2 substrate was used for all device fabrication. Three inches diameter doped silicon (ρ~0.001-0.005 Ω·m) wafers with a thermally grown 90 nm or 300 nm-thick dioxide layer on both the front polished and the back surface were used, ordered from MTI Corporation.

In order to electrically contact the backgate, we first chemically etched the oxide on the wafer back side and then metallized a 300 nm-thick aluminum layer.

A grid of metallic marks [Ti(5 nm)/Au(60 nm)] with the combination of symbols and numbers was defined by optical lithography, metal deposition and lift off on the front surface to locate flakes for the following process. Then, the wafers are diced in 6 $\times$8 mm^2 pieces in order to fit the chips used for electrical measurements.

4.1.3 Mechanical exfoliation

Our original focus is to isolate single large flakes of V_2CT_x MXenes, that can be examined and measured, particularly for electrical, optical and thermal properties.

As for other 2D inorganic graphene analogues discussed in the Chapter 1.2.1, we will show that mechanical cleavage as originally applied in peeling off the graphene from graphite allows to mechanically isolate fewer layer MXene flakes from as-etched V_2CT_x MXenes.

First, as-etched V_2CT_x MXenes was placed on the sticky side of a medium-track blue tape. This residue-free tape promised to leave little to no sticky residue on the substrate(See Figure 4.4(a)). Then, the tape was folded more than 10 times so as to peel off multilayers V_2CT_x sheets. We proceed with a transfer on a fresh piece of tape. As generally known, the interlayer bond are stronger than graphite, even after the etching process. In order to maximize the shear force, it is necessary to use the fresh tape to continue the exfoliation process.

Then, the exfoliated V_2CT_x sheets stuck on the tape was directly transferred onto

a piece of Si/SiO_2 substrate (See Figure 4.4(b)). The flakes can be identified by optical microscopy contrast with SiO_2, similar as graphene. Meanwhile, the position of flakes can be identified according to the metallic mark system.

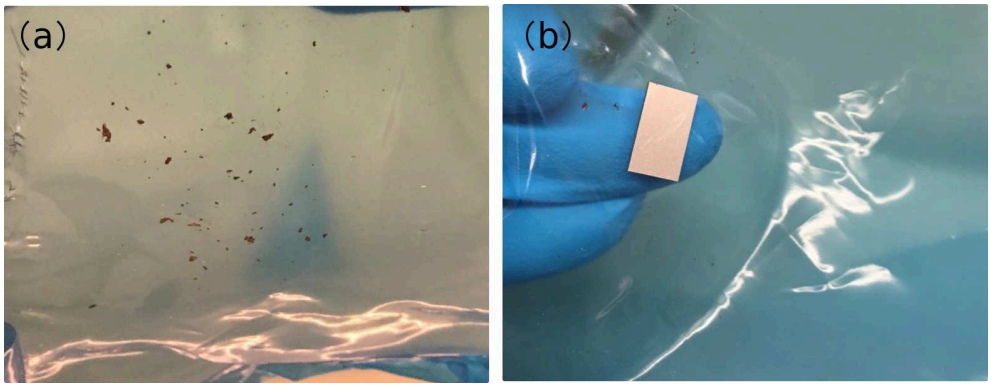

Figure 4.4: *Blue tape exfoliation. (a) Status of exfoliation after ~ 10 times of folding-unfolding of the tape on VC-f. (b) Transfer on a piece of Si/SiO_2.*

4.1.4 Material characterization

4.1.4.1 X-ray diffraction

X-ray diffraction is an analytical technique used to characterize materials atomic structure. In a $\theta - 2\theta$ configuration, θ corresponds to the angle between (hkl) plane and the incident X-ray and the diffracted X-ray. The detector is placed at an angle 2θ to the incident X-ray. The results are usually presented as the intensity vs 2θ. According to the Bragg's law:

$$n\lambda = 2d_{hkl}sin\theta \tag{4.1}$$

the interplane atomic spacing d_{hkl} can be calculated from the peak position. For MXene phase, the (002) plane is one of the most intense peaks observed, whose 2θ position is therefore used to determine the c-lattice parameter.

In the present experiments, X-ray diffraction on V_2AlC before and after HF etching were performed on a Mar345 image plate using Mo Kα radiation (l= 0.071074 nm) (Rigaku Ultra X18S rotating anode, Xenocs fox 3d mirror). Data images were integrated by Fit 2d software. Crystals were picked up using grease. For the following discussion, the data was converted under the wavelength of Cu Kα radiation in order to compare with the 2θ value in the literature.

4.1.4.2 Micro Raman

The unpolarized Raman spectra were collected on a LabRAM HR800 (Horiba Jobin-Yvon, France) equipped with an air-cooled CCD array detector in the backscattering configuration. An Argon ion laser (514.5 nm) was used as the excitation source. An objective with numerical aperture of 1.25 was used. The spot size of the laser was focused to 2 μm. The spectral resolution was grooves/mm with grating 1800, 2400 and 150.

4.1.4.3 SEM, TEM with EDS and AFM

The microstructure morphology and elemental analysis of V_2CT_x MXene sheets were characterized by a field emission scanning electron microscope (JSM-7600F, JEOL, Japan) equipped with Energy Dispersive Spectroscopy (EDS). A TEM (LEO922) also equipped with EDS detector, was used to observe the microstructure of the sample and investigate the element distribution. Flake thickness and surface topology was tested by AFM using Bruker Multimode Nanoscope VIII under using Peak-force or normal Tapping mode.

4.2 Structural characterization of as-etched V_2AlC single crystal

4.2.1 SEM and EDS

Work towards isolating large single V_2CT_x MXenes flakes began with the idea that starting the process with large V_2AlC single crystal would lead to eventual separation of large flakes. As-grown V_2AlC crystals were firstly employed as raw materials ready for HF etching. As can be seen in Figure 4.5, showing the SEM image of V_2AlC crystals after etching by 45%HF for two weeks, the as-produced samples were neither fully delaminated, nor were they as large as we desired. No typical accordion-like morphology of MXenes are observed, combined with EDS spectrum results, indicating that the Al was not completely removed from the parent MAX phase. It is evident that delamination has not occurred. Yet, comparing to the EDX results before and after etching, it is undeniable that that the etching process act on the V_2AlC single crystal,

though reaction kinetics are limited by the etchant concentration, crystal size as well as reaction temperature.

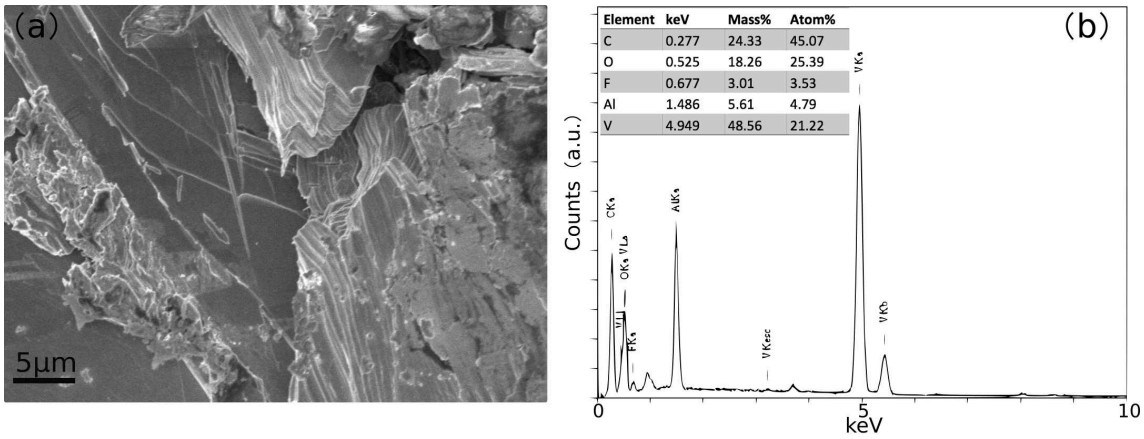

Figure 4.5: *(a) SEM image and (b) the corresponding EDS spectrum of as-etched V_2AlC single crystal.*

4.2.2 AFM

AFM image of the steps of as-etched V_2AlC shows that the step height is around 1.3 to 1.4 nm, which is very close to value of the c-lattice parameter of V_2AlC (See Figure 4.6). No clear change of interlayer space was detected after two weeks etching.

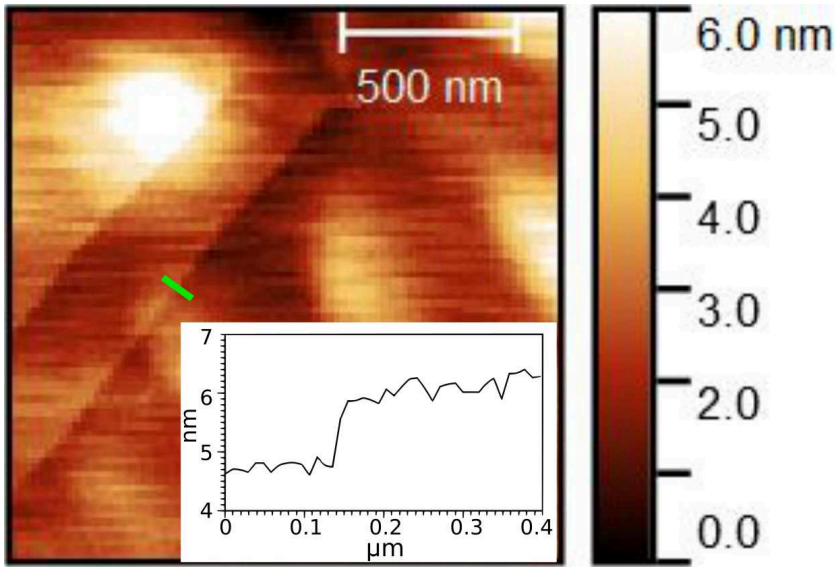

Figure 4.6: *AFM image indicating the step height of the V_2AlC crystal after etching for 14 d.*

Apparently, increasing the crystal size of the parent MAX phase makes it impossible to extract MXene flakes through chemical etching. Hence, to ease the etching process,

a simple mechanical disruption was introduced to break apart the large single crystal by using sharp tweezers to scratch the surface. Figure 4.7 shows the optical images of the same sample before and after mechanical disruption. Additional macro and micro cracks are generated by the mechanical force during sonication process and lead to acceptable size for chemical etching. The effect of these intentional defects on the improvement of preferential etching will be discussed in the following part.

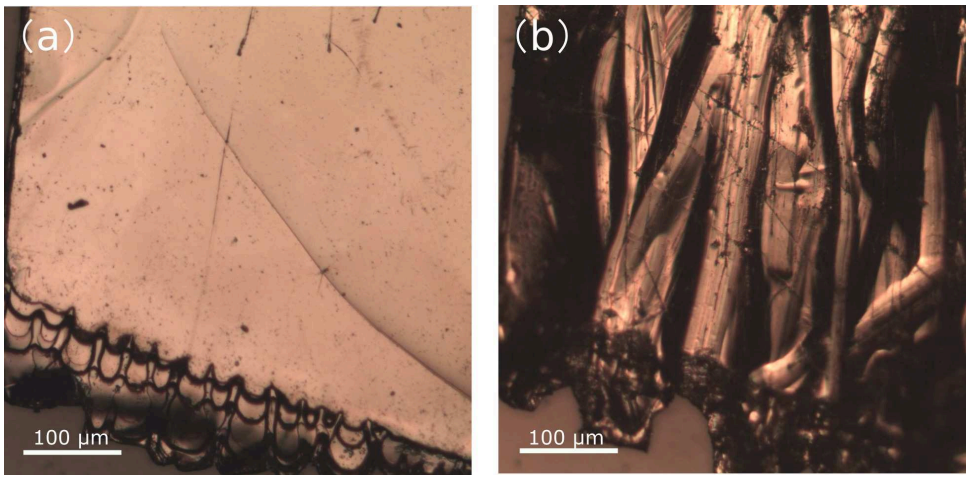

Figure 4.7: *Optical images of crystals before and after mechanical disruption.*

4.3 Structural characterization of as-etched V_2CT_x MXenes

4.3.1 XRD

The structure and phase composition before and after HF exfoliation were characterized by XRD. The typical XRD patterns of the raw material V_2AlC and V_2CT_x samples are presented in Figure 4.8. Here, it is worth mentioning that the broaden peaks at 11° is the signal from the grease on sample holder from the XRD patterns of VC-p. Similar as other MAX phase to MXenes transformation, the degree of order as measured by XRD clearly decreased and VC-p exhibit a more disordered structure than that of VC-f. The (002) peaks on both VC-p and VC-f samples broaden and shift to lower angles after acid treatment, indicating the larger *d* spacings. Yet, from the XRD pattern of VC-f, we can still observe the (002) peak with decreased intensity comparing to the original crystal, indicating unreacted crystals. From the XRD pattern of VC-p, one observed an evident shift of 2θ from 13.5° to 7.4° , corresponding to *c*-LPs changing from 13.107 Åto 23.872 Å,

for V_2AlC and V_2CT_x, respectively. Such phenomenon has been attributed to the water intercalation in between the layers after delamination in an aqueous solution. Indeed, water intercalation is common and has been observed in other MXenes such as Nb_2CT_x, $Nb_4C_3T_x$ [132, 133]. The value of the *c*-LPs is almost comparable to that reported in previous works on V_2CT_x powders, yet, the (006) (103) peaks in the present seemingly vanished [134].

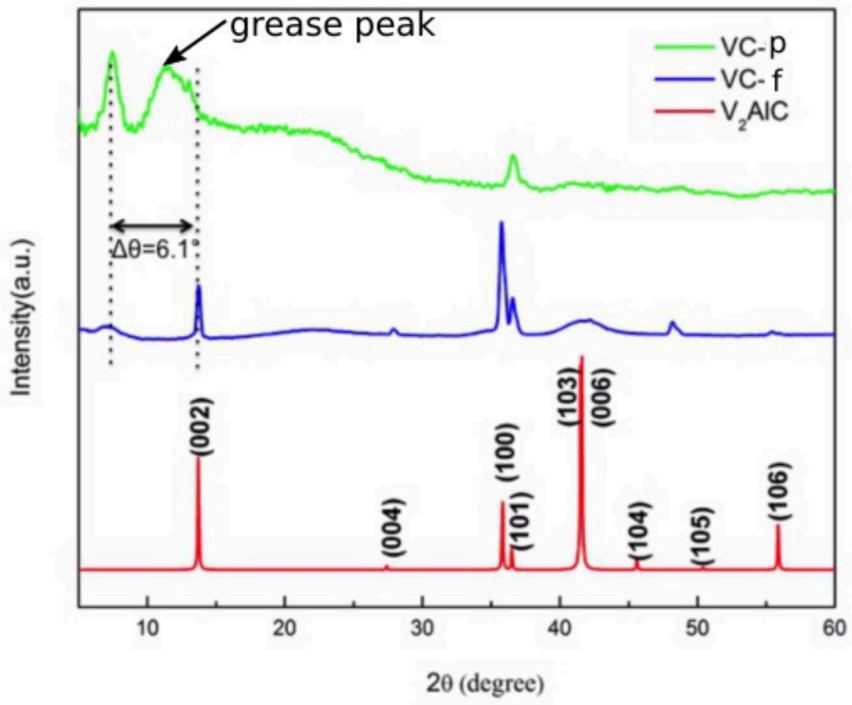

Figure 4.8: *XRD patterns of V_2AlC and V_2CT_x (VC-p and VC-f).*

Also, as mentioned in the chapter I for most of the 2D materials, the delamination process consists of intercalating a large organic molecule to weaken the bonds between layers and using ultrasonication to completely separate the layers. It has been demonstrate that mixing $Ti_3C_2T_x$ with DMSO at room temperature can successfully yield $Ti_3C_2T_x$ MXene with enlarged *c* lattice parameter. The lattice parameter *c* of exfoliated $Ti_3C_2T_x$ was 19.9 Å. After intercalation, the (002) peak further shifted to 2θ =7.0° and c increased to 25.3 Å[135].

In our experiment, DMSO was also introduced as intercalant. Figure 4.9(a) shows the collected V_2CT_x (VC-p) samples with and without treatment of DMSO. We can see from the patterns that, contrary to $Ti_3C_2T_x$, there is no obvious further shift of (002) peak corresponding to the expansion of interplane distance on the $V_2CT_x$with treatment

of DMSO. Although we did not try any other intercalant molecule, we would like to mention that a relatively large molecules organic base, namely tetrabutylammonium hydroxide (TBAOH) was recently demonstrated to be effective for the delamination of V_2CT_x (See in the Figure 4.9(b,c)). The (002) peak shifted from a 2θ of 8.9° to 4.6° (*c*-LP from 19.9 Åto 38.6 Å) after 2 h mixing in TBAOH solution. By doubling the time to 4 h, a very slight down shift in the (002) peak position was observed (shifted down to 4.56°). Also this intercalant works well for large-scale delamination of carbonitrides MXene, such as Ti_3CNT_x as well.

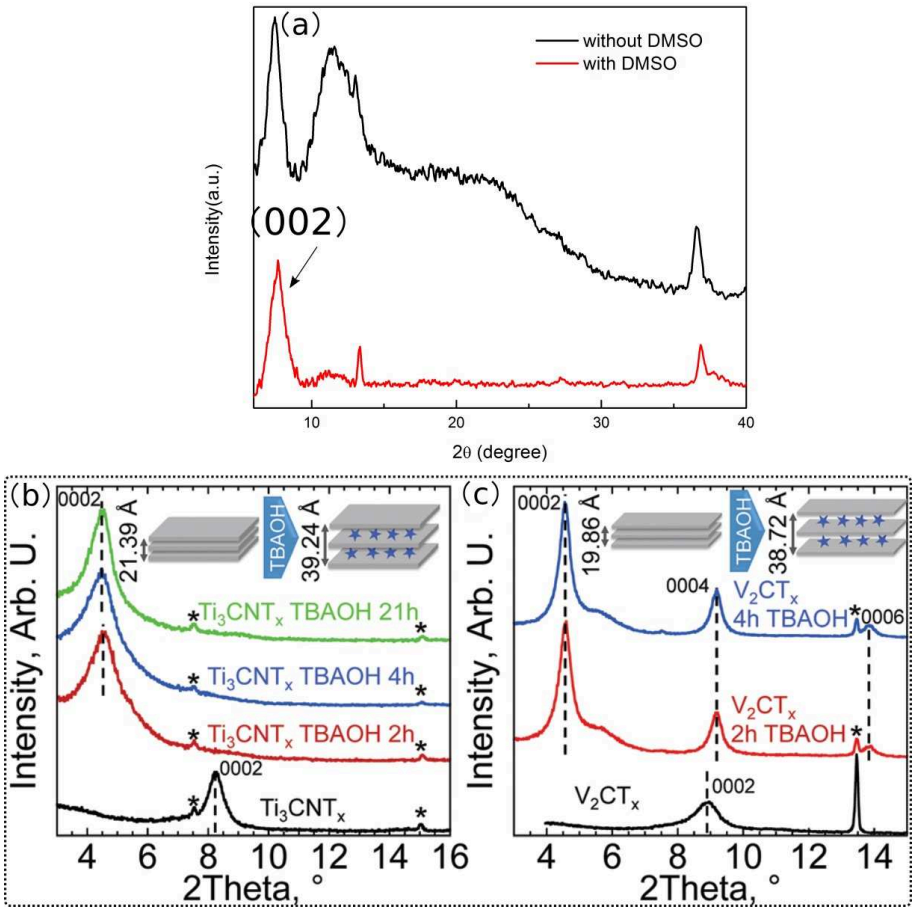

Figure 4.9: *(a) XRD patterns of V_2CT_x MXenes with and without treatment of DMSO and (b,c) XRD patterns of Ti_3CNT_x and V_2CT_x before and after mixing with TBAOH [71].*

4.3.2 SEM and EDX

Figure 4.10 shows the cross-section SEM images of the mechanically disrupted V_2AlC single crystals after sonication in 45% HF at 80°C for 12 h. Apparently, the etching

process occurred from the defective area along the grain boundaries, and the shear force induced micro cracks created a large number of channels for etchant penetration. All these facilitate the etching by accelerating the etching rate and dramatically reducing the etching time for relatively large single crystals.

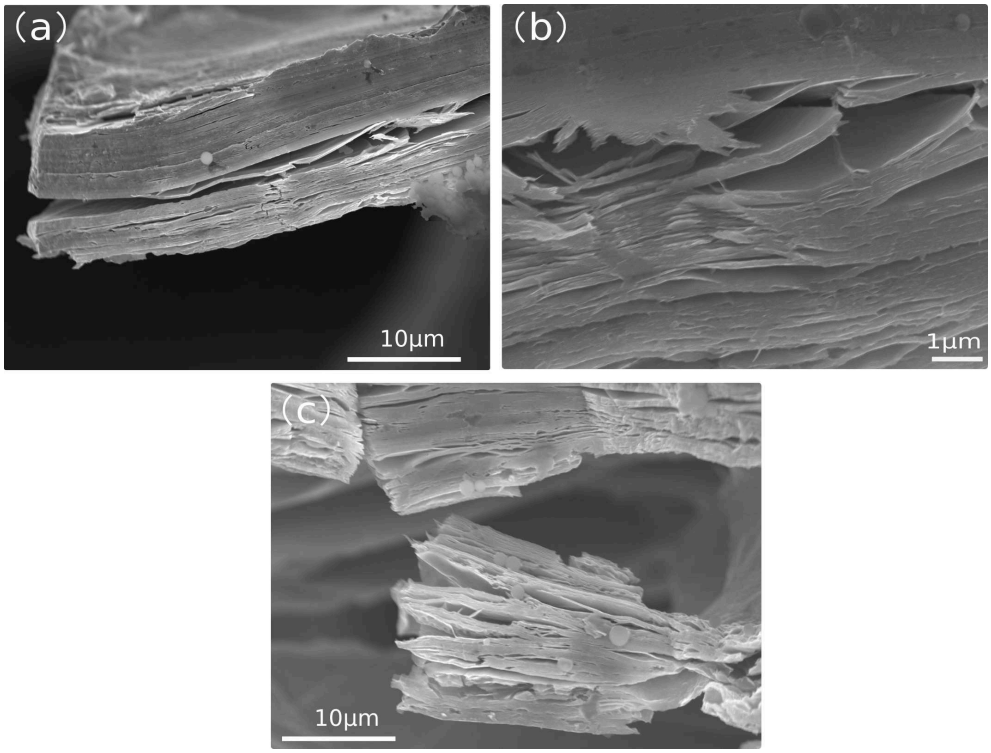

Figure 4.10: *Cross-section SEM images of the as-mechanically destructed V_2AlC single crystals after sonication in 45% HF at 80°C for 12h.*

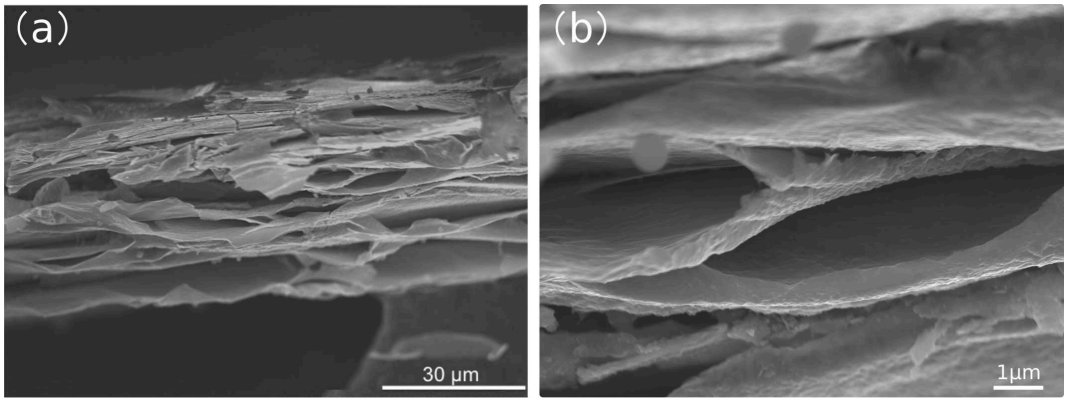

Figure 4.11: *Cross-section SEM images of the as-etched V_2CT_x after immersed in 45% HF for 120 h.*

Moreover, with the etching time increasing, indications of etching V_2AlC to form V_2CT_x was also found in SEM (See Figure 4.11). The magnified view of the cross section reveals the typical MXene morphology with clearly visible open layering. This exfoliation phenomenon is similar to that of graphite, where the layers are obviously

split from each other compared to the untreated sample, forming paper-like stacking of layers.

Figure 4.12(a) showed the distribution of V_2CT_x MXene grain sizes after sonication, from few micrometers to hundreds of micrometers. Comparing to small delaminated V_2CT_x particles [134], and even most well-studied case $Ti_3C_2T_x$ with grain sizes of tens of micrometers, Figure 4.12(b) demonstrates that the crystals with grain size larger than 100 µm could be successfully exfoliated by HF acid. From the magnified image (Figure 4.12(c)) of the area marked in the Figure 4.12(b), we can clearly see the delaminated accordion-like delaminated morphology. EDS spectra was acquired under low magnification, on the sample of Figure 4.12(b). The results indicate that Al is almost completely removed from the etched samples (See Figure 4.12(d)). No fluorine was detected in the sample, which is a probable indication that -OH groups functionalize most of the V_2CT_x surface.

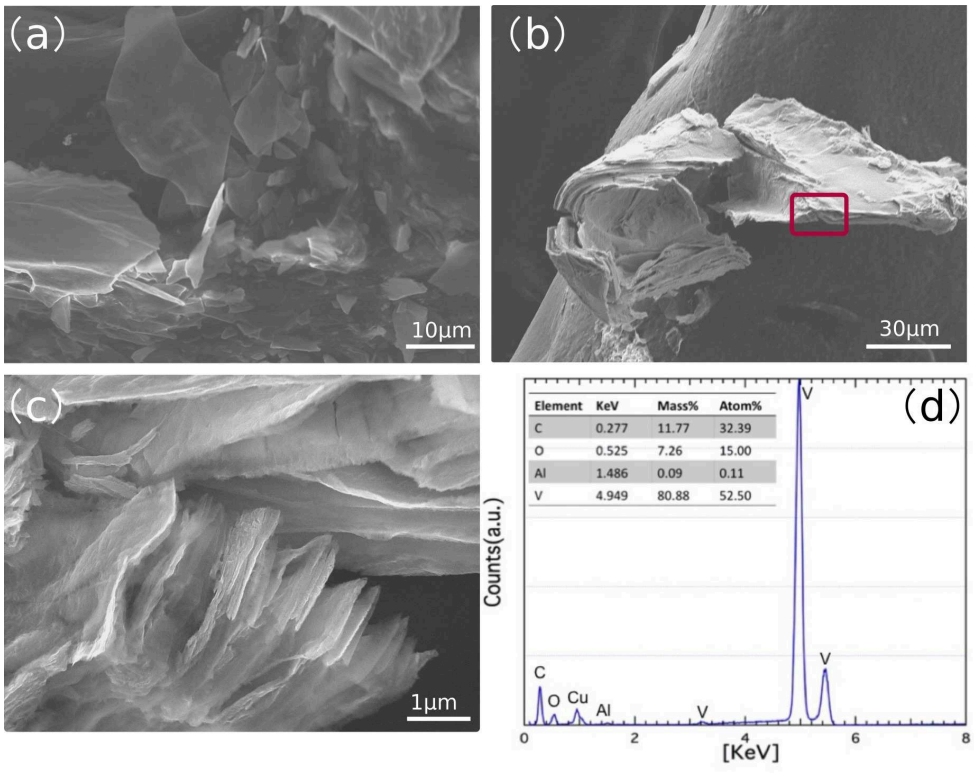

Figure 4.12: *SEM images indicating (a) V_2CT_xMXenes with various sizes and (b) 100 µm large particles, (c) Enlarge part of areas marked in (b) and (d) EDS spectrum of (b).*

Note that at early stage trials of the etching experiments, the etched samples terminated by a mixture of functional groups -F and -OH were found, as shown in the Figure

4.13. We then improved cleaning, drying and collection of the as-etched sample and it became rare to detect -F in EDS spectrum.

More and more evidences show that hydroxide groups directly bond to the MXene, with a layer of water hydrogen-bonded to the hydroxide surface while fluoride moieties bonded to the MXene surface. This is confirmed by direct measurement of surface termination groups of V_2CT_x MXenes using NMR spectroscopy [136].

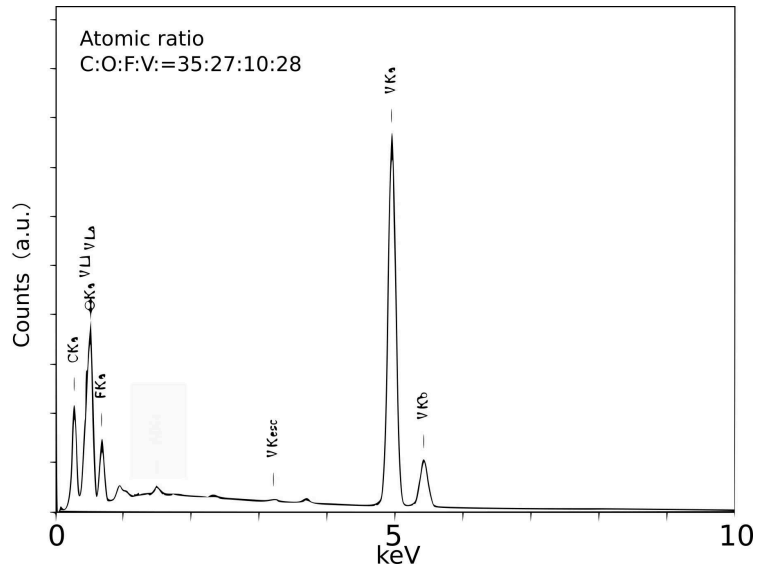

Figure 4.13: *EDS spectrum of as-etched sample in the early stage of our experiments.*

Although no work have addressed the case of V_2CT_x, early theoretical models predicted $Ti_3C_2T_x$ configurations, in which surface termination groups were energetically favoured to be located either above the hollow sites between three neighbouring C atoms or above the C atoms on both sides of the Ti_3C_2 plane or a combination of the aforementioned [74, 137] (as show in Figure 4.14).

However, recent computational studies revealed more complexity in the locations and orientations of surface groups depending on the species and elemental compositions. Xie et al. [138] suggested that =O and/or –OH terminated MXenes were the most stable, because -F terminations were readily replaced by -OH groups, which could occur when they were washed and/or stored in H_2O. During the high temperature treatments and/or metal adsorption processes, -OH was converted to =O terminations.

The structural, elemental and chemical properties of single and double sheets of $Ti_3C_2T_x$ by aberration-corrected atomic-resolution scanning transmission electron microscopy (STEM)-electron energy loss spectroscopy (EELS), and confirmed that the inherited close-packed structure of $Ti_3C_2T_x$ is observed as atomic positions of two $Ti_3C_2T_x$ sheets remained laterally aligned and coverage of O-based surface groups,

native point defects such as Ti vacancies and oxidized titanium adatoms (TiO_x) are also observed [139]. By analogy, we can infer that the absence of -F group in our end product is not surprising.

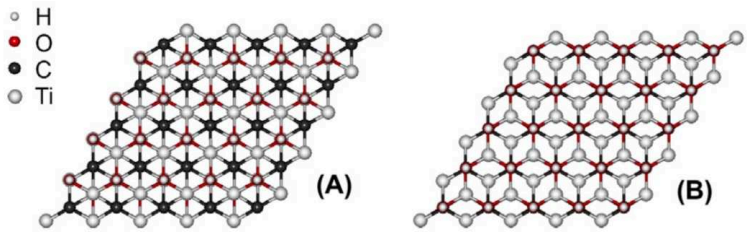

Figure 4.14: *The considered types of -OH terminated $Ti_3C_2T_x$ MXenes (a) -OH groups are placed at the hollow site between three neighbouring carbon atoms, (b) -OH groups are placed at the top site of the carbon atom.*

4.3.3 TEM

As collected V_2CT_x (VC-p) were dispersed in the DI water and isopropanol (IPA), respectively. Digital photos of V_2CT_x nano sheets dispersed in water and IPA with typical Tyndall effect indicates their excellent hydrophilicity and dispersity (See Figure 4.15). Furthermore, a drop of the colloidal solution of V_2CT_x MXenes were placed on a lacey carbon coated TEM copper grid and allowed to dry in the vacuum at 40 °C overnight, ready for the TEM observation.

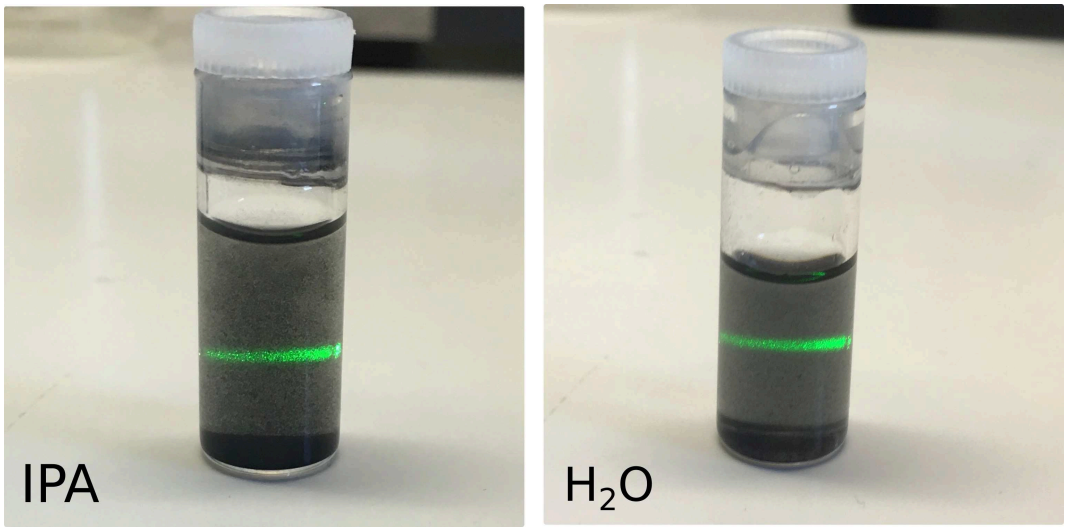

Figure 4.15: *Optical photos of dispersed colloidal solution of V_2CT_x MXenes.*

Figure 4.16 shows TEM micrographs of DI water dispersed V_2CT_x nanosheets. Electron transparent sheets of different lateral sizes, from hundreds of nanometres

up to few micrometers were imaged (See Figure 4.16). We found that the flakes size distribution can be controlled more precisely by adjusting sonication times and powers. Similar to the graphene and other MXene flakes[64, 140], typical flake morphology was observed in the Figure 4.16(b), where their transparency suggests that the sheets are a few layers thick. Selected-area electron diffraction (SAED) (inset in Figure 4.16(b)) of these V_2CT_x flakes viewed normal to the basal (002) plane confirms their single-crystal nature, and the fact that the hexagonal symmetry of the parent MAX phase after exfoliation is retained.

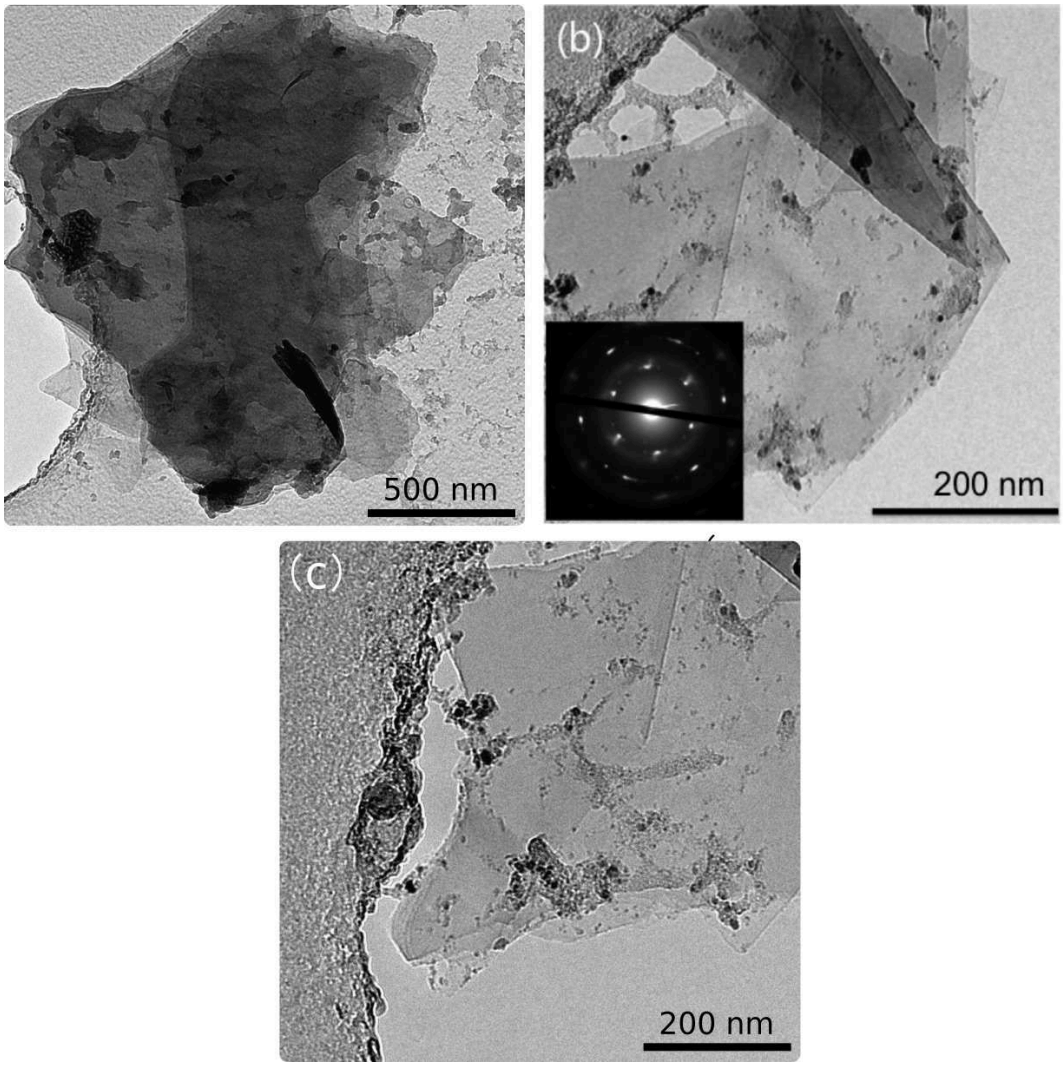

Figure 4.16: *TEM images and SAED pattern of V_2CT_x nanosheets (DI water dispersed colloidal solution).*

Figure 4.17 shows the TEM and corresponding EDS of IPA dispersed V_2CT_x nanosheets. In comparison with DI water dispersed sample exhibiting well-defined and clean edges, the IPA dispersed ones have uneven edges and easily roll up. The $a - LP$ of this flake from SAED, inheriting the hexagonal basal plane symmetry of the parent V_2AlC phase, is measured to be ~2.9 Å, which is similar to that of the V_2AlC precursor [141]: as

found for all other MXenes synthesized to date, removing Al did not alter the in-plane structure. In addition, no Al element signal was detected with EDS spectrum (See Figure 4.17(c)).

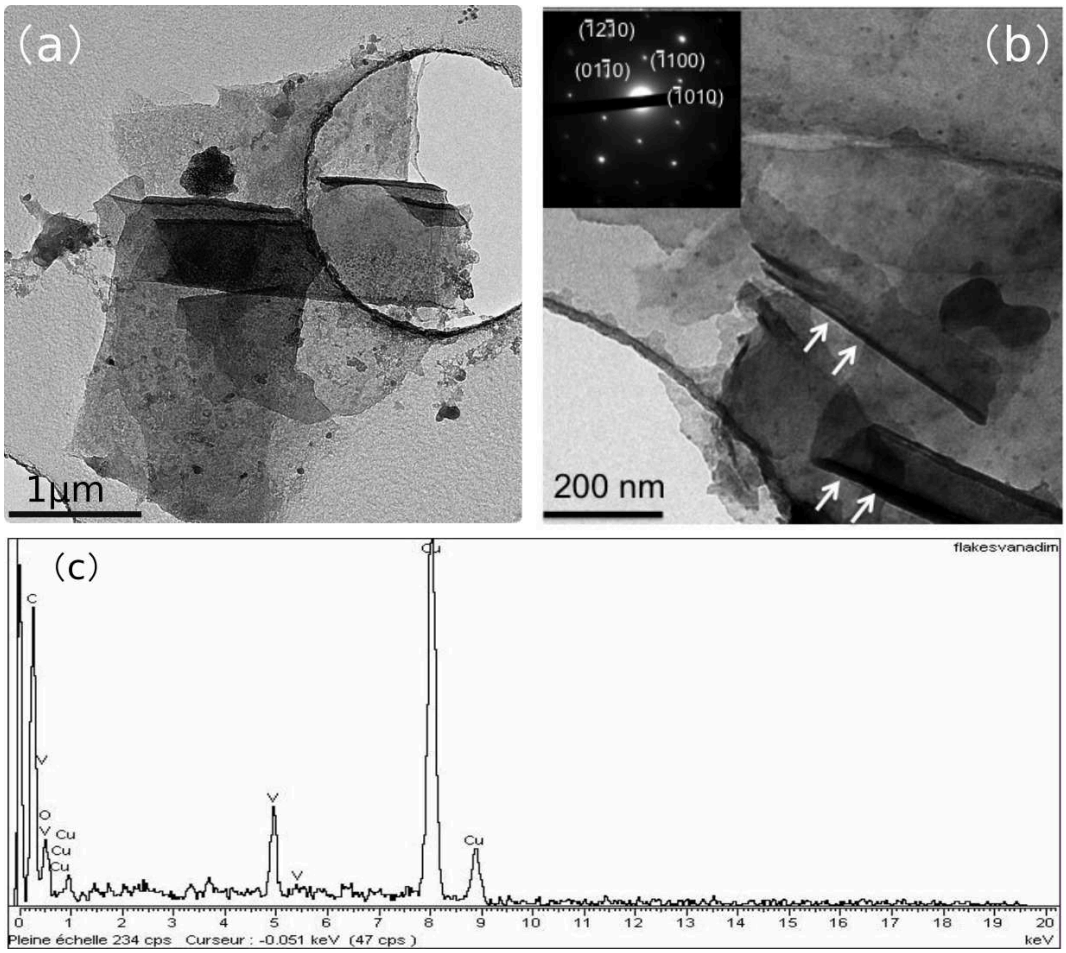

Figure 4.17: *TEM images and SAED patterns (a,b) and EDS spectrum (c) of V_2CT_x nanosheets (IPA dispersed colloidal solution).*

Although only weak residual forces hold and prevent HF etched multi-layered MXenes from separation into individual layers, a sonication procedure without former intercalation of species between the layers can only result in low yield production of single/few layered MXenes nanosheets and scrolls. Figure 4.18 shows the morphology of the electron transparent monolayer V_2CT_x flake.

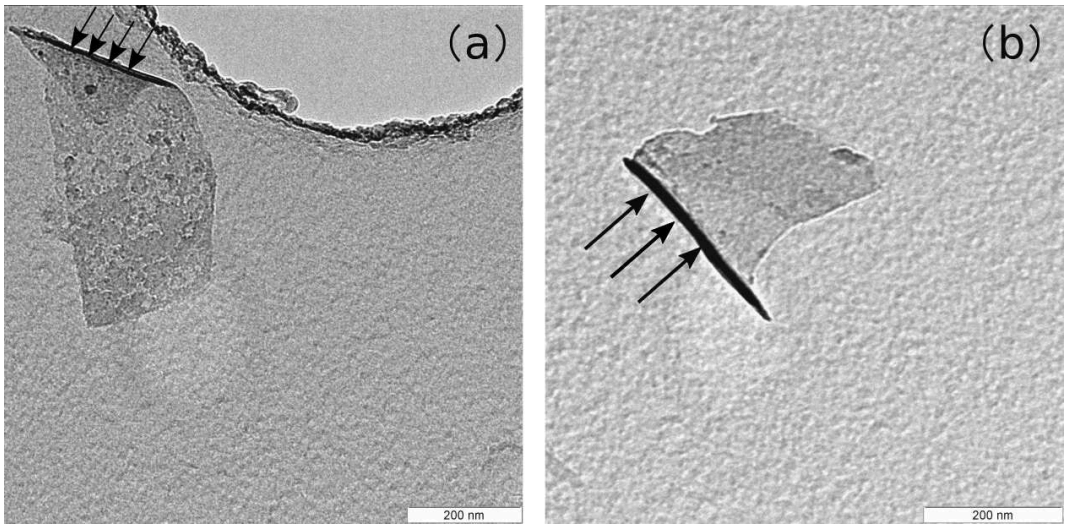

Figure 4.18: *TEM images of individual monolayer V_2CT_x flake.*

4.3.4 Raman spectrum

The Raman spectra of the untreated V_2AlC and HF-treated V_2CT_x are shown in Figure 4.19(a) and the corresponding optical images in Figure 4.19(b). In comparison to clean flat crystal surface before etching, highly defective surfaces were obtained, especially etching holes tend to appear at those places where there are more growth defects. The Raman spectrum of original V_2AlC has consistent peak position as previously reported. The observed vibration modes of certain symmetry groups of V_2AlC, $E_{2g}(\omega_1), E_{2g}(\omega_2), E_{1g}(\omega_3), A_{1g}(\omega_4)$ are labelled after fitting the spectra with Gaussian fitting. Furthermore, peak at 257.1 cm^{-1} is assigned to E_{1g} group vibration which corresponds to in-plane (shear) modes of V atoms. This peak should be observed in the V_2CT_x spectrum after etching V_2AlC.

We observed a reduced peak intensity and broadened shape, which is probably due to the increased interlayer spacing of the MXene structure. This change in the Raman spectra can be analogous to the relatively low G band intensity in monolayer graphene. The peak at 358.6 cm^{-1} is assigned to A_{1g} group vibration, which reflects the out-of-plane vibrations of V atoms. Therefore, if the Al interlayer is removed, the corresponding peak in MXene is expected to red-shift, broaden and change the peak shape, in analogy with the 2D-band of graphene. The E_{2g} modes ω_1 (155.7 cm^{-1}) and ω_2 (239.5 cm^{-1}) are in-plane vibration of V and Al atoms. After etching, the Al atoms are supposed to be replaced with lighter atoms (such as F, O or H), hence these peaks involving V-Al coupled vibration are more affected compared to those of E_{1g}, the intensities of which reduced dramatically. Also the broadening of these peaks in the Raman spectrum could be the result of the higher disorder degree of the structure due to the introduction of

various surface termination. All these features present in the Raman spectrum of V_2CT_x corroborate removal of Al layer.

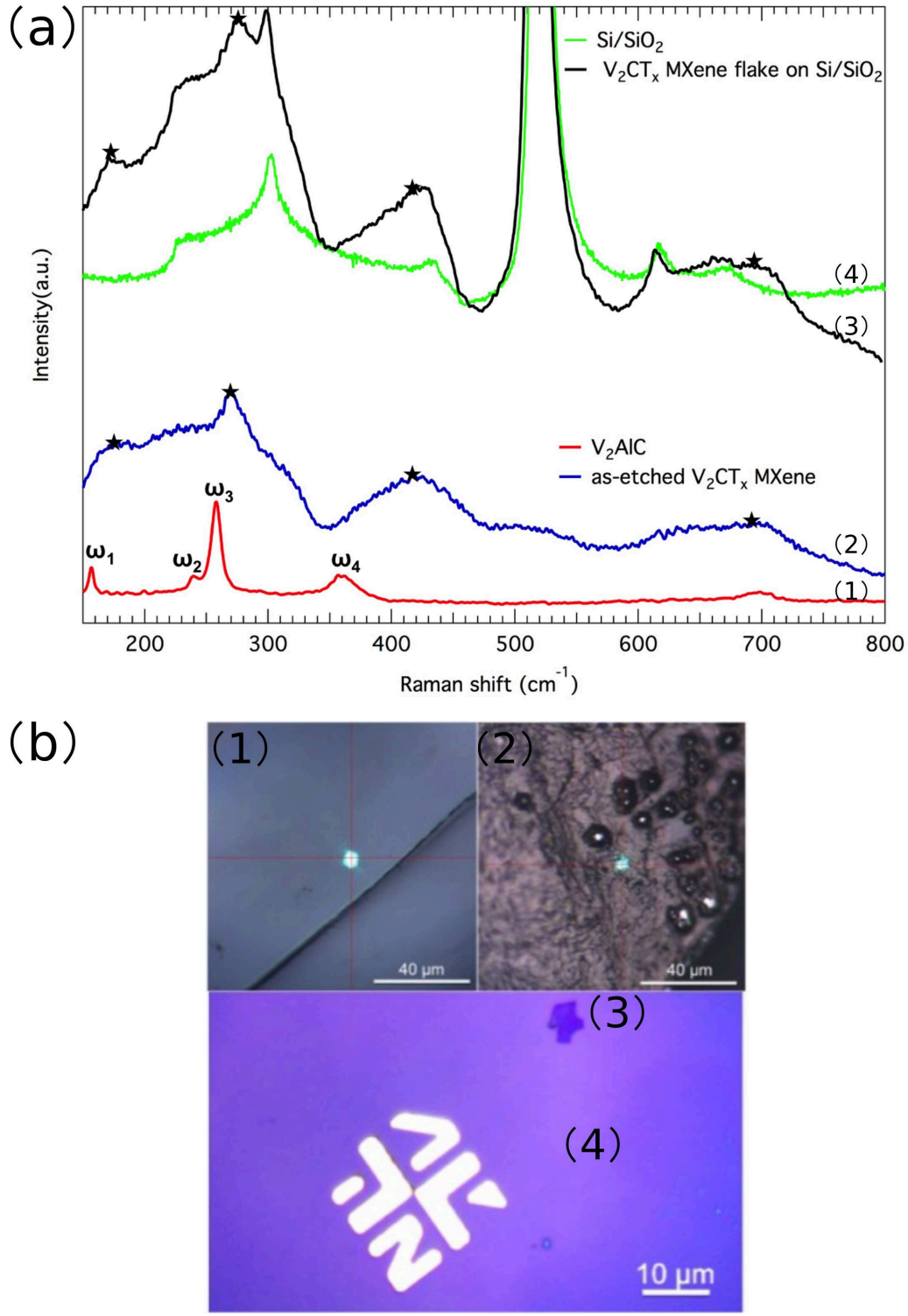

Figure 4.19: *Raman spectra (a) and corresponding optical images (b) of the V_2AlC, as-etched V_2CT_x and as-exfoliated flake on the Si/SiO_2 substrate.*

The Raman spectrum of V_2CT_x flake transferred on the Si/SiO_2 substrate exhibits the same peaks at the same positions as those observed on the "bulk MXene" materials, in addition to peaks characteristic of phonon modes of the substrate.Yet, it is intriguing to find that, when the layer thickness is down to below 10 nm, the signal of Raman spectrum could not be detected on the thin layers.

4.3.5 AFM

The thickness and shapes of the flakes produced by mechanical exfoliation and transferred on Si/SiO_2 were investigated by atomic force microscopy (AFM), as can be seen Figure 4.20. The AFM height profiles measured along the color lines showed that V_2CT_x flakes have the similar heights of $\approx$ 10-20 nm and are identified as multilayers. The lateral sizes of flakes is several µm. It is worth mentioning that the measured AFM height of the flake relative to the Si/SiO_2 substrate is overestimating the actual height due to the presence of surface adsorbates, such as water molecules, that are trapped under the V_2CT_x flake; similar observations have been previously reported for other 2D materials as well [142, 143].

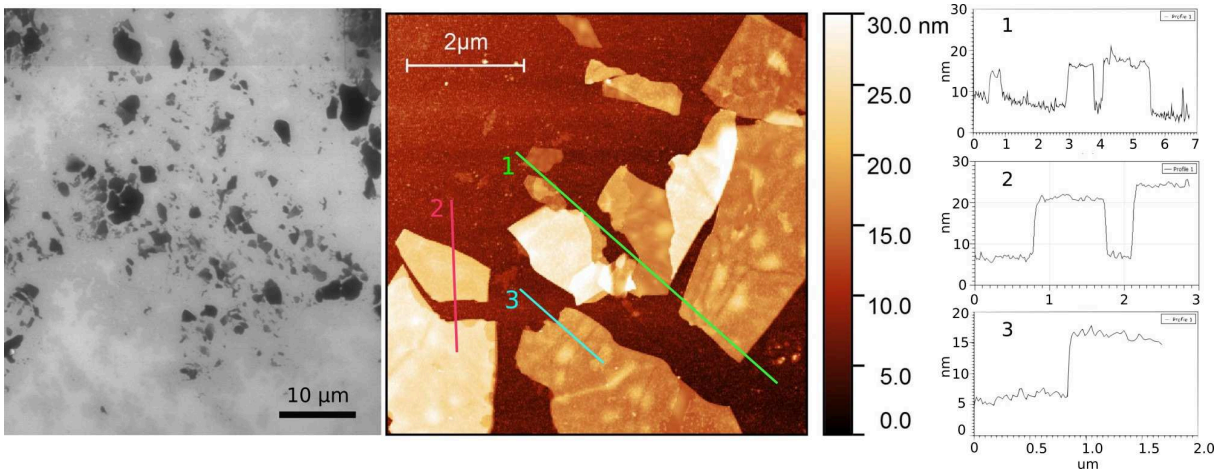

Figure 4.20: *SEM and AFM images with corresponding cross section profile indicating sizes and thickness distributions of isolated V_2CT_x flake on the Si/SiO_2 substrate.*

Moreover, the as-etched V_2CT_x MXene treated with intercalant DMSO were also applied as starting materials to obtain mechanically exfoliated V_2CT_x MXene flakes, with the aim to take advantage of weaker interlayer bonds after intercalation. Figure 4.21 showed the flake size and thickness. The comparison of AFM images in Figure 4.20 and Figure 4.21 shows that the thickness of V_2CT_x flakes produced from two different precursor materials are not significantly different, which means the intercalation is not as we expected, which is consistent with the results obtained by other materials

characterization methods, such as XRD. However, it is also noticeable that the flake produced from the sample obtained after DMSO treatment is rougher along the edge and surface, which might be due to the stirring and sonication time.

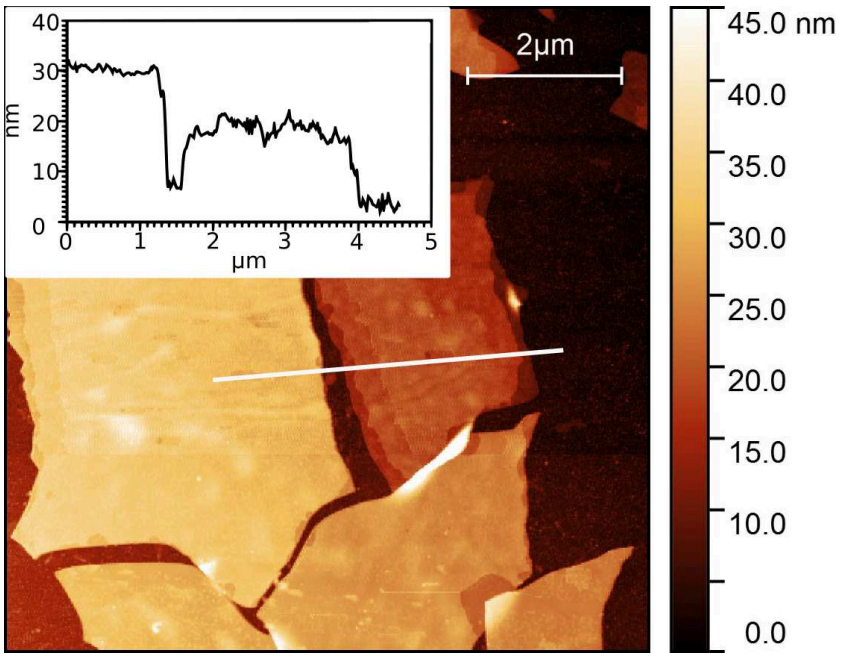

Figure 4.21: *AFM images indicating sizes and thickness distributions of isolated V_2CT_x flake on the Si/SiO_2 substrate starting from the as-etched V_2CT_x MXene treated with intercalant DMSO.*

AFM can also be used to examine the tape residues on the flakes. In our experiments, several tapes have been utilized. It turns out the “ultra clean” medium tack tape, traditionally used for graphene exfoliation, is the most residue-free one. Tape residues in fact increased significantly if we changed to thermal release tape or other high tack tape. Even using the "ultra clean" tape, from Figure 4.22, on can clearly observe tape residues, which might affect the device fabrication and measurement afterwards.

After examining the thickness of the transferred flakes by AFM, we found flakes with thickness in the range 5-7 nm with average size smaller than 5 μm which is not large enough for four-contact device fabrication.(See Figure 4.23(a)), Here we use the flake who has the thickness around 20 nm or thicker with average size larger than 10 μm to proceed with contact fabrication (See Figure 4.23(b)).

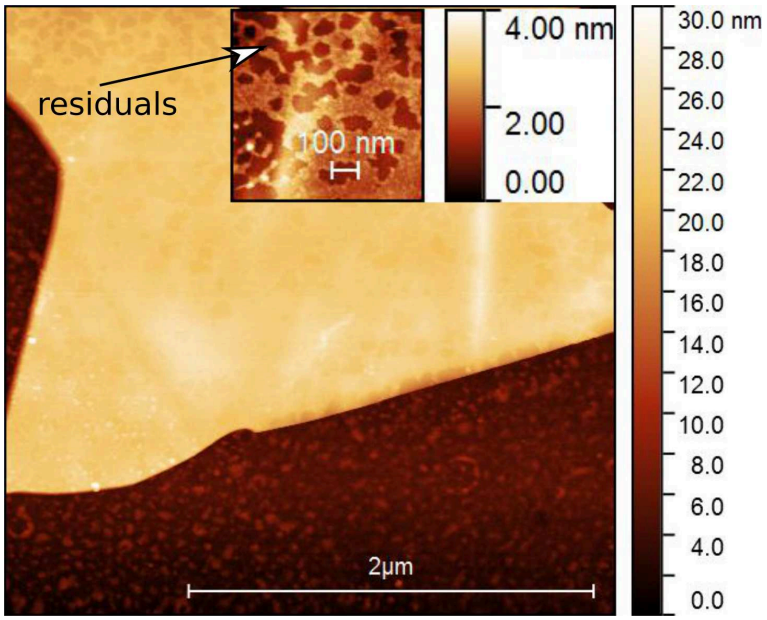

Figure 4.22: *AFM images of the flake indicating tape residue.*

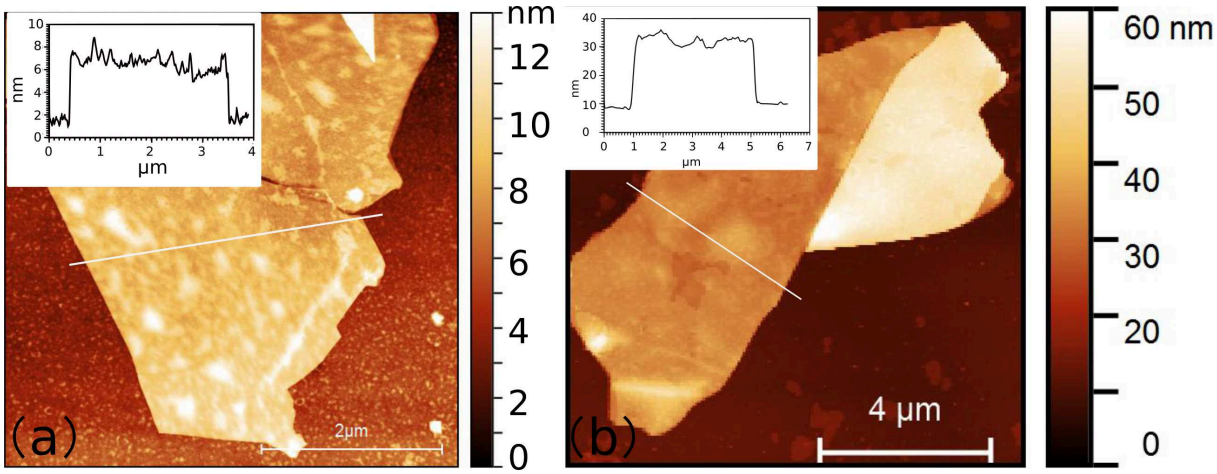

Figure 4.23: *AFM images of two typical flakes: (a) 5-7 nm thick, smaller than 5 µm (b) 15-20 nm thick, larger than 10 µm.*

4.4 Ti_2CT_x MXene

As discussed in the Charpter I, the bonds between $M_{n+1}X_n$and A are weaker than those of M-X, and are thus chemically more reactive. Therefore, selectively etching only the A layers from the MAX phase is possible. An effective way to extract A layer without destroying the layered morphology is the chemical etching. Alternative method as direct mechanical exfoliation has never been proved to be successful in delamination of 2D MXene layer. It is well known that the mechanical exfoliation is closely related to the mechanical properties of materials including elastic constants C_{ij}, bulk mechanical moduli (K, G, and E).

From the calculated elastic coefficients and mechanical properties of the MAX phase compounds (See Table 4.1), we can find that the elastic constants of MAX phases with large atomic radius A elements smaller than that with those of small atomic radius element. Here, if we compare C_{33} of Ti_2SnC to that of Ti_3AlC_2, it clearly indicates lower C_{33} which should ease the mechanical deformation along c-axis. By checking the atomic radius of Al (143 pm) and Sn (158 pm) [144], the bond energy of Ti-Sn is weaker than that of Ti-Al. In this case, HF-etching combined with mechanical exfoliation were also applied on the as-grown Ti_2SnC aiming at synthesizing Ti_2CT_x MXenes.

Crystals	C_{11}	C_{33}	C_{44}	C_{66}	C_{12}	C_{13}	K	G	E	η	G/K
Ti_3AlC_2	358.1	292.6	122.0	136.0	83.9	74.8	163.1	127.3	303.1	0.190	0.78
Ti_3SiC_2	370.0	349.4	150.6	135.4	99.2	110.6	192.2	138.1	334.3	0.210	0.72
Ti_3GeC_2	356.8	324.7	128.1	127.1	99.6	97.0	180.4	126.2	307.1	0.216	0.70
Ti_2AlC	300.5	266.4	106.4	115.8	68.9	61.7	138.8	110.6	262.2	0.185	0.80
Ti_2GaC	303.2	254.6	99.1	116.8	72.1	62.6	138.9	106.9	255.2	0.194	0.77
Ti_2InC	290.5	236.3	86.4	112.3	70.7	58.0	131.5	98.3	236.1	0.201	0.75
Ti_2SiC	311.4	324.2	146.1	112.5	85.8	111.5	173.6	122.0	296.6	0.215	0.70
Ti_2GeC	286.3	288.9	119.8	99.7	84.1	99.9	158.7	105.8	259.6	0.227	0.67
Ti_2SnC	252.8	254.4	92.9	79.2	91.4	74.1	137.6	87.5	216.5	0.238	0.64
Ti_2PC	269.2	344.3	173.8	66.1	132.3	151.3	191.5	102.7	261.3	0.273	0.54
Ti_2AsC	224.0	293.9	140.6	33.9	156.9	123.9	166.7	71.7	188.2	0.312	0.43
Ti_2SC	339.3	359.9	161.2	116.8	101.4	110.1	186.7	134.1	324.6	0.210	0.72
Ti_2AlN	316.0	290.7	128.6	123.1	72.0	94.8	160.6	119.6	287.4	0.202	0.74
V_2AlC	330.1	316.9	147.9	127.9	73.0	104.3	171.1	130.0	311.1	0.197	0.76
Nb_2AlC	314.7	295.4	138.6	112.3	88.8	117.3	174.6	116.3	285.6	0.227	0.67
Cr_2AlC	364.5	356.1	139.8	140.0	84.4	107.4	187.0	136.1	328.6	0.207	0.73
Ta_2AlC	348.5	337.8	154.7	115.4	118.9	132.7	200.3	126.5	313.5	0.239	0.63
α-Ta_3AlC_2	441.2	381.7	174.8	154.7	132.1	138.0	230.8	157.0	383.9	0.223	0.68
α-Ta_4AlC_3	445.0	378.2	178.7	141.3	162.6	150.8	243.2	151.7	376.8	0.242	0.62
Ta_5AlC_4	466.5	410.4	187.6	158.6	147.6	164.4	254.9	163.0	403.1	0.236	0.64

Table 4.1: *Calculated elastic coefficients and mechanical properties of the 20 MAX phase compounds (Unit:GPa)[145].*

4.4.1 Ti_2SnC etching

The average size of as-grown Ti_2SnC crystal is around 10-100 μm, exhibiting hexagonal morphology (as shown in Figure 4.24). Ti_2CT_x MXene was synthesized by immersing Ti_2SnC in 45% concentrated HF solution for 72 h at room temperature. The low yield of crystal limited the raw materials that we can use in the experiment, hence the amount of particles is not enough to form a suspension as that of V_2CT_x after rinsing with DI water.

Another method used, henceforth referred to as drop casting, consisted of filling a pipette with Ti_2CT_x MXene solution and dispensing a drop on a glass slide or Si/SiO_2 substrate that had been cleaned in ethanol. The substrate would then be left to dry in air. This was intended as a quick and easy method that might result in dispersion of colloidal MXene particles. The goal was the evidence of a potential route for non-Al containing MAX phase etching.

Theoretically, when the water in the drop dried, a thin layer of flakes might be left behind. To help with flake adhesion, positively charged hydrophilic glass slides were used, since MXene flakes are negatively charged and the aqueous solution spreading itself along the slide surface was desirable. Finally analysis consisted of optical microscopy, Raman spectroscopy, and ToF-SIMS spectrometry were performed.

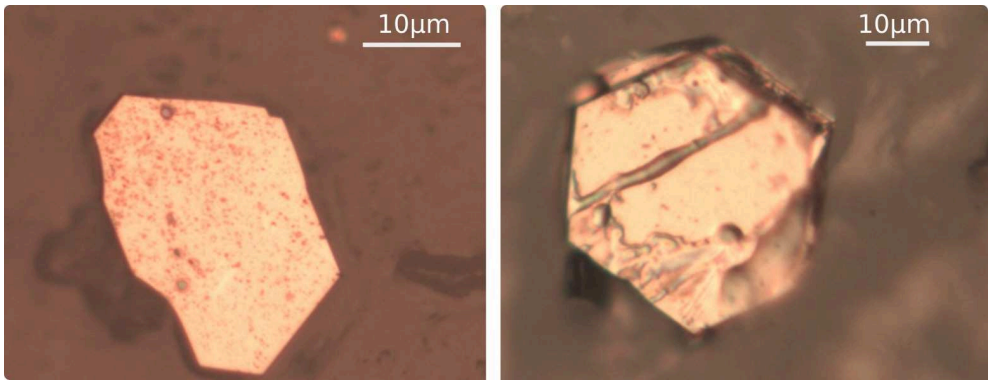

Figure 4.24: *Optical micrographs of Ti_2SnC.*

4.4.2 Optical microscopy of HF-etching Ti_2SnC

Unlike dry method, drop casting resulted in extremely uneven coverage of the drop area with MXenes particles as well as a very large amount of solution residues on the Si/SiO_2 substrate as can be seen in Figure 4.25(a,b). A single droplet of MXenes solution was placed on top of the glass substrate and allowed to dry, as shown in Figure 4.25(c,d).

4.4.3 Raman spectroscopy of HF-etching Ti_2SnC

Figure 4.26 is the Raman spectrum of Ti_2SnC before and after HF-etching. The peaks at 243.2 cm^{-1} and 365.1 cm^{-1} in the Ti_2SnC spectrum can be assigned to E_{2g} and A_{1g} modes, where E_{2g} involves the in-plane vibration of Ti-Sn atoms while A_{1g} involves out of plane vibration of Ti. After etching with HF acid, the E_{2g} peaks vanished by removing the Al. Meanwhile, two peaks appears centred at 403.3 cm^{-1} and 650.4 cm^{-1}, close to the Raman peaks found for Ti_2CT_x MXene in the literature, representing the vibration modes which can be assigned to nonstoichiometric titanium carbide[146, 147].

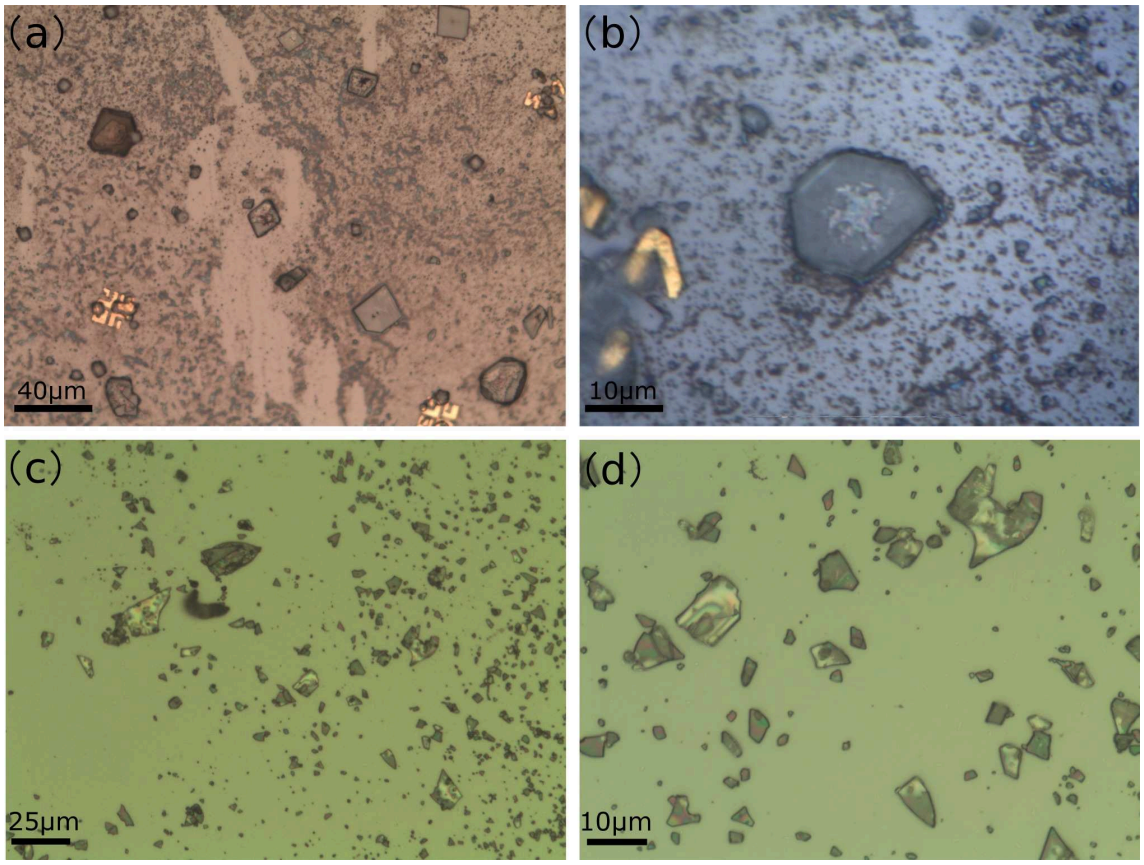

Figure 4.25: *Drop coat with MXene solution on (a,b) Si/SiO_2 substrate and (c,d) Glass substrate.*

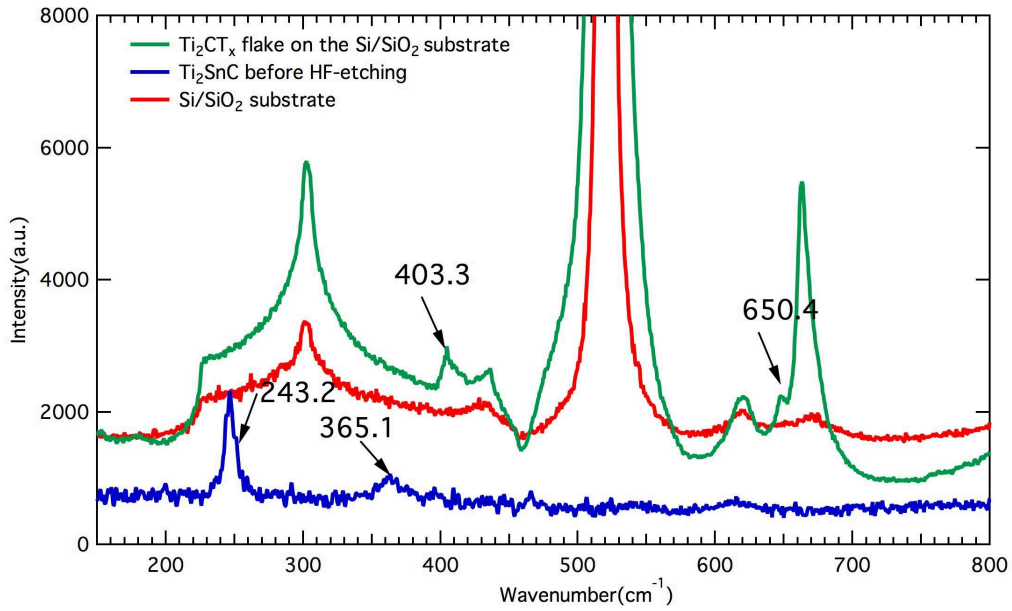

Figure 4.26: *Raman spectra of Ti_2SnC before and after HF-etching (on the Si/SiO_2 substrate).*

By changing the substrate from Si/SiO_2 to the glass and consequently avoid the peaks from silicon substrate, we can further clearly see the Ti_2CT_x peaks appeared on

the different substrate as well.

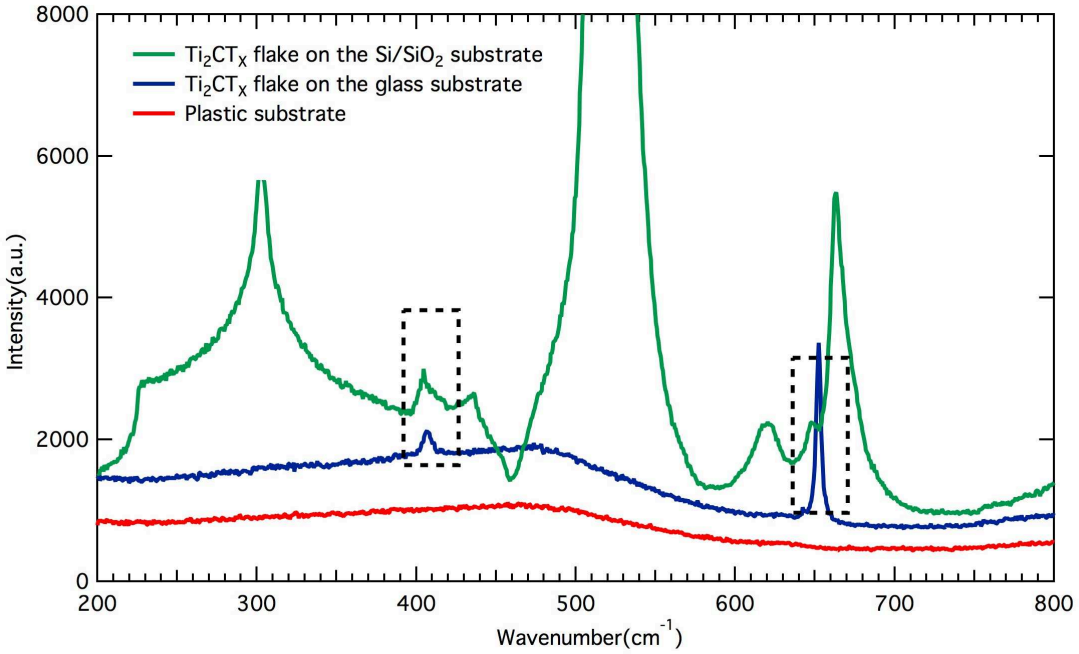

Figure 4.27: *Raman spectrum of Ti_2CT_x MXene on different substrates.*

Therefore, one can say that the Ti_2SnC can be etched by HF acid and some Ti_2CT_x MXenes flakes are present, as shown by a Raman spectrum. Despite this, based on the relatively low number of visible MXenes and abundant amount of residues, it appears that drop casting is not a particularly effective method for device-quality MXene.

4.5 Conclusion

In summary, large scale V_2CT_x MXene flakes was obtained by conventional HF-etching of V_2AlC single crystals. Mechanical delamination of multilayered V_2CT_x flakes into few layer flake and transfer on Si/SiO_2 substrate was also achieved. Structural characterization demonstrated an enlarged interplane distance, while prior DMSO intercalation seems to have no effect on this type of MXenes. Typical 2D material morphology was derived in SEM and TEM images. From EDS results, we concluded that -OH terminations on V_2CT_x is dominating, and the most energetically favourable, compared to -F and -O functional groups. Isolated V_2CT_x flake on the Si/SiO_2 substrate are suitable for the fabrication of electrical device and measurements, which will be discussed in next Chapter.

chapter 5

Electron transport in MXenes devices

In this chapter, protocols employed for fabrication of V_2CT_x MXene device suitable for electrical transport measurements will be firstly introduced. Then, methods to measure the carrier transport properties of 2D V_2CT_x MXene are discussed. Measurements have been performed from room to low temperature. First-hand electron transport data were obtained for this new 2D material and we discuss the salient features emerging from these data.

5.1 Fabrication of V_2CT_x MXene device

5.1.1 Electrical contacts

Figure 5.1 shows AFM profile and the corresponding Raman spectrum of a representative V_2CT_x MXene flake on a Si/SiO_2 substrate before processing MXene device.

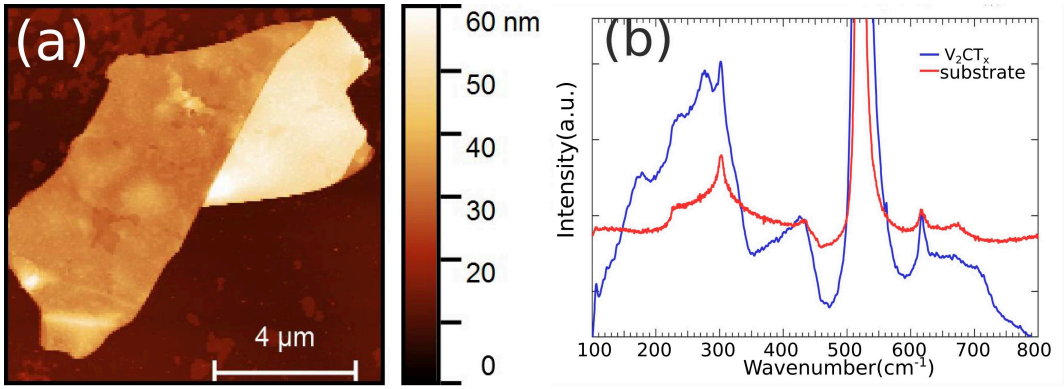

Figure 5.1: *AFM image (a) and its corresponding Raman spectrum (b) of V_2CT_x MXenes.*

Here, electron beam lithography (EBL) was performed using a SEM (FEI/Philips XL30 FEG) equipped with a Raith laser interferometer controlled stage and the Elphy Plus software (remote control for Ebeam writing). This equipment is capable of writing patterns with a resolution down to 10 nm.

A metallic mark close to the flake was firstly located by SEM imaging in TLD mode (~10 KeV, magnification of $\times$2000, spot 3). SEM imaging corrections including wobble, astigmatism and focus, were performed as the alignment and focus are closely related to the precision of beam writing. It is worth mentioning that a calibration is necessary to know the relative position of the electron beam with respect to the mark coordinate system in Elphy Plus. Based on the SEM image of the target flake, one can easily draw the flake shape in the Elphy Plus layout editor according to the values of the cartesian coordinates. Once the drawing of flake was done in the Elphy Plus file, the electrical contacts were designed by using Layout Editor.

Once the pattern file is ready, the process of electrical contact fabrication is conducted in sequence. Figure 5.2 shows the schematic diagram of the steps for electrical contact fabrication.

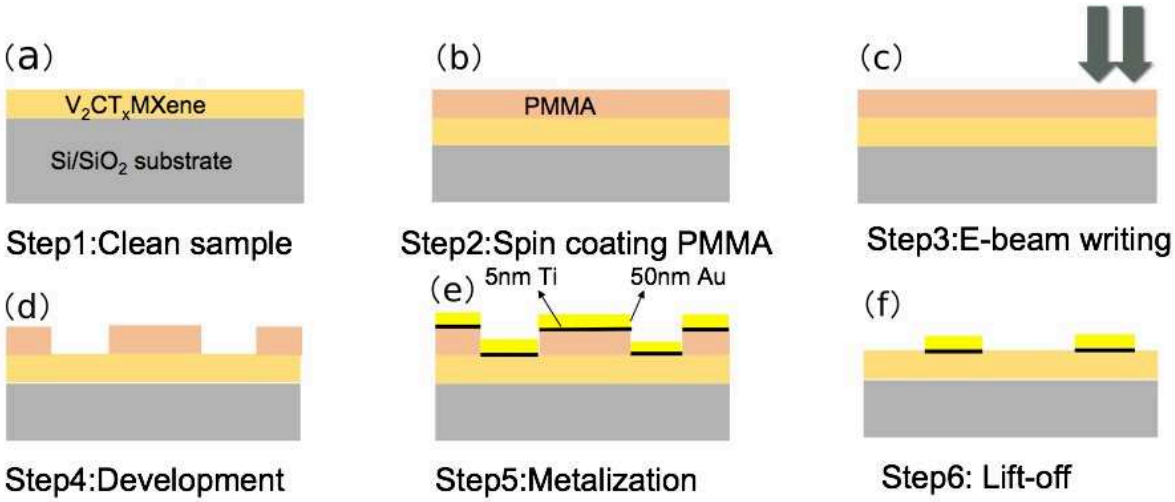

Figure 5.2: *Schematic diagram of the steps for electrical contact fabrication: (a) Side view of the sample (b) Spin-coating of PMMA layer on the sample (c) EBL writing the electrical contact pattern on PMMA layer (d) Development for removing the non-exposed PMMA areas (e) deposition of the Ti/Au layer (f) Lift-off to remove the rest of PMMA layer.*

500 nm-thick PMMA layer (initially diluted at 7% or 9 % in anisole), a positive electron-sensitive resist, was spin-coated on the sample (6000 rpm, 1 min) and annealed at 150 °C for 1 h in the furnace. Then, two EBLs were applied to pattern the electrical contact on the PMMA layers using the Elphy Plus software. The first one was designed to pattern the central part of the contact layout with high resolution configuration within a 43 $\times$43 μm^2 area. (E_{beam}~30 keV, spot 1, magnification $\times$2000, dose ~ 250 $\mu C/cm^2$); The second one aimed for the pattering of the contact pads themselves (200 x 200 μm^2) as well as the path to these contacts. Due to larger working area and lower requirements for the resolutions, a smaller magnification and higher beam current were chosen to optimize the expose time (E_{beam}~30keV, spot 5, magnification $\times$400, dose ~300 $\mu C/cm^2$).

Following this, the sample was developed in a MIBK/IPA (1:3) solution for 90 seconds and then rinsed in the IPA for 30 seconds. After development, the sample was put in the high vacuum chamber (~2 $\times 10^{-7}$mbar) of an E-gun vacotec metal evaporation system. Then a first metal deposition of a 5 nm thick Ti layer as adhesion layer followed by a second metallization of a Au layer was performed. The deposition rate for both layers is ~ 1 Å/s.

The last step (lift-off) process consists in immersing the sample in an acetone solution. The device is ready after rinsing in IPA and drying with nitrogen gun.

5.1.2 Thermal annealing under an inert gas flow

Prior to the bonding, the sample to be annealed was placed in the chamber of a Rapid Thermal Annealing (RTA) system (ULVAC Mila-5000) in the Winfab cleanroom.

First, the annealing chamber was purged during 10 min under inert atmosphere (a Ar/H_2 flow in our experiment). Then the sample was heated using a near-infrared lamp from room temperature to 500 °C for 1 hour and maintained at 500 °C for 4 hours, always under Ar/H_2 flow. Afterwards, the sample was cooled down back to room temperature.

Due to the lack of the reference on the contact fabrication on MXene sample, no standard protocol was available for this process. The effect of the annealing on the contact performance was still unclear. The condition applied in the sample of $Ti_3C_2T_x$ MXenes were varied from 140 °C to 300 °C for 15 min to 30 min [77, 148].

5.1.3 The bonding

The last fabrication step is to contact the metallic leads of the device to the pins of the sample holder (Dual-in-line non-magnetic holder, 2 x 7 metallic pins) which is adapted for electrical (magneto) transport measurements in the cryostat.

First, all the pins of the chip were short circuited using a gold wire (diameter = 0.025 mm and purity of 99.99% from GoodFellow) bonded using silver epoxy (Epoxy Technology). The chip was then annealed at 140 °C for 1 h to dry the silver epoxy to become electrically conductive. This procedure, along with with the a grounded wrist band are useful to avoid the electric discharge through the device during the bonding step. In fact, according to our previous experience on mesoscopic device of graphene device, such discharge could strongly damage the device. Though seemingly the MXene device was more robust, same procedure was retained.

Then, the backgate of the sample was glued on the chip using silver paint (Agar Scientific) and contacted to one of the sample holder pins using the same gold wire and silver epoxy. After all the metallic leads were contacted to the pins, the sample was again annealed under the same conditions as for the previous step. Afterwards, the chip was plugged on the measurement setup and grounded. Finally, the wires short circuiting the pins on the chip were carefully cut using tweezer.

Figure 5.3 shows a micrograph of as-contacted device at the end of this process. Note

that different contact geometries have been tested, depending on the flake geometry and size. In order to obtain the resistivity of the MXene device, the dimensions of the device, length l, and width w, were measured as indicated in Figure 5.3.

Figure 5.3: *Optical images of electrically contacted V_2CT_x MXene device.*

Device No.	thickness, t(nm)	width, w(μm)	length, l(μm)
I	20	8.7	2.5
II	38	3.7	2.5
III	22	2.8	2

Table 5.1: *Dimensions of V_2CT_x MXene devices.*

It is worth mentioning that some very thin flakes were also electrically contacted as shown in Figure 5.4. It is, however, due to the size of the flake that can not define four contacts. In the present thesis, only devices with four contacts successfully deposited on the flakes will be discussed. In table 5.1 we list the size and characteristics of the flakes that were used to produce devices, as described below.

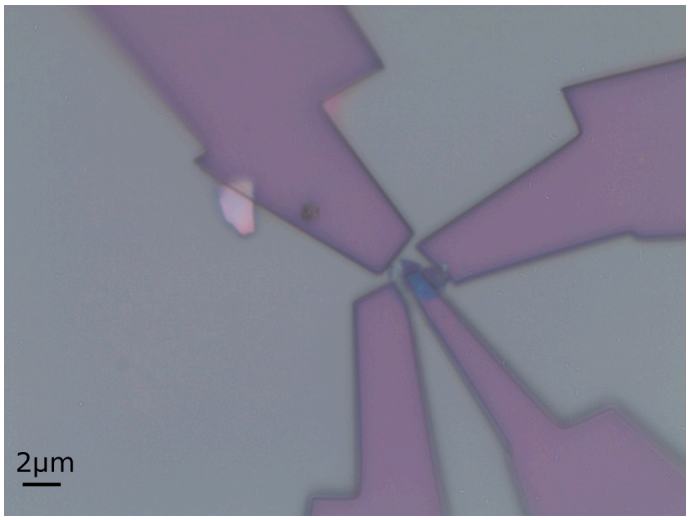

Figure 5.4: *Two contacts on the V_2CT_x MXenes flakes.*

5.2 Electronic properties measurement of V_2CT_x MXene device

5.2.1 Theoretical calculations on electronic transport of MXenes

Though there have been a large number of theoretical calculations on the electron transport properties of MXenes, very few experimental studies addressed the topic with only two reports on contacted few-layer MXene([67, 78]).

Coherent transport calculations were performed by other researchers via a non equilibrium Green's function (NEGF) technique which have already been applied to low-dimensional system for the electron transport. The simulation results predict that the pristine MXenes are highly conductive[149]. In the first paper on $Ti_3C_2T_x$, a small band gap of 0.05 eV with -OH termination and 0.01 eV with -F termination were predicted. Since then, dependence of the electronic band structure on chemical termination groups have been widely studied [150, 151, 79, 66, 152, 153, 154].

According to the theoretical results, most of the functionalized MXenes are metallic or have small band gaps which could be possibly missed experimentally. While Sc_2CT_2 (T= F, OH, and O), Ti_2CO_2, Zr_2CO_2 and Hf_2CO_2 become semiconducting with the surface functionalization. The energy gaps are estimated to be 1.03, 0.45 and 1.8 eV for Sc_2CT_2 with T= F, OH, and O, respectively, 0.24 eV for Ti_2CO_2, 0.88 eV for Zr_2CO_2 [155].

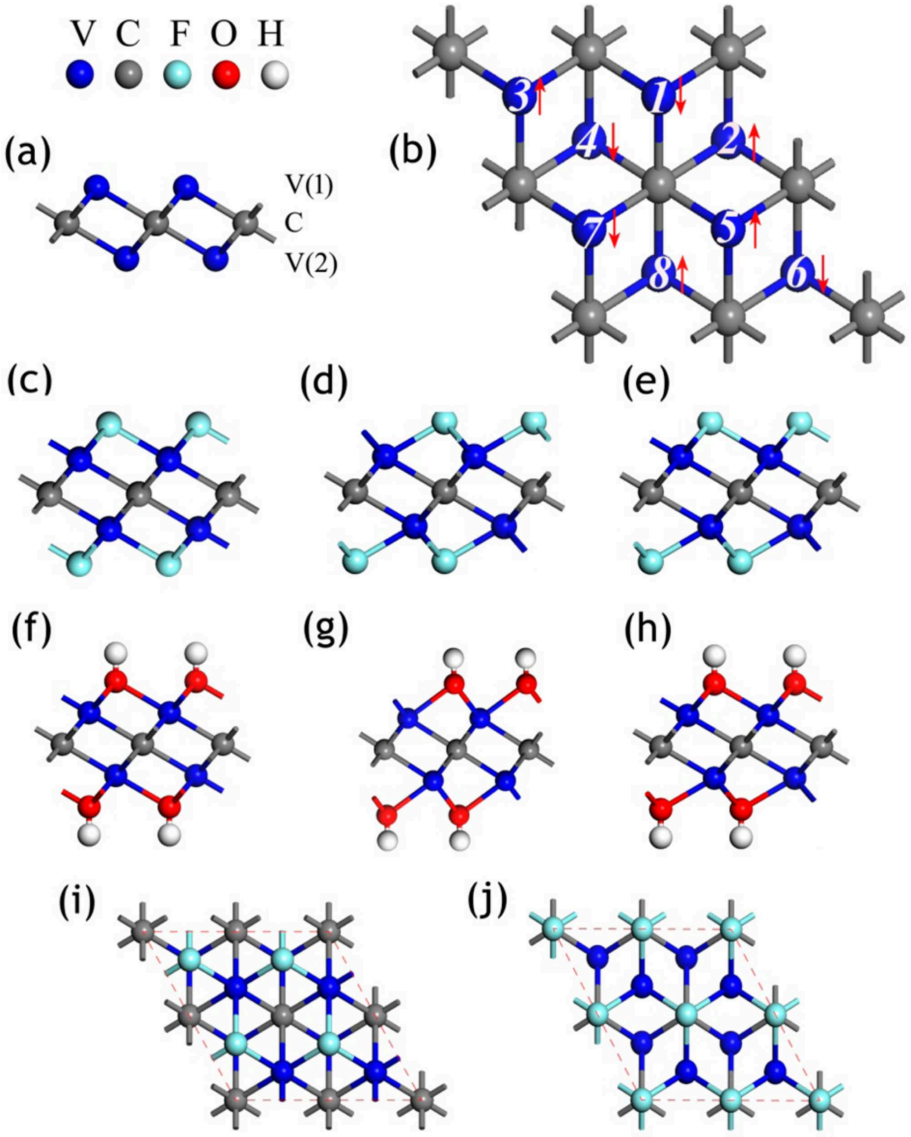

Figure 5.5: *Optimized structural geometries of the free-standing V_2C monolayer and its fluorinated and hydroxylated derivatives. (a) Side view of the bare V_2C monolayer consists of a triple-layer with V(1) CV(2) stacking sequence. (b) Top view of the V_2C monolayer with T5 magnetic configuration. (c-h) Side views of (c) I-V_2CF_2, (d) II-V_2CF_2, (e) III-I-V_2CF_2, (f) I-V_2COH_2, (g) II-V_2COH_2, and (h) III-V_2COH_2. (i, j) top views of I-V_2CF_2 and II-V_2CF_2 [151].*

Specifically, for the V_2CT_x MXenes, V_2C monolayer is predicted to be metallic with antiferromagnetic configuration, while its derived V_2CF_2 and $V_2C(OH)_2$ in their most stable configuration are small-gap antiferromagnetic semiconductor ([151, 156]). According to the calculation results of [151], Figure 5.5 shows the optimized structural geometries of the free-standing V_2C monolayer and its fluorinated and hydroxylated derivatives. Figure 5.6 shows the total density of states (TDOS) of V_2C, V_2CF_2 and $V_2C(OH)_2$ monolayer. For bare V_2C, the resulting DOS indicates that it is metallic with antiferromagnetic configuration. In contrast, when V_2C is passivated by F or OH, the generated V_2CF_2 or $V_2C(OH)_2$ monolayer would turn into a semiconductor regardless

of the specific adsorption configurations of functional groups. The calculated DOS results showed that the C atoms have almost no contribution to states near the Fermi level, namely, the metallic electronic character is determined by free electrons from V atoms. The termination group -F or -OH could saturate the free electrons of V atoms, resulting in the nonmetal character of fluorinated and hydroxylated of V_2C monolayer. Different adsorption configurations merely result in different band gaps.

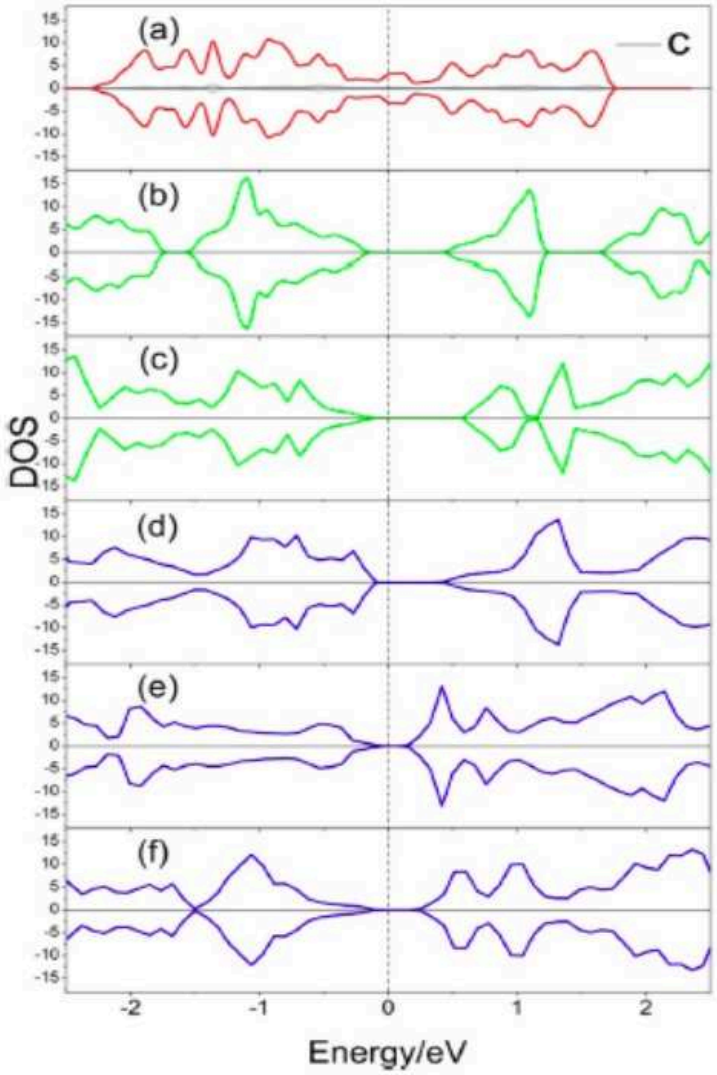

Figure 5.6: *TDOS of (a) V_2C (b) I-V_2CF_2 (c) III-V_2CF_2 (d) I-$V_2C(OH)_2$ (e) II-$V_2C(OH)_2$and (f) III-$V_2C(OH)_2$ .The Fermi levels are set to zero. In each panel, the upper curve and the lower curve correspond to the DOS of the two spin species. [151]*

On the contrary, the electronic band structure calculated by our collaborator [157](as shown in Figure 5.7) by using hybrid functional or GW corrections which can precisely determine the location of the orbitals for each species indicates the metallic behaviour of V_2C monolayer and the fact that V_2CF_2, and $V_2C(OH)_2$ monolayer structures preserve their metallic character. Hence, the divergence between different theoretical calculations

results trigger our motivation on improving the understanding the electronic properties of V_2CT_x MXenes through the experiments. Regarding the method I used (DFT), the advantage is that it is really fast and it already gives a good idea of the electronic density of states and the contribution of each atomic species.

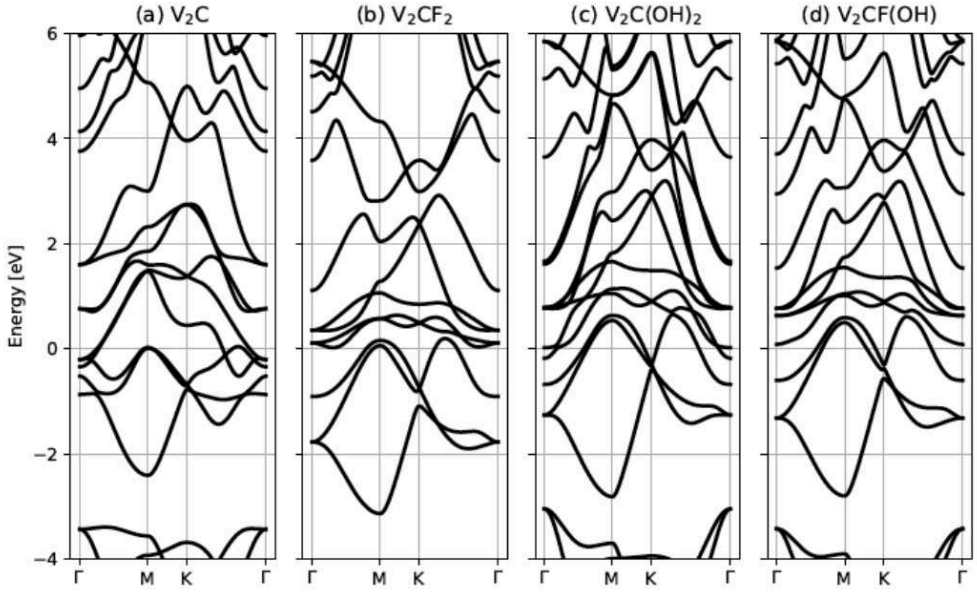

Figure 5.7: *Electronic band structures of (a) V_2C, (b) V_2CF_2, (c) $V_2C(OH)_2$ and (d) $V_2CF(OH)$ in their high-symmetric configuration. The Fermi level is fixed as the reference of zero energy [157].*

5.2.2 Electrical characterization of V_2CT_x MXenes

5.2.2.1 I-V curve

First electrical characterization was carried out by sweeping the source-drain voltage, V_{DS}, from -4 V to 4 V and record the current, I_{DS}. Figure 5.8 shows the typical $I-V$ curve obtained at room temperature for Device I. Current was swept through contacts 1 and 4 while the voltage difference between contact 2 and 3 was measured. An ohmic character is observed with a constant resistivity 2.46 $\times 10^{-2}$ Ω·m which is two orders of magnitude higher than reported value of Ti_2CT_x MXenes [66] and one order of magnitude higher than reported value of $Ti_3C_2T_x$ [148]. The contact resistance in our first trial is relatively high, staying in the range of few MΩs, which might be due to the PMMA residuals after contact fabrication and some attempts are therefore made to improve the contact and lower the contact resistance.

Improvement on the contact fabrication procedure were achieved after several attempts on the device measurement. It is confirmed that thermal annealing is a way to get rid of organic contaminants. The detailed process can be referred to the experimental part: Section 5.1.2.

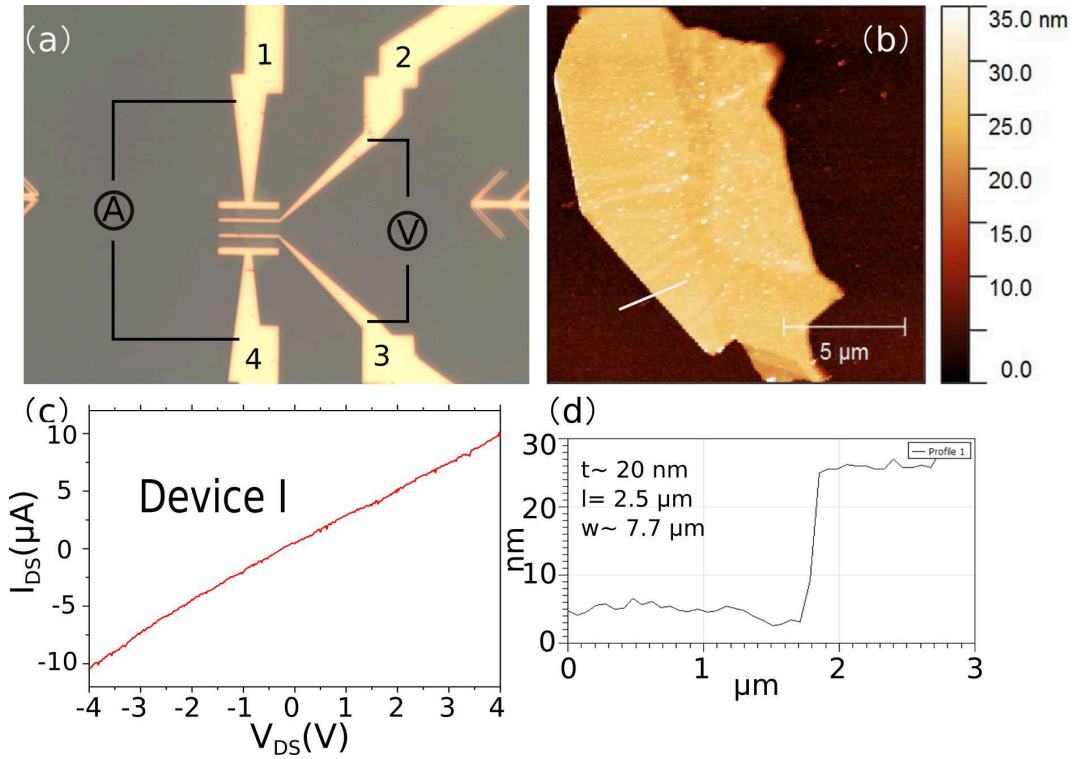

Figure 5.8: *(a) Optical microscopy (OM), (b) AFM image, (c) Dimensions and (d) Current-voltage (I-V) characteristic of V_2CT_x MXene device I measured at room temperature.*

5.2.2.2 Temperature dependency of resistivity

To investigate the carrier transport properties of the V_2CT_x MXenes, the resistivity as the function of temperature was measured on the devices with four contacts after annealing procedure. Current was swept through contacts 1 and 4 while the voltage between contact 2 and 3 was measured as in the previous configuration. Figure 5.9 and Figure 5.10 present the resistance as a function of the temperature for the two annealed samples : the high-temperature value is three orders of magnitude below the resistivity value for the samples which was not annealed. With decreasing temperature, a drop on the resistivity from, 1.68 $\times 10^{-5}$ $\Omega\cdot$ m and 2.35 $\times 10^{-5}$ $\Omega\cdot$ m at 200 K, to 1.66 $\times 10^{-5}$ $\Omega\cdot$m and 2.20 $\times 10^{-5}$ $\Omega\cdot$m at 10 K, as measured respectively, for device II and device III. Clearly, the resistance increases with the increasing temperature, unlike the reported temperature dependence reported for $Ti_3C_2T_x$ [148] and Ti_2CT_x [77], where in both cases, the resistance decreased with increasing temperature.However, the change in

temperature is rather modest, compared e.g. to that observed in the corresponding MAX phase.

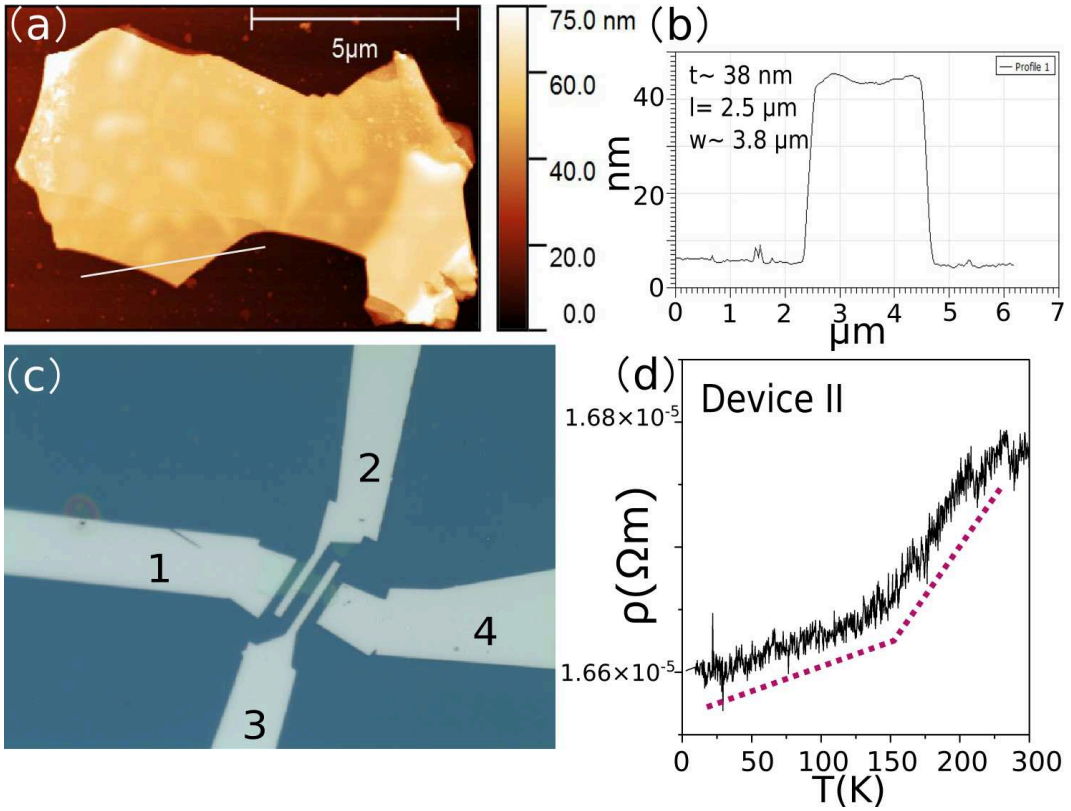

Figure 5.9: *(a,b) AFM profile of as contacted flake,(c) Optical micrograph of the device and (d) Resistivity versus temperature curve of V_2CT_x MXene device II.*

In the case of Ti_2CT_x results from literature (see Figure 5.11 (a)), within the temperature range (100 K to 200 K), the temperature dependence of resistance was found to follow the Arrhenius law and is given by $R(T) = R_0 exp(\Delta E/k_B T)$, where k_B is the Boltzmann constant, T is the temperature, and $\triangle E$ is the activation energy. The activation energy for the excitation of charge carrier can be therefore obtained from the slope of the plot of ln (R) versus $1/T$. While in the case of $Ti_3C_2T_x$ (see Figure 5.11(b)), with decreasing temperature, the resistance first decreases until about 250 K and then increases slightly all the way down to 2.5 K. We can see that the results varied from sample to sample dramatically, though different regimes of the resistance variation with the temperature were reported.

In the case of V_2CT_x MXenes, two regimes were also clearly observed from our plots where there exist two slopes of linear variation dependence, one sharper than another. Metallic behaviour (decreasing resistance with decreasing temperature) is observed in both samples. However, one would expect the resistance to reach a constant value at low temperature due to impurity scattering, which is not observed. Moreover, the

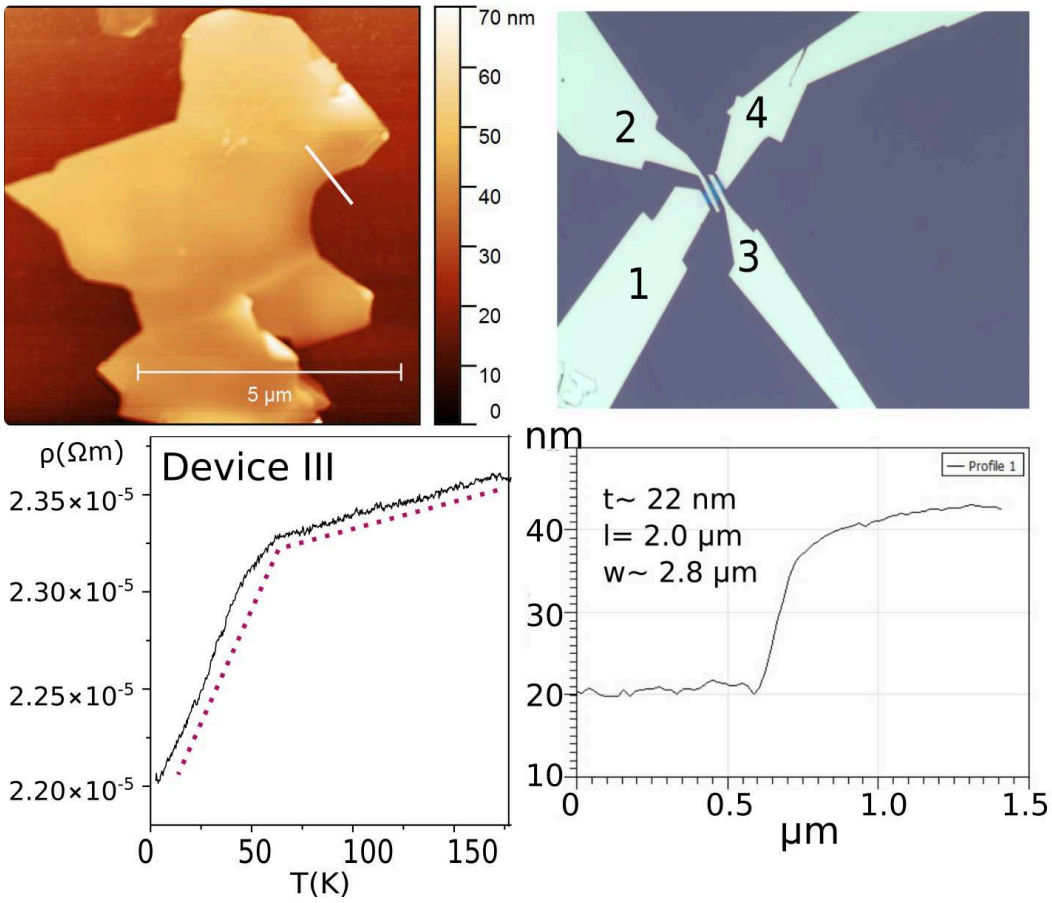

Figure 5.10: *(a,b) AFM profile of as contacted flake , (c) Optical micrograph of the device and (d) Resistivity versus temperature curve of V_2CT_x MXene device III.*

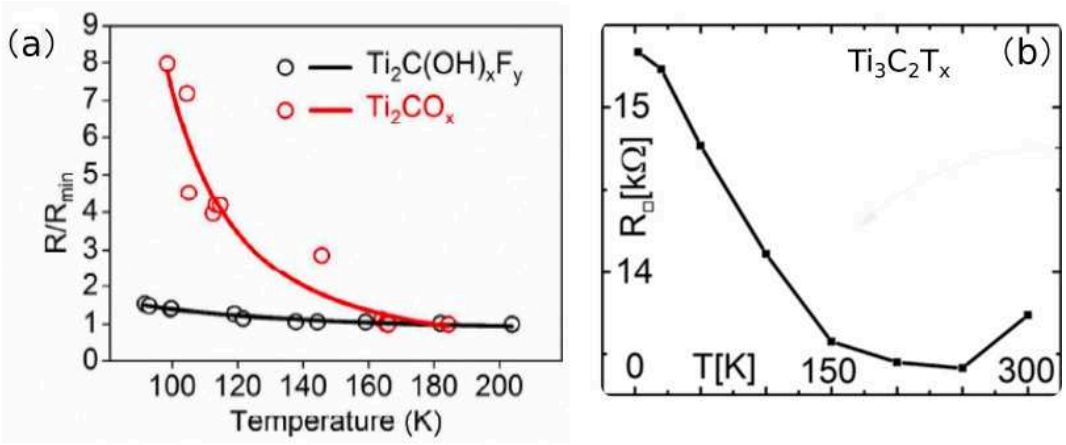

Figure 5.11: *Resistance versus temperature curves of (a) Ti_2CT_x [66] and (b) $Ti_3C_2T_x$ [148].*

change of slope, at a sample-dependent temperature, is intriguing. Possible explanations could involve the presence of two (or more) different conducting paths in the sample, for example two stacks of ideal MXene mono-crystals separated by a stacking fault, corresponding to a large inter-stack resistance. If both stacks are well connected to the

metal contacts, then one could expect a behaviour such as the one observed in Figure 5.10, where the change of slope would correspond to switching the "easy transport path" from one stack to the other. If only one stack is well connected to the contacts (e.g. the top part) then it could happen that, with temperature, the inter-stack resistance is gradually reduced. In that case, one could imagine that in the high temperature regime, only the top stack contributes to the measured resistance, while in the low temperature regime, the whole MXene crystal contributes to transport, and the resistance becomes smaller (as in Figure 5.9).

Another hypothesis is that the anisotropy ratio (ρ_{ab}/rho_c) in the case of V_2CT_x MXene follows the same trend as in the V_2AlC MAX phases (see Figure 3.10). In that case, since the anisotropy factor exhibits a factor-of-two change between room temperature and low temperature, this could explain a transition between different regimes in the temperature dependence of the in-plane resistance of V_2CT_x , especially if the electrical contacts to each MXene layer inside the stack are not homogeneous (i.e. better contacts to some layers).

We compared resistivity values of two samples in Figure 5.12. As demonstrated, the shape of the flake is irregular, leading to non homogeneous. Considering the maximum and minimum value used for the calculation of resistivity, the error bar is calculated and shown in Figure 5.12(a). From the data on both measured samples, we can find out the average value of resistivity of V_2CT_x is around $2\times10^{-5}\Omega\cdot$m. To the best of our knowledge, this is the highest-conductivity MXene device ever reported. More details can be found in the Table 5.2. Furthermore, from Figure 5.12 (b), the residual resistivity varies quite strongly depending on the amount of impurities and other crystallographic defects. In our present test, it implies that the thinner flake device has better quality than thicker one. Therefore, the resistivity of V_2CT_x MXene is highly sensitive to defects and also to the layers thickness.

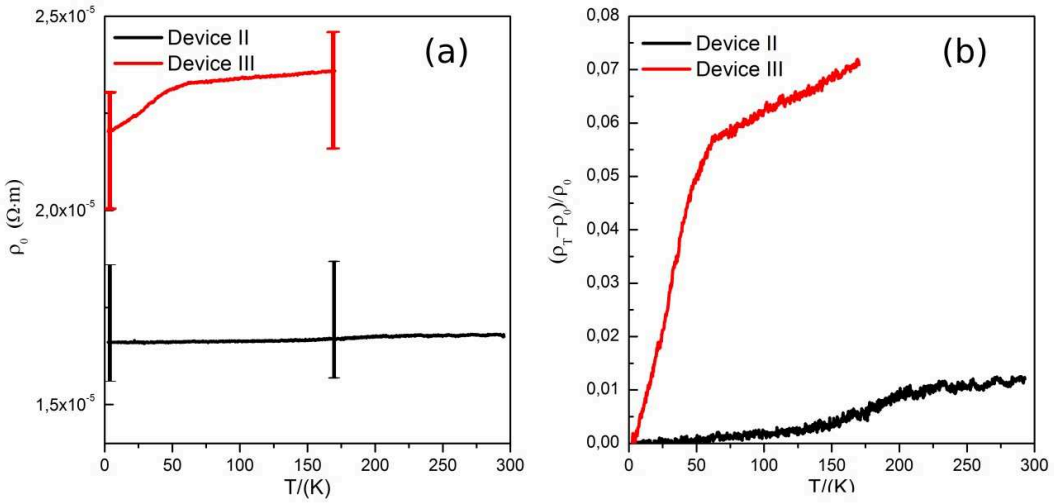

Figure 5.12: *Temperature dependency of resistivity of Device II and III (a)Resistivity (b)Residual-resistance.*

5.2.2.3 Field effect of V_2CT_xMXene device

Using the Si substrate as backgate electrode, transport in V_2CT_x MXene device II was investigated by sweeping the backgate voltage, V_G. As can be observed in Figure 5.13(b). We can see that the transfer characteristics of the V_2CT_x MXene device exhibits p-type behavior, as Ti_2CT_x [66].

From a linear fit of the data, the field effect mobility, μ_{FE} can be determined from the standard relation

$$\mu_{FE} = \frac{\Delta I_D}{\Delta V_G} \frac{t}{\epsilon V_{DS}} \frac{L}{W} \tag{5.1}$$

where t and ϵ are the thickness and permittivity of the SiO_2 layer, L and W are the length and width of the MXene device, respectively. Based on the results shown in Figure 5.13(a), a 1.6 K field effect mobility μ_{FE} , 22.7 $\pm$ 10 $cm^2/V{\cdot}s$ is calculated the error bar is due to the error on linear fitting), which does not seem unphysical, considering the reported values of mobility in the literature : 0.6 $cm^2/V{\cdot}s$ [148], 4.23 $cm^2/V{\cdot}s$ [77] for $Ti_3C_2T_x$ and 10215 $cm^2/V{\cdot}s$ for Ti_2CT_x [66].

From $\sigma = \mu n_0 e$, we calculate that the charge carrier density n_0 of V_2CT_x MXene is $1.66{\times}10^{20}$ cm^{-3}, while the density of $Ti_3C_2T_x$ MXenes was measured to be $8{\times}10^{21}$ cm^{-3} [148].

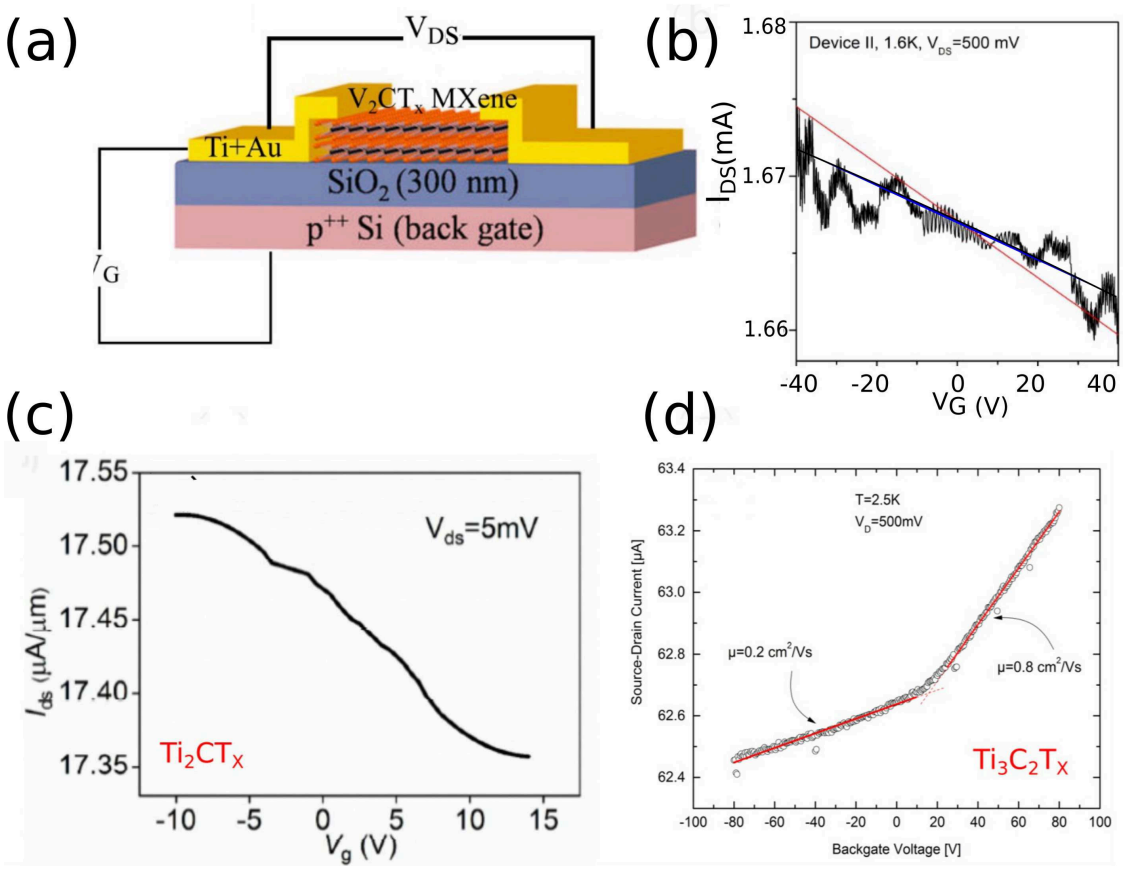

Figure 5.13: *(a)Schematic diagram of the MXenes transistor (b,c,d) functional dependence of source-drain current I_{DS} (for a constant V_{DS}) on backgate voltage on different MXenes device (b) V_2CT_x (c) T_2CT_x [66](d) $Ti_3C_2T_x$ [148].*

5.2.2.4 Magnetoresistance of V_2CT_xMXene device

Finally, we consider the effects of magnetic fields on the transport properties, as shown in Figure 5.14. The current applied I_{DS} is 100 μA. Unlike other MXene samples, we did not observe clearly visible, quadratic increase of the conductance with increasing magnetic field. The irreproducible fluctuation of the curve indicates there is no clear phenomenon of universal conductance fluctuations (UCF). After symmetrizing the raw data, by using the two-band model, MR=αB^2, where $\alpha = \mu_n \mu_p$. Assuming $\mu_n = \mu_p$, the fitting $\alpha_{II} = 2.11 \times 10^{-4}, \alpha_{III} = 9.47 \times 10^{-5}$, the hall mobility $\mu = 145.2$ cm^2/V·s for Device II and 97.3 cm^2/V·s for Device III, the average value is 121.3 cm^2/V·s.

Herein, on can notice the disparity between Hall mobility and field-effect mobility. It is well known that most experimental work on 2D materials mobilities has concentrated on Hall mobility μ_H, and *field-effect* mobilities, μ_{FE}. The former represents the bulk mobility and the interface, as well as the quantization effect, while the latter depends greatly on the active states on the surface. Therefore a direct comparison of μ_H and

μ_{FE} would be misleading as μ_{FE} is the mobility of carriers confined to the surface space charge layer which depends mainly on the surface scattering mechanisms which in turn depend on the surface condition, surface phonons, ionized impurities on the surface and potential fluctuations within the surface layers under the influence of an external gate field. On the other hand, μ_H depends predominantly on the lattice scattering in the bulk.

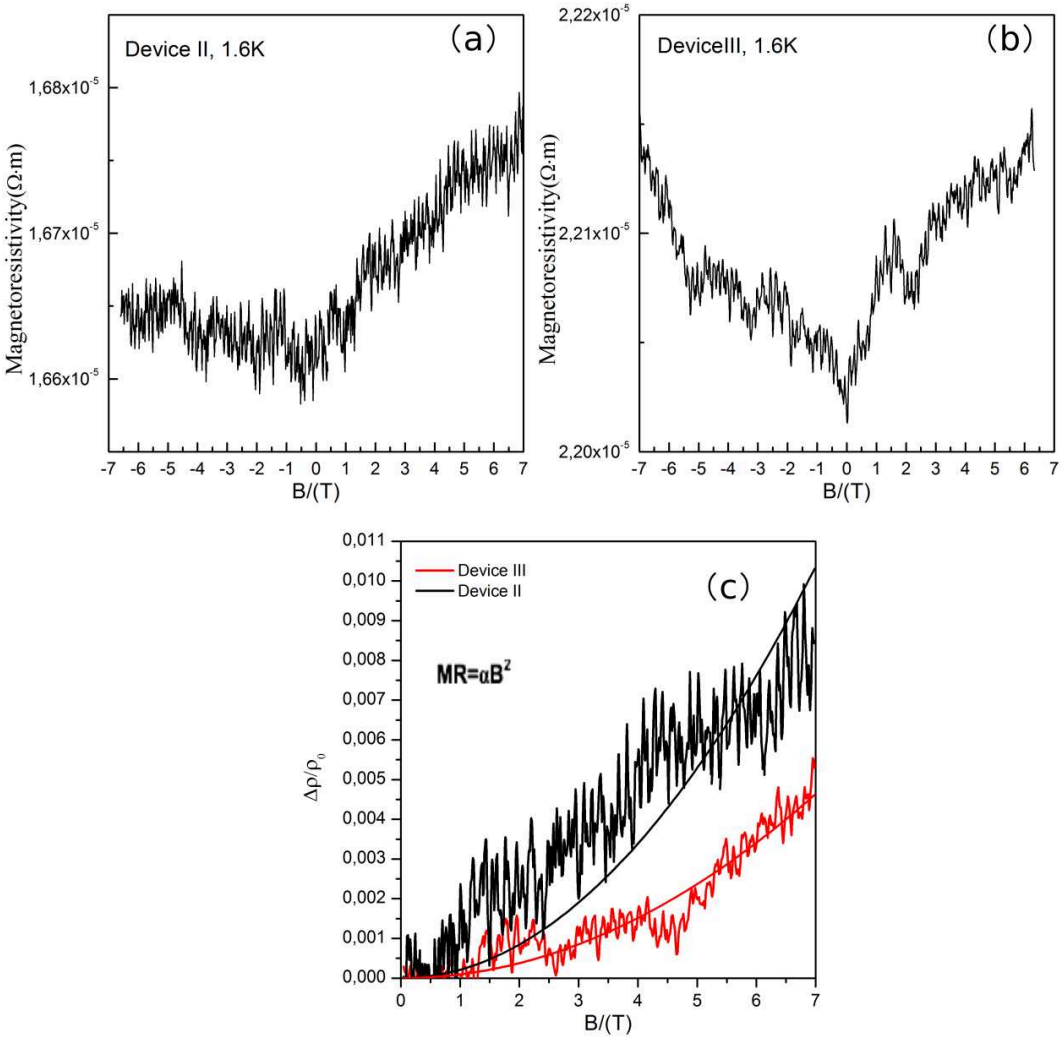

Figure 5.14: *Effect of magnetic fields on V_2CT_x MXenes device.(a) Magnetoresistance of Device II at 1.6K (b) Magnetoresistance of Device III at 1.6 K(c) Magnetoresistance after symmetry and fitting with $MR = \alpha B_2$*

Table 5.2 lists the electronic transport of MXene device and comparison with the MAX phases. Undoubtedly, electronic transport data on this new family of 2D material is still deficient. Even, the reported results of mostly studied Ti_2CT_x and Mo_2CT_x varies dramatically. If we compare the resistivity of our V_2CT_x samples, the average

	Resistivity,	Hall mobility,	Field effect mobility,	Concentration,	Ref
	ρ,$\Omega \cdot$ m	μ_H, cm^2/V·s	μ_{EF}, cm^2/V·s	n, cm^{-3}	
V_2CT_x	(1.68-2.22)$\times 10^{-5}$	97.3 ; 145.2	22.7	1.66×10^{20}	
$Ti_3C_2T_x$(f)	(2.22-3.92)$\times 10^{-5}$				[158]
Mo_2 C T_x(p)	0.02-20				[76]
Mo_2 C T_x(p)	3.37×10^{-5}				[159]
$Ti_3C_2T_x$(s)			0.7 ± 0.2	$8 \pm 3 \times 10^{21}$	[148]
$Ti_3C_2T_x$(m)	sheet resistivity, 1590		4.23		[77]
Ti_2CT_x(m)		9375	>10000		[66]
V_2AlC	2×10^{-7}	(80-120)		$(2-4) \times 10^{21}$	
*NOTE f:film; p:paper; s:single layer; m:multi-layer					

Table 5.2: *Electronic transport data of MXenes device.*

value of $2\times10^{-5}\Omega$m is of the same order of magnitude as reported other MXene sample (thickness 20-30 nm), and about 2 orders of magnitude higher than its corresponding MAX phase sample, where the charge carrier concentration deduced from field-effect measurement is 1 order of magnitude lower than the reported data.

5.3 Conclusion

We can conclude that we successfully obtained some first hand transport data on V_2CT_x MXenes. The average value for the resistivity of Device II and Device III is 2×10^{-5} Ω·m, not far from value reported other MXene samples. The temperature dependence is relatively small and unusual compared to a normal metal, but is also sample dependent, so it is probably related to defects and the corresponding conduction mechanism between layers. The field effect measurement indicates field effect mobility μ_{FE}, 22.7 ± 10 cm^2/V·s. The magnetoresistance surprisingly does not show any feature nor a clear classical parabolic dependence which could allow to extract very reliable information on charge carriers. We obtained the μ_H is in the order of magnitude 10^2 cm^2/V·s, comparable to its parent MAX phase.

As demonstrated in the literature [160], understanding magneto-transport in MXenes is undoubtedly challenging for several reasons: (a) When the A layers are etched from MAX phase, they are replaced by =O, -F and -OH terminations. With different surface chemical termination, the transport properties certainly vary. The terminations group characterization is still under exploration, which limits the understanding of relationship between chemical function and electronic properties. (b) The interlayer space is intercalated by cations and water molecules, and the exact arrangement of stacking in multilayered particles can vary from flake to flake, from device to device. (c) The possible presence of a large fraction of defects in the 2D sheets, especially when aggressive etchants such as 50% HF are used, also limit the reproducibility of experimental results from sample to sample.In solids, in general and 2D solids in particular it is difficult to characterize and quantify point defects.

It is assured that with further knowledge of the structure of MXenes, their electronic transport properties will be further understood thoroughly.

Conclusion and perspectives

At the end of this thesis, let us look back on our initiatives of this project: the primary objective is firstly involving the crystal growth of single crystal MAX phases and the characterization of their intrinsic physical properties, mainly magneto-electronic transport properties and more specifically, probing the anisotropic properties. Then, second objective of this project is focused on the synthesis of MXenes derived from MAX phase single crystals by a combined chemical etching and mechanical exfoliation. Fabrication of MXene-based nano device and electronic properties cryo measurement are also proposed in the beginning of the thesis.

Then, it is the time to examine the degree of completion of this project:

First of all, several MAX phase single crystal have been successfully grown by using high temperature solution growth and slow cooling technique, including Ti_2SnC, Ti_3SiC_2, V_2AlC and Cr_2AlC. Structural characterization confirms the single crystalline character of the samples by X-ray measurements and Raman spectroscopy. The most favorable case is that of Cr-Al-C, attributed to its extreme high carbon solubility. Fortunately, the size of as-obtained crystals are only limited by the size of the crucible, leading to relatively large Cr_2AlC crystals ready for the subsequent device measurement. V_2AlC, as a starting basis for forming MXenes with macroscopic area, permits the selective etching after HF-treatment and cleavage of the platelets parallel to the basal plane.

Then, MAX devices for in-plane and out-of-plane transport measurement were fabricated. A full set of experimental data were consequently obtained from single crystals of V_2AlC and Cr_2AlC as a function of temperature and magnetic field. In comparison with the resistivity value of polycrystalline samples, the resistivity of Cr_2AlC single crystal is three times lower, while for that of V_2AlC, four times lower. In particular, we obtain a very high ratio between the in-plane and parallel to the c-axis resistivity, which is very substantial, in the range of a few hundreds to thousands. From MR and Hall

effect measurement, in-plane transport behaviour of MAX phases have been studied.As in the case of the polycrystalline phases, we observe a magneto-resistance of a few per cent, among them, only MR curve of Cr_2AlC exhibits parabolic-like curves, as reported for polycrystalline MAX phases. One can notice that Hall resistivity varies linearly with magnetic filed, and this phenomena is temperature independent, indicating the systems are in the weak-field limit. R_H is small, as previously noticed for polycrystalline samples. The extracted mobility is in the range from 50 to 120 cm^2/Vs, which is the same order as magnitude of polycrystalline sample. Thermal transport measurement was also conducted on Cr_2AlC samples. Similar as higher electronic conductivity compared to its polycrystalline counterpart, higher thermal conductivity is verified. The sign of Seebeck coefficient is not in consistent with that of Hall coefficient in which this discrepancy can still be partly explained by a compensation between holes and electrons. Attempts to measure the out-of-plane magnetoelectronic transport were also performed. Though we observed an interesting anomalous magnetoresistance in the absence of Lorentz-force, the mechanism of a field-induced transport along c-axis is still unclear. Theoretically, a general, yet simple model was proposed for describing the weak field magneto-transport properties of nearly free electrons in two-dimensional hexagonal metals. It was then modified to be applicable for the transport properties of layered MAX phases. We argue that the values of the in-plane Hall coefficient and the in-plane parabolic magneto-resistance are due to the specific shape of the Fermi surface of almost two-dimensional hole and electron bands. If the contribution of the electron pockets to in-plane resistivity is often predicted to be a minor one, in contrast, both holes and electrons should substantially contribute to the overall value of the in-plane Hall coefficient.

Additionally, large scale V_2CT_x MXene flakes were successfully synthesized by conventional HF-etching of V_2AlC single crystals. Efforts have been made on the optimization of reaction conditions and general protocol for etching V_2AlC was proposed. Mechanical delamination of multilayered V_2CT_x flakes into few layer flake and transfer on Si/SiO_2 substrate was also achieved. Structural characterization demonstrated an enlarged interplane distance, while prior DMSO intercalation seems to have no effect on V_2CT_x MXenes. Typical 2D material morphology was found in SEM and TEM images. From the XRD pattern , one observed an evident shift of 2θ from 13.5° to 7.4°, corresponding to c-LPs changing from 13.107 Åto 23.872 Å. Such phenomenon has been attributed to the water intercalation in between the layers after delamination in an aqueous solution.The $a - LP$ of this flake from SAED, inheriting the hexagonal basal plane symmetry of the parent V_2AlC phase, is measured to be ~2.9 Å, which is similar

to that of the V_2AlC precursor.

In the end, we detailed the electrical device fabrication process and proceed with electrical measurements result. We can conclude that -OH terminations on V_2CT_x is dominate, and the most energetically favourable, compared to -F and -O functional groups. Finally, we can conclude that we successfully obtained some first hand transport data on V_2CT_xMXenes, though compared to other reported MXenes, the average value for the resistivity of Device II and Device III is 2×10^{-5} Ω·m, which is in consistent with reported other MXene samples. The temperature dependence is unusual compared to a normal metal, but is also sample dependent, so it is probably related to defects and the corresponding conduction mechanism between layers. The field effect measurement indicates field effect mobility μ_{FE} , 22.7$\pm$10 $cm^2/V\cdot s$. The magnetoresistance surprisingly does not show any feature nor classical parabolic dependence which could allow to get more information on charge carriers. The obtained μ_H is in the same order of magnitude as its parent MAX phase.

At the end of this work, one can also point out a few directions that could be investigated in future studies, in light of the difficulties and hindrances that I have faced, and of the new opportunities that emerged.

The first aspect concerns sample fabrication including improvement of single crystal growth. The crystal size matters in all the following measurements. In order to understand the anisotropic magneto resistance, the crystal size is the prerequisite.

Sample fabrication also involves the fabrication of MXene device. To the best of our knowledge, among synthesis methods of MXene, there are very rare reports on the mechanical exfoliation of MXene. Up to now, no single layer MXene is obtained by mechanical exfoliation. As explained in the last chapter, understanding magneto-transport in MXenes is undoubtedly challenging. The terminations group characterization is still under exploration,which limits the understanding of relationship between chemical function and electronic properties, let alone the effect of defects introduced due to the harsh etchant. So as to get the high quality flake for the device fabrication, dry method would definitely be more favourable than wet method. Micro-mechanical exfoliation could be approached in the future.

Due to the lack of single-crystalline/single flake transport data on the MAX phases and MXenes, there is still much to be done before a thorough picture of the physical mechanisms governing magnetotransport. Here list some future work: i) thorough

investigation of magnetotransport properties in magnetic MAX phases; ii)assess correlation between anisotropy ratio and crystal quality; iii) out-of-plane magnetoelectronic transport; iv) deep understanding of the termination group of MXenes according to different fabrication process; v) more experimental endeavours on MXene electronic measurement.

Publication

2015

- T. Ouisse, **L. Shi**, B. A. Piot, B. Hackens, V. Mauchamp, and D. Chaussende. Magnetotransport properties of nearly-free electrons in two-dimensional hexagonal metals and application to the $M_{n+1}AX_n$ phases. *Physical Review B*, 92: 045133, 2015.
- **L. Shi**, T. Ouisse, E. Sarigiannidou, O. Chaix-Pluchery, H. Roussel, D. Chaussende, B. Hackens. Synthesis of single crystals of V_2AlC phase by high-temperature solution growth and slow cooling technique. *Acta Materialia*, 83: 304-309, 2015.

2017

- S. Q. Zhang, **L. Shi**, F. Mercier,O. Chaix-Pluchery, D. Chaussende, I. Gelard, B. Hackens and T. Ouisse. Conversion of MAX phase single crystals in highly porous carbides by high temperature chlorination. *Ceramic International*, 43(11):8246-8254, 2017.

Submitted

- A. Champagne, **L. Shi,** T. Ouisse, B. Hackens, and J-C Charlier. Electronic and vibrational properties of V_2C-based MXenes: from experiments to first-principles modeling.

Under preparation

- **L. Shi**, N. Kryvutsa,T. N. Bui, A. Champagne, D. Cabosart, J-C Charlier, T. Ouisse and B. Hackens. Large-scale delamination and electronic properties of multi-layers V_2CT_XMXene flakes.

Bibliography

[1] Michel W. Barsoum. The $M_{n+1}AX_n$ phases: A new class of solids. *Progress in Solid State Chemistry*, 28(1):201–281, 2000.

[2] Z. M. Sun. Progress in research and development on MAX phases: a family of layered ternary compounds. *International Materials Reviews*, 56(3):143–166, 2011.

[3] Michel W. Barsoum. MAX Phases: Properties of Machinable Ternary Carbides and Nitrides. Wiley, 2013.

[4] Per Eklund, Manfred Beckers, Ulf Jansson, Hans Högberg, and Lars Hultman. The $M_{n+1}AX_n$ phases: Materials science and thin-film processing. *Thin Solid Films*, 518(8):1851–1878, 2010.

[5] Szilvia Sasvari Per O. A. Persson Jens Emmerlich, Hans Hogberg and Lars Hultman. Growth of Ti_3SiC_2 thin films by elemental target magnetron sputtering. *Journal of Applied Physics*, 96(9):4817–4826, 2004.

[6] Johannes Etzkorn, Martin Ade, and Harald Hillebrecht. V_2AlC, V_4AlC_{3-x} (x=0.31), and $V_{12}Al_3C_8$: Synthesis, Crystal Growth, Structure, and Superstructure. *Inorganic Chemistry*, 46(18):7646–7653, 2007.

[7] F. Mercier, T. Ouisse, and D. Chaussende. Morphological instabilities induced by foreign particles and Ehrlich-Schwoebel effect during the two-dimensional growth of crystalline Ti_3SiC_2. *Physical Review B*, 83(7):075411, 2011.

[8] Frederic Mercier, Odette Chaix-Pluchery, Thierry Ouisse, and Didier Chaussende. Raman scattering from Ti_3SiC_2 single crystals. *Applied Physics Letters*, 98(8):081912, 2011.

[9] Jing-Feng Li, T. Matsuki, and R. Watanabe. Fabrication of highly dense Ti_3SiC_2 ceramics by pressureless sintering of mechanically alloyed elemental powders. *Journal of Materials Science*, 38(12):2661–2666, 2003.

[10] Michal Lopacinski, Jan Puszynski, and Jerzy Lis. Synthesis of Ternary Titanium Alumimum Carbides Using Self-Propagating High-Temperature Synthesis Technique. *Journal of the American Ceramic Society*, 84(12):3051–3053, 2001.

[11] C. L. Yeh and Y. G. Shen. Effects of TiC and Al_4C_3 addition on combustion synthesis of Ti_2AlC. *Journal of Alloys and Compounds*, 470(1–2):424–428, 2009.

[12] Songlan Yang, Zheng Ming Sun, and Hitoshi Hashimoto. Reaction in Ti_3SiC_2 powder synthesis from a Ti-Si-TiC powder mixture. *Journal of Alloys and Compounds*, 368(1–2):312–317, 2004.

[13] Jinshan Yang, Shaoming Dong, Yusheng Ding, Zhen Wang, Haijun Zhou, and Bo Lu. Fabrication of High-Purity Ti_3SiC_2 Powders by an In Situ Reaction of Polycarbosilane and Metal Titanium. *Journal of the American Ceramic Society*, 93(8):2117–2120, 2010.

[14] Sylvain Dubois, Thierry Cabioc'h, Patrick Chartier, Véronique Gauthier, and Michel Jaouen. *A New Ternary Nanolaminate Carbide:* Ti_3SnC_2, *pages*401 − −403. *JohnWileySons*, *Inc.*, 2009.

[15] T. El-Raghy, S. Chakraborty, and M. W. Barsoum. Synthesis and characterization of Hf_2PbC, Zr_2PbC and M_2SnC (M=Ti, Hf, Nb or Zr). *Journal of the European Ceramic Society*, 20(14–15):2619–2625, 2000.

[16] Zhijun Lin, Yanchun Zhou, Meishuan Li, and Jingyang Wang. In-situ hot pressing/solid-liquid reaction synthesis of bulk Cr_2AlC. *Zeitschrift fur Metallkunde*, 96(3):291–296, 2005.

[17] Wei Zhang, Nahum Travitzky, Chunfeng Hu, Yanchun Zhou, and Peter Greil. Reactive Hot Pressing and Properties of Nb_2AlC. *Journal of the American Ceramic Society*, 92(10):2396–2399, 2009.

[18] Jianfeng Zhang, Lianjun Wang, Lu Shi, Wan Jiang, and Lidong Chen. Rapid fabrication of Ti_3SiC_2–SiC nanocomposite using the spark plasma sintering-reactive synthesis (SPS-RS) method. *Scripta Materialia*, 56(3):241–244, 2007.

[19] Lu Shi, Jianfeng Zhang, Lianjun Wang, Wan Jiang, and Lidong Chen. Fabrication, Microstructure and Mechanical Properties of $TiC/Ti_2AlC/TiAl3$ in situ Composite. *Journal of Materials Science Technology*, 27(3):239–244, 2011.

[20] Ziqi Sun, Meishuan Li, Longfei Hu, Xinpo Lu, and Yanchun Zhou. Surface Chemistry, Dispersion Behavior, and Slip Casting of Ti_3AlC_2 Suspensions. *Journal of the American Ceramic Society*, 92(8):1695–1702, 2009.

[21] H. Högberg, P. Eklund, J. Emmerlich, J. Birch, and L. Hultman. Epitaxial Ti_2GeC, Ti_3GeC_2, and Ti_4GeC_3 MAX-phase thin films grown by magnetron sputtering. *Journal of Materials Research*, 20(4):779–782, 2005.

[22] S. Jacques, H. Di-Murro, M. P. Berthet, and H. Vincent. Pulsed reactive chemical vapor deposition in the C-Ti-Si system from $H_2/TiCl_4/SiCl_4$. *Thin Solid Films*, 478(1–2):13–20, 2005.

[23] C. Hoglunda and M. Beckers. Topotaxial growth of Ti_2AlN by solid state reaction in AlNaTi(0001) multilayer thin films. *Applied Physics Letters*, 90(17):174106, 2007.

[24] Marie Sonestedt, Jenny Frodelius, Mats Sundberg, Lars Hultman, and Krystyna Stiller. Oxidation of Ti_2AlC bulk and spray deposited coatings. *Corrosion Science*, 52(12):3955–3961, 2010.

[25] S. Gupta and M. W. Barsoum. Synthesis and Oxidation of V_2AlC and $(Ti_{0.}5V_{0.5})_2AlC$ in Air. *J. Electrochem. Soc.*, 151(2):D24–D29, 2004.

[26] J. D. Hettinger, S. E. Lofland, P. Finkel, T. Meehan, J. Palma, K. Harrell, S. Gupta, A. Ganguly, T. El-Raghy, and M. W. Barsoum. Electrical transport, thermal transport, and elastic properties of M_2AlC (M=Ti, Cr, Nb, and V). *Physical Review B*, 72(11):115120, 2005.

[27] P. Finkel, M. W. Barsoum, J. D. Hettinger, S. E. Lofland, and H. I. Yoo. Low-temperature transport properties of nanolaminates Ti_3AlC_2 and Ti_4AlN_3. *Phys. Rev. B*, 67:235108, 2003.

[28] P. Finkel, B. Seaman, K. Harrell, J. Palma, J. D. Hettinger, S. E. Lofland, A. Ganguly, M. W. Barsoum, Z. Sun, Sa Li, and R. Ahuja. Electronic, thermal, and elastic properties of $Ti_3Si_{(1-x)}Ge_xC_2$ solid solutions. *Phys. Rev. B*, 70:085104, 2004.

[29] P. Finkel, J. D. Hettinger, S. E. Lofland, M. W. Barsoum, and T. El-Raghy. Magneto-transport properties of the ternary carbide Ti_3SiC_2 Hall effect, magnetoresistance, and magnetic susceptibility. *Phys. Rev. B*, 65:035113, 2001.

[30] T. Scabarozi, A. Ganguly, J. D. Hettinger, S. E. Lofland, S. Amini, P. Finkel, T. El-Raghy, and M. W. Barsoum. Electronic and thermal properties of $Ti_3Al(C_{0.5}, N_{0.5})_2$, $Ti_2Al(C_{0.5},N_{0.5})$ and Ti_2AlN. *Journal of Applied Physics*, 104(7):073713, 2008.

[31] GuoZhu Jia and LiJun Yang. Ab initio calculations for properties of Ti_2AlN and Cr_2AlC. *Physica B: Condensed Matter*, 405(21):4561 – 4564, 2010.

[32] M. Bugnet, M. Jaouen, V. Mauchamp, T. Cabioc'H, and G. Hug. Experimental and first-principles investigation of the electronic structure anisotropy of Cr_2AlC. *Physical Review B - Condensed Matter and Materials Physics*, 90(19), 2014.

[33] Jochen M. Schneider, Zhimei Sun, Raphael Mertens, Fatih Uestel, and Rajeev Ahuja. Ab initio calculations and experimental determination of the structure of Cr_2AlC. *Solid State Communications*, 130(7):445 – 449, 2004.

[34] Yang Z.J., Li J., Linghu R.F., Song X.S., Cheng X.L., and Yang X.D. Electronic and phononic properties of V_2AlC via first principles. *Canadian Journal of Physics*, 91(10):822–825, 2013.

[35] C. Zhang, Z. Zhang, P. Wang, Y. Wang, J. Dong, and N. Xing. First-principles study of electronic structure of V 2AlC and V 2AlN. *Solid State Communications*, 144(7-8):347–351, 2007.

[36] H. I. Yoo, M. W. Barsoum, and T. El-Raghy. Materials science: Ti_3SiC_2 has negligible thermopower. *Nature*, 407(6804):581–582, 2000.

[37] Laurent Chaput, Gilles Hug, Pierre Pecheur, and Hubert Scherrer. Anisotropy and thermopower in Ti_3SiC_2. *Phys. Rev. B*, 71:121104, 2005.

[38] Martin Magnuson, Maurizio Mattesini, Ngo Van Nong, Per Eklund, and Lars Hultman. Electronic-structure origin of the anisotropic thermopower of nanolaminated Ti_3SiC_2 determined by polarized x-ray spectroscopy and Seebeck measurements. *Phys. Rev. B*, 85:195134, 2012.

[39] Y. Zhou and Z. Sun. Electronic structure and bonding properties in layered ternary carbide Ti_3SiC_2. *Journal of Physics Condensed Matter*, 12(28), 2000.

[40] A. K. Geim and I. V. Grigorieva. Van der Waals heterostructures. *Nature*, 499(7459):419–425, 2013.

[41] Yenny Hernandez, Valeria Nicolosi, Mustafa Lotya, Fiona M. Blighe, Zhenyu Sun, Sukanta De, I. T. McGovern, Brendan Holland, Michele Byrne, Yurii K. Gun'Ko, John J. Boland, Peter Niraj, Georg Duesberg, Satheesh Krishnamurthy, Robbie Goodhue, John Hutchison, Vittorio Scardaci, Andrea C. Ferrari, and Jonathan N. Coleman. High-yield production of graphene by liquid-phase exfoliation of graphite. *Nat Nano*, 3(9):563–568, 2008.

[42] Chunyi Zhi, Yoshio Bando, Chengchun Tang, Hiroaki Kuwahara, and Dimitri Golberg. Large-Scale Fabrication of Boron Nitride Nanosheets and Their Utiliza-

tion in Polymeric Composites with Improved Thermal and Mechanical Properties. *Advanced Materials*, 21(28):2889–2893, 2009.

[43] Zhiyuan Zeng, Ting Sun, Jixin Zhu, Xiao Huang, Zongyou Yin, Gang Lu, Zhanxi Fan, Qingyu Yan, Huey Hoon Hng, and Hua Zhang. An Effective Method for the Fabrication of Few-Layer-Thick Inorganic Nanosheets. *Angewandte Chemie International Edition*, 51(36):9052–9056, 2012.

[44] Liang Li, Renzhi Ma, Yasuo Ebina, Nobuo Iyi, and Takayoshi Sasaki. Positively Charged Nanosheets Derived via Total Delamination of Layered Double Hydroxides. *Chemistry of Materials*, 17(17):4386–4391, 2005.

[45] Qiang Wang and Dermot O'Hare. Recent Advances in the Synthesis and Application of Layered Double Hydroxide (LDH) Nanosheets. *Chemical Reviews*, 112(7):4124–4155, 2012.

[46] Alfonso Reina, Xiaoting Jia, John Ho, Daniel Nezich, Hyungbin Son, Vladimir Bulovic, Mildred S. Dresselhaus, and Jing Kong. Large Area, Few-Layer Graphene Films on Arbitrary Substrates by Chemical Vapor Deposition. *Nano Letters*, 9(1):30–35, 2009.

[47] Li Song, Lijie Ci, Hao Lu, Pavel B. Sorokin, Chuanhong Jin, Jie Ni, Alexander G. Kvashnin, Dmitry G. Kvashnin, Jun Lou, Boris I. Yakobson, and Pulickel M. Ajayan. Large Scale Growth and Characterization of Atomic Hexagonal Boron Nitride Layers. *Nano Letters*, 10(8):3209–3215, 2010.

[48] Yi-Hsien Lee, Xin-Quan Zhang, Wenjing Zhang, Mu-Tung Chang, Cheng-Te Lin, Kai-Di Chang, Ya-Chu Yu, Jacob Tse-Wei Wang, Chia-Seng Chang, Lain-Jong Li, and Tsung-Wu Lin. Synthesis of Large-Area MoS_2 Atomic Layers with Chemical Vapor Deposition. *Advanced Materials*, 24(17):2320–2325, 2012.

[49] Sukang Bae, Hyeongkeun Kim, Youngbin Lee, Xiangfan Xu, Jae-Sung Park, Yi Zheng, Jayakumar Balakrishnan, Tian Lei, Hye Ri Kim, Young Il Song, Young-Jin Kim, Kwang S. Kim, Barbaros Ozyilmaz, Jong-Hyun Ahn, Byung Hee Hong, and Sumio Iijima. Roll-to-roll production of 30-inch graphene films for transparent electrodes. *Nat Nano*, 5(8):574–578, 2010.

[50] Mark P. Levendorf, Carlos S. Ruiz-Vargas, Shivank Garg, and Jiwoong Park. Transfer-Free Batch Fabrication of Single Layer Graphene Transistors. *Nano Letters*, 9(12):4479–4483, 2009.

[51] Paola De Padova, Osamu Kubo, Bruno Olivieri, Claudio Quaresima, Tomonobu Nakayama, Masakazu Aono, and Guy Le Lay. Multilayer Silicene Nanoribbons. *Nano Letters*, 12(11):5500–5503, 2012.

[52] Jiehua Liu and Xue-Wei Liu. Two-Dimensional Nanoarchitectures for Lithium Storage. *Advanced Materials*, 24(30):4097–4111, 2012.

[53] Sasha Stankovich, Dmitriy A. Dikin, Geoffrey H. B. Dommett, Kevin M. Kohlhaas, Eric J. Zimney, Eric A. Stach, Richard D. Piner, SonBinh T. Nguyen, and Rodney S. Ruoff. Graphene-based composite materials. *Nature*, 442(7100):282–286, 2006.

[54] Goki Eda, Giovanni Fanchini, and Manish Chhowalla. Large-area ultrathin films of reduced graphene oxide as a transparent and flexible electronic material. *Nat Nano*, 3(5):270–274, 2008.

[55] Michael Naguib, Murat Kurtoglu, Volker Presser, Jun Lu, Junjie Niu, Min Heon, Lars Hultman, Yury Gogotsi, and Michel W. Barsoum. Two-Dimensional Nanocrystals Produced by Exfoliation of Ti_3AlC_2. *Advanced Materials*, 23(37):4248–4253, 2011.

[56] Chenyang Shi, Majid Beidaghi, Michael Naguib, Olha Mashtalir, Yury Gogotsi, and Simon J. L. Billinge. Structure of Nanocrystalline Ti_3C_2 MXene Using Atomic Pair Distribution Function. *Phys. Rev. Lett.*, 112:125501, 2014.

[57] Xuefeng Wang, Xi Shen, Yurui Gao, Zhaoxiang Wang, Richeng Yu, and Liquan Chen. Atomic-Scale Recognition of Surface Structure and Intercalation Mechanism of Ti_3C_2X. *Journal of the American Chemical Society*, 137(7):2715–2721, 2015.

[58] Babak Anasori, Maria R. Lukatskaya, and Yury Gogotsi. 2D metal carbides and nitrides (MXenes) for energy storage. 2:16098, 2017.

[59] Linda Karlsson. PhD Thesis of Linkoping University. 2016.

[60] L. Farbera M. Amerb R. Christinic M. W. Barsouma, T. El-Raghya and A. Adamsc. The Topotactic Transformation of Ti_3SiC_2 into a Partially Ordered Cubic TiiC0.67Si0.06) Phase by the Diffusion of Si into Molten Cryolite. *J. Electrochem. Soc.*, 146(10):3919, 1999.

[61] Michael Ghidiu, Maria R. Lukatskaya, Meng-Qiang Zhao, Yury Gogotsi, and Michel W. Barsoum. Conductive two-dimensional titanium carbide /'clay/' with high volumetric capacitance. *Nature*, 516(7529):78–81, 2014.

[62] J. Yang, M. Naguib, M. Ghidiu, L.-M Pan, J. Gu, J. Nanda, J. Halim, Y. Gogotsi, and M.W. Barsoum. Two-Dimensional Nb-Based M_4C_3 Solid Solutions (MXenes). *Journal of the American Ceramic Society*, 99(2):660–666, 2016.

[63] Babak Anasori, Yu Xie, Majid Beidaghi, Jun Lu, Brian C. Hosler, Lars Hultman, Paul R. C. Kent, Yury Gogotsi, and Michel W. Barsoum. Two-Dimensional, Ordered, Double Transition Metals Carbides (MXenes). *ACS Nano*, 9(10):9507–9516, 2015.

[64] Michael Ghidiu, Maria R Lukatskaya, Meng-Qiang Zhao, Yury Gogotsi, and Michel W Barsoum. Conductive two-dimensional titanium carbide 'clay' with high volumetric capacitance. *Nature*, 516(7529):78–81, 2014.

[65] A. Feng, Y. Yu, F. Jiang, Y. Wang, L. Mi, Y. Yu, and L. Song. Fabrication and thermal stability of NH_4HF_2-etched Ti_3C_2 MXene. *Ceramics International*, 43(8):6322–6328, 2017.

[66] Shen Lai, Jaeho Jeon, Sung Kyu Jang, Jiao Xu, Young Jin Choi, Jin-Hong Park, Euyheon Hwang, and Sungjoo Lee. Surface group modification and carrier transport properties of layered transition metal carbides (Ti_2CT_x, T: -OH, -F and -O). *Nanoscale*, 7:19390–19396, 2015.

[67] J. Xu, J. Shim, J.-H. Park, and S. Lee. MXene Electrode for the Integration of WSe_2 and MoS_2 Field Effect Transistors. *Advanced Functional Materials*, 26(29):5328–5334, 2016.

[68] Olha Mashtalir, Michael Naguib, Vadym N Mochalin, Yohan Dall'Agnese, Min Heon, Michel W Barsoum, and Yury Gogotsi. Intercalation and delamination of layered carbides and carbonitrides. *Nat Commun*, 4:1716, 2013.

[69] Olha Mashtalir, Maria R. Lukatskaya, Meng-Qiang Zhao, Michel W. Barsoum, and Yury Gogotsi. Amine-Assisted Delamination of Nb_2C MXene for Li-Ion Energy Storage Devices. *Advanced Materials*, 27(23):3501–3506, 2015.

[70] O. Mashtalir, M.R. Lukatskaya, A.I. Kolesnikov, E. Raymundo-Piñero, M. Naguib, M.W. Barsoum, and Y. Gogotsi. The effect of hydrazine intercalation on the structure and capacitance of 2D titanium carbide (MXene). *Nanoscale*, 8(17):9128–9133, 2016.

[71] Michael Naguib, Raymond R. Unocic, Beth L. Armstrong, and Jagjit Nanda. Large-scale delamination of multi-layers transition metal carbides and carbonitrides "MXenes". *Dalton Trans.*, 44:9353–9358, 2015.

[72] Mohammad Khazaei, Masao Arai, Taizo Sasaki, Chan-Yeup Chung, Natarajan S. Venkataramanan, Mehdi Estili, Yoshio Sakka, and Yoshiyuki Kawazoe. Novel Electronic and Magnetic Properties of Two-Dimensional Transition Metal Carbides and Nitrides. *Advanced Functional Materials*, 23(17):2185–2192, 2013.

[73] Yu Xie, Yohan Dalla Agnese, Michael Naguib, Yury Gogotsi, Michel W. Barsoum, Houlong L. Zhuang, and Paul R. C. Kent. Prediction and Characterization of MXene Nanosheet Anodes for Non-Lithium-Ion Batteries. *ACS Nano*, 8(9):9606–9615, 2014.

[74] Qing Tang, Zhen Zhou, and Panwen Shen. Are MXenes Promising Anode Materials for Li Ion Batteries? Computational Studies on Electronic Properties and Li Storage Capability of Ti_3C_2 and $Ti_3C_2X_2$ (X = F, OH) Monolayer. *Journal of the American Chemical Society*, 134(40):16909–16916, 2012.

[75] Hongming Weng, Ahmad Ranjbar, Yunye Liang, Zhida Song, Mohammad Khazaei, Seiji Yunoki, Masao Arai, Yoshiyuki Kawazoe, Zhong Fang, and Xi Dai. Large-gap two-dimensional topological insulator in oxygen functionalized MXene. *Phys. Rev. B*, 92:075436, 2015.

[76] J. Halim, S. Kota, M.R. Lukatskaya, M. Naguib, M.-Q. Zhao, E.J. Moon, J. Pitock, J. Nanda, S.J. May, and M.W. Gogotsi, Y.and Barsoum. Synthesis and Characterization of 2D Molybdenum Carbide (MXene). *Advanced Functional Materials*, 26(18):3118–3127, 2016.

[77] A. Lipatov, M. Alhabeb, M.R. Lukatskaya, A. Boson, Y. Gogotsi, and A. Sinitskii. Effect of Synthesis on Quality, Electronic Properties and Environmental Stability of Individual Monolayer Ti_3C_2 MXene Flakes. *Advanced Electronic Materials*, 2(12), 2016.

[78] A. Miranda, J. Halim, M.W. Barsoum, and A. Lorke. Electronic properties of freestanding $Ti_3C_2T_x$ MXene monolayers. *Applied Physics Letters*, 108(3), 2016.

[79] Babak Anasori, Chenyang Shi, Eun Ju Moon, Yu Xie, Cooper A. Voigt, Paul R. C. Kent, Steven J. May, Simon J. L. Billinge, Michel W. Barsoum, and Yury Gogotsi. Control of electronic properties of 2D carbides (MXenes) by manipulating their transition metal layers. *Nanoscale Horiz.*, 1:227–234, 2016.

[80] Chen Si, Jian Zhou, and Zhimei Sun. Half-Metallic Ferromagnetism and Surface Functionalization-Induced Metal Insulator Transition in Graphene-like Two-Dimensional Cr_2C Crystals. *ACS Applied Materials & Interfaces*, 7(31):17510–17515, 2015.

[81] Zheng Ling, Chang E. Ren, Meng-Qiang Zhao, Jian Yang, James M. Giammarco, Jieshan Qiu, Michel W. Barsoum, and Yury Gogotsi. Flexible and conductive MXene films and nanocomposites with high capacitance. *Proceedings of the National Academy of Sciences*, 111(47):16676–16681, 2014.

[82] K. Hantanasirisakul, M.-Q. Zhao, P. Urbankowski, J. Halim, B. Anasori, S. Kota, C.E. Ren, M.W. Barsoum, and Y. Gogotsi. Fabrication of $Ti_3C_2T_x$ MXene Transparent Thin Films with Tunable Optoelectronic Properties. *Advanced Electronic Materials*, 2(6), 2016.

[83] C. Zhang, S.J. Kim, M. Ghidiu, M.-Q. Zhao, M.W. Barsoum, V Nicolosi, and Y. Gogotsi. Layered Orthorhombic Nb_2O_5@$Nb_4C_3T_x$ and TiO_2@$Ti_3C_2T_x$ Hierarchical Composites for High Performance Li-ion Batteries. *Advanced Functional Materials*, 26(23):4143–4151, 2016.

[84] Maria R. Lukatskaya, Olha Mashtalir, Chang E. Ren, Yohan DallAgnese, Patrick Rozier, Pierre Louis Taberna, Michael Naguib, Patrice Simon, Michel W. Barsoum, and Yury Gogotsi. Cation Intercalation and High Volumetric Capacitance of Two-Dimensional Titanium Carbide. *Science*, 341(6153):1502–1505, 2013.

[85] Qianku Hu, Dandan Sun, Qinghua Wu, Haiyan Wang, Libo Wang, Baozhong Liu, Aiguo Zhou, and Julong He. MXene: A New Family of Promising Hydrogen Storage Medium. *The Journal of Physical Chemistry A*, 117(51):14253–14260, 2013.

[86] J. Ran, G. Gao, F.-T. Li, T.-Y. M, A. Du, and S.-Z. Qiao. Ti_3C_2 MXene co-catalyst on metal sulfide photo-absorbers for enhanced visible-light photocatalytic hydrogen production. *Nature Communications*, 8, 2017.

[87] Xu Zhang, Zihe Zhang, Jielan Li, Xudong Zhao, Dihua Wu, and Zhen Zhou. Ti_2CO_2 MXene: a highly active and selective photocatalyst for CO_2 reduction. *J. Mater. Chem. A*, 5:12899–12903, 2017.

[88] R. B. Rakhi, Pranati Nayak, Chuan Xia, and Husam N. Alshareef. Novel amperometric glucose biosensor based on MXene nanocomposite. 6:36422, 2016.

[89] Hui Liu, Congyue Duan, Chenhui Yang, Wanqiu Shen, Fen Wang, and Zhenfeng Zhu. A novel nitrite biosensor based on the direct electrochemistry of hemoglobin immobilized on MXene-Ti_3C_2. *Sensors and Actuators B: Chemical*, 218(Supplement C):60 – 66, 2015.

[90] Y. Manawi, V. Kochkodan, M.A. Hussein, M.A. Khaleel, M. Khraisheh, and N. Hilal. Can carbon-based nanomaterials revolutionize membrane fabrication for water treatment and desalination? *Desalination*, 391:69–88, 2016.

[91] Jianxin Guo, Qiuming Peng, Hui Fu, Guodong Zou, and Qingrui Zhang. Heavy-Metal Adsorption Behavior of Two-Dimensional Alkalization-Intercalated MXene by First-Principles Calculations. *The Journal of Physical Chemistry C*, 119(36):20923–20930, 2015.

[92] Bengt Hallstedt, Denis Music, and Zhimei Sun. Thermodynamic evaluation of the Al-Cr-C system. *Zeitschrift fur Metallkunde*, 97(5):539–542, 2006.

[93] Bengt Hallstedt. Thermodynamic evaluation of the Al-V-C system. *Calphad*, 41:156 – 159, 2013.

[94] H. Okamoto. Al-V (Aluminum-Vanadium). *J. Phase Equilib. Diffus.*, 33:491, 2012.

[95] Volker Presser, Michael Naguib, Laurent Chaput, Atsushi Togi, Gilles Hug, and Michel W. Barsoum. Erratum: First-order Raman scattering of the MAX phases: Ti_2AlN, $Ti_2AlC_{0.5}N_{0.5}$, Ti_2AlC, $(Ti_{0.5}V_{0.5})_2AlC$, V_2AlC, Ti_3AlC_2, and Ti_3GeC_2. *Journal of Raman Spectroscopy*, 44(7):1060–1060, 2013.

[96] Jingyang Wang, Yanchun Zhou, Zhijun Lin, Fanling Meng, and Feng Li. Raman active phonon modes and heat capacities of Ti_2AlC and Cr_2AlC ceramics: first-principles and experimental investigations. *Applied Physics Letters*, 86(10):101902, 2005.

[97] Jonathan E. Spanier, Surojit Gupta, Maher Amer, and Michel W. Barsoum. Vibrational behavior of the $M_{n+1}AX_n$ phases from first-order Raman scattering (M=Ti,V,Cr,A=Si,X=C,N). *Phys. Rev. B*, 71:012103, 2005.

[98] Ranran Su, Hongliang Zhang, Xiangpeng Meng, Liqun Shi, and Chaozhuo Liu. Synthesis of Cr_2AlC thin films by reactive magnetron sputtering. *Fusion Engineering and Design*, page in press, 2017.

[99] Frederic. Mercier, Thierry. Ouisse, and Didier. Chaussende. Morphological instabilities induced by foreign particles and Ehrlich-Schwoebel effect during the two-dimensional growth of crystalline Ti_3SiC_2. *Phys. Rev. B*, 83:075411, 2011.

[100] W. Kossel. Zur Energetik von Oberflachenvorgangen. *Annalen der Physik*, 413(5):457–480, 1934.

[101] V. V. Voronkov. *Structure of a Crystal Surface and Kossel's Model*, pages 1–17. Springer US, Boston, MA, 1976.

[102] Volker Presser, Michael Naguib, Laurent Chaput, Atsushi Togo, Gilles Hug, and Michel W. Barsoum. First-order Raman scattering of the MAX phases: Ti_2AlN, $Ti_2AlC0.5N0.5$, Ti_2AlC, $Ti_{0.5}V_{0.5})_2AlC$, V_2AlC, Ti_3AlC_2, and Ti_3GeC_2. *Journal of Raman Spectroscopy*, 43(1):168–172, 2012.

[103] W. K. Burton, N. Cabrera, and F. C. Frank. The Growth of Crystals and the Equilibrium Structure of their Surfaces. *Philosophical Transactions of the Royal Society of London A: Mathematical, Physical and Engineering Sciences*, 243(866):299–358, 1951.

[104] Le Thi Mai Hoa, T. Ouisse, and D. Chaussende. Critical assessment of birefringence imaging of dislocations in 6H silicon carbide. *Journal of Crystal Growth*, 354(1):202 – 207, 2012.

[105] Olga Kruglova, Fabian Brau, Didier Villers, and Pascal Damman. How Geometry Controls the Tearing of Adhesive Thin Films on Curved Surfaces. *Phys. Rev. Lett.*, 107:164303, 2011.

[106] Dipanjan Sen, Kostya S. Novoselov, Pedro M. Reis, and Markus J. Buehler. Tearing Graphene Sheets From Adhesive Substrates Produces Tapered Nanoribbons. *Small*, 6(10):1108–1116, 2010.

[107] K. S. Novoselov, D. Jiang, F. Schedin, T. J. Booth, V. V. Khotkevich, S. V. Morozov, and A. K. Geim. Two-dimensional atomic crystals. *Proceedings of the National Academy of Sciences of the United States of America*, 102(30):10451–10453, 2005.

[108] L. B. Valdes. Resistivity Measurements on Germanium for Transistors. *Proceedings of the IRE*, 42(2):420–427, 1954.

[109] L. J Van der Pauw. A Method of Measuring Specific Resistivity and Hall Effect of Discs of Arbitrary Shape. *Philips Research Reports.*, 12:1–9, 1958.

[110] H. C. Montgomery. Method for Measuring Electrical Resistivity of Anisotropic Materials. *Journal of Applied Physics*, 42(7):2971–2975, 1971.

[111] M.Charalambous. PhD Thesis of University of Grenoble. 1992.

[112] Melissa Charalambous, Jacques Chaussy, and Pascal Lejay. Evidence from resistivity measurements along the c axis for a transition within the vortex state for Hab in single-crystal $YBa_2Cu_3O_7$. *Phys. Rev. B*, 45:5091–5094, 1992.

[113] Nie Luo and G.H. Miley. Kohler's rule and relaxation rates in high-Tc superconductors. *Physica C: Superconductivity*, 371(4):259 – 269, 2002.

[114] M. K. Chan, M. J. Veit, C. J. Dorow, Y. Ge, Y. Li, W. Tabis, Y. Tang, X. Zhao, and M. Greven. In-Plane Magnetoresistance Obeys Kohler's Rule in the Pseudogap Phase of Cuprate Superconductors. *Phys. Rev. Lett.*, 113:177005, 2014.

[115] A. Narduzzo, A. Enayati-Rad, S. Horii, and N. E. Hussey. Possible Coexistence of Local Itinerancy and Global Localization in a Quasi-One-Dimensional Conductor. *Phys. Rev. Lett.*, 98:146601, 2007.

[116] Wenbo Yu. PhD Thesis of University of Poitiers. 2014.

[117] H Rosenberg. *The Solid State*. Oxford University Press, 2004.

[118] M. F. Crommie and A. Zettl. Thermal-conductivity anisotropy of single-crystal $Bi_2Sr_2CaCu_2O_8$. *Phys. Rev. B*, 43:408–412, 1991.

[119] B. Podor and G. Remenyi. Parabolic negative magnetoresistance in two-dimensional electron gas in InGaAs/InP. In *2008 31st International Spring Seminar on Electronics Technology*, pages 195–200, 2008.

[120] Johannes Jobst, Daniel Waldmann, Igor V. Gornyi, Alexander D. Mirlin, and Heiko B. Weber. Electron-Electron Interaction in the Magnetoresistance of Graphene. *Phys. Rev. Lett.*, 108:106601, 2012.

[121] D. Y. Xing, M. Liu, and C. S. Ting. Out-of-plane transport mechanism in the high-T_c oxide Y-Ba-Cu-O. *Phys. Rev. B*, 38:11992–11995, 1988.

[122] K.-H. Yoo, D. H. Ha, Y. K. Park, and J. C. Park. Out-of-plane transport properties of $Bi_2Sr_2CaCu_2O_8$ single crystals in normal and mixed states. *Phys. Rev. B*, 49:4399–4402, 1994.

[123] N. E. Hussey, J. R. Cooper, Y. Kodama, and Y. Nishihara. Out-of-plane magnetoresistance of $La_{2-x}Sr_xCuO_4$: Evidence for intraplanar scattering in the *c*-axis transport. *Phys. Rev. B*, 58:R611–R614, 1998.

[124] N. W. Ashcroft and N. D. Mermin. Solid State Physics. Saunders College, Philadelphia, 1976.

[125] Vincent Mauchamp, Wenbo Yu, Loik Gence, Luc Piraux, Thierry Cabioch, Veronique Gauthier, Per Eklund, and Sylvain Dubois. Anisotropy of the resistivity and charge-carrier sign in nanolaminated Ti_2AlC: Experiment and ab initio calculations. *Phys. Rev. B*, 87:235105, 2013.

[126] L. Chaput, G. Hug, P. Pécheur, and H. Scherrer. Thermopower of the 312 MAX phases Ti_3SiC_2, Ti_3GeC_2, and Ti_3AlC_2. *Phys. Rev. B*, 75:035107, 2007.

[127] J. M. Ziman. Electrons and phonons. Clarendon press, Oxford, 1960.

[128] N. C. Banik and A. W. Overhauser. Hall coefficient of a holelike Fermi surface. *Phys. Rev. B*, 18:1521–1532, 1978.

[129] N. P. Ong. Geometric interpretation of the weak-field Hall conductivity in two-dimensional metals with arbitrary Fermi surface. *Phys. Rev. B*, 43:193–201, 1991.

[130] Vincent Mauchamp, Wenbo Yu, Loik Gence, Luc Piraux, Thierry Cabioc'h, Veronique Gauthier, Per Eklund, and Sylvain Dubois. Anisotropy of the resistivity and charge-carrier sign in nanolaminated Ti_2AlC: Experiment and ab initio calculations. *Phys. Rev. B*, 87:235105, 2013.

[131] Michael Naguib, Joseph Halim, Jun Lu, Kevin M. Cook, Lars Hultman, Yury Gogotsi, and Michel W. Barsoum. New Two-Dimensional Niobium and Vanadium Carbides as Promising Materials for Li-Ion Batteries. *Journal of the American Chemical Society*, 135(43):15966–15969, 2013. PMID: 24144164.

[132] A.M. Byeon, A.and Glushenkov, B. Anasori, P. Urbankowski, J. Li, B.W. Byles, B. Blake, K.L. Van Aken, S. Kota, E. Pomerantseva, J.W. Lee, Y. Chen, and Y. Gogotsi. Lithium-ion capacitors with 2D Nb_2CTx (MXene) – carbon nanotube electrodes. *Journal of Power Sources*, 326:686–694, 2016.

[133] M. Ghidiu, M. Naguib, C. Shi, O. Mashtalir, L. M. Pan, B. Zhang, J. Yang, Y. Gogotsi, S. J. L. Billinge, and M. W. Barsoum. Synthesis and characterization of two-dimensional Nb_4C_3 (MXene). *Chem. Commun.*, 50:9517–9520, 2014.

[134] Jing Chen, Ke Chen, Dingyi Tong, Youju Huang, Jiawei Zhang, Jianming Xue, Qing Huang, and Tao Chen. CO_2 and temperature dual responsive "Smart" MXene phases. *Chem. Commun.*, 51:314–317, 2015.

[135] Dandan Sun, Mingshan Wang, Zhengyang Li, Guangxin Fan, Li-Zhen Fan, and Aiguo Zhou. Two-dimensional Ti_3C_2 as anode material for Li-ion batteries. *Electrochemistry Communications*, 47:80 – 83, 2014.

[136] Kristopher J. Harris, Matthieu Bugnet, Michael Naguib, Michel W. Barsoum, and Gillian R. Goward. Direct Measurement of Surface Termination Groups and Their Connectivity in the 2D MXene V_2CT_x Using NMR Spectroscopy. *The Journal of Physical Chemistry C*, 119(24):13713–13720, 2015.

[137] A.N. Enyashin and A.L. Ivanovskii. Atomic structure, comparative stability and electronic properties of hydroxylated Ti_2C and Ti_3C_2 nanotubes. *Computational and Theoretical Chemistry*, 989:27 – 32, 2012.

[138] Yu Xie, Michael Naguib, Vadym N. Mochalin, Michel W. Barsoum, Yury Gogotsi, Xiqian Yu, Kyung-Wan Nam, Xiao-Qing Yang, Alexander I. Kolesnikov, and Paul R. C. Kent. Role of Surface Structure on Li-Ion Energy Storage Capacity of Two-Dimensional Transition-Metal Carbides. *Journal of the American Chemical Society*, 136(17):6385–6394, 2014.

[139] Linda H. Karlsson, Jens Birch, Joseph Halim, Michel W. Barsoum, and Per O. Å. Persson. Atomically Resolved Structural and Chemical Investigation of Single MXene Sheets. *Nano Letters*, 15(8):4955–4960, 2015.

[140] Xianfen Wang, Satoshi Kajiyama, Hiroki Iinuma, Eiji Hosono, Shinji Oro, Isamu Moriguchi, Masashi Okubo, and Atsuo Yamada. Pseudocapacitance of MXene nanosheets for high-power sodium-ion hybrid capacitors. *Nat Commun*, 6:6544, 2015.

[141] L. Shi, T. Ouisse, E. Sarigiannidou, O. Chaix-Pluchery, H. Roussel, D. Chaussende, and B. Hackens. Synthesis of single crystals of V_2AlC phase by high-temperature solution growth and slow cooling technique. *Acta Materialia*, 83:304 – 309, 2015.

[142] Horacio Coy Diaz, Rafik Addou, and Matthias Batzill. Interface properties of CVD grown graphene transferred onto $MoS_2(0001)$. *Nanoscale*, 6:1071–1078, 2014.

[143] O. Ochedowski, B. Kleine Bussmann, and M. Schleberger. Graphene on Mica - Intercalated Water Trapped for Life. *Scientific Reports*, 4:6003, 2014.

[144] http://www.wiredchemist.com/chemistry/data/atomic-and-ionic-radii.

[145] Wai-Yim Ching, Yuxiang Mo, Sitaram Aryal, and Paul Rulis. Intrinsic Mechanical Properties of 20 MAX-Phase Compounds. *Journal of the American Ceramic Society*, 96(7):2292–2297, 2013.

[146] B. Ahmed, D.H. Anjum, M.N. Hedhili, Y. Gogotsi, and H.N. Alshareef. H_2O_2 assisted room temperature oxidation of Ti_2C MXene for Li-ion battery anodes. *Nanoscale*, 8(14):7580–7587, 2016.

[147] K. J Cai, Y. Zheng, P. Shen, and S. Y. Chen. TiCx-Ti_2C nanocrystals and epitaxial graphene-based lamellae by pulsed laser ablation of bulk TiC in vacuum. *CrystEngComm*, 16:5466–5474, 2014.

[148] A. Miranda, J. Halim, M. W. Barsoum, and A. Lorke. Electronic properties of freestanding $Ti_3C_2T_x$ MXene monolayers. *Applied Physics Letters*, 108(3):033102, 2016.

[149] Mohammad Khazaei, Ahmad Ranjbar, Mahdi Ghorbani-Asl, Masao Arai, Taizo Sasaki, Yunye Liang, and Seiji Yunoki. Nearly free electron states in MXenes. *Phys. Rev. B*, 93:205125, 2016.

[150] J. He, P. Lyu, and P. Nachtigall. New two-dimensional Mn-based MXenes with room-temperature ferromagnetism and half-metallicity. *Journal of Materials Chemistry C*, 4(47):11143–11149, 2016.

[151] Junping Hu, Bo Xu, Chuying Ouyang, Shengyuan A. Yang, and Yugui Yao. Investigations on V_2C and V_2CX_2 (X = F, OH) Monolayer as a Promising Anode Material for Li Ion Batteries from First-Principles Calculations. *The Journal of Physical Chemistry C*, 118(42):24274–24281, 2014.

[152] X Guo, P Zhang, and J Xue. Ti_2CO_2 Nanotubes with Negative Strain Energies and Tunable Band Gaps Predicted from First-Principles Calculations. *Journal of Physical Chemistry Letters*, 7(24):5280–5284, 2016.

[153] L. Li. Lattice dynamics and electronic structures of $Ti_2C_2O_2$ and $Mo_2TiC_2O_2$ (MXenes): The effect of Mo substitution. *Computational Materials Science*, 124:8–14, 2016.

[154] Y. Zhou, K. Luo, X. Zha, Z. Liu, X. Bai, Q. Huang, Z. Guo, C.-T. Lin, and S. Du. Electronic and transport properties of Ti_2CO_2 MXene nanoribbons. *Journal of Physical Chemistry C*, 120(30):17143–17152, 2016.

[155] Mohammad Khazaei, Masao Arai, Taizo Sasaki, Chan-Yeup Chung, Natarajan S. Venkataramanan, Mehdi Estili, Yoshio Sakka, and Yoshiyuki Kawazoe. Novel Electronic and Magnetic Properties of Two-Dimensional Transition Metal Carbides and Nitrides. *Advanced Functional Materials*, 23(17):2185–2192, 2013.

[156] Guoying Gao, Guangqian Ding, Jie Li, Kailun Yao, Menghao Wu, and Meichun Qian. Monolayer MXenes: promising half-metals and spin gapless semiconductors. *Nanoscale*, 8:8986–8994, 2016.

[157] Aurelie Champagne, Lu Shi, Thierry Ouisse, Benoit Hackens, and Jean-Christophe Charlier. Electronic and vibrational properties of V_2C-based MXenes: from experiments to first-principles modelling. *submitted*.

[158] Joseph Halim, Maria R. Lukatskaya, Kevin M. Cook, Jun Lu, Cole R. Smith, Lars-Åke Näslund, Steven J. May, Lars Hultman, Yury Gogotsi, Per Eklund, and Michel W. Barsoum. Transparent Conductive Two-Dimensional Titanium Carbide Epitaxial Thin Films. *Chemistry of Materials*, 26(7):2374–2381, 2014.

[159] Quanzheng Tao, Martin Dahlqvist, Jun Lu, Sankalp Kota, Rahele Meshkian, Joseph Halim, Justinas Palisaitis, Lars Hultman, Michel W. Barsoum, Per O. Å. Persson, and Johanna Rosen. Two-dimensional $Mo_{1.33}C$ MXene with divacancy ordering prepared from parent 3D laminate with in-plane chemical ordering. 8:14949, 2017.

[160] Thierry Ouisse and Michel W. Barsoum. Magnetotransport in the MAX phases and their 2D derivatives: MXenes. *Materials Research Letters*, 0(0):1–14, 0.

List of Figures

List of Tables